SEASONAL AND INTER-ANNUAL CHANGES IN THE COMPUTATION OF AURA MLS HCL DEPLETION AND PSC-INDUCED AREAS IN THE ANTARCTIC POLAR STRATOSPHERE: 2005-2010 CLIMATE-CHEMISTRY ASSESSMENT. THE ROLE OF CLOUDS IN THE ANTARCTIC MIDDLE ATMOSPHERE

A Dissertation

by

ANDOLSA AREVALO TORRES

Submitted in partial fulfillment of the requirements for the

degree of Master of Science in Physics

in the University of Canterbury

Department of Physics and Astronomy,

Christchurch, New Zealand

June 2012

Seasonal and Interannual Changes in the Computation of Aura MLS HCl Depletion and PSC-Induced Areas in the Antarctic Stratosphere: 2005-2010 Climate-Chemistry Assessment. *The Role of Clouds in the Antarctic Middle Atmosphere*

Preface

The work described in this publication was performed by Andolsa Arévalo Torres, member of the Department of Physics and Astronomy of the University of Canterbury from August 2008 to June 2012, under joint research fund: College of Science Scholarship and research fund "N30" with the College of Science for New Zealand's University of Canterbury and Dirección General de Relaciones Internacionales (DGRI) for Mexico's Secretaría de Educación Pública (SEP), respectively.

This specific work was performed in accordance with the up-to-date postgraduate research administrative guidelines of the University of Canterbury's Department of Physics and Astronomy.

Abstract

An examination of the seasonal and spatial distribution of Polar Stratospheric Clouds (PSCs) inferred from standard temperature profiles in the lower-middle atmosphere above Antarctica, as derived from the Earth Observing System (EOS) Aura Microwave Limb Sounder (MLS) satellite observations and NCEP/NCAR assimilations, is provided. Chemical volume mixing ratio (VMR) observations of EOS Aura MLS v2.2 hydrogen chloride (HCl) were used to show the interannual variability of PSC formation with respect to stratospheric chlorine partitioning during five Southern Hemisphere Antarctic seasons from 2005 to 2009. A remarkable first set of results, obtained from an algorithm developed for modelling HCl depletion areas in the Antarctic polar vortex region, and based on satellite observations, is presented. In particular, the analysis of HCl concentration data obtained from 2006 indicated that the area processed for HCl was larger than the area of PSC during some periods of Antarctic winter, and that this result was robust with respect to the various PSC formation and HCl depletion thresholds utilized. The results suggest that an underestimation in chlorine activation area can occur when temperature thresholds for PSC formation thresholds are employed. The work presented here also evaluated chlorine activation via sulfate aerosol (SA) in the Southern Hemisphere 2006 stratosphere, based on satellite measurements of water vapor (H_2O) and constant values of SA, by implementing the T_{ACL} formula of *Drdla and Müller* [2010] in contrast to the T_{NAT} formula of *Hanson and Mauersberger* [1988]. The results indicated that the former formula was not completely sufficient for accurately modeling areas of depleted HCl and chlorine deactivation for all pressure surfaces in the Antarctic stratosphere.

Based on the results of this study, the role of SA in chlorine activation appears to be more important at lower altitudes than for areas higher in the stratosphere.

Keywords: Chlorine activation, Polar Stratospheric Clouds, satellite observations, Antarctic stratosphere, hydrogen chloride, sulfate aerosol.

Key Points: HCl removal (and Cl activation) occurs so high up [*Solomon*, 2011].

Early-season underestimation of Cl activation area can occur for 195 K threshold.

Sulfate aerosol in Cl activation alone might be more important at low stratospheric altitudes than higher up in the Antarctic stratosphere.

DEDICATION

To my father[†]

Acknowledgements

I would like to thank my committee chair, Dr. Fraser, and my committee members, Dr. Morgenstern, and Prof. Cottrell, for their guidance and support throughout the course of this research.

Thanks also to my friends and colleagues and the department faculty and staff for making my time at University of Canterbury a fine experience. I also want to extend my gratitude to Antarctica New Zealand for support to the KO55 (2008, 2011) event and the United States' McMurdo General Hospital. Funding for this work was provided by the University of Canterbury and the SEP–GRI program (Secretaría de Educación Pública – Dirección General de Relaciones Internacionales; Programa Becas Complemento; postgraduate research fund No. 30).

The Aura MLS v2.2 Level 2 data used in this work were obtained from the website of the Goddard Earth Sciences Data and Information Services Center (GES DISC) of the National Aeronautics and Space Administration (NASA), at http://mirador.gsfc.nasa.gov/. The NCEP/NCAR reanalysis data were obtained, on request, from the datastore node of the Atmospheric Group of the University of Canterbury. B. A. is thanked for fruitful discussions prior to the preparation of this work. Three anonymous reviewers are thanked for their useful comments, which improved this work. R. D. Graham, S. Berthet, J. Sheinbaum, M. L. Santee and C. J. Wright are thanked for further discussions.

Nomenclature

The following notation is used throughout this document:

ΔHX	Depletion Threshold, where X = Cl^-
APV	Antarctic Polar Vortex
APVR	Antarctic Polar Vortex Region
AH	Arrival Heights, Antarctica
CH_4	Methane
Cl Activation	Chlorine Activation
Cl_y	Odd chlorine family Cl_y= Cl + ClO + $2Cl_2O_2$ + OClO + ClOO + + $2Cl_2$ + HCl + HOCl + $ClONO_2$ + $ClNO_2$ + BrCl
ClO	Chlorine Monoxide
ClOO	Chlorine peroxyl radical
Cl_2O_2	ClO dimer (dichlorine peroxide)
$ClONO_2$	Chlorine Nitrate
COSMIC GPS-RO	Constellation Observing System for Meteorology, Ionosphere and Climate (COSMIC) Global Positioning System Radio Occultation (GPS-RO)
EOS	Earth Observing System
GC	Grid Cell (definition)
H_2O	Water Vapor
HCl	Hydrogen Chloride (hydrochloric acid)
HNO_3	Nitric Acid

JPL	Jet Propulsion Laboratory
LST	Local Solar Time
MLS	Microwave Limb Sounder
NASA	National Aeronautics and Space Administration
NAT	Nitric Acid Trihydrate ($HNO_3 \cdot 3H_2O$)
NO	Nitric oxide
N_2O	Nitrous oxide
NCEP/NCAR	**"reanalysis"** The National Centers for Environmental Prediction (NCEP)/National Center for Atmospheric Research (NCAR)
NDACC Data	Network for the Detection of Atmospheric Composition Change (NDACC) data
O_2	Molecular oxygen
OClO	Chlorine Dioxide
OH	Hydroxyl Radical
P	Pressure
ppb(m)v	Parts per billion (million) of volume
PSC	Polar Stratospheric Cloud
SA	Sulfate Aerosol
SAT	Sulfuric Acid Trihydrate
SB	Scott Base, Antarctica
SH	Southern Hemisphere
SZA	Solar Zenith Angle
T	Temperature
T_{ACL}	Chlorine Activation temperature threshold [*Drdla and Müller*, 2010]

T_{ice} or T_{ICE}	Ice frost point [*Marti and Mauersberger*, 1993; *Murphy and Koop*, 2005]
T_{NAT}	NAT equilibrium (saturation) temperature threshold [*Hanson and Mauersberger*, 1988]
UT	Universal Time
VMR	Volume Mixing Ratio

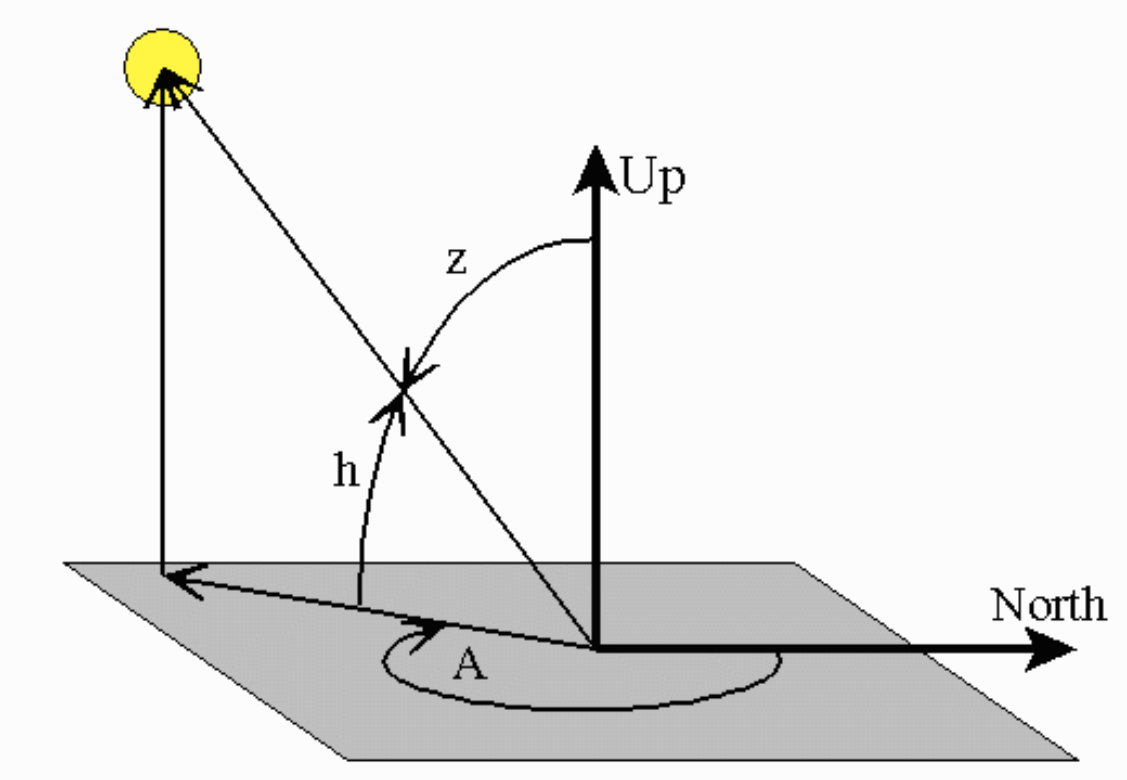

Figure i.1. Illustration of the Solar Zenith and SZA ('z'), Azimuth angle ('A') and elevation angle ('h') identified. [Available from NASA, (http://www.nasa.gov)].

Table of Contents

Page

PREFACE ..... **iii**

ABSTRACT ..... **iv**

ACKNOWLEDGEMENTS ..... **vi**

NOMENCLATURE vii

TABLE OF CONTENTS ..... **viii**

LIST OF FIGURES ..... **xv**

LIST OF TABLES ..... **xxvi**

1. INTRODUCTION **1**

1.1 The importance of research/purpose 1

1.2 Objectives 3

1.2.1 General Objective 3

1.2.2 Specific Objectives 3

1.3 Scope 4

2. EOS AURA MLS **5**

2.1 Mission 5

2.1.1 Introduction 5

2.1.2 Database version issue correction 6

2.1.3 Chemical Aura MLS data 7

2.1.3.1 HCl data overview 7

2.1.3.1.1 Aura MLS HCl data assessment 9

2.1.3.2 ClO and N_2O data: overview 10

2.1.3.3 HNO_3 satellite measurements 13

2.1.3.4 Water vapor data 16

2.1.3.5 Other Chemical data: data review 20

2.1.4 Aura MLS Temperature 25

2.1.4.1 Temperature databases: v1.5 vs. v2.2 27

2.1.4.2 COSMIC GPS-RO vs. Aura MLS v2.2 Temperature 29

2.1.5 Aura MLS HCl, ClO and Temperature: analysis. Introduction .. 31

2.1.6 Aura MLS Hydroxyl Radical 66

2.2 NCEP/NCAR 2.5º assimilations 66

3. POLAR STRATOSPHERIC OZONE CHEMISTRY: BACKGROUND ... 73

3.1 The Stratosphere 73

3.2 Polar Ozone Depletion: History 76

3.3 The Missing Link in Ozone Depletion: PSC 81

3.4 Catalytic Chemical Reactions 86

3.5 The Seasonal Cycle of Ozone Depletion 90

4. PSC MODELING AND ALGORITHM DEVELOPMENT I: METHODS 92

4.1 PSC Classification/Definition 92

4.2 PSC Modeling. Algorithm Development: First Generation 93

4.2.1 Literature Recourse 93

4.2.2 UTM–UPS Grid 96

4.2.2.1 UTM Grid Specifications 97

4.2.2.2 Projection: UPS. Description 100

4.2.3 Lunar Method 102

4.2.4 Triangulation Method 102

4.2.5 Proportions Approach 106

4.2.6 Spherical Trigonometry 108

4.2.7 Discussion 122

4.3 NCEP/NCAR and EOS MLS v2.2 data sets 131

4.4 PSC surface area calculation error analysis 134

4.5 T_{NAT} and PSC area 136

5. PSC MODELING AND ALGORITHM DEVELOPMENT II: VALIDATION 154

5.1 PSC algorithm development (inclusion) 154

5.1.1 Monte Carlo Simulation 156

5.2 PSC temperature threshold integration 156

6. POLAR STRATOSPHERIC CHLORINE-CHEMISTRY - PRIMARY STUDY CASE: ANTARCTICA 162

6.1 Chlorine Activation via surface reactions 162

6.2 The HCl depression algorithm and the HCl threshold definition 164

6.3 The extent of HCl depletion 167

6.4 HCl depletion and PSC surface areal coverage 170

6.4.1 Pearson's r correlation coefficients (PCCs) computation 173

6.5 Other Aura MLS products linked to chlorine activation 176

7. TEMPERATURE VS. HCL DEPLETION ISSUE RECONCILIATION 180

7.1 Interannual Variability 180

7.2 The Role of Frozen Aerosol 181

7.2.1 HCl depletion, T_{NAT}, and T_{ACL} 181

7.3 HCl depletion and PSC surface areal coverage: Second generation 188

7.3.1 Antarctic winter 2010: a closer chemical look 196

8. OROGRAPHIC GRAVITY WAVES AND PSC 197

8.1 Introduction 197

8.2 Aura MLS validation 199

9. DISCUSSION, SUMMARY AND CONCLUSIONS, FUTURE WORK 237

9.1 Discussion 237

9.2 Summary and conclusions 241

9.3 Future work 243

9.3.1 Cl Activation Threshold: A Robust parameterization 243

9.3.2 Photochemical model 244

9.3.3 Small-scale Temperature fluctuations, PSC and Cl activation 244

9.3.4 Methane and chlorine nitrate data 244

9.3.5 AH's FTIR 245

A EOS MLS v2.2 temperature: Quality Control Analysis 246

B EOS MLS measurement locations and objectives 249

C T_{NAT}, T_{ice} and T_{STS} computation derived from Aura MLS v.2.2--2005-- 251

D UT, LST and SZA programming routines 253

REFERENCES I 256

REFERENCES II 272

LIST OF FIGURES

FIGURE **Page**

i.1 Illustration of the Solar Zenith xii

2.1 Schematic of NASA's Aura satellite..... 6

2.2 Number of data points available per month and per year from the Aura MLS v2.2 HCl dataset 8

2.3 Time series of MLS v2.2 HCl daily global means 9

2.4 Time series of MLS v2.2 HCl daily global means at different altitudes.... 10

2.5 Number of data points available per month and per year from the Aura MLS v2.2 ClO dataset 12

2.5 Comparison between standard MLS ClO data and daytime MLS ClO data 13

2.6 Mean day-night differences of HCl and ClO 13

2.7 Number of data points available per month per year from the Aura MLS v2.2 HNO_3 dataset 15

2.8 Contour plot of Aura MLS HNO_3 16

2.11 Lowering the quality threshold over the entire polar region 27

2.11 Latitude versus Aura MLS LST 27

2.12 Number of data points available per month and per year from the Aura MLS v2.2 Temperature dataset 29

2.13 Hövmoller Diagrams of MLS temperatures and COSMIC temperatures.. 30

2.14 Hövmoller Diagrams of MLS temperatures and COSMIC temperatures.. 31

2.15 Seasonal evolution of zonally averaged Aura MLS standard temperature,

HCl, and daytime ClO as function of latitude at approximately 17 km..... 32

2.16 Seasonal evolution of zonally averaged Aura MLS standard temperature, HCl, and daytime ClO as function of latitude ~20 km..... 33

2.17 Seasonal evolution of zonally averaged Aura MLS standard temperature, HCl, and daytime ClO as function of latitude ~23 km..... 33

2.18 Seasonal evolution of zonally averaged Aura MLS standard temperature, HCl, and daytime ClO as function of latitude ~26 km..... 34

2.19 Seasonal evolution of zonally averaged Aura MLS standard temperature, HCl, and daytime ClO as function of latitude ~29 km..... 34

2.20 MLS HCl data MLS HCl data interpolated and smoothed 37

2.21 The algorithm of HCl turning points calculation's results over Antarctic Band 1 38

2.22 The algorithm of HCl turning points calculation's results over Antarctic Band 2 39

2.23 The algorithm of HCl turning points calculation's results over Antarctic Band 3 40

2.24 The algorithm of HCl turning points calculation's results over Antarctic Band 4 41

2.25 The algorithm of HCl turning points calculation's results over Antarctic Band 5 42

2.26 Onset and end of an MLS south viewing period for each stratospheric event: ClO, HCl and PSC 43

2.27 HCl curves..... 45

2.28 Example of how the algorithm for ClO activation/deactivation and respective dates are calculated..... 48

2.29 Timeseries of uncorrected daytime (SZA < 92º) ClO data at different stratospheric altitudes 50

2.30 Diagram to present the two different phases--we divide up the HCl evolution patterns over the Antarctic polar vortex region 53

2.31 Evolution of HCl, Temperature and daytime ClO over APVR..... 56

2.32 Time series of vortex average MLS HCl 57

2.33 Timeseries of MLS HCl for only day 1 to day 180 data 61

2.34 Correlation between HCl and T during phase A from MLS measurements 61

2.35 Timeseries of MLS HCl for only day 200 to day 365 data 62

2.36 Correlation between HCl and T during phase B from MLS measurements 62

2.37 Temporal evolution of Cl_y 64

2.38 Pearson's Correlation Coefficients (PCC) for different samples of temperature over SH..... 67

3.1 Schematic representation of the thermal structure of the atmosphere with its different layers 75

3.2 Variation in temperature and ozone concentration up through the atmosphere..... 77

3.3 A timeline of key events associated with ozone chemistry and the Ozone Hole 80

3.4 A historic depiction of the first reported sight of Polar Stratospheric Clouds in Antarctica 81

3.5 A schematic of the chemical reactions that occur on PSC particles in the stratosphere 83

3.6 Microscopic images of ice crystal appearance 84

3.7 A photograph of Polar Stratospheric Clouds..... 85

3.8 The catalytic chlorine ozone destruction cycle ClO-ClO..... 88

3.9 The catalytic chlorine ozone destruction cycle BrO-ClO 89

3.10 The seasonal evolution of Antarctic ozone depletion 91

4.1 Map projection of the area of an irregularly curved surface showing transformation of the area 97

4.2 Illustration of azimuth angle 101

4.3 Implementation of a Delaunay Matlab refinement algorithm to construct conforming triangulations and 2D mesh 103

4.4 Implementation of a Delaunay refinement algorithm to construct conforming triangulations and 2D meshes over North America 104

4.5 Implementation of a Delaunay refinement algorithm to construct conforming triangulations and 2D meshes for the Antarctic region..... 105

4.6 Delaunay triangulation applied to the dataset of EOS MLS and half the Earth 106

4.7 EOS MLS dataset points on the SH with PSC Temperature formation on and Delaunay triangulation applied to the sample 107

4.8 Illustration of an orthodrome in the Earth 108

4.9 Schematic of a spherical triangle of vertices A, B and C..... 109

4.10 A schematic diagram of a great circle 110

4.11 Calculation of SH surface area from June to October 2005 with two different methods 111

4.12 Calculation of SH surface area by Jun-Oct 2005 using triangulation and spherical trigonometry 113

4.13 Calculation of SH surface area by Jun-Oct 2005 using triangulation and spherical trigonometry where extra points were added to reduce variations in the area calculations along with the time 114

4.14 PSC surface areas measured in 2005 using triangulation and spherical trigonometry..... 115

4.15 PSCs surface areas measured at a pressure level of 100 hPa in 2004. 122

4.16 PSC surface area vs. time in 2005 using EOS MLS data level-2 version 1.5, Pressure = 68.1292 hPa 126

4.17 As in Figure 4.14, but in this case considering that the average temperature of all the vertices for each triangle is below the PSC threshold..... 127

4.18 As in Figure 4.17, but for two additional pressure surfaces..... 128

4.19 Percentage of temperature removed points considering 2 and 4 quality flags on PSCs surface area calculation using EOS MLS v2.2 data in 2005 131

4.20 Percentage of temperature removed points considering 2 and 4 quality flags on PSCs surface area calculation using EOS MLS v2.2 data in 2006 132

4.21 Percentage of temperature removed points considering 2 and 4 quality flags on PSCs surface area calculation using EOS MLS v2.2 data in 2007 133

4.23 Type I PSC area at different T_{NAT} derived from EOS MLS in 2005 at 17.5 km..... 138

4.24 Computation of mean T_{ice} derived from Aura MLS water vapor concentrations..... 139

4.25 Variation in area calculation by removing points randomly from the temperature dataset on 29 July, 2005..... 141

4.26 Variation in area calculation by removing points randomly from the

temperature dataset on 29 July, 2005 143

4.27 Linear interpolation on the temperature data on a random day. Spline and Cubic interpolations on that same data 144

4.28 An example of how temperature dataset is affected by removing the 'bad' values 145

4.29 Inferred Type I PSC area from EOS MLS v2.2 over APVR for 2005 to 2008 and altitude range of 12-24 km 146

4.30 Type II PSC area [millions of km^2] from EOS MLS v2.2 over APVR in 2005-06 and altitude range of 12-24 km 147

4.31 Type I PSC area from NCEP/NCAR analyses over APVR for 2005 to 2008, and altitude range of 12-24 km 148

4.32 Difference in Type I PSC area over APV region between NCEP/NCAR analyses and EOS MLS dataset derivations 149

4.33 Year: 2005 and approximate altitude: 17 km 150

4.34 Year: 2005 and approximate altitude: 20 km 151

4.35 Year: 2005 and approximate altitude: 23 km 151

4.36 Year: 2005 and approximate altitude: 26 km 152

4.37 Year: 2005 and approximate altitude: 29 km 152

4.38 Timeseries of Type I PSC area at 195 K inferred from MLS temperatures and uncorrected daytime ClO 153

5.1 Triangulated mesh of data points in a random day in Antarctica 159

5.2 PSC-induced areas as a function of height (km) for the 2005-2009 Antarctic seasons using the algorithm developed 160

5.3 2-D histogram of zonal mean NAT saturation calculated temperatures at the 46 hPa pressure surface 161

6.1 The seasonal evolution of HCl/Cl_y roughly estimated from available MLS HCl and ClO in 2006 at 46 hPa..... 166

6.2 Changes in chlorine partitioning and minimum observed temperatures.... 168

6.a HCl depleted areas versus PSC inferred areas over the Antarctic region .. 171

6.3 The time-height contour plot of the daytime ClO mixing ratio and PSC area 177

6.4 The time-height contour plot of H_2O volume mixing ratios 179

7.a PPCs as a function of year for PSC and HCl depletion areas 184

7.b HCl depleted areas versus T_{ACL} areas..... 186

7.1 HCl depleted areas over APVR in 2005..... 189

7.2 HCl depleted areas over APVR in 2006..... 190

7.3 HCl depleted areas over APVR in 2007..... 191

7.4 HCl depleted areas over APVR in 2008..... 192

7.5 HCl depleted areas over APVR in 2009..... 193

7.6 HCl depleted areas over APVR in 2010 at ~26 km 196

8.1 Mean water vapour measurements and mean temperatures over Peninsula grid cell 1 201

8.2 Mean water vapour measurements and mean temperatures over Peninsula grid cell 2 202

8.3 T_{ICE} calculations derived from mean MLS water vapour concentrations in 2007 over Peninsula grid cell 1 and Peninsula grid cell 2 203

8.4 Mean MLS H_2O mixing ratio over Antarctic Peninsula grid cell 1 and grid cell 2..... 204

8.5 T_{NAT} calculations derived from mean MLS H_2O and HNO_3 concentrations in 2007 over Peninsula grid cell 1 and Peninsula grid cell 2 205

8.6 Illustrated version of Table 8.1 207

8.7 Interpolation of zonally averaged T_{ice} versus Potential Temperature 209

8.8 Interpolation of zonally averaged T_{NAT} versus Potential Temperature..... 210

8.9 Interpolation of zonally averaged T_{NAT} versus Potential Temperature but for T_{NAT} as function of Aura MLS HNO_3 set constant..... 211

8.10 Mean T_{ice} as function of time and potential temperature in 2007 derived from Aura MLS H_2O zonally averaged over Antarctic grid cells 1, 2, 3 & 4 212

8.11 Mean T_{ice} as function of time and potential temperature in 2007 derived from Aura MLS H_2O zonally averaged over Antarctic grid cells 5, 6, 7 & 8 213

8.12 Mean T_{ice} as function of time and potential temperature in 2007 derived from Aura MLS H_2O zonally averaged over Antarctic grid cells 9, 10, 11 & 12..... 214

8.13 Mean T_{ice} as function of time and potential temperature in 2007 derived from Aura MLS H_2O zonally averaged over Antarctic grid cells 13, 14, 15 & 16..... 215

8.14 Mean T_{ice} as function of time and potential temperature in 2007 derived from Aura MLS H_2O zonally averaged over Antarctic grid cells 17, 18, 19 & 20..... 216

8.15 Mean T_{ice} as function of time and potential temperature in 2007 derived from Aura MLS H_2O zonally averaged over Antarctic grid cells 21, 22, 23 & 24..... 217

8.16 Mean T_{ice} as function of time and potential temperature in 2007 derived from Aura MLS H_2O zonally averaged over Antarctic grid cells 25, 26, 27 & 28..... 218

8.17 Mean T_{ice} as function of time and potential temperature in 2007 derived from

Aura MLS H_2O zonally averaged over Antarctic grid cells 29 & 30 219

8.18 Mean T_{NAT} as function of time and potential temperature in 2007 derived from Aura MLS H_2O zonally averaged over Antarctic grid cells 1, 2, 3 & 4 220

8.19 Mean T_{NAT} as function of time and potential temperature in 2007 derived from Aura MLS H_2O zonally averaged over Antarctic grid cells 5 to 9.... 221

8.20 Mean T_{NAT} as function of time and potential temperature in 2007 derived from Aura MLS H_2O zonally averaged over Antarctic grid cells 10 to 14 222

8.21 Mean T_{NAT} as function of time and potential temperature in 2007 derived from Aura MLS H_2O zonally averaged over Antarctic grid cells 15 to 19 223

8.22 Mean T_{NAT} as function of time and potential temperature in 2007 derived from Aura MLS H_2O zonally averaged over Antarctic grid cells 20 to 24 224

8.23 Mean T_{NAT} as function of time and potential temperature in 2007 derived from Aura MLS H_2O zonally averaged over Antarctic grid cells 25, 26 & 27 225

8.24 Mean T_{NAT} as function of time and potential temperature in 2007 derived from Aura MLS H_2O zonally averaged over Antarctic grid cells 28, 29 & 30 226

8.25 Mean Temperature as function of time and potential temperature in 2007 derived from Aura MLS measurements over Antarctic Grid Cells (GC) 1, 2 & 3 227

8.26 Mean Temperature as function of time and potential temperature in 2007 derived from Aura MLS measurements over Antarctic Grid Cells (GC) 4, 5 & 6 228

8.27 Mean Temperature as function of time and potential temperature in 2007

derived from Aura MLS measurements over Antarctic Grid Cells (GC) 7, 8 & 9 229

8.28 Mean Temperature as function of time and potential temperature in 2007 derived from Aura MLS measurements over Antarctic Grid Cells (GC) 10, 11 & 12 230

8.29 Mean Temperature as function of time and potential temperature in 2007 derived from Aura MLS measurements over Antarctic Grid Cells (GC) 13, 14 & 15 231

8.30 Mean Temperature as function of time and potential temperature in 2007 derived from Aura MLS measurements over Antarctic Grid Cells (GC) 16, 17 & 18 232

8.31 Mean Temperature as function of time and potential temperature in 2007 derived from Aura MLS measurements over Antarctic Grid Cells (GC) 19, 20 & 21 233

8.32 Mean Temperature as function of time and potential temperature in 2007 derived from Aura MLS measurements over Antarctic Grid Cells (GC) 22, 23 & 24 234

8.33 Mean Temperature as function of time and potential temperature in 2007 derived from Aura MLS measurements over Antarctic Grid Cells (GC) 25, 26 & 27 235

8.34 Mean Temperature as function of time and potential temperature in 2007 derived from Aura MLS measurements over Antarctic Grid Cells (GC) 28, 29 & 30 236

9.1 Zonal averages of HCl and HNO_3 over geographic 5º-wide bands around the entire Antarctic polar region at ~17 km in 2006 245

9.2 Zonal averages of HCl and HNO_3 over geographic 5º-wide bands around the entire Antarctic polar region at ~20 km in 2006 245

9.3 Zonal averages of HCl and HNO_3 over geographic 5º-wide bands around the entire Antarctic polar region at ~23 km in 2006 246

9.4 Zonal averages of HCl and HNO_3 over geographic 5º-wide bands around the entire Antarctic polar region at ~26 km in 2006 247

9.5 Zonal averages of HCl and HNO_3 over geographic 5º-wide bands around the entire Antarctic polar region at ~29 km in 2006 247

LIST OF TABLES

TABLE **Page**

2.1 Pressure level categorization and its equivalence in units of hPa for both EOS Aura MLS level-2 data set versions (v1.5 and v2.2)..... 28

2.2 Corresponding Aura MLS standard mean temperature observations for three different HCl turning points (days 123, 124 and 125) in over the Antarctic region (60ºS–80ºS) in 2005. 32

2.3 Results from our algorithm for Aura MLS HCl signal calculation in 2005... 46

2.4 Results for daytime ClO activation/deactivation dates calculation in 2005-2007 at three stratospheric altitudes. 48

2.5 Results for PSC formation/evaporation dates calculation in 2005-2009 at three stratospheric altitudes.. 49

6.1 PCCs and the differences calculated between the HCl depleted area and the PSC area ($A_{HCl\text{-}depleted} - A_{PSC}$). The values reported are based on two HCl thresholds ($\Delta HCl(n)$, n = 2,4) and three different PSC formation temperature threshold scenarios derived from observed temperatures and MLS chemical data in the Antarctic polar stratosphere in 2006..... 174

7.1 The equivalence of pressure level to pressure (in hPa), as per the Aura MLS v2.2 Level 2 dataset for ClO, HCl, O_3, and HNO_3 181

7.2 Correlation coefficients and differences between HCl depleted area based on three thresholds versus the PSC area. Values derived at four stratospheric altitudes from 2005 to 2009 194

8.1 Auxiliary table produced for *Alexander et al.* [2011] (not shown in the paper), in order to divide up the Antarctic region [60º–80º]S into grid cells of different size using both COSMIC and Aura MLS datasets 206

Chapter 1

1 INTRODUCTION

1.1 THE IMPORTANCE OF RESEARCH/PURPOSE

The results provided here seek to help foster a deeper understanding of chlorine activation, the immediate preceding stage of massive ozone depletion in Antarctica. This thesis describes work undertaken to detect polar stratospheric chlorine activation and infer Polar Stratospheric Clouds using NASA's MLS instrument on-board Aura satellite and NCEP/NCAR assimilations in the Earth's Antarctic stratosphere. For this work, measurements of hydrogen chloride (HCl), as retrieved by the Aura Microwave Limb Sounder (MLS) instrument, were the main focus since HCl plays an important role in the reaction shown in Equation 1.1.1:

$$HCl(s) + ClONO_2(g) \rightarrow Cl_2(g) + HNO_3(s) \qquad (1.1.1)$$

where (g) refers to species in the gas phase and (s) refers to those adsorbed onto the surface of a PSC crystal [*Leu and Keyser*, 2009].

Previous studies have shown that HCl and $ClONO_2$ reservoirs make up more than 95% of inorganic chlorine ($Cl_y = HCl + ClONO_2 + HOCl + Cl_x$) in the Antarctic lower stratosphere before the onset of chlorine activation, whereas reactive chlorine species ($Cl_x = ClO + Cl_2 + 2\ Cl_2O_2 + OClO$) represent the predominant forms inside the activated vortex [*Wilmouth et al.*, 2006]. Based on aircraft measurements, *Jaeglé et al.* [1997] suggested that 60-75% of Cl_y was HCl at the beginning of Antarctic winter,

while *Michelsen et al*. [1999] suggested that nearly 80% of Cl_y was HCl at the beginning of Antarctic winter. *Santee et al*. [2008b] also indicated that HCl made up the majority of the total chlorine in the polar stratosphere, and existing evidence supports the supposition that HCl is the principal reservoir of inert chlorine in the middle and upper stratosphere (e.g. *Morgenstern et al.*, [2009]). Therefore, HCl plays an important role in ozone depletion. The fraction of HCl/Cl_y is altitude dependent and, therefore, variations in the abundance of HCl provide a useful proxy for chlorine partitioning in the stratosphere.

For this thesis, the year-to-year variations of PSC formation and chlorine partitioning derived from EOS Aura MLS measurements and NCEP/NCAR re-analyses in the Southern Hemisphere, for the 2005-2009 winter seasons, were examined concurrently. In particular, the roles of NAT (Nitric Acid Trihydrate) particle formation namely, [1]T_{NAT} and sulfate aerosol, aka [2]T_{ACL}, in chlorine activation in the Antarctic winter 2006 season were quantified and further analysed. The Antarctic winter 2006 season was chosen as the focus since PSC existence was particularly extensive, as observed by CALIOP and pointed out by *Pitts et al.* [2009], with a record-breaking ozone hole. Therefore, peculiar conditions for PSC formation and ozone depletion in the Antarctic stratosphere were observed in 2006 and offered a good scenario for concurrently analyzing HCl depletion.

This document is organized into the following major sections. In Chapter 2 the characteristics of the Aura MLS satellite instrument and more briefly, the NCEP/NCAR reanalysis of temperature, is described. The algorithms conceived for

[1] $T_{NAT} \equiv f(H_2O_{[ppmv]}, HNO3_{[ppbv]}, \text{pressure})$ [*Hanson and Mauersberger*, 1988].

[2] $T_{ACL} \equiv f(H_2O_{[ppmv]}, SA_{[\mu m^2 cm^{-3}]}, \text{pressure})$ [*Drdla and Müller*, 2010].

modeling in this study are also presented, and include the following: 1) the PSC areal coverage from temperature data, and 2) the geographic regions of significant changes and/or the depletion of gas-phase HCl in Chapters 4 and 5, and 6, respectively. A comparison of calculated HCl depletion and PSC areal coverage in Antarctica during 2006 in the lower-middle stratosphere is shown in Chapter 6. Year-to-year variability and the role of sulfate aerosol in chlorine activation in the polar Antarctic stratosphere is quantified and presented in Chapter 7; an application that contents of this thesis had in the parallel writing of a manuscript on wave-induced PSC is presented in Chapter 8 and the interpretation and first implications for this thesis' results are presented in Chapter 9.

1.2 OBJECTIVES

1.2.1 General Objective

Development of PSC area calculator algorithm fit for measuring geographic aerial coverage of PSC above Antarctica by thresholding satellite and reanalysis standard temperature. The latter as input parameter.

1.2.2 Specific Objectives

- Use of two different temperature data sets for calculation of PSC areas applying the algorithm developed.

- Selection of PSC temperature formation threshold schemes (in current use in the relevant literature, which will be of help to accomplish general objective).

- Comparison and validation of PSC area calculated with those from any available in the literature.

- Analysis of chemical data for the examination of the role that stratospheric chlorine activation currently has with PSC formation in Antarctica and with ozone depletion, ultimately.

- Further chemical analysis as needed for the most important results obtained from previous objective.

- Comparison of geographic PSC areas versus areas where stratospheric chlorine is likely activated, using a HCl depression identification algorithm developed for different scenarios during the PSC season.

- Presentation of the role of dynamical waves in PSC formation and composition [*Alexander et al.*, 2011].

- Introductory developtment of the relationship between the temperature fluctuations and chlorine activation in PSC formation.

1.3 SCOPE

Due to the magnitude, complexity, and capability in the Institutional resources, pertinent data issues that are within and beyond the scope of this project were devised during the advanced stages of this project. The data issues that are beyond the University scope of this research, but relevant for future work, are pointed out in Chapter 9.

Chapter 2

EOS AURA MLS

2.1 MISSION

2.1.1 INTRODUCTION

The work presented here employed observations from the EOS Aura Microwave Limb Sounder (MLS), one of the four instruments on NASA's Aura satellite. The Aura MLS instrument has been in orbit since 15 July 2004 and is a sun-synchronous limb sounding instrument with a ~1345 LST ascending node. The Aura MLS measures thermal emissions of the atmosphere at microwave wavelengths in five spectral regions from 118 GHz to 2.5 THz. The Earth's limb is scanned from the surface up to the lower thermosphere every 25 s [*Waters et al.*, 2006], providing 240 scans per orbit that are spaced at 1.5º (~165 km) intervals with a total of ~3500 vertical profiles per day covering a nearly global latitude region from 82ºN to 82ºS for every orbit. The longitudinal separation of MLS measurements is 10º-20º over low and middle latitudes, with a much finer sampling in polar regions [*Santee et al.*, 2008a; *Schwartz et al.*, 2008].

Figure 2.1. Schematic of NASA's Aura satellite and the Microwave Limb Sounder (MLS) sensor, on-board identified. [Available from NASA, (http://www.nasa.gov)].

Temperature data were used for the identification of regions where the up-to-date Type I PSC formation thresholds used were met; and variations for this condition were analyzed for modifying geographical PSC areal coverage in the Antarctic polar region. In order to examine the co-occurrence of PSC-induced and chorine activation (through HCl) events for the specific time frame defined, chlorine chemistry over Antarctica was also tracked using HCl and ClO observations measured using the Aura MLS over the PSC formation altitude range.

2.1.2 Database version issue correction

In this work, Level 2 temperature and chemical concentration data from version 2.2 (v2.2) of the EOS Aura MLS satellite dataset, henceforth referred to as Aura MLS, was utilized. That a later database, version 3.3 (v3.3), is available is now known; however,

by the time this work was prepared there was no significant reason to wait until the release was effective [*Santee, 2010*]. The existing v2.2 algorithms are still in use in addition to the new v3.3 algorithms in data analysis [available from NASA's GSFC, http://disc.sci.gsfc.nasa.gov/gesNews/mls_new_data_version_release], contrary to the suggestion of [*Manney*, 2011] to employ v3.3. In Sect. 2.1.3 the interpretation of the differences between v2.2 and v3.3 data, and the data correction relevant to the present work are briefly described.

2.1.3 Chemical Aura MLS data

2.1.3.1 Aura HCl data: overview

Aura MLS HCl data has been shown to be of high quality for the 37 pressure levels distributed from 100 hPa to 0.15 hPa [*Froidevaux et al.*, 2008; *Santee*, 2010]. *Froidevaux et al*. [2008] indicated that four data quality thresholds, provided for every data profile, should be used for selecting data, and that the precision of individual HCl profiles is 0.3 ppbv and 0.2 ppbv, at the 100 hPa and 10 hPa pressure surfaces, respectively. A comparison with solar occultation ACE-FTS measurements indicated that HCl average differences were within 5% for the upper stratosphere, and near zero for the lower stratosphere. Furthermore, *Froidevaux et al.* [2008] also reported a comparison of HALOE and Aura MLS HCl observations. The study argued that MLS values were ~10 to 20% larger throughout most of the stratosphere, although HALOE HCl measurements have been shown to be consistently smaller than those from other data sets [*Froidevaux et al.*, 2008 and references therein].

As discussed in detail in Chapter 6, the most important calculations that have been made directly on HCl data involved the derivation of the mean and the variance of

autumn values which were, in turn, used to define regions of depressed HCl. The analysis presented here derived nominal values of HCl in the beginning of Southern Hemisphere autumn and precluded the period where HCl production occurs [*Douglass et al.*, 1995; *Michelsen et al.*, 1999]. The figure 2.2 shows the number of data Number of data points available per month and per year from the Aura MLS v2.2 HCl dataset from 2005 to 2009, that will be useful for the calculation of the regions of processed HCl which are described further un Chapter 6. The difference between the concentration of HCl during nominal and depleted periods was larger than the precision of the HCl data within the pressure range recommended by *Livesey et al.* [2007] and *Froidevaux et al.* [2008]. Recently *Livesey et al.* [2011] stated that the conclusions of the latter study remain *essentially unchanged* for standard v3.3 HCl profiles.

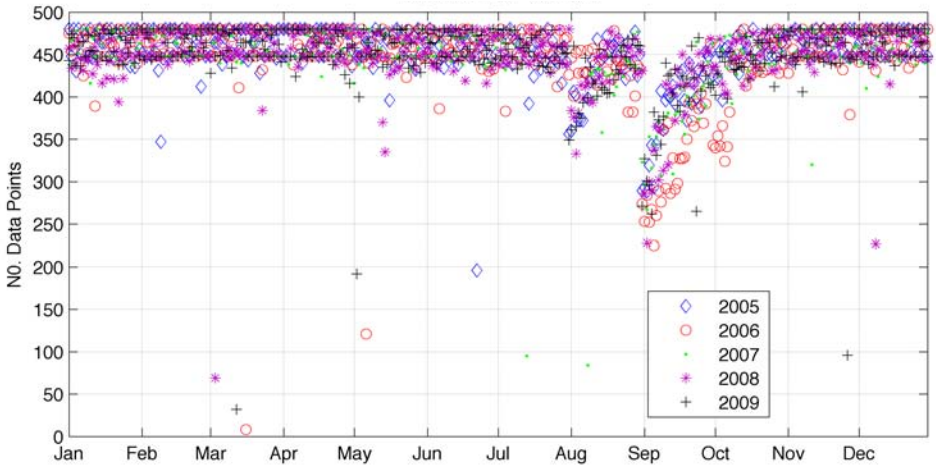

Figure 2.2. Number of data points available per month and per year from the Aura MLS v2.2 HCl dataset from 2005 to 2009, over the geographic polar region enclosed by [60ºS–80ºS], valid for different pressure levels applying the quality control guidelines discussed Section 2.1.2.

2.1.3.1.1 Aura MLS HCl data assessment

The motivation behind Figure 2.3 was in order to compare it with [*Froidevaux et al.*, 2008]'s Figure 8 and it results evident the good agreement between the data of that Figure and Figure 2.3 in this thesis. Similarly, Figure 2.4 shows time series of MLS v2.2 HCl, in 2005 for an altitude range of 17.5 km - 55.4 km., providing additional details of the general behavior of HCl as per *Froidevaux et al.* [2008].

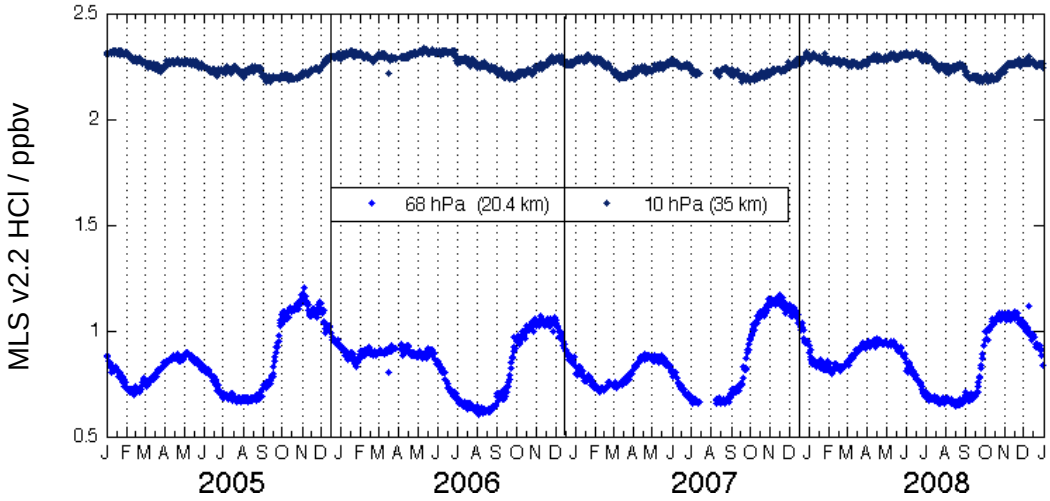

Figure 2.3. Time series of MLS v2.2 HCl daily global means for different years at 20.4 km (in blue) and 35 km (in dark blue). Missing data by mid year in 2007 is due to unavailability of MLS data. Adapted from *Froidevaux et al.* [2008].

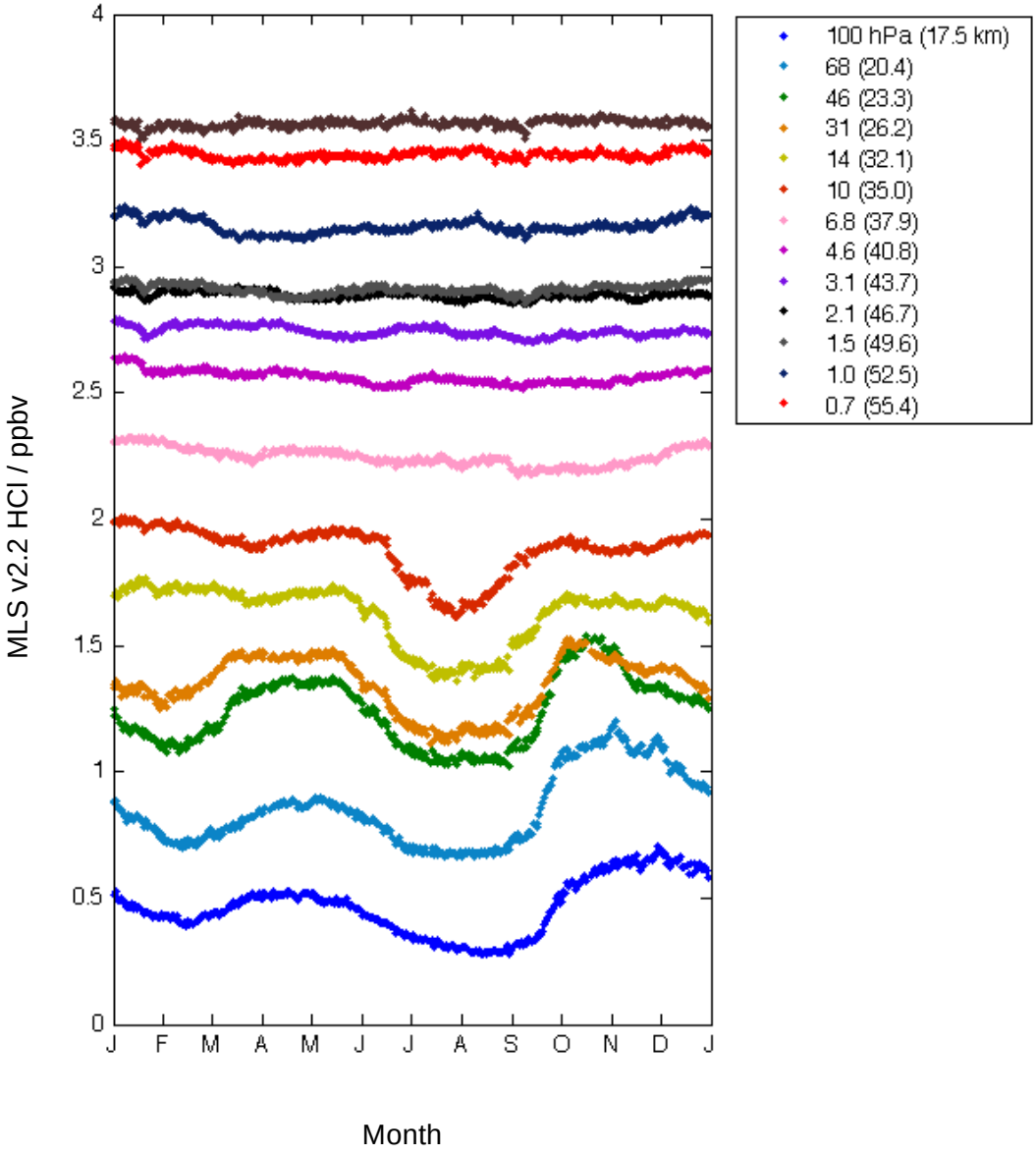

Figure 2.4. Time series of MLS v2.2 HCl daily global means in 2005 at different altitudes (from 17.5 km to 55.4 km).

2.1.3.2 ClO and N_2O data: overview

The analysis also employed two additional MLS stratospheric chemical species, as follows: ClO and N_2O which are distributed vertically between 100 hPa and 1 hPa.

Additionally, Aura MLS water vapor (H_2O) and nitric acid (HNO_3) species were used between 316 hPa and 0.002 hPa, and 215 hPa to 3.2 hPa, respectively (non-inclusive).

Aura MLS ClO and N_2O measurements have been validated by *Santee et al*. [2008a] and *Lambert et al*. [2007], respectively. For both cases, four quality thresholds, for removing poor quality data, were available for every data profile. The precision of the ClO data ranged from ±0.1 ppbv to ±0.3 ppbv. For N_2O retrievals the precision varied from 25 ppbv to 14 ppbv over the validated pressure range.

To account for the substantial (~0.1–0.4 ppbv) negative bias present in v2.2 ClO data (at pressures larger than 22 hPa inside the winter polar vortices) it was necessary to subtract systematic bias values from the data affected at each retrieval level (see *Santee et al*., [2008a], Table 2). *Santee et al.* [2010] suggested that MLS nighttime ClO abundances inside the winter polar vortices generally increased with increasing temperature. The analysis of the daytime minus nighttime difference for v2.2 ClO (and HCl) observations in 2006 at the various pressure levels of the Antarctic stratosphere (not shown) corroborated the findings by *Santee et al.* [2010] that displayed progressively (climatological) larger differences over the Antarctic winter season, and a peak in the ClO daytime-nighttime difference by September, 2006. However, neither the ClO nor the HCl data utilized in this study considered the incorporation of these temperature-related differences and the guidelines for Aura ClO data usage indicated by *Santee et al.* [2008a] were used. In addition, an examination of the zonal mean daytime-nighttime differences in HCl (see Figure 2.6) showed to be fairly negligible for both of the periods from January to September and from October to December in the Antarctic region [60º–80º] during 2006. From September to October of 2006 there was a slightly greater than zero daytime-nighttime difference in the HCl data that may

be due to the fact that during this period of time (~1 month) the number of v2.2 HCl (and ClO) measurements dropped for approximately 50% for all observations in the region [60ºS-80ºS] during the five years examined (2005-2009) (see Figures 2.2 and 2.5). *Livesey et al.* [2011] reported that v3.3 ClO data includes a *largely mitigated* v2.2 negative bias through new product (CH_3Cl) inclusion.

Santee et al. [2008a] defines daytime and nighttime as follows and the daytime criterion was applied for creation of Figure 2.5 (bottom, right).

(SZA < 92º), (10:00 < LST < 15:00) → daytime

(SZA > 100º), (22:00 < LST < 04:00) → nighttime

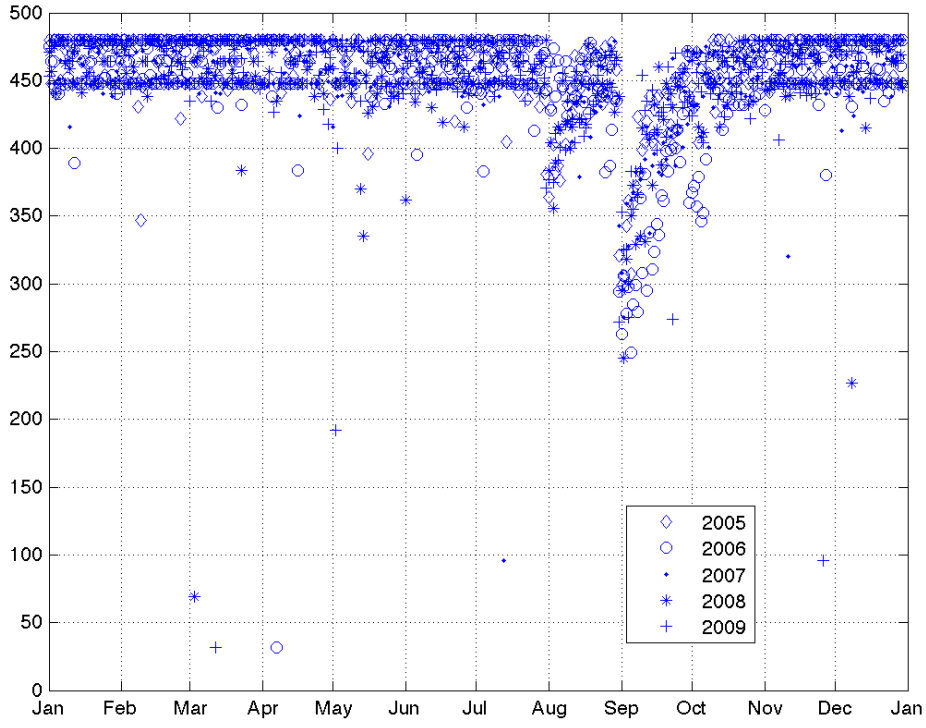

Figure 2.5. [Top] Number of data points available per month and per year from the Aura MLS v2.2 ClO dataset, from 2005 to 2009, over the geographic polar region enclosed by [60ºS–80ºS], applying the quality control guidelines discussed in previous sections 2.1.2 at ~26 km.

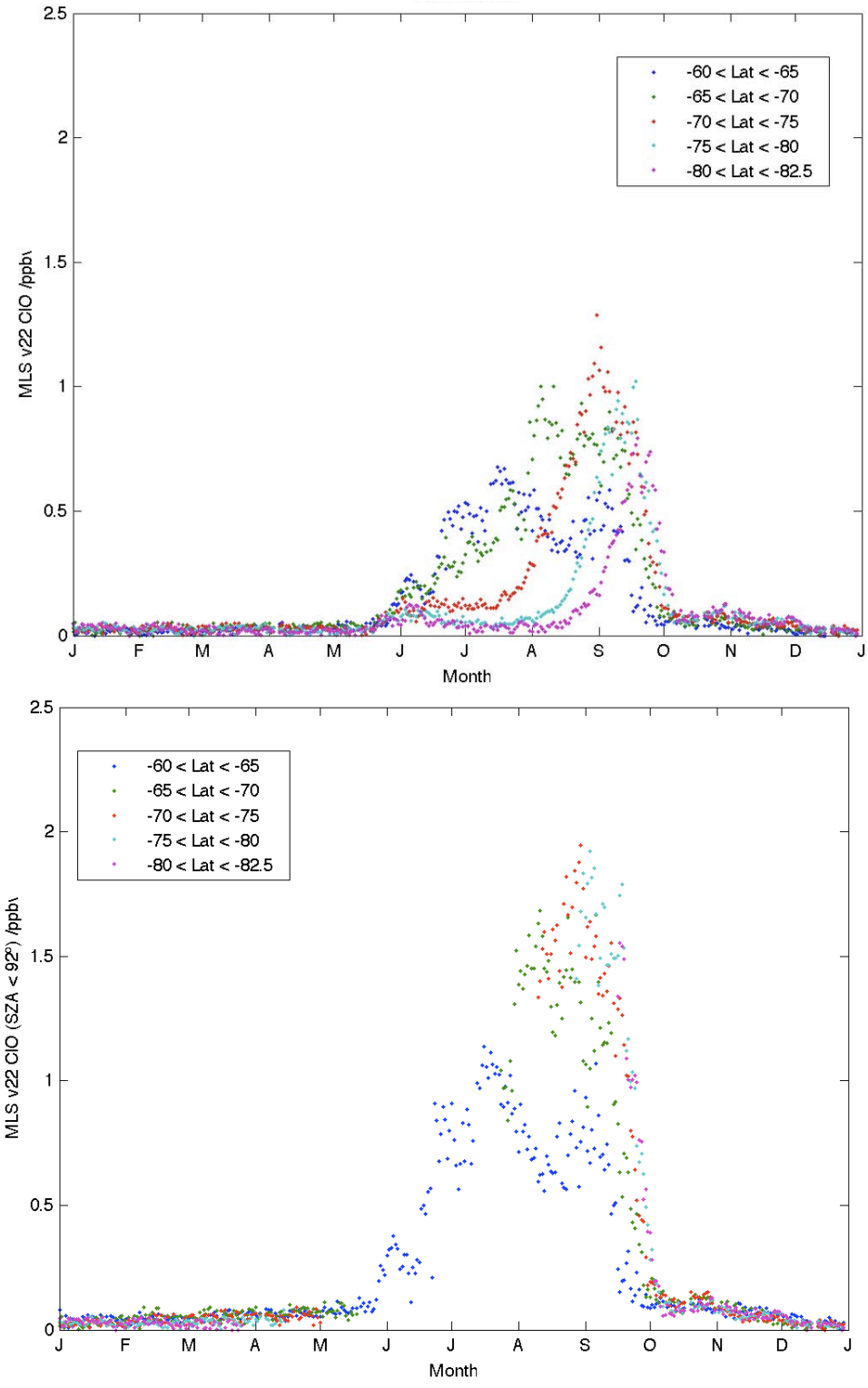

Figure 2.6. [Top] Comparison between standard MLS ClO data at 26 km in 2005 [bottom] and daytime MLS ClO data at the same altitude and year.

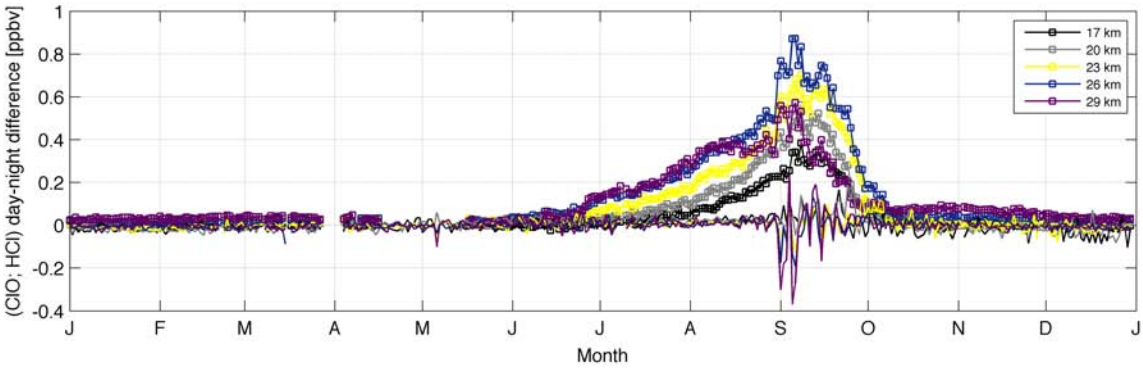

Figure 2.6. Mean day-night differences of HCl (solid lines) and ClO (line plus open square) above the south polar region (60ª–80º) in 2006, from the Aura MLS database.

2.1.3.3 HNO_3 satellite measurements

Aura MLS HNO_3 observations have been validated by *Santee et al*. [2007] and have a precision of ± 0.7 ppbv over the pressure range previously identified. However, MLS v2.2 HNO_3 mixing ratios are known to be uniformly biased low, by 10-30%, throughout most of the stratosphere [*Santee et al*., 2007], especially for surfaces where the atmospheric pressure $p \geq 100$ hPa [*Livesey et al*., 2011]. In comparison to HNO_3 measurements for other space-borne sensors such as the Sub-Millimeter Radiometer (SMR) on board the Swedish-led Odin satellite, and the HNO_3 observations used in the present analysis, the work of *Urban et al.* [*2009*] indicated a larger positive bias, on the order of 2-3 ppbv (~20%), surrounding the profile peak in Odin/SMR Chalmers version 2.0 middle-stratospheric observations. *Livesey et al.* [2011] suggested that the low bias for HNO_3 in v2.2 (for $p \geq 100$ hPa) has been *largely eliminated* in v3.3 HNO_3.

As per the relevancy of the presented analysis, which, in fact, is defined over the pressure range from (20 hPa $\leq p \leq$ 100 hPa), *Bevilacqua et al*. [2002] and *McDonald et al*. [2009] suggested that for typical concentrations of water vapor and nitric acid,

T_{NAT} varied strongly as a function of water vapor. *Alexander et al.* [2011] suggested that even with a worst-case scenario of a 30% low bias for HNO_3, the error in T_{NAT} was less than 1 K at PSC formation altitudes.

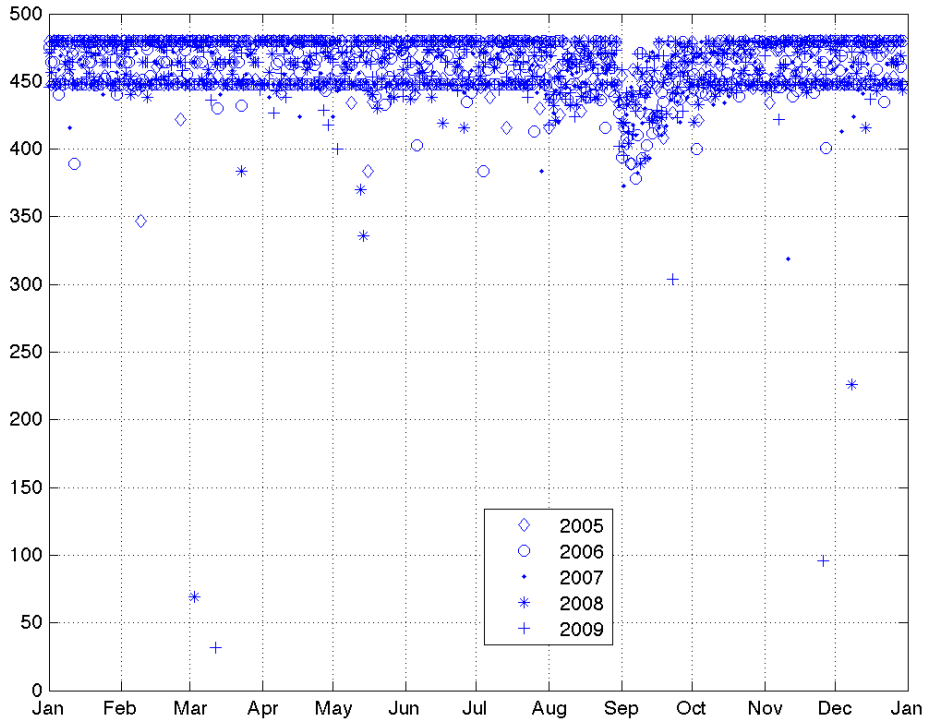

Figure 2.7. Number of data points available per month per year from the Aura MLS v2.2 HNO_3 dataset from 2005 to 2009, over the geographic polar region enclosed by [60ºS–80ºS], applicable to different pressure levels applying the quality control guidelines discussed in previous sections 2.1.2.

Studying EOS MLS v2.2 Nitric Acid HNO_3

We applied the four quality flags: 'Quality,' 'Convergence,' 'Precision,' and 'Status' as suggested by *Santee et al.* [2007] to the Aura MLS v2.2 nitric acid profile. According to *Santee* [2010], the way we have been using the quality controls is correct,

and the observed negative values are expected, since there is not at the moment: 2010 any correction algorithm, as there is one for the water vapour profile. *Santee* [2010] has suggested some ways to deal with those negative mean values, but they do not seem to work out well (not shown). See Figure 2.7 that shows the number of Aura MLS v2.2 HNO_3 data points available over the geographic region enclosed by [60ºS–80ºS], applicable to different pressure levels after applying the quality control previously discussed and discussed further in Section 2.1.2. Once we were *satisfied* enough with quality on the nitric acid and water vapour values read from the EOS MLS v2.2, we plotted the mean daily mixing ratios for each one from 2005 to late 2010 at different pressure levels (see Figure 2.8).

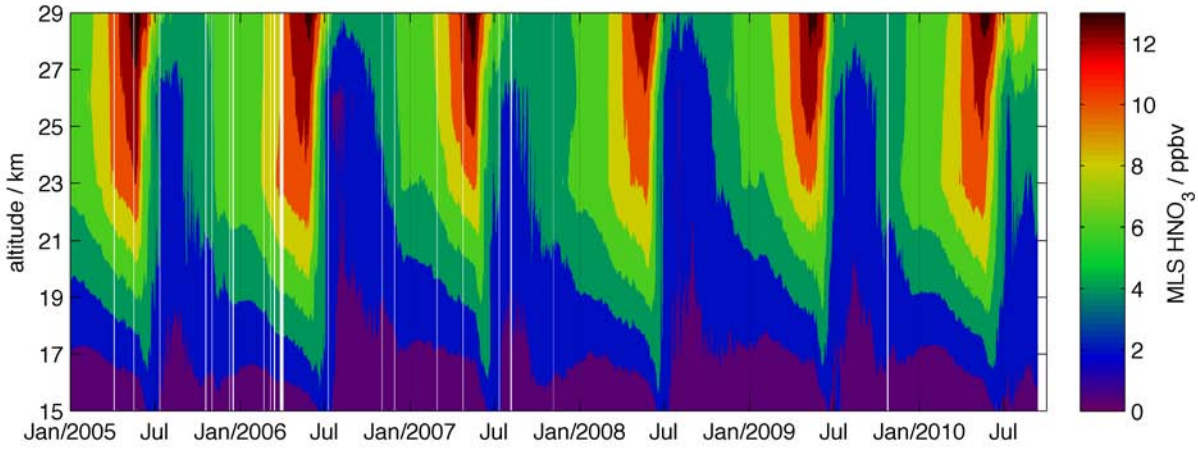

Figure 2.8. Contour plot of Aura MLS HNO_3 averaged over the polar region 60ºS – 80ºS at different altitudes from 2005 to late 2010 in the Antarctic stratosphere.

2.1.3.4 Water vapor data

Aura MLS H_2O observations, above 316 hPa, were validated by *Lambert et al.* [2007] and *Read et al.* [2007]. Since it has not been found necessary to screen H_2O profiles on the basis of the "Convergence" quality threshold [*Lambert et al.*, 2007],

only three quality thresholds have been provided for identifying poor quality data. The precision of H_2O data over the pressure range from 100 to 10 hPa varies from 4% to 10%. *Livesey et al.* [2011] reported that the *zig-zag* artifact in v2.2, between 31 and 26 hPa, has been removed in v3.3. The reader should note that the MLS H_2O data utilized in this study was corrected for large amplitude oscillations in bias for the two pressure levels relevant, in other words, where the v2.2 H_2O data were most likely to be impacted (31.6 hPa and 21.6 hPa) by following the algorithm presented by *Lambert et al*. [2007].

A relatively closer look at EOS MLS v2.2 Water Vapour H_2O

In order to study the EOS MLS v2.2 water vapour data, we worked firstly on applying all the quality suggestions described in the section above. Thus, we used three quality flags: ‘Quality,’ ‘Precision,’ and ‘Status’ to discard those poor quality values, and also the algorithm for correction of oscillation of *Lambert et al.* [2007] in levels 19 and 20 (collectively termed "simple quality ctrl", see Appendix A relevant for the temperature profile). Since there were still observed bad values, we applied again the flag ‘Precision’ (called it *double quality-ctrl*) and finally, it was included a statistical analysis in which we calculate the weighted mean of the water vapour error (we called ‘err’) to get an upper flag = mean(err) + 3std(err) and a lower flag = mean(err) - 3std(err), so if that daily err is greater than our upper flag or lower than the lower one, outliers were identified as lying at least 3 standard deviations away from the mean values. These data values were excluded from further analyses.

2.1.3.5 Other Chemical data: data review

Products from datasets

From the European Space Agency (ESA): It was found that the following instruments measured at least one of the chlorine species of interest for this project. See databases and relevant chlorine species highlighted as follows:

Global Ozone Monitoring by Occultation of Stars (GOMOS)

(H_2O, NO_2, NO_3, OClO), temperature and aerosols.

Temporal Coverage: 2002-03-01 to current day
Spatial Coverage: 90 N, 90 S, 180 W, 180 E

The Scanning Imaging Absorption Spectrometer for Atmospheric Cartography (SCIAMACHY)

- In the stratosphere: O_3, O_2, O_2*, O_4, NO, NO_2, BrO, N_2O, CO, CO_2, H_2O, CH_4, plus under volcanic eruption SO_2, plus under ozone hole conditions OClO and ClO.

Temporal Coverage: 2002-07-18 to current day
Spatial Coverage: 90 N, 90 S, 180 W, 180 E

From NASA, EOS MLS v2.2:

Temporal Coverage: July 15, 2004 - to current day
Latitude Coverage: 82 N, 82 S

Products: BrO, CH_3CN, ClO (100 – 1 hPa), CO, GPH, H_2O, HCl (100 – 0.15 hPa), HCN, HNO_3, HO_2, HOCl (10 – 2.2 hPa), IWC, IWP, N_2O, O_3, OH, RHI, SO_2, Temperature.

From the Atmospheric Chemistry Experiment,

(ACF-FTS):

Version 1.0: H_2O, O_3, N_2O, CO, CH_4, NO, NO_2, HNO_3, HF, HCl, N_2O_5, $ClONO_2$, CCl_2F_2, CCl_3F, COF_2, CHF_2Cl, HDO, SF_6

Version 2.0: H_2O, O_3, N_2O, CO, CH_4, NO, NO_2, HNO_3, HF, HCl, N_2O_5, $ClONO_2$, CCl_2F_2, CCl_3F, COF_2, CHF_2Cl, SF_6, OCS, HCN, CF_4, CH_3Cl, C_2H_2, C_2H_6, N_2

Version 2.1: H_2O, O_3, N_2O, CO, CH_4, NO, NO_2, HNO_3, HF, HCl, N_2O_5, $ClONO_2$, CCl_2F_2, CCl_3F, COF_2, CHF_2Cl, SF_6, OCS, HCN, CF_4, CH_3Cl, C_2H_2, C_2H_6, N_2, ClO

Version 2.2: H_2O, O_3, N_2O, CO, CH_4, NO, NO_2, HNO_3, HF, HCl, N_2O_5, $ClONO_2$, CCl_2F_2, CCl_3F, COF_2, CHF_2Cl, HDO, SF_6, OCS, HCN, CF_4, CH_3Cl, C_2H_2, C_2H_6, N_2, ClO, etc..

Version 3.0: H_2O, O_3, N_2O, CO, CH_4, NO, NO_2, HNO_3, HF, HCl, N_2O_5, $ClONO_2$, CFC-12 (CCl_2F_2), CFC-11 (CCl_3F), COF_2, HCFC-22 ($CHClF_2$), HDO, SF_6, OCS, HCN, CF_4, CH_3Cl, C_2H_2, C_2H_6, N_2, CO_2, H_2CO, H_2O_2, O_2, HO_2NO_2, HCOOH, CH_3OH, $COCl_2$, CCl_4, COClF, HCFC-142b (ClF_2C-CH_3), CFC-113 (Cl_2FC-$CClF_2$), HCFC-141b (Cl_2FC-CH_3), etc..

Access to the current Level 2 ACE data (version 2.2) is only available to ACE Science Team members and other authorized users, but version 1.0 has public access. The advantage in getting the ACE-FTS data is that *Santee et al.* [2008] already compared the ACE-FTS 2.2 and EOS MLS v1.5 (not v2.2!) and there seems to be good agreement between both versions. So a previous study provides further validation of these data.

Relevant datasets held by the BADC (British Atmospheric Data Centre) NASA & United Kingdom Natural Environment Research Council HIRDLS (High Resolution Dynamics Limb Sounder): carried on Aura mission, part of the NASA's EOS system.

Global distributions of temperature, clouds, aerosols, and 10 trace species O_3, H_2O, CH_4, N_2O, NO_2, HNO_3, N_2O_5, CFC_{11}, CFC_{12}, and $ClONO_2$ in the stratosphere and upper troposphere. *Personal Note:* CFC_{11} *corresponds to* CCl_3F *and* CFC_{12} to: CCl_2F_2

Latest data: Version 4.00 (public access). There are other versions but the access is restricted by the time this thesis was written.

BUT due to "the position of the blockage (a piece of plastic material that came loose during launch)"… The single azimuth-coverage only extends to 65°S, thus missing all of Antarctica and the S. Polar cap. In the Northern Hemisphere (N.H.) it reaches 82° N. (Taken from HIRDLS EOS Data Description and Quality Version 004--HIRDLS Version 2.04.19--August, 2008).

NDACC (Network for the Detection of Atmospheric Composition Change):

Taken from: http://www.ndsc.ncep.noaa.gov

NDACC Southern Hemisphere High-Latitude Stations:

Site	Instrument	Species	Notes	Dates	Early Public Release
Faraday (65S, 159E)	UV Vis	Total Column: NO_2	Complete	90 - 95	
Dumont d'Urville	Lidar	Aerosol Profiles	Complete	89 - 98	Yes
		Aerosol Profiles		06 - 07	Yes

(67S, 140E)		Ozone Profiles	Complete	91 - 98	Yes
	Ozonesonde	Ozone Profiles		91 - 03 03 - 06	Yes
	UV Vis	Total Column: NO_2, O_3		88 - 07	Yes
Rothera (68S, 68W)	UV Vis	Total Column: NO_2		96 - 07	
Syowa Base (69S, 40E)	UV Vis	Total Column: NO_2, O_3	Complete	90 - 95	
Neumayer (71S, 8E)	Ozonesonde	Ozone Profiles		92 - 08	Yes
	UV Vis	Total Column: NO_2, O_3		99 - 07	
Arrival Heights (78S, 167E)	Dobson	Total Column: O_3		88 - 08	Yes
	FTIR	Total Column: HCl, HNO_3	Bomem/Eocom Complete	91 - 96	
	FTIR	Total Column: CH_4, $ClONO_2$, HCl, HNO_3, N_2O, O_3	Bruker	97 - 08	
	UV Vis	Total Column: NO_2	Seasonal	91 - 08	Yes
McMurdo (78S, 167E)	Lidar	Aerosol Profiles	Seasonal Seasonal	90 - 02 03 - 04	
	Ozonesonde	Ozone Profiles	Seasonal	86 - 08	Yes
	UV Vis	Total Column: NO_2, O_3	Complete	91 - 94	
Scott Base (78S, 167E)	Microwave	ClO Profiles	Seasonal	96 - 07	
South Pole Station (90S)	Dobson	Total Column: O_3		63 - 08	Yes
	Ozonesonde	Ozone Profiles		91 - 08	Yes

From the Reactive Chlorine Emissions Inventory (RCEI):

RCEI is one of the projects of the Global Emissions Inventory Activity (GEIA), an integrating project of AIMES/International Geosphere-Biosphere Program. This GEIA project developed a global emissions inventory for major, reactive chlorine species in the troposphere. Principal objectives were: 1) To develop and verify individual global emissions inventories on a 1° x 1° grid scale for particulate Cl^-, HCl, other inorganic chlorated gases, CH_3Cl, CH_3CCl_3, CCl_2, $CHCl{=}CCl_2$, CH_2Cl_2, $CHCl_3$, and HCFCs […].

In terms of chlorine reservoirs available for the present research project, the disadvantage with the ACE–FTS database: it only provides chlorine nitrate ($ClONO_2$) data. Since HCl is already measured by EOS MLS v2.2 BUT we would not have, in

fact, any other chlorine reservoir, only 1: chlorine nitrate plus HCl measured by Aura MLS as ACE–FTS data were not possible to gather.

2.1.4 Aura MLS Temperature

Version 2.2 Aura MLS temperature data is vertically distributed on 47 pressure levels from 316 hPa to 0.001 hPa, and has been validated by *Schwartz et al*. [2008]. Similar to the HCl product, in order to identify poor quality data, four quality thresholds are provided for every data profile. The study of *Schwartz et al*. [2008] indicated that the vertical resolution of Aura MLS temperature measurements varies from 3.5 to 5 km in the lower-middle stratosphere, and that v2.2 temperature data has systematic biases between -2.5 K and +1 K in the range from 316 hPa to 10 hPa, with a precision varying from ± 1 K to ± 0.6 K.

Schwartz et al. [2008] indicated that a considerable amount of polar temperature measurements have a low quality poleward of 70º during autumn, and in early winter. If required, a different quality criterion may be applied in order to relax the cutoff of polar data. However, a standard quality threshold was employed because the analysis indicated that at any pressure level in the lower-middle stratosphere (approximately 100 hPa to 21.6 hPa), over the period spanning from 2005-2009, the typical number of temperature retrievals that would be added by lowering the quality threshold over the entire polar region only varied between 0 and 5 data points for each day during the five years examined (see Figure 2.11--Top). Therefore, reducing the quality thresholds did not appear to provide any significant improvement. On the other hand, according to *Livesey et al.* [2011] the standard v3.3 and v2.2 temperature products are very similar. Figure 2.12 shows the number of data points available per month and per year from the Aura MLS v2.2 Temperature dataset from 2005 to 2009, over the geographic polar

region enclosed by [60ºS–80ºS], after applying the quality control guidelines are discussed further Section 2.1.4.

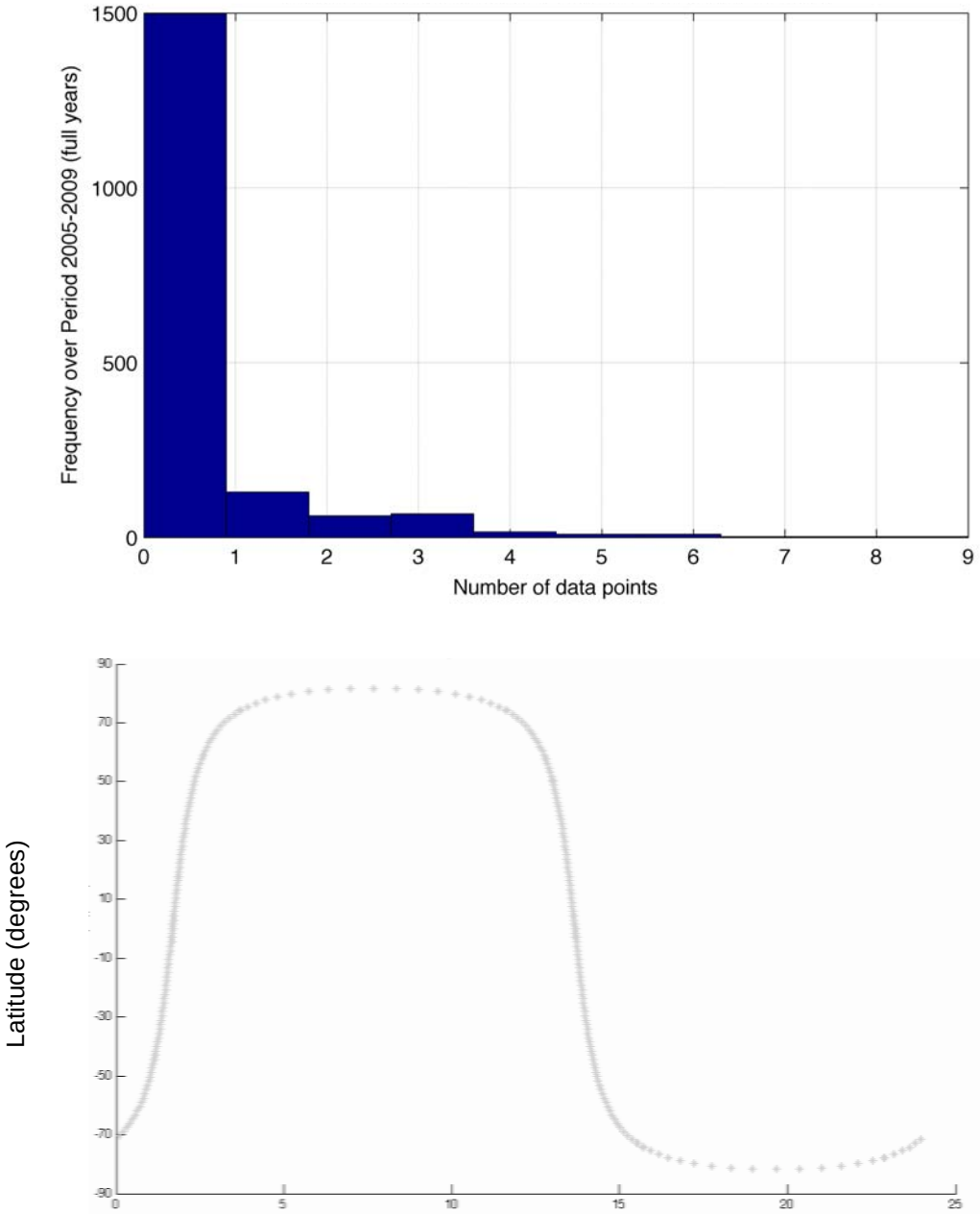

Figure 2.11. [Top] Lowering the quality threshold over the entire polar region. [Bottom] Latitude versus Aura MLS LST obtained from temperature measurements in 2005 at 100 hPa (~17 km). Crosses give locations of profile measurements (temperature in this case). Adapted from *Waters et al.* [2006].

2.1.4.1 Temperature databases: v1.5 vs. v2.2

The Aura MLS data set, version 1.5 (v1.5), was the first publicly available data set [*Froidevaux et al., 2006; Schwartz et al.,* 2008] in contrast to the version 2.2 (v2.2) that was the second public release of MLS data. According to the latter study, v2.2 has a ~2.5K cold bias relative to v1.5 throughout the stratosphere and mesosphere; however, both retrieval versions have biases in the temperature profile. In addition, EOS MLS data level-2 v2.2 data set has 47 pressure levels whereas EOS MLS data level-2 v1.5 has 37, so we found the respective coincidences in pressure levels for both versions (see Table 2.1) in order to make a good comparison of plot results when we are running our algorithms relevant for each different EOS MLS data set version.

Pressure (hPa)	Pressure Level Number	
	EOS MLS v1.5 database	EOS MLS v2.2 database
100	7	13
82.5404	N/A	14
68.1292	8	15
56.2341	N/A	16
46.4159	9	17
38.3119	N/A	18
31.6228	10	19
26.1016	N/A	20
21.5443	11	21
14.6780	12	22
10	13	23

Table 2.1. Pressure level categorization and its equivalence in units of hPa for both EOS Aura MLS level-2 data set versions (v1.5 and v2.2), from temperature retrievals information.

In order to determine how different the EOS MLS version 2.2 was in contrast to the EOS MLS version 1.5, Figure 2.38 show Pearson's correlation coefficients calculated, and confirm the cold bias in the v2.2 data reported by *Schwartz et al*. [2008].

As it also is noted, the different correlation coefficients show good matching between the two data set versions. Nonetheless, *Schwartz et al.* [2008] report that v2.2 temperature will generally be preferred over v1.5 for scientific studies due to the fact

that overall, v2.2 has slightly better vertical resolution. For this work, v2.2 temperature data were, along with v2.2 chemical data, selected for consistency. Although, in some cases, initial PSC calculations involving v1.5 and v2.2 temperature data may be shown in this work as part of the test processing for the PSC model algorithm development. Tests involving v1.5 temperature data will be indicated where they correspond.

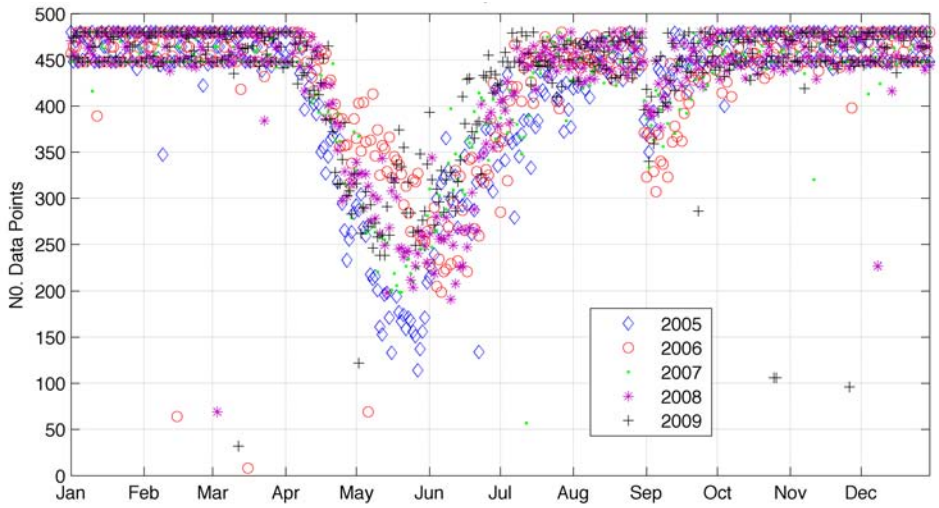

Figure 2.12. Number of data points available per month and per year from the Aura MLS v2.2 Temperature dataset from 2005 to 2009, over the geographic polar region enclosed by [60ºS–80ºS], for different pressure levels after applying the quality control guidelines discussed in Section 2.1.4.

2.1.4.2 COSMIC GPS-RO vs. Aura MLS v2.2 Temperature retrievals.

Validation

Southern hemisphere polar COSMIC temperatures and the respective Aura MLS v2.2 temperatures are generally similar (see Figures 2.13 and Figures 2.14) to each other. By the earliest time that this work was in preparation the--work in this area and literature available--findings comparing COSMIC and Aura v2.2 temperatures were scarce. The diagrams shown below are a novel attempt of data management for

comparison of temperature profiles retrieved by the Aura MLS v2.2 and the GPS constellation in the COSMIC radio-occultation mission in the Antarctic middle stratosphere in 2007. The COSMIC constellation measures a significant number of profiles each day due to the high number of GPS satellites, and these profiles are distributed irregularly in both time and space [*Wright et al.,* 2010b; *Barnett et al.,* 2008]. Thus, comparison of Aura Temperature observations versus COSMIC temperature retrievals offers a good way to see Aura in contrast with other databases such as COSMIC. It should be noted that MLS–COSMIC temperature comparison originally was not included in the work of *Schwartz et al.* [2008] on the validation of the Aura Microwave Limb Sounder temperature. Therefore, the present thesis is, unwittingly, a contribution to this previous work.

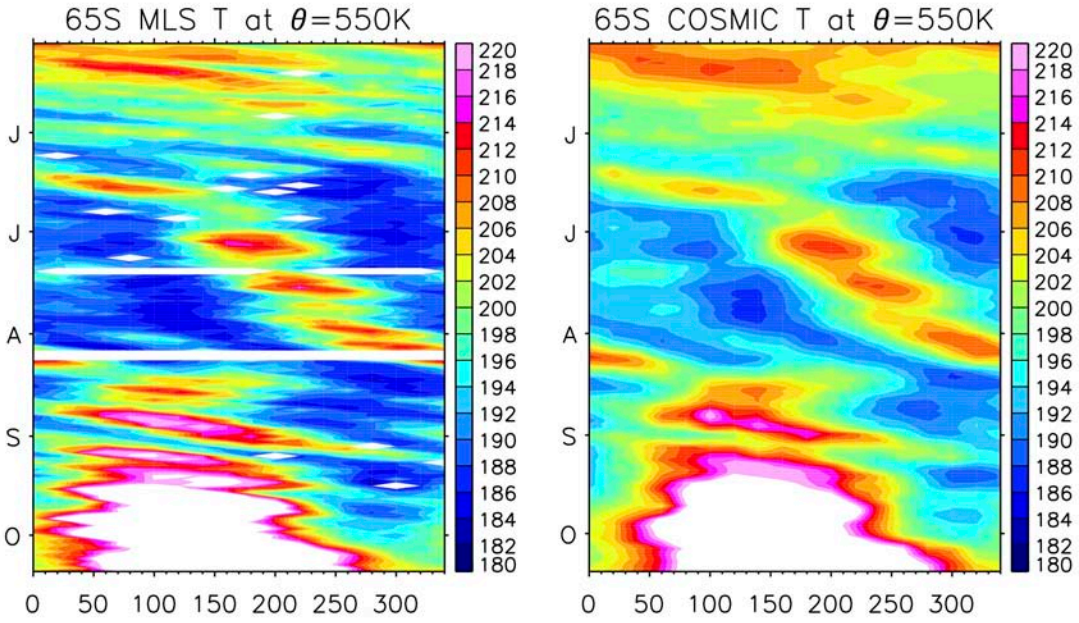

Figure 2.13. Time-Longitude diagrams (Hövmoller Diagrams) of MLS temperatures [left] and COSMIC [right] temperatures at the 550 K isentropic level and 60ºS–70ºS (units of K) in 2007. Note that COSMIC appear smoother due to the 7 day averaging done to these data. MLS data follows the quality control described in the present chapter. From *Alexander* [2011], and from MLS data provided by the author.

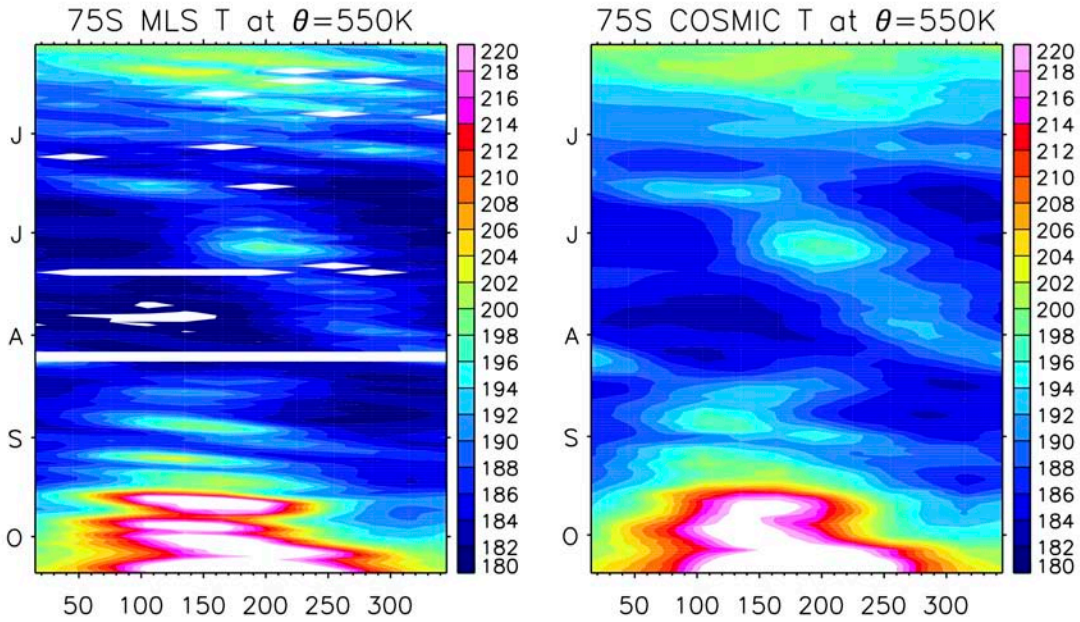

Figure 2.14. As per Figure 2.13 but at 70ºS–80ºS.

2.1.5 Aura MLS HCl, ClO and Temperature: analysis. Introduction.

As we can see in Figures 2.15 to 2.19, Temperature and HCl are strongly correlated. Additionally, the seasonal region where all Temperature, HCl, and ClO changes occur is very evident (roughly from June to October) in this set of diagrams.

The first *experiments* to find the day of the year in which HCl first starts to decrease were carried out and explained as follows: we have been calculating turning points in the APVR of Mean HCl curves by running a programming routine, for that matter. As we see, the days of the year we have found over 17-29 km altitude range are quite systematic (roughly on days 123- 125). Interestingly, the standard satellite temperatures in those days at every altitude are:

Height (km) (approximately)	Temperature (K)	Day 123	Day 124	Day 125
17		213.2	212.8	213.4
20		208.6	208.2	208.4
23		207.2	206.7	206.6
26		205.5	205.0	204.6
29		207.0	206.5	205.6

Table 2.2. Corresponding Aura MLS standard mean temperature observations for three different HCl turning points (days 123, 124 and 125) over the Antarctic region (60ºS–80ºS) in 2005.

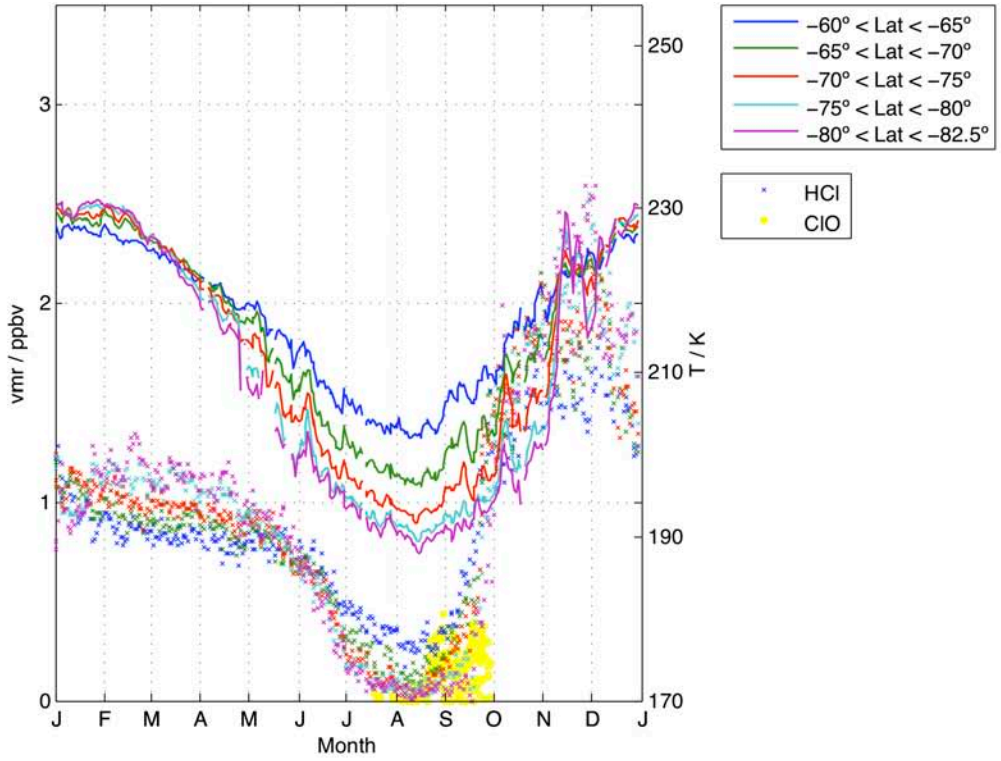

Figure 2.15. Seasonal evolution of zonally averaged Aura MLS standard temperature (Right axis – Thick lines), HCl (Left axis – asterisks), and daytime ClO (Left axis – yellow full dots) as function of latitude at approximately 17 km in 2005.

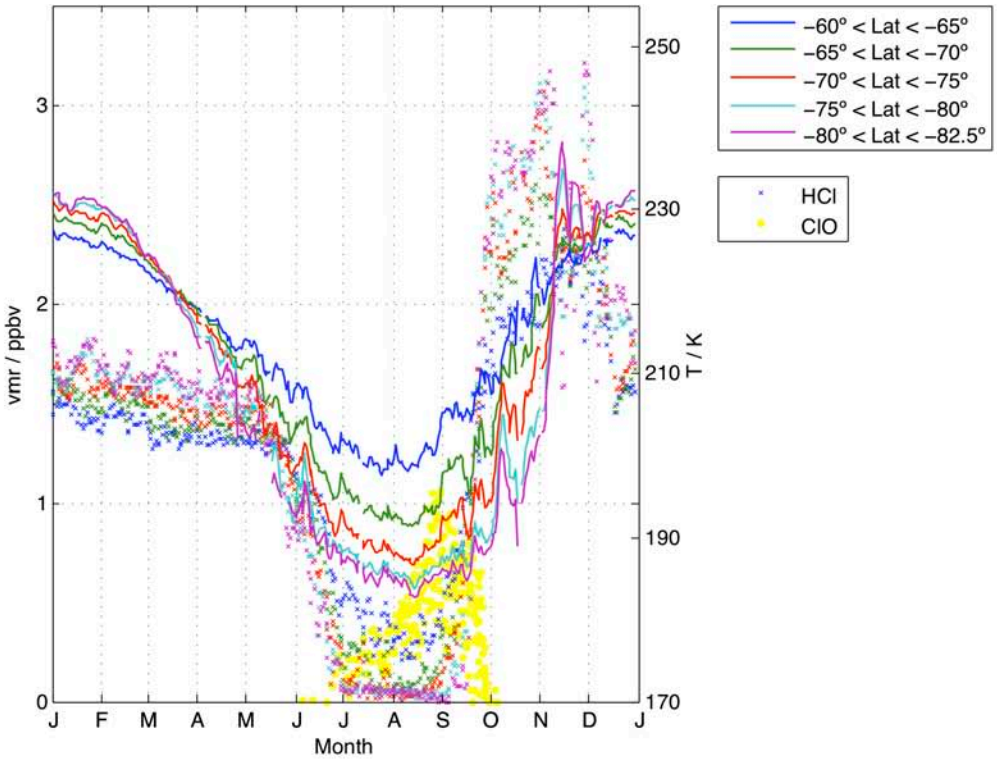

Figure 2.16. As per Figure 2.15 but at ~20 km.

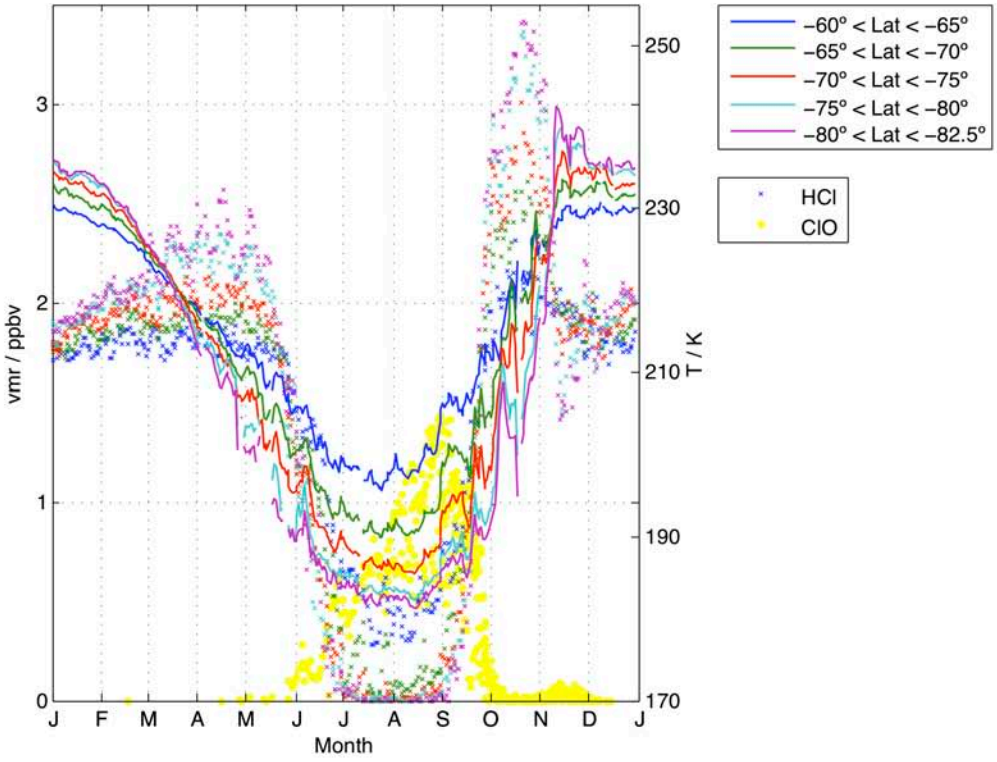

Figure 2.17. As per Figure 2.15 but at ~23 km.

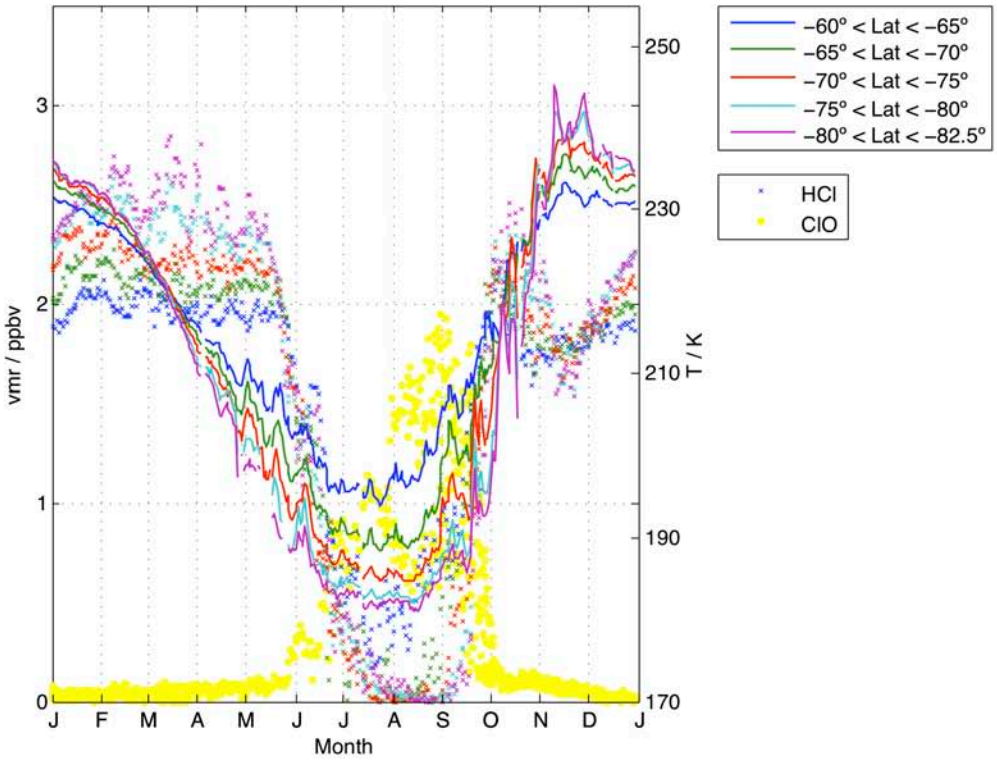

Figure 2.18. As per Figure 2.15 but at ~26 km.

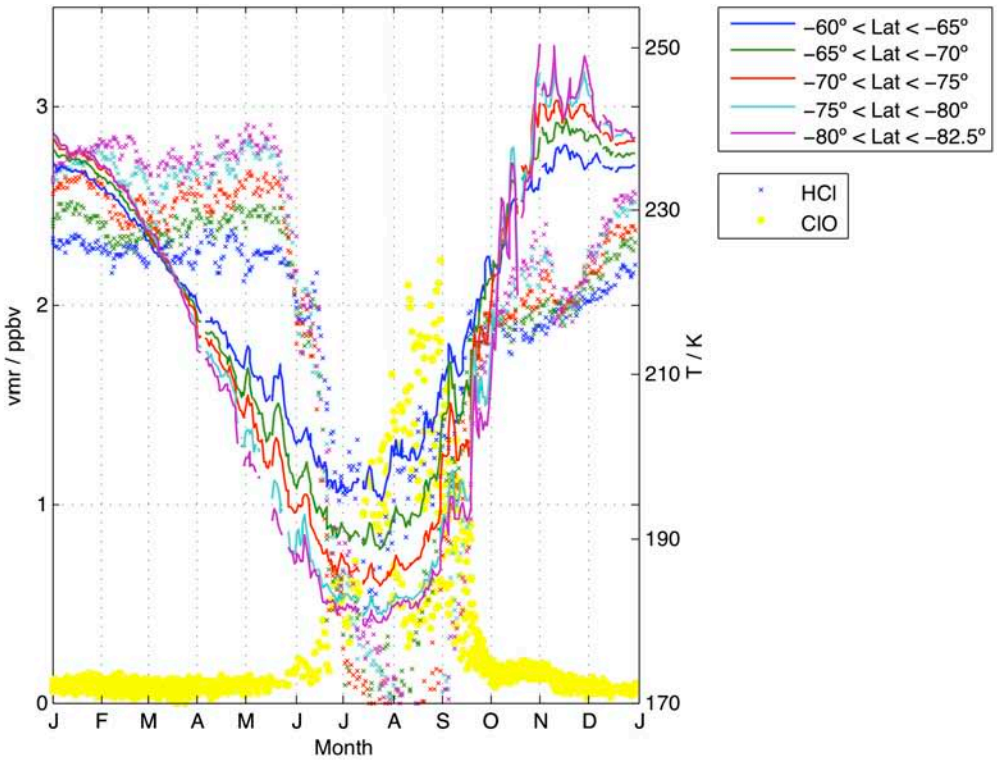

Figure 2.19. As per Figure 2.15 but at ~29 km.

Thus, see Figure 2.20 and those points mentioned above labeled with keys in different colors. Also, a few lines of explanation here for subsequent schematic diagrams:

- Band 1 means Geographic Latitude band over APVR from -60º up to -65º
- Band 2: like Band 1 but from -65º up to -70º
- Band 3: like Band 1 but from -70º up to -75º
- Band 4: like Band 1 but from -75º up to -80º
- Band 5: like Band 1 but from -80º up to -82.5

The upper slide of figure 2.20 shows MLS HCl data at 20 km in 2005 over Band 5. This region was chosen in order to assure that we would see very cold conditions i.e., more enhanced changes in HCl; as it is the polar region closer to the Pole.

The bottom of the same figure shows as Top but with data interpolated (linearly) and smoothed. Reason for interpolation of data: In 2005, at 20 km, there are around 10 days which did not contain any HCl data, and especially around May, so it was decided to run an Interpolation in those days just to guarantee accuracy on the calculation of change points. Working with smoothed data is also more comfortable--less spiky data (as we see on the upper figure 2.20 and easier to work with if we calculate gradients as it is the case.

The Yellow key indicates the first change point should occur anytime around May (see Figures 2.15 to 2.19). It is the point where HCl significantly starts to decrease. It indicates as well the time in which chlorine activation roughly occurs (‘roughly’ because HCl is not the only one reservoir playing a role in chlorine activation).

The Green key symbolizes that point when HCl has reached a minimum from its ‘fast’ descent. We figure we can correlate this point with the presence of very cold temperatures, (actually the coldest), of the austral winter.

The Magenta key is the point when HCl starts to recover. Here, we assume that the Magenta key day minus the Green key day -> should tell us about the period of time when ClO shows to have higher concentrations, PSC area are maximized, and temperatures are lowest.

The Cyan key indicates that those points during this 'cyan' period either indicate (roughly) that winter is over, and HCl is going to get a mean value to start with when we see it in January again, in a different year. See how at lower altitudes, this point occurs when HCl shows higher VMR than the yellow key one. But at higher altitudes, this value is lower. The Cyan key is not at the same level as the yellow key when the winter is over because of different conditions for HCl to be produced and the degree of ozone depletion in the stratosphere.

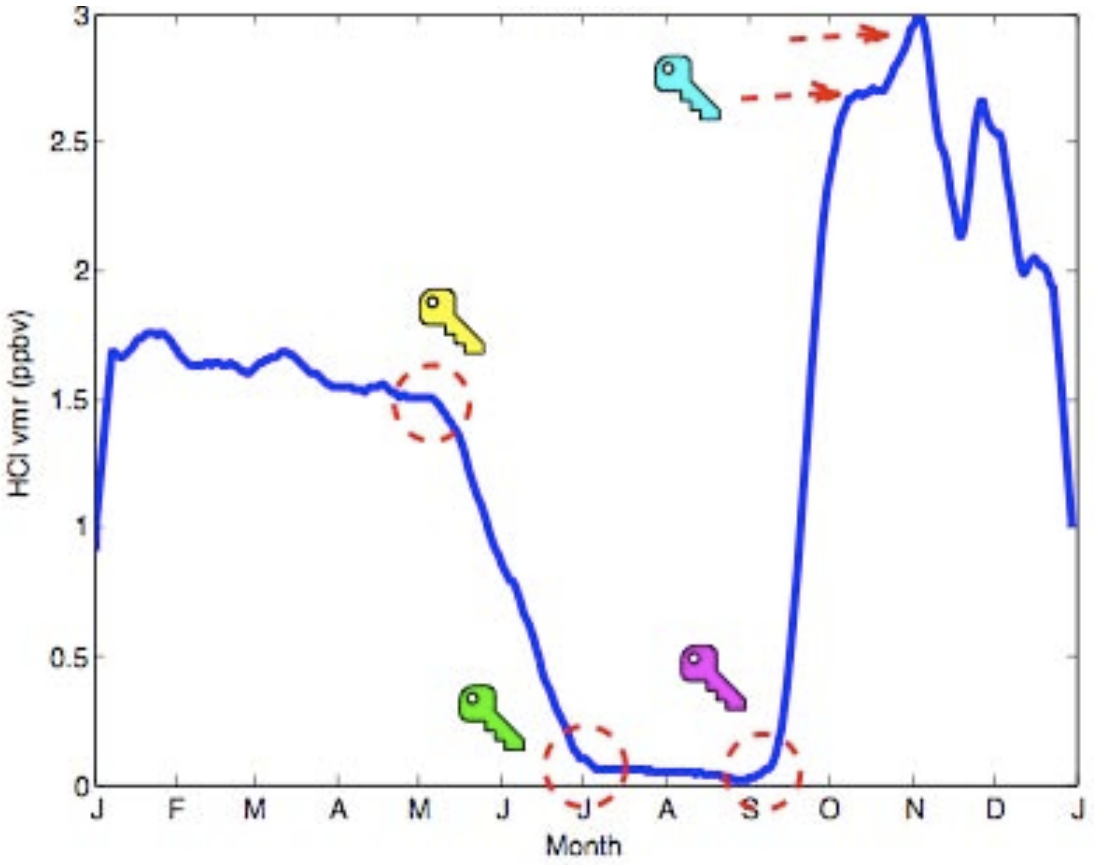

Figure 2.20. FIGURE 2.20 Motivation. Identification of seasonally HCl turning points. Data were interpolated and smoothed. A simple moving average smoother and interpolation to the data on this figure have both been used. Keys in different colors show suggested points for eventual calculation, bearing in mind that the Yellow one seems to be the most important to start with in the present work.

The algorithm for HCl turning points calculation--first part: In figures 2.21 to 2.25 you can see how the algorithm for HCl change points currently works. It basically is taking into consideration the first and second derivative tests. These calculations are made on already interpolated and smoothed data. We therefore look for those points where the slope is getting lower or greater; we easily find those points where

fluctuations occur, but we focus on those points where the period of fluctuation is longer--only downward at the moment (i.e. HCl depletion phase).

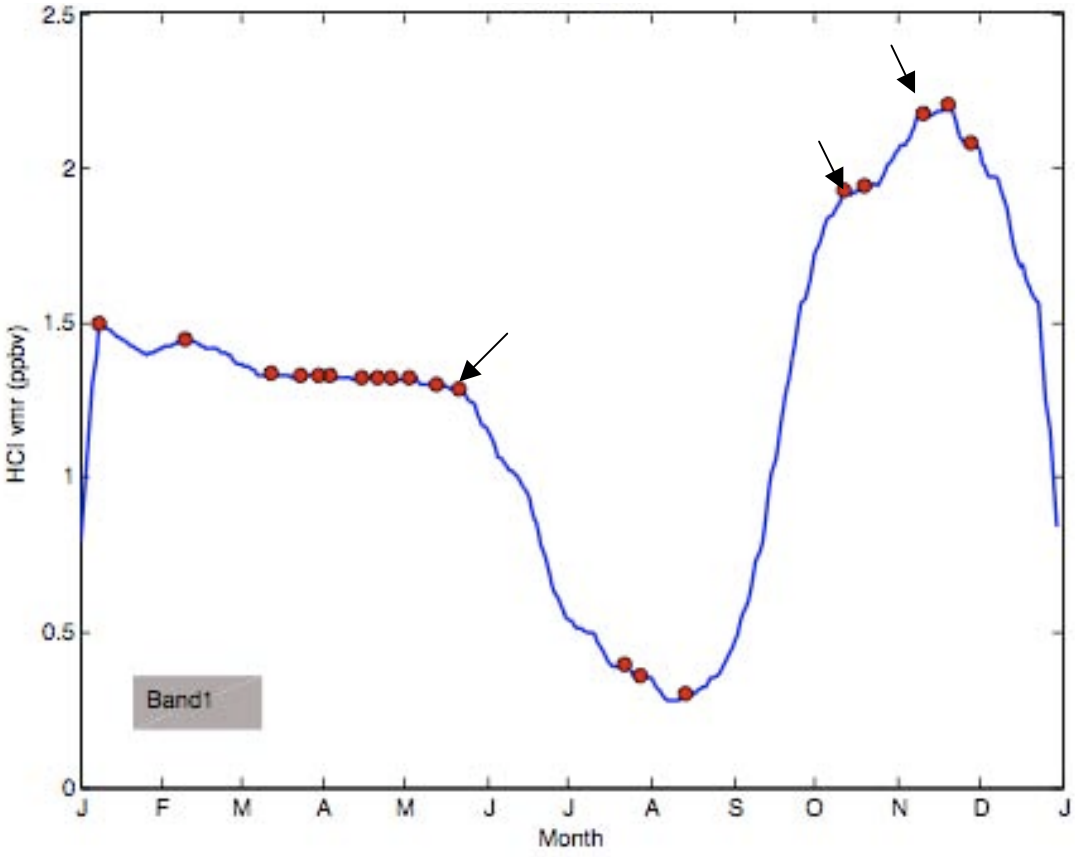

Figure 2.21. The algorithm of HCl turning points calculation's results (red filled circles) over Antarctic Band 1 in 2005 at 20 km. Arrows point different status of HCl concentrations precluding from depletion phase (left) and showing HCl production phase (right).

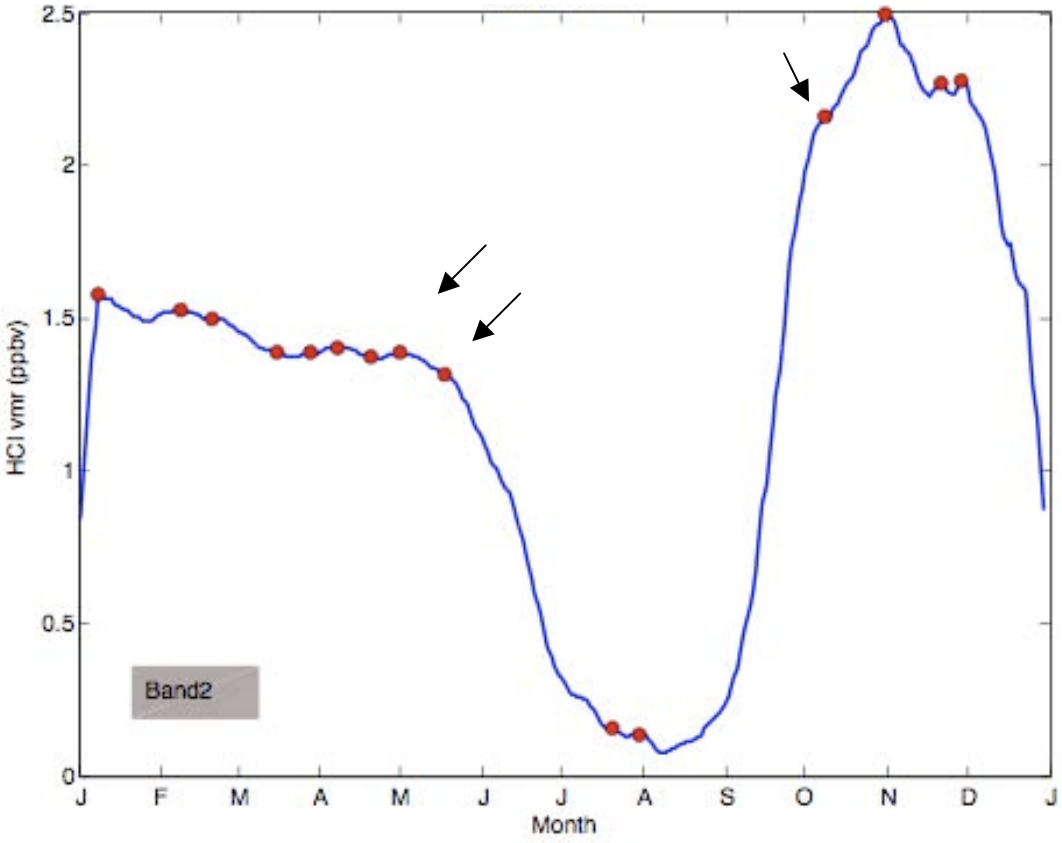

Figure 2.22. As per Figure 2.21 but for Antarctic Band 2.

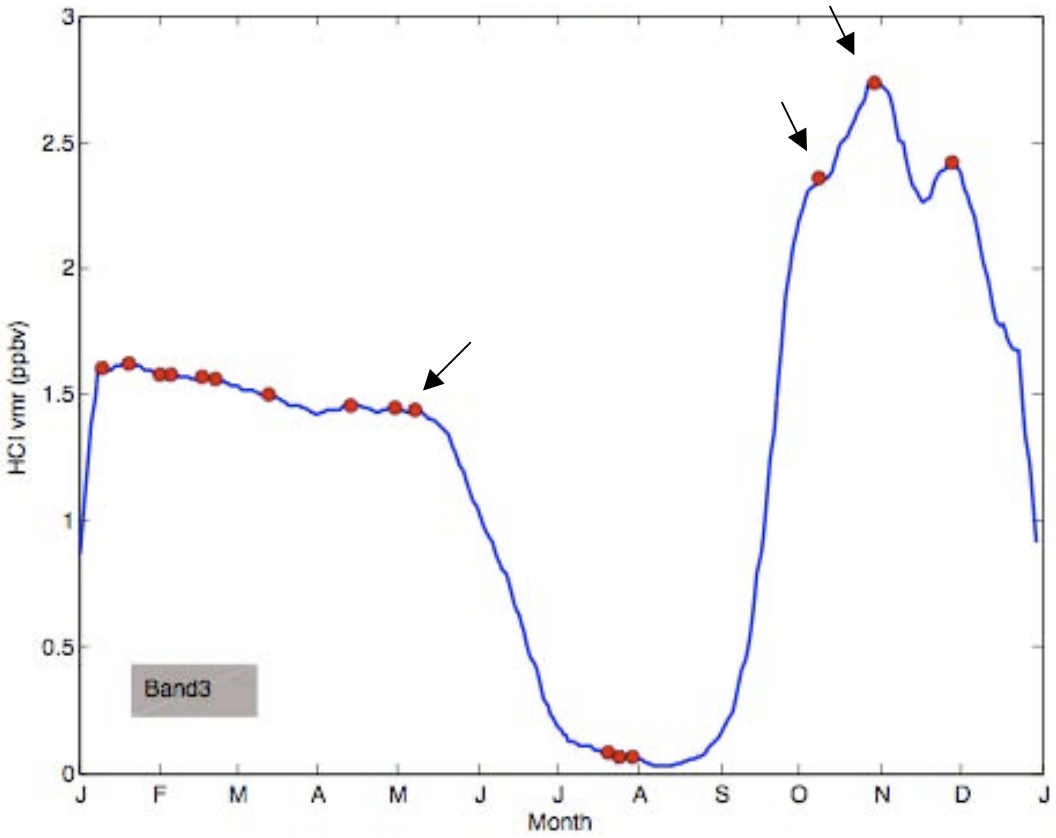

Figure 2.23. As per Figure 2.21 but for Antarctic Band 3.

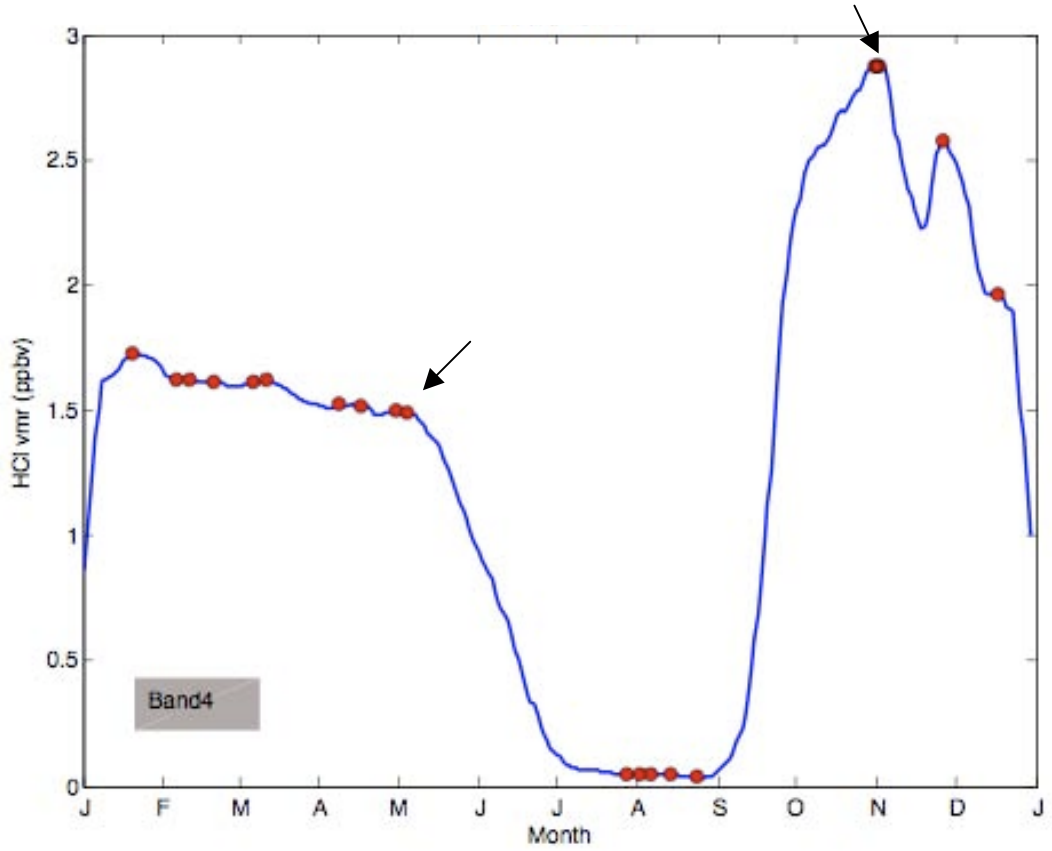

Figure 2.24. As per Figure 2.21 but for Antarctic Band 4.

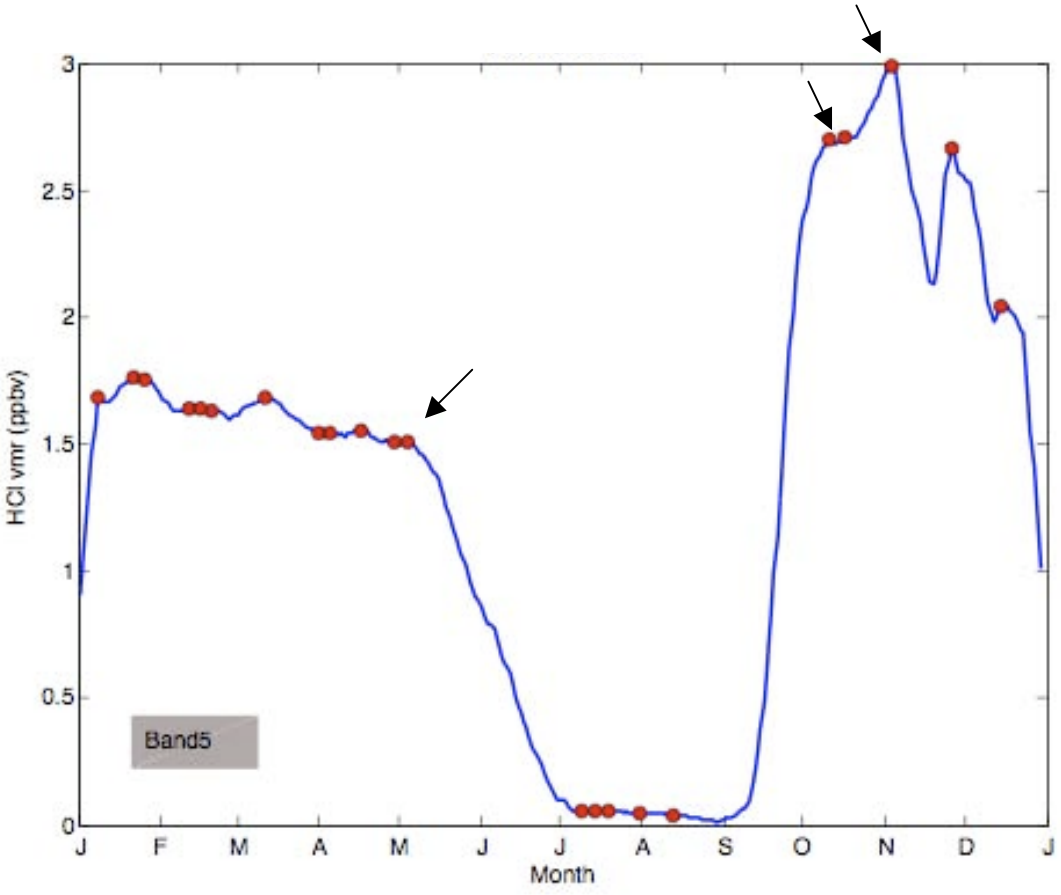

Figure 2.25. As per Figure 2.21 but for Antarctic Band 5.

Previously, we described how the algorithm worked for calculation of HCl signals. In the present lines, we are going to explain how this algorithm and its current improvements actually work. The first start was to focus on the calculation of points labeled as the *yellow keys*, i.e., HCl depletion start date. The aim was to calculate also the ClO and PSC start dates, and then plot all those points to gain a whole overview of the stratospheric chemistry in every year, and at different altitudes, and learn how each different stratospheric onset happens with respect to the others. All this was obtained, and can be seen through Figure 2.26 here.

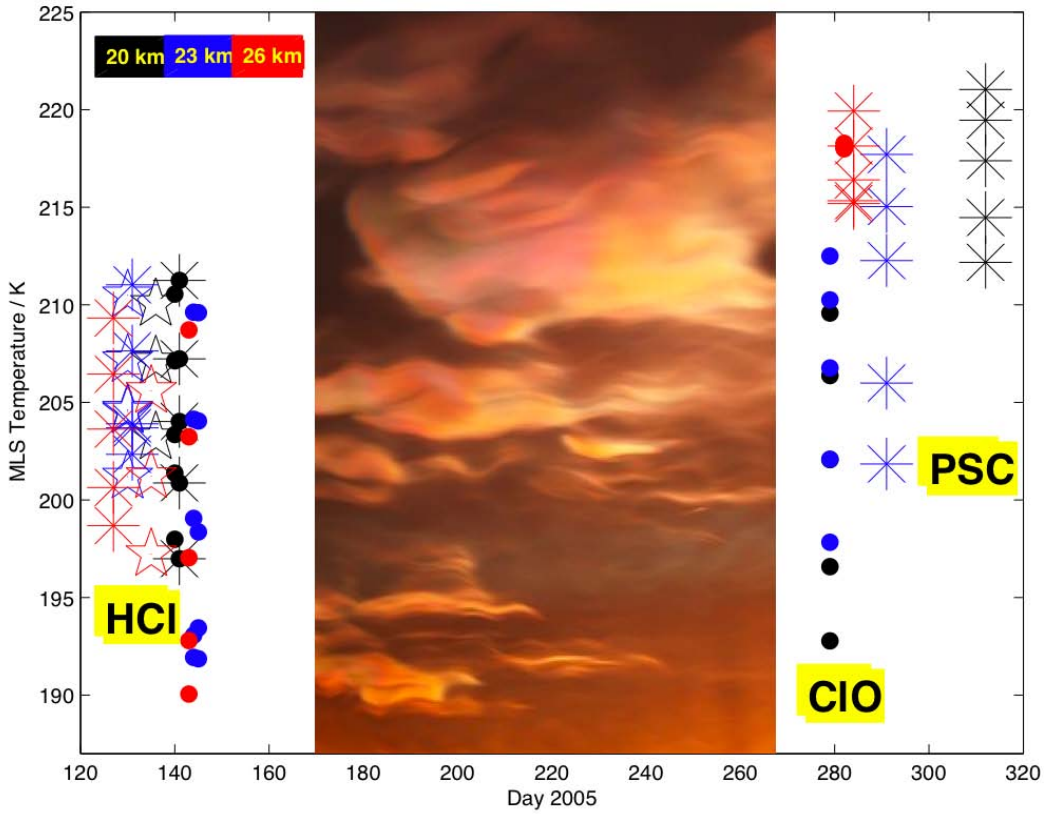

Figure 2.26. Different symbols show the onset and end of an MLS south viewing period for each stratospheric event: ClO, HCl and PSC (labeled with dots, stars and asterisks, respectively). Black, blue and red symbols mean those onset/end dates at 20km, 23km and 26km, respectively.

What figure 2.26 shows is important, because we focus on the range of temperatures in which the first/last MLS south-viewing periods occur for each stratospheric event relevant to the present work:

- HCl uptake/recovery,
- ClO activation/deactivation, and
- PSC formation/evaporation

We are saying here that all those events occur at temperatures ranging from ~ 190 K to ~ 225 K over the Antarctic Polar Vortex region. This matches well with *Zhang et al.* [1994], in which they experimentally show that the reaction probabilities for:

$ClONO_2 + H_2O \rightarrow HOCl + HNO_3$ and

$ClONO_2 + HCl \rightarrow Cl_2 + HNO_3$

are investigated on SAT surfaces at temperatures between 190 K and 230 K. (This study is based on SAT surfaces but, as *Zondlo et al.* [2000] shows, both NAT and SAT formation temperatures occur at roughly 195 K.)

HCl curve was analysed based on the calculation of gradients inspired at first from the idea of calculating turning points. Therefore, interpolation and smoothing of data was made on EACH curve corresponding to different latitudinal bands over APV, altitude, and year. The same level of smoothing was applied to all curves in order to be systematic. The algorithm uses a recurring technique to find the day of the year in which the first gradient is always negative for three weeks ahead of that point (dayA). The algorithm--(this is just a refinement)--finds a second point, (dayB), which corresponds to the day of the year immediately after dayA where the HCl uptake rate is equal or larger than the 50% of the mean rate found from dayA to the minimum of the curve. DayB was calculated too in order to see the day of the year in which the beginning of a fast descent occurs. This can either be associated with more suitable conditions in the atmosphere for HCl to be reducing more rapidly, or it is just a normal trend of this chlorine reservoir in particular: it starts decreasing and then does it faster until it gets to a point of maximum reduction. See, for example, Figure 2.27 [Top]

where HCl uptake starts on day 116, (dayA), at a random rate, but from day 139, (dayB), it goes down at a more steady and faster rate.

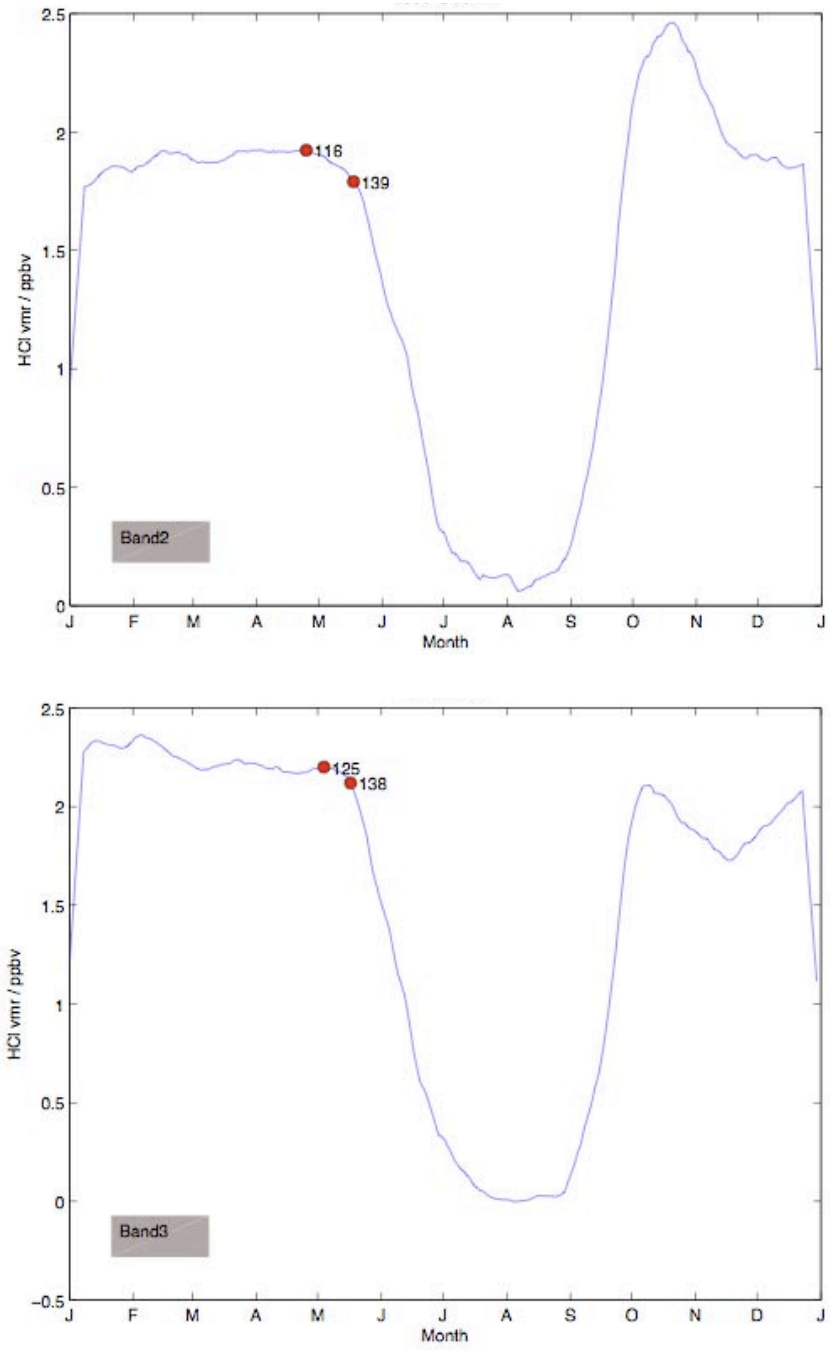

Figure 2.27. HCl curves in 2005 at 23 km (Band 2: -65º up to -70º) [top] and 26 km (Band 3: (-70º up to -75º) [bottom] in order to show how our HCl_signal_calculation algorithm works on the calculation of the HCl uptake (first point calculated), and faster HCl uptake (second point) signal calculations.

The values found in 2005 at 20 km–26 km are shown in Table 2.3, but and other years too. These are the values reading them straight from our algorithm calculations, and by doing the calculation of the mean value between dayA and dayB. The FIRST row of each grey sub-section in Table 2.3 corresponds to a curve of averaged HCl over a geographic latitude bin from -60º up to -65º.

SECOND row as in first row but GeogLatBin = -65 up to -70º,

THIRD row: -70 up to -75º,

FOURTH: -75 up to -80º and

LAST row: -80 up to -82.5º.

The smaller table appended through a downward arrow on the bottom shows the mean values at each altitude in different years from the values colored in violet (maximum and minimum values) of the main Table 2.3. These are the numbers that were used to create the stars on Figure 2.26.

2005	2006	2007	2008	2009
HCl uptake onset @ 20 km (n^{th} day of the year)				
144	145	140.5	139.5	139.5
142	140.5	135	124.5	134
135	133.5	119	131	129.5
128	118	126	124	134.5
128	117.5	133.5	132.5	119
HCl uptake onset @ 23 km (n^{th} day of the year)				
135	123	145.5	130.5	140.5
127.5	131	139.5	116	132
126	134	131.5	123.5	133
128.5	130	124	123.5	128
129	128.5	122.5	120.5	122.5
HCl uptake onset @ 26 km (n^{th} day of the year)				
140	132	140	139	151
134	138	139.5	139.5	132
131.5	136.5	135.5	128.5	129.5
132.5	136.5	131	122.5	126
129.5	137.5	121.5	121	126.5

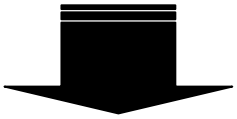

@ ALTITUDE: 20km, 23km, 26km (top to bottom, respectively)				
136	131	130	132	129
130	128	134	123	131
135	135	131	130	138

Table 2.3. Results from our algorithm for Aura MLS HCl signal calculation in 2005.

ClO curves--we worked with daytime ClO curves (SZA < 92º) over the APV region from -60º up to -82.5º. However, given that the calculation of daytime ClO data produces such sporadic curves (see Figure 2.5--bottom; right--), especially at higher latitudes (regions with poor sunlight exposure), it was decided to calculate the mean value of those 5 curves over APVR in order to have just one curve to work with.

We did not interpolate or smooth of ClO data, as further working with the gradient technique is not needed, as the calculation of signals for this kind of ClO curves is simpler (see Figure 2.28). We used the same recurring technique as in HCl calculation to find the point from which the curve is always growing for at least 21 days (dayA2). As a similar way to find dayB in HCl data, we calculated a second point in ClO data occurring right after dayA2, where the increase happens faster. Similar to dayA2, we found the day in which ClO starts to decrease. Results are shown in Table 2.4.

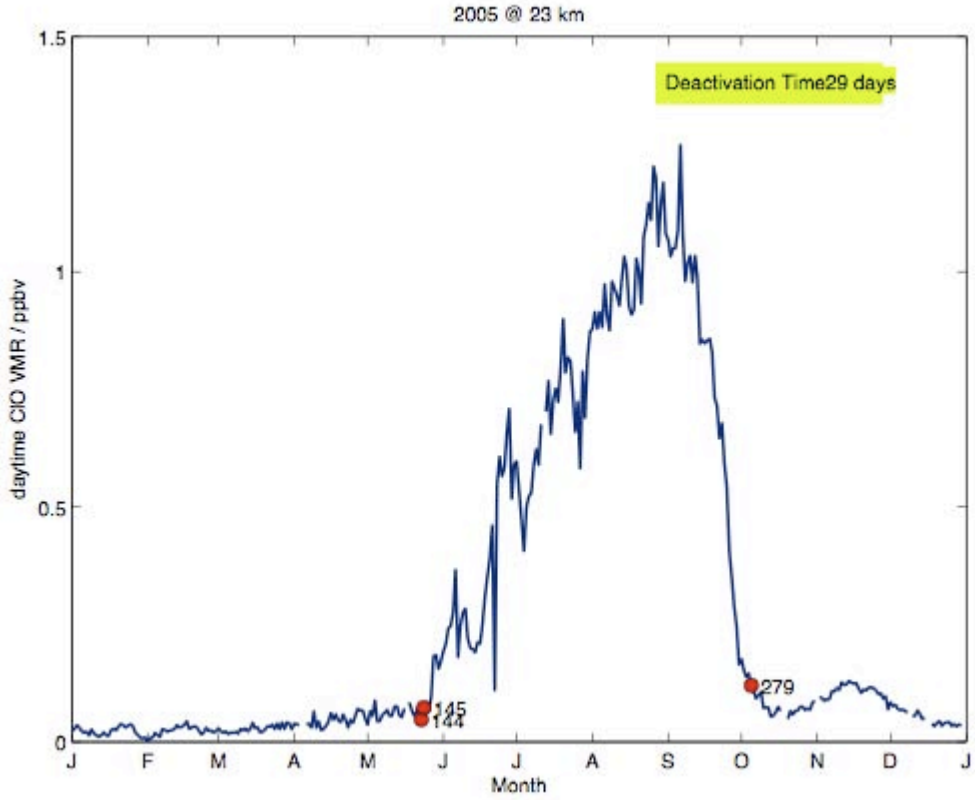

Figure 2.28. Example of how our algorithm for ClO activation/deactivation and respective dates are calculated.

ClO daytime activation/deactivation dates (n^{th} day of the year) @ ALTITUDE: 20km, 23km, 26km (top to bottom, respectively)		
2005	**2006**	**2007**
140-141/279	143-144/290	138-139/286
144-145/279	138/285	121/278
143/282	138/287	123/281

Table 2.4. Results for daytime ClO activation/deactivation dates calculation in 2005-2007 at three stratospheric altitudes.

PSC curves--both Type I PSC formation and evaporation dates were calculated over PSC curves assuming a PSC formation threshold of 195 K. We used this temperature just to produce quick PSC results that we may compare with other studies, but in the future, we will keep calculating Type I PSC and Type II formation thresholds derived from

MLS nitric acid and water vapour parameters by following *Hanson and Mauersberger* [1988], and *Marti and Mauersberger* [1993] formulations, respectively. The calculation of both dates was done following a simple algorithm in which we find the first day of the year in which the first and last viewings of PSC occur. Results are presented in Table 2.5.

PSC formation/evaporation dates (n^{th} day of the year) @ ALTITUDE: 20km, 23km, 26km (top to bottom, respectively)				
2005	**2006**	**2007**	**2008**	**2009**
141/312	137/321	144/301	149/309	135/307
131/291	131/308	122/289	126/296	127/297
127/284	125/293	121/283	122/285	121/289

Table 2.5. Results for PSC formation/evaporation dates calculation in 2005-2009 at three stratospheric altitudes.

In order to see both together--PSC and ClO temporal variations--Figure 4.32 was created. It shows there the timeseries of Type I PSC area below 195 K in contrast to uncorrected daytime data (SZA < 92º), both over APV region (-60º up to -82.5º), in different years, covering an altitude range from 17 km to 29 km. Note that MLS ClO data below 17 km is not scientifically accurate. From this figure, we can see a slightly stronger temporal variability in ClO data at altitudes below 26 km as at 26-29 km, (green-yellow colours--see Figure 2.29 for a better degree of detail). The variability remains almost constant, which probably tells us of an altitude region for more likely Type I PSC occurrence at roughly 17 km to 25 km, even though ClO mixing ratios seem to be larger as height goes up.

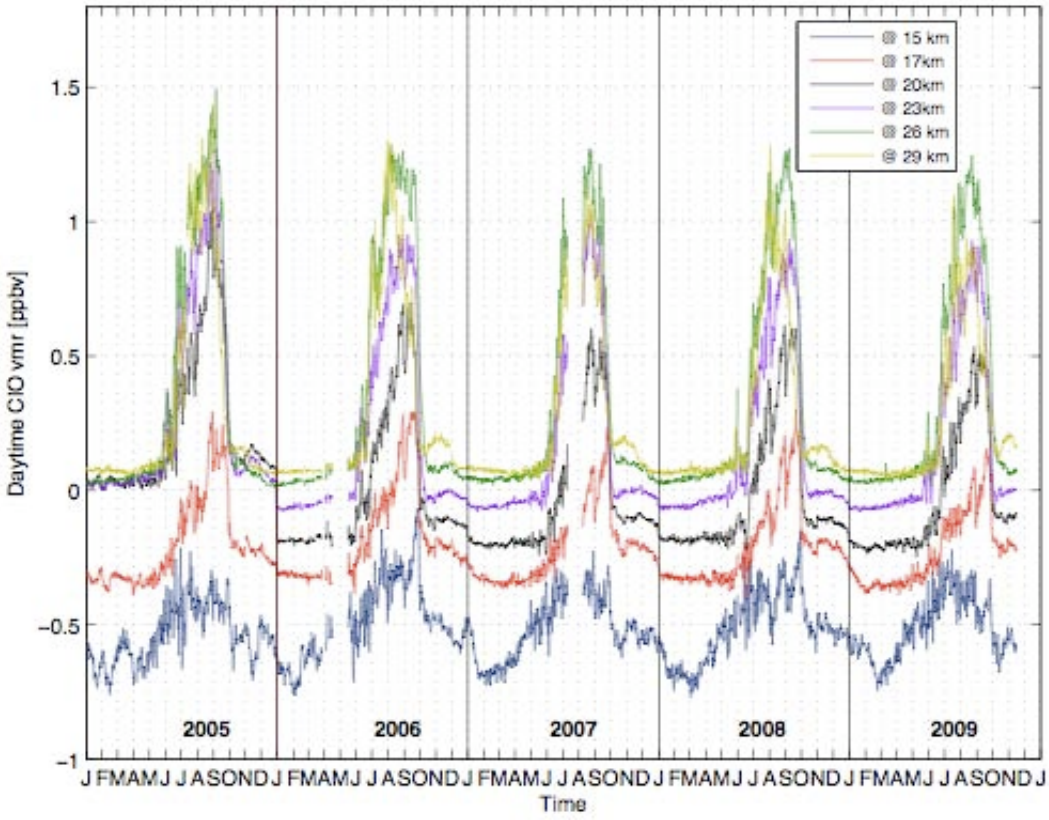

Figure 2.29. Timeseries of uncorrected daytime (SZA < 92º) ClO data at different stratospheric altitudes.

For example, from Figures 2.14 to 2.19, we laid some new questions on the table such as,

What factors control the evolution of the stratospheric HCl in the Antarctic vortex region? [Q1]

Apparently not only Temperature is associated with these low-high VMRs structures. Figures 2.14 to 2.19 seem to show a peculiar HCl pattern, with fluctuations in concentrations where T variations are not observed.

In order to elaborate well an answer for Q1, we went to search for studies that could likely have formed the basis of similar questions to Q1. *Seinfeld and Pandis* [1997] suggest that Temperature, latitude and altitude of the air parcel control the evolution of chlorine reservoirs as HCl and chlorine nitrate.

1) Having a look at Figures 2.21 to 2.25, specifically over the region mid- winter to late winter, we see that the HCl recovery rates seem to have a different pattern depending upon different altitudes, and even with respect to different positions over the Antarctic vortex. (Band 1 means a latitude band closer to an edge vortex chosen to be 60ºS, and Band 5 means those high latitudes closer to the geographic South Pole).

   Why is this happening? i.e., why does the HCl seem to have a different pattern on the phase of uptake, from that when it is in recovery? [Q2]

The first answer for Q2 was based on the clear HCl <-> T correlation we had gleaned from MLS data analysis (see Figures 2.21 to 2.25), given that there a few other studies that corroborate this, such as *Cox et al.* [1994], which concluded that there

exists a temperature dependence of HCl. They reached this conclusion after using laboratory measurements of the reaction rates and solubilities of the two main chlorine reservoirs and HOCl, to describe the activation of chlorine radicals from their reservoirs. Using a different experimental model, *Zhang et al.* [1994] concludes that the HCl uptake depends strongly on the thermodynamic state of the SAT surface, seeing this correlation as function of temperature and H_2O partial pressures.

Going back to our own work: Figures 2.21 to 2.25 plus Figures 2.14 to 2.19, we suggest a division of the HCl curves into two <u>different</u> phases (Figure 2.30 in this thesis).

A) HCl uptake. It takes place from January to roughly mid-winter

B) HCl production (recovery) from mid-winter to late winter.

If we do this, we could then be able to determine more easily which factors model (A) phase and see if they are different to those from (B) phase. The following diagram aims to summarize these concepts. However, we should not forget that all this is assumed to happen on the surface of NAT/ICE/SAT particles at least for phase A.

Figure 2.33 is presented in order to give an additional answer to Q2. As can be seen, the pattern following during [phase A] is relatively consistent in all years at each specified altitude. This points to a consistency in the heterogeneous reactions/factors that model phase A.

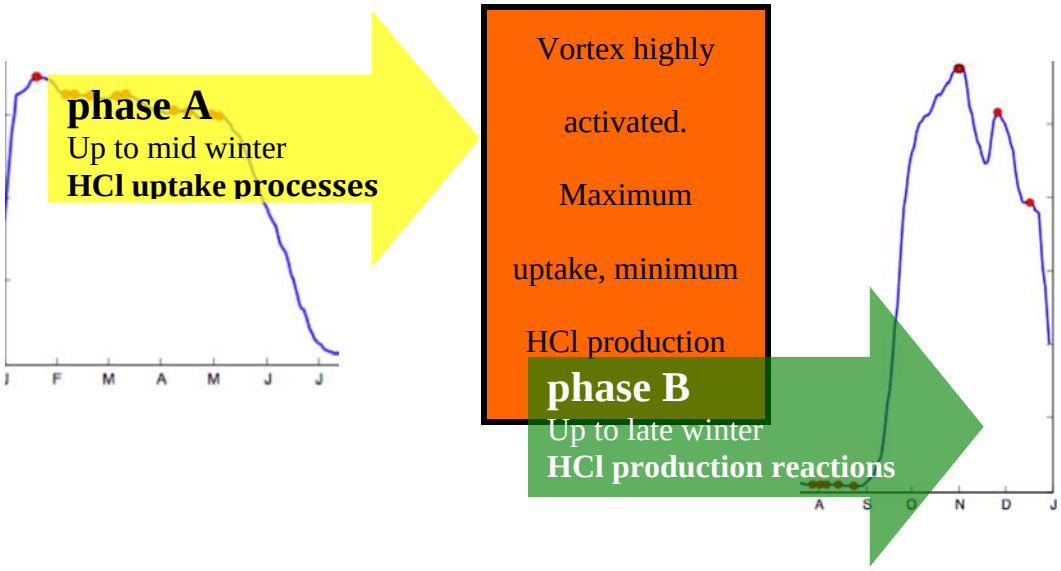

Figure 2.30. Diagram to present the two different phases--we divide up the HCl evolution patterns over the Antarctic polar vortex.

Given the point of view of the stratospheric chemistry that occurs, the HCl uptake process may involve different factors other than the HCl production phase, because different chemical reactions happen, and the vortex conditions are different. The uptake and production phases will involve different factors' these being light, T and NOx HOx conditions that are very different.

As it is known, during the phase of HCl uptake taking place on the surface of PSC particles, heterogeneous reactions involve chlorine reservoirs for those to occur. These reactions are strongly dependent on temperature [e.g. *Wilmouth et al*, 2006]. Also, apart from a HCl uptake, a $ClONO_2$ uptake also occcurs, but both happening at the different rates given:

i) The chemical nature of each chlorine reservoir by itself and

ii) The presence (of chlorine reservoirs) in the stratosphere occurs in different amounts over a PSC formation altitude range. This difference is more evident in the Arctic than in its counterpart the Antarctic though.

The Bond energy of the HCl (measured at STP conditions) is 428 $kJmol^{-1,}$ whereas the $ClO\text{-}NO_2$ bond energy at those same conditions is 111.5 $kJmol^{-1}$ [*Zou et al.,* 2003]. Similarly, we know that the $ClO\text{-}NO_2$ bond is the weakest, and the (ClONO)-O bonds are the strongest.

This implies that a larger amount of energy is required to break up the HCl bond in contrast to the energies for dissociation of either $ClO\text{-}NO_2$ or ClONO isomers bonds, which are smaller compared to those for the HCl.

Thus, in the reaction,

$$HCl + ClONO_2 \rightarrow Cl_2 + HNO_3 \qquad (2.1.1)$$

the chlorine reservoir that controls the making of chlorine radicals should be the HCl, given that its chemical bond is roughly four times stronger than that for the chlorine nitrate. For reaction shown in equation 2.1.1 to occur, it also depends on the total initial amounts of HCl and $ClONO_2$ when the vortex is still not active but HCl it is in larger amounts. *Jaeglé et al.* [1997] concludes that chlorine activation begins with 60-75% of inorganic chlorine as HCl, this derived from ER-2 aircraft observations.

In conclusion, because of (i) and (ii), having an answer for Q1 is important, because a good understanding of HCl evolution in the Antarctic stratosphere is going to allow us to correlate better those key events associated with ozone depletion:

• Activation of the Antarctic Vortex (low temperatures <-> PSC formation <-> heterogeneous reactions involving chlorine reservoirs <-> chlorine activation. *Could HCl measurements be used as an indicator of the Antarctic vortex edge position / APV activation date? [Q3]*

To answer this question, let is take a look at a previous picture shown in Figure 2.31 of this Thesis. Note that outside of the vortex period and during phase A and B, larger amounts of HCl are observed in higher polar latitudes, whereas smaller concentrations seem to be at polar lower latitudes (see in blue “lower polar latitudes” and magenta the “higher ones”). But once the vortex is highly active (mid-winter), the lowest concentrations of HCl are now present at the higher latitudes but blue crosses (HCl from low polar latitudes) did not go that low--they were just partially depleted. This pattern is also observed at other altitudes. Therefore, is this indicative of a correlation between latitude and HCl?

If blue HCl (averaged over a latitude band from -60º up to -65º) does not deplete at all, then it means that choosing a vortex edge of -60º is not that accurate, i.e., the vortex edge should be measured by measurements of the next latitude band. In this case, blue crosses should be ruled out, and thus we should consider green crosses instead (the next latitude band below -60º up to -65º) in order to find a right vortex edge position. It may be also valid to say that this blue HCl pattern says something about vortex edge asymmetries.

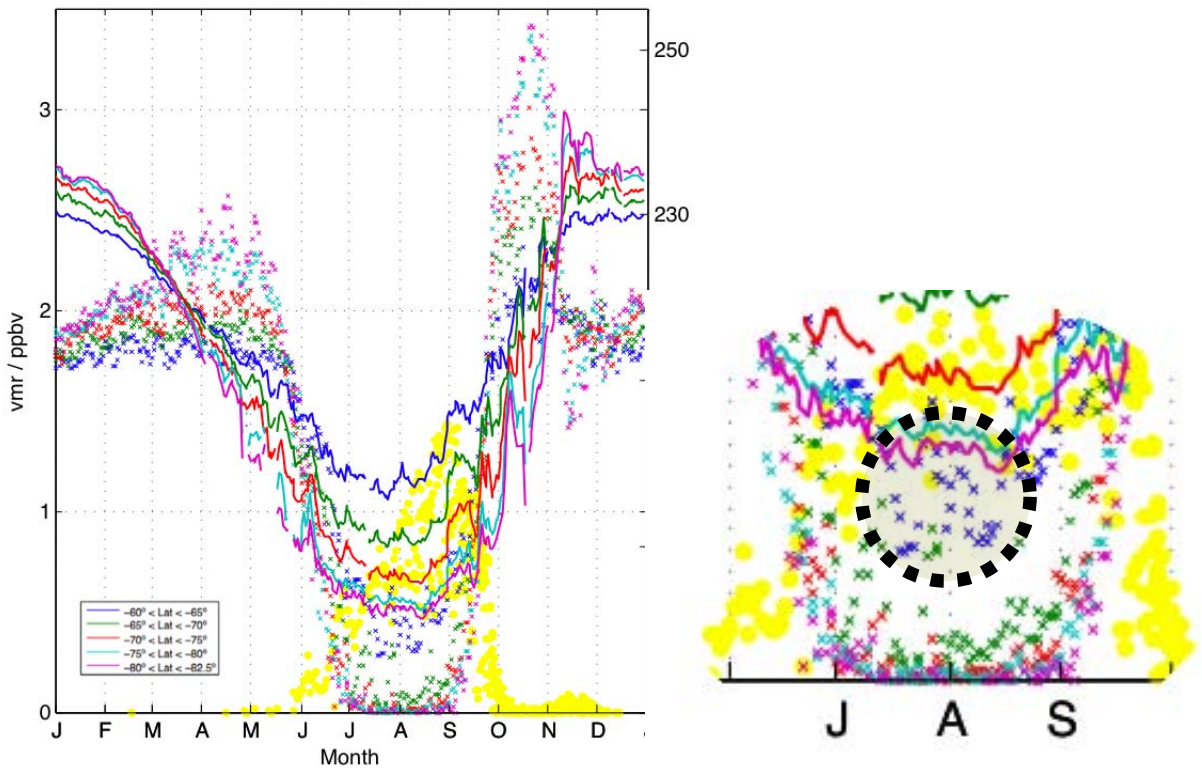

Figure 2.31. Evolution of HCl (crosses), Temperature (solid lines) and daytime ClO (yellow dots) over APVR at 23 km in 2005, derived from MLS observations [left]. Figure 2.17 has been zoomed out [right] in order to demonstrate a way to find the vortex edge position by using HCl measurements.

Could we use HCl to determine an altitude range for PSC observation? [Q4]

Figure 2.32 answers Q4 as: yes, we could.

Depletion of HCl occurs from 15 km to 29 km (see figure 2.32), and probably at 32 km, but at this altitude, 100% depletion is not actually occurring. Therefore, if heterogeneous reactions involving chlorine reservoirs (like HCl) take place on the surface of PSC particles, and we can derive from HCl observations that HCl reaches a maximum of uptake over 15-29 km, we could associate this altitude range with very likely observations of PSC events.

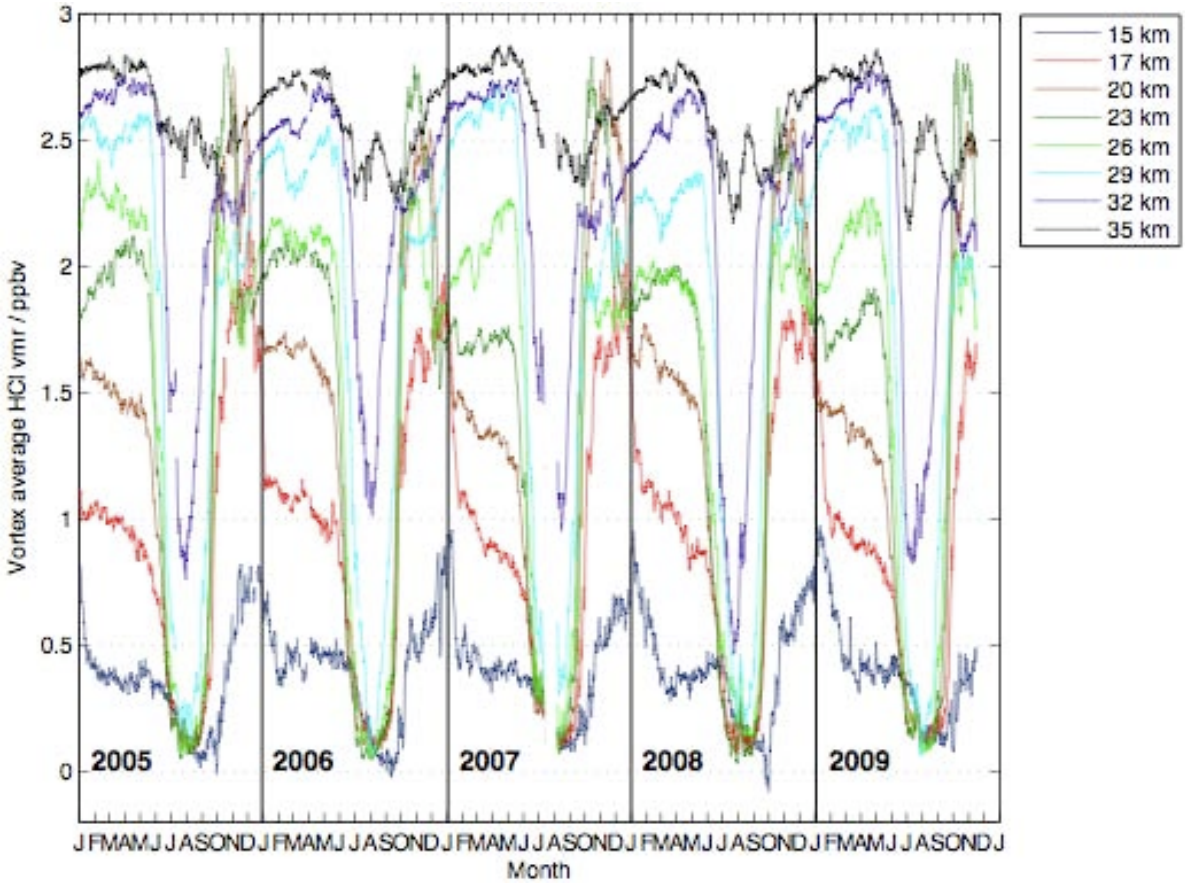

Figure 2.32. Time series of vortex average MLS HCl (ppbv) at different stratospheric altitudes and years over APV region and choosing a vortex edge equal to 60º S.

Figure 2.34--left shows a 4th-degree polynomial correlation between HCl and T in phase A for MLS 2005 data at 20 km, only during the first half of year (day 1 to 180). It is worthy of mention that an exponential fitting (not shown) also gives good results for HCl–T correlation, as the alternative definition of the exponential function seen as a Taylor series expansion. Figure 2.34--right shows the same as in Figure 2.34--left, but for 23 km.

Figures 2.35 and 2.36 are like figures 2.33 and 2.34, respectively, but for HCl and T measurements only from day 200 to day 365, in 2005-2009.

We see from Figure 2.35 that the temporal pattern during the HCl recovery (phase B) is not as consistent as for its phase A. This may tell us that factors less stable year-to-year actually control this phase. Different reactions [2.1.2 to 2.1.4] for HCl production may take place [*Wilmouth et al.,* 2006].

$ClO + OH \rightarrow HCl + O_2$ (2.1.2)

$ClO + HO_2 \rightarrow HCl + O_3$ (2.1.3)

$Cl + CH_4 \rightarrow HCl + CH_3$ (2.1.4)

From [Eqn 2.1.2 to Eqn 2.1.4] it is possible to note that Cl, HO_x and methane concentrations are likely to govern the production of HCl in the lower-middle atmosphere. Thus, phase B may be more complex to analyze than phase A, given that there are apparently more factors affecting B.

It actually would be interesting to see what the data HO_x and methane data look like, in order to see if there is any kind of correlation between the amounts of those species and of HCl during the phase of recovery.

From the MLS data set, we have measurements of HO_x radicals, but only at 26 km-higher in the case of OH data. Recommended data are available from 29 km, and higher for HO_2.

However, we took no notice of those MLS team suggestions and we created some OH figures from these data in order to be able to see via pictures how true is reaction 2.1.2 (not shown). We saw that there occurs a build-up of OH species by mid-winter, and that those are the necessary amounts for production of HCl in reaction shown in

equation 2.1.2, though we cannot say too much from this OH-analysis, as a clear OH build-up is only marginally observed.

We know that it is possible to get CH_4 information from SOCOL data which is generally available at the University of Canterbury. The question here is: How feasible would it be to actually obtain this methane information from 2005 to 2009 in order to compare MLS HCl--Phase B 2005-09 patterns with SOCOL CH_4 measurements during that same period of time, and covering an altitude region of roughly 15-29 km? This might be a good way, to explain better the difference in patterns observed on the HCl recovery phase for different Antarctic winters that we have data from (see figure 2.35). This data where not available during the write-up of the present document. Thus, during the time this thesis was being reviewed, a local expedition was carried out in order to ask local modellers able to provide support on the use of a model for inclusion of results in this document. The only two models we were able to contact were:

a) Méso-NH model[3] (France) and

b) SOSA model[4] (Finland).

However, none of these models appear to be of help to these results nor are

[3] Méso-NH model is the non-hydrostatic mesoscale atmospheric model of the French research community. The model is intended to be applicable to all scales ranging from large (synoptic) scales to small (large eddy) scales and it is coupled with an on-line atmospheric chemistry module. So, the possibility to use it in order to run PSC simulations is very complicated, due to nothing already exist for this kind of run. The chemical scheme has not all the reactions needed for stratosphere [*Berthet,* 2011].

[4] In particular, in the need of a model to run stratospheric chemistry over the southern stratosphere, with the horizontal long-range transport, the model SOSA is not able to help, since it is only a column model for troposphere and cannot be valid against horizontal long-range transport [*Zhou,* 2011].

photochemical models. Therefore, a future search for those using photochemical models will continue.

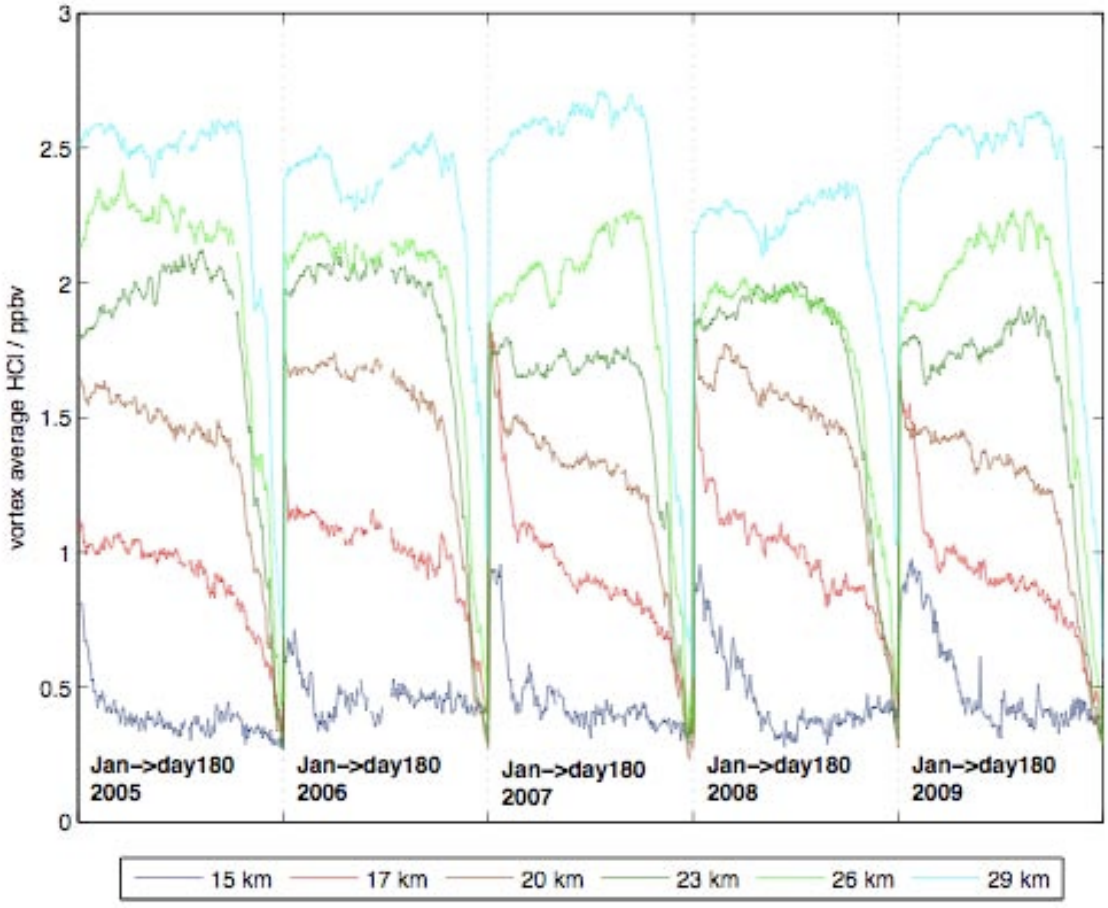

Figure 2.33. Timeseries of MLS HCl for only day 1 to day 180 data in 2005-2009 at different altitudes. (Phase A analysis).

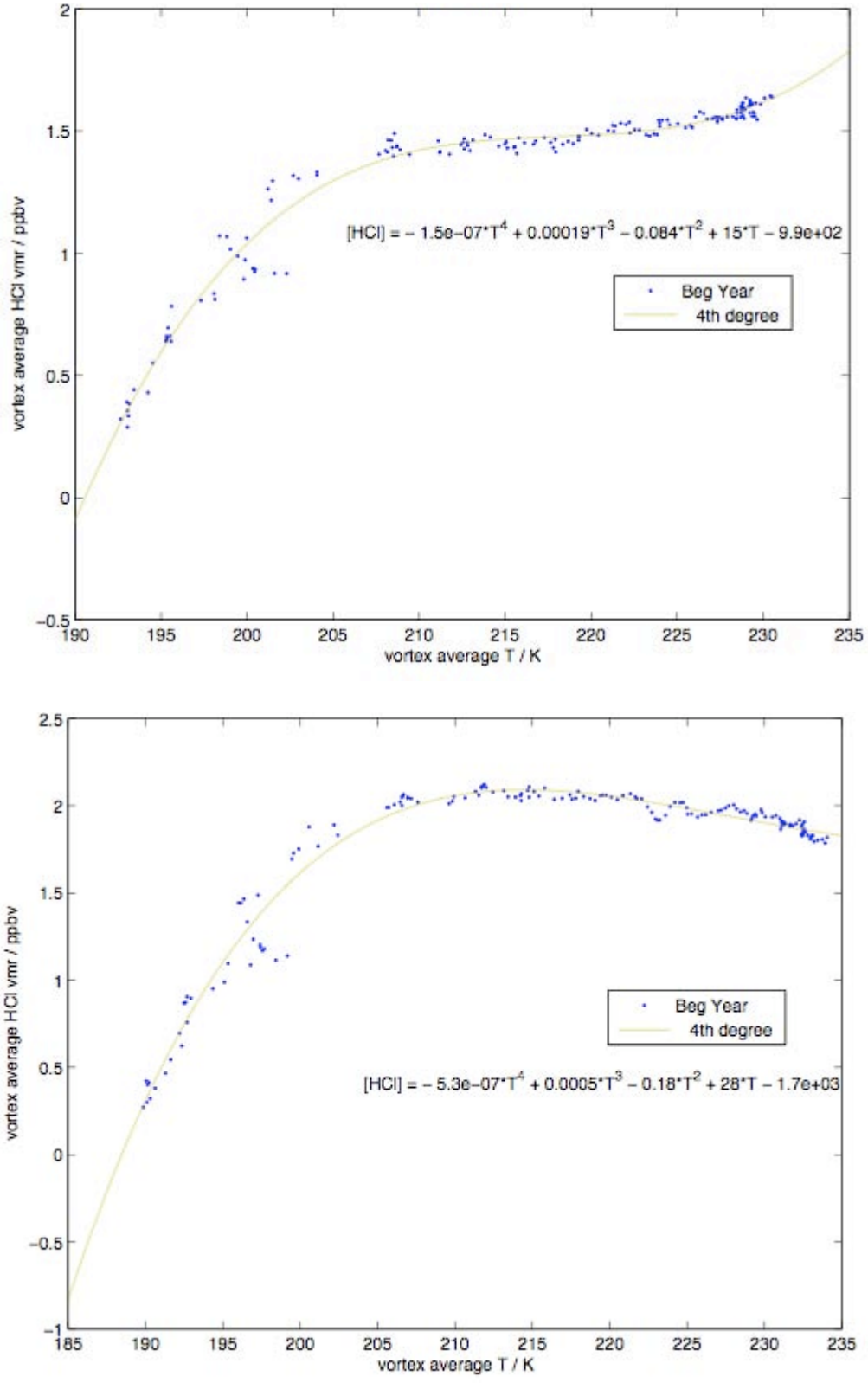

Figure 2.34. Correlation between HCl and T during phase A from MLS measurements in 2005 at 20 km and only data from Jan- day 180 were used at 20 km [top] and 23 km [bottom].

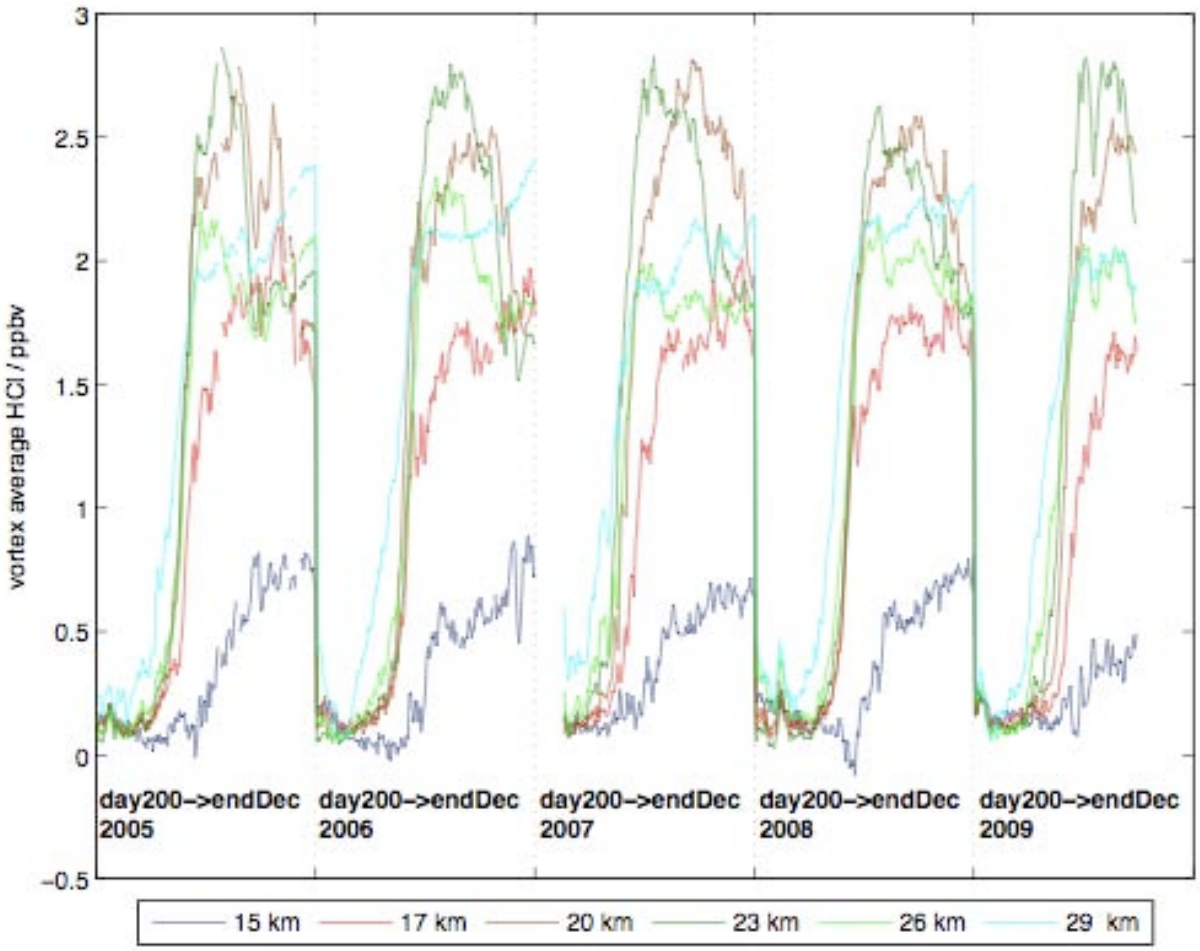

Figure 2.35. Timeseries of MLS HCl for only day 200 to day 365 data in 2005-2009 at different altitudes. (Phase B analysis).

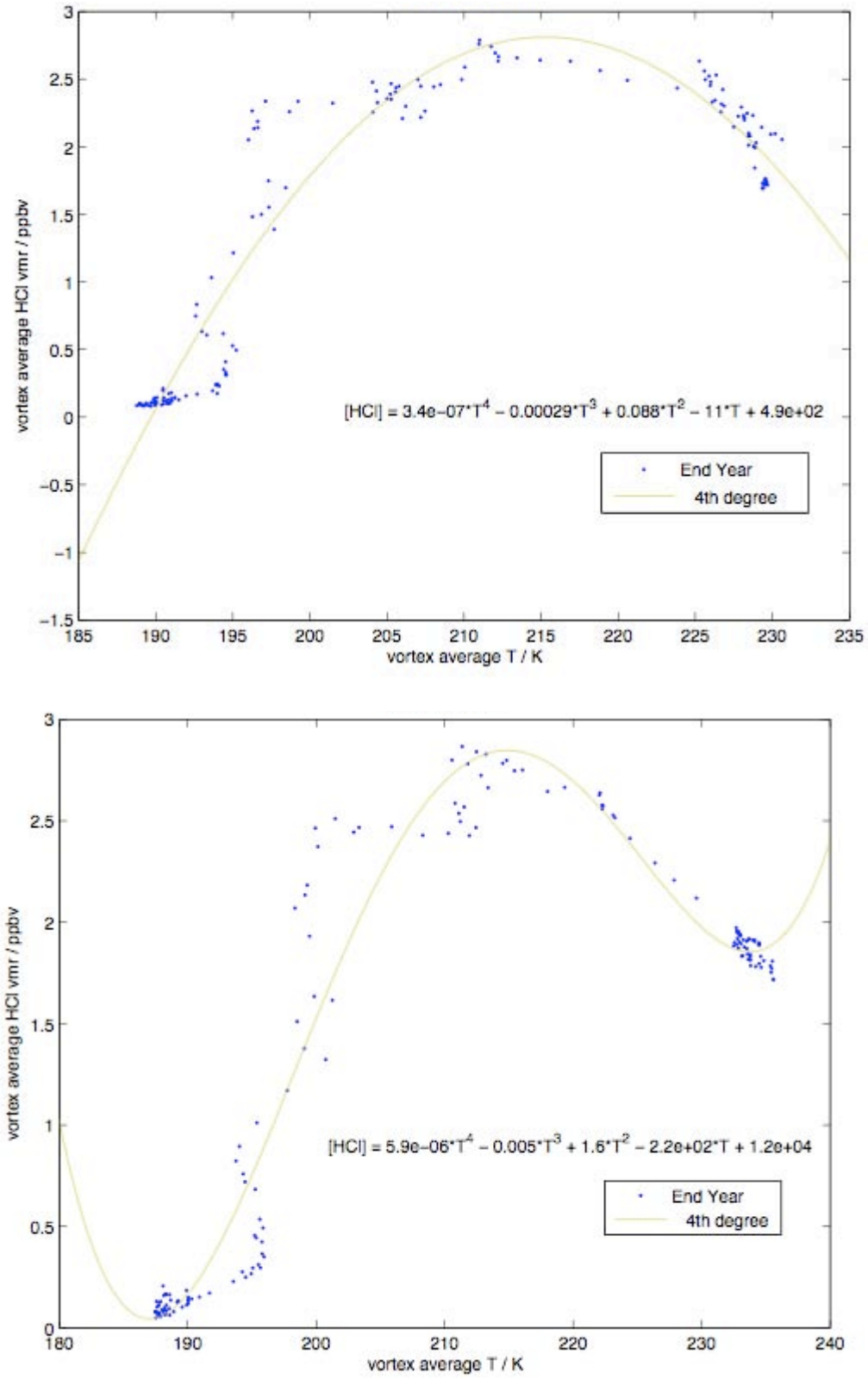

Figure 2.36. Correlation between HCl and T during phase B from MLS measurements in 2005 at 20 km and only data from day 200-day 265 were used at 20 km [left] and 23 km [right].

Inorganic Chlorine Budget derived from MLS available chlorine species: Given that we only have direct information from one of the chlorine reservoirs (HCl), and similarly only information from one of the chlorine reactive forms (ClO) from the MLS dataset, we are apparently unable to evaluate the inorganic chlorine budget (ClO_x + $ClONO_2$ + HCl/Cl_y) for different Antarctic winters. However, we actually can examine an alternative chlorine budget that we have defined as:

$$\text{Cl budget} = HCl/Cl_y \quad (2.1.5)$$

$$Cl_y \approx HCl + ClO \text{ (daytime)} \quad (2.1.6)$$

Thus, with reactions shown through equations [2.1.5] and [2.1.6] in hand, it was produced Figure 6.1 (see Chapter 6) in order to see how variable is this vortex region average chlorine budget at two different altitudes compared to HCl and daytime ClO concentrations. It is interesting to note on these figures how the Cl budget is a normalized form of the HCl pattern, with a very stable evolution outside the vortex.

Finally, Figures 2.37 I-IV show temporal Aura MLS Cl_y variation in five different years and different altitudes. Those were done with the idea of seeing any possible year-to-year pattern variability, which tells of any missing chlorine species are not taken into account. It is clear that we see those different patterns particularly during the first months of every year. So, a conservation of Cl_y is not achieved from only using MLS available chlorine species, though those variations are not significantly large. This suggests the lack of consideration of the chlorine nitrate species into Cl_y calculations. But we think our results via [2.1.5, 2.1.6] are good enough to keep working with by looking at Figure 2.37.

[I]

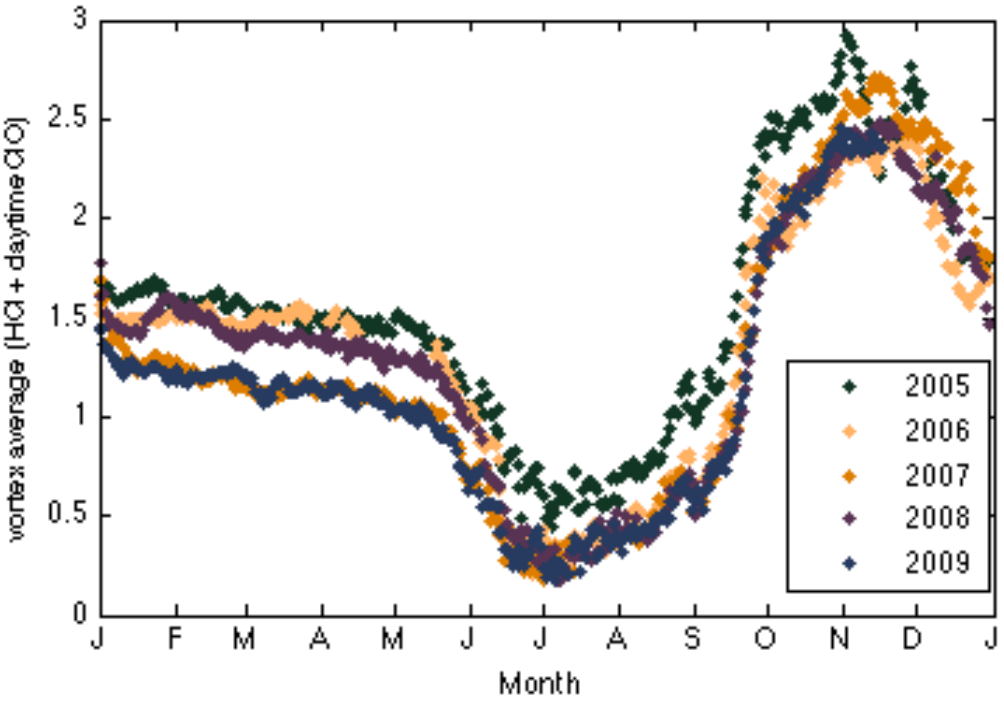
vortex average (HCl + daytime ClO)
3
2.5
2
1.5
1
0.5
0
J F M A M J J A S O N D J
Month
2005
2006
2007
2008
2009

[II]

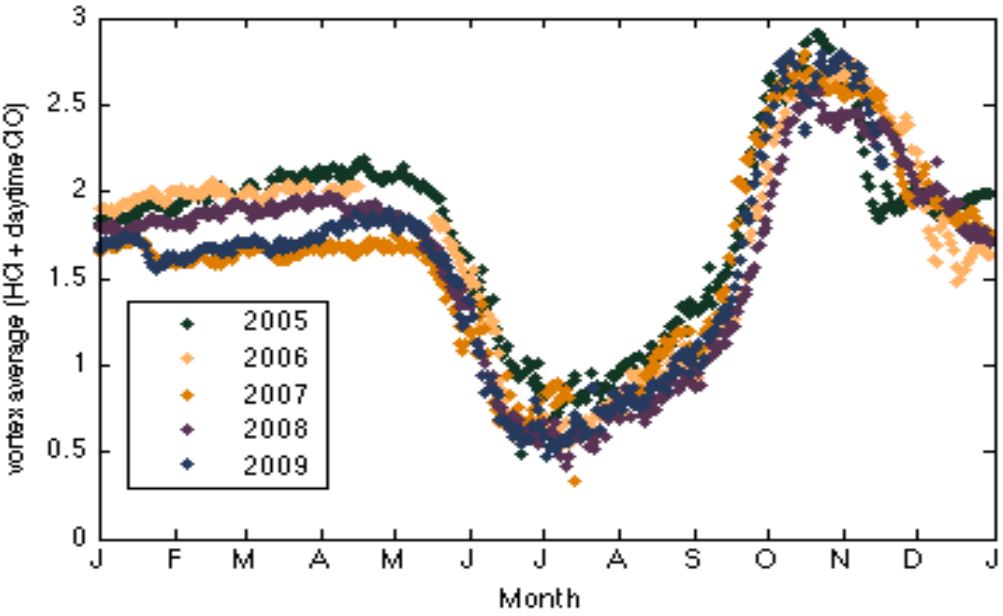
vortex average (HCl + daytime ClO)
3
2.5
2
1.5
1
0.5
0
J F M A M J J A S O N D J
Month
2005
2006
2007
2008
2009

[III]

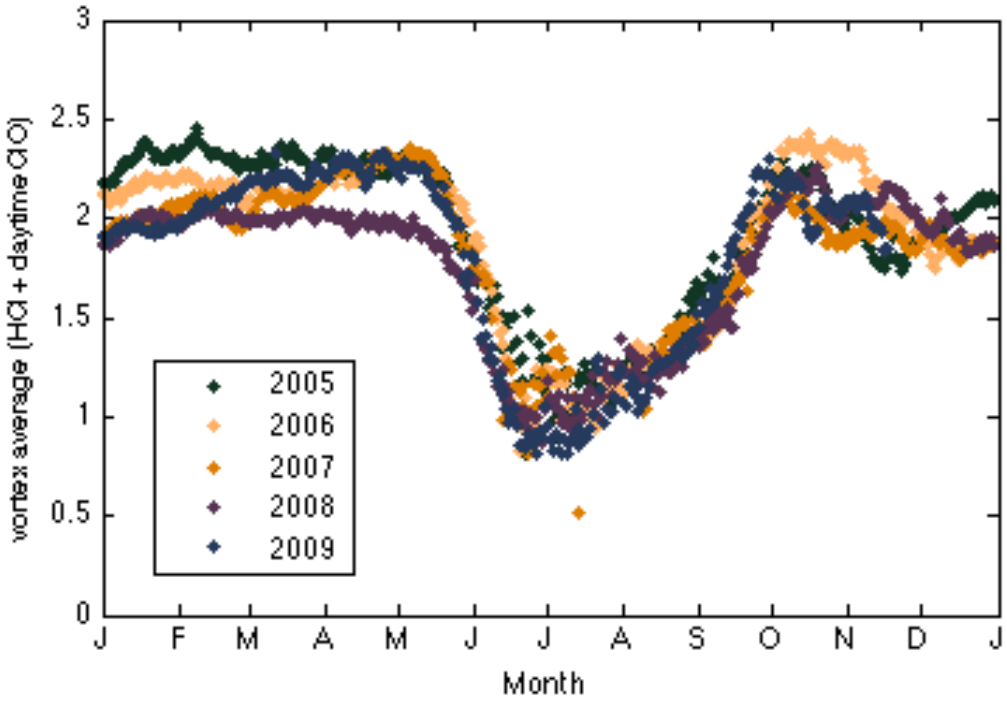

[IV]

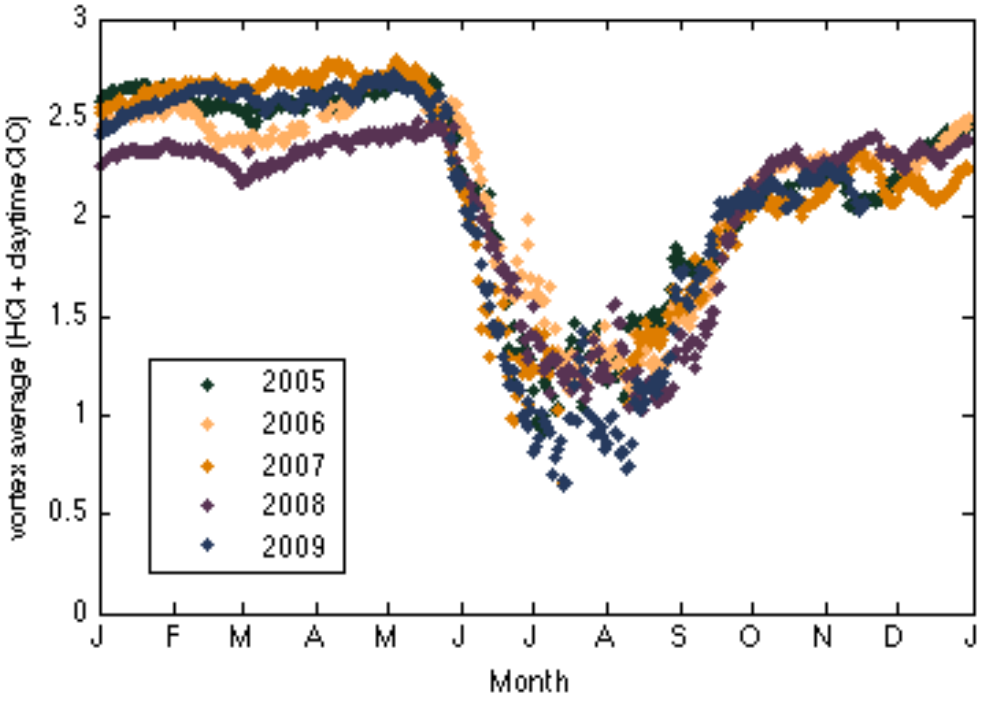

Figure 2.37. Temporal evolution of Cl_y calculated via [h] at 20,23, 26 and 29 km [I,II,III,IV, respectively] in 2005-09 from MLS measurements. Vortex region averages were calculated over APV region with a vortex edge of 60ºS.

2.1.6 Aura MLS Hydroxyl Radical

The hydroxyl (OH^-) radical is the most important oxidant in the atmosphere [*Brasseur and Solomon,* 2005; *Mogensen et al.,* 2011]. As indicated below, *Wilmouth et al.* [2006]'s reaction, in its equation 16, shows the sole known HCl-loss gas-phase reaction via hydroxyl radical oxidation:

$$HCl + OH^- \rightarrow Cl^- + H_2O \qquad (2.1.7)$$

This reaction in equation 2.1.7 acts in the absence of heterogeneous reactions [*Wilmouth et al.,* 2006] is relevant to chlorine activation; however, the MLS OH^- concentrations readily accessible for this study in, for example, 2006 were only available for the middle stratosphere. Nonetheless, v2.2 OH^- daytime and nighttime data in 2006 in the Southern Hemisphere were determined (not shown) to be near zero ppbv at ~23 km and only slightly higher until 1 July 2006. Thus, this gas-phase mechanism reaction is not included in the present study since an extensive examination is required in future work.

2.2. NCEP/NCAR 2.5º assimilations

The NCEP/NCAR temperature product provides information on a 2.5º x 2.5º latitude-longitude grid, with global coverage from 90ºN to 90ºS [*Kalnay et al*., 1996]. In order to compare the PSC area results inferred from Aura MLS and this dataset, the present study employed NCEP/NCAR temperature data from 2006, over the pressure levels from 100 hPa to 20 hPa. By using both of these datasets, possible defects in either dataset and a greater certainty in PSC area patterns for a comparison with HCl depletion areas could be examined.

Figure 2.38. Pearson's Correlation Coefficients (PCC) for different samples of temperature over SH (-60° up to -82°) using EOS MLS Version 2.2 and *old* Version 1.5.

Year: 2005, Day: 25th, 46.4159 hPa

a) April PCC = 0.9858

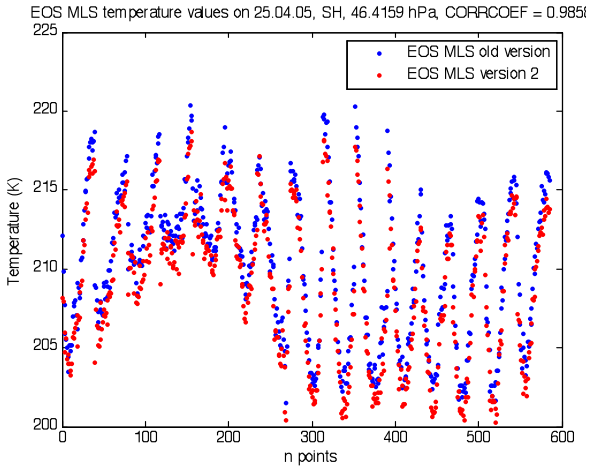

Year: 2005, Day: 25th, 100 hPa

b) April PCC = 0.9732

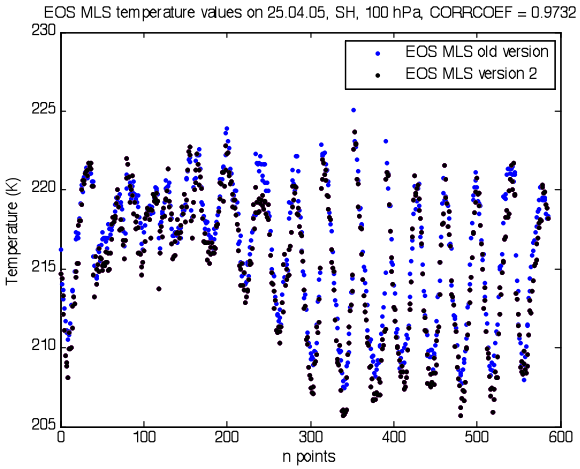

Year: 2005, Day: 25th, 10 hPa

c) April PCC = 0.95

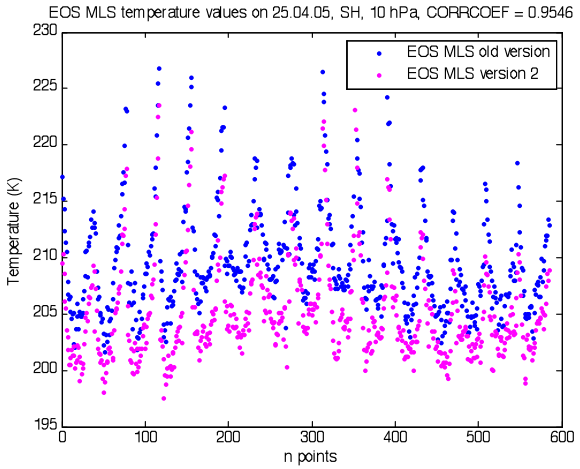

Figure 2.38. Continuation.

d) May PCC = 0.9908

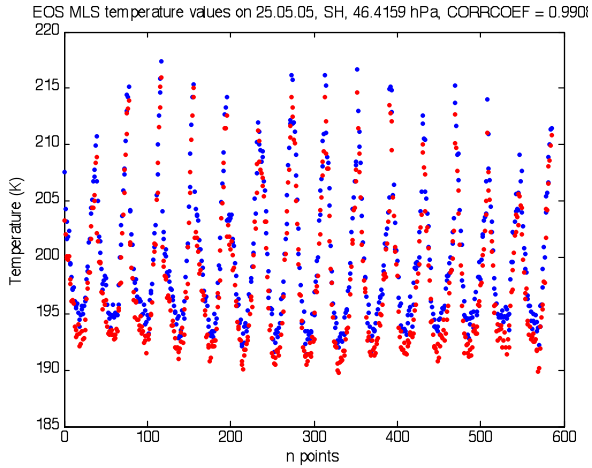

e) May PCC = 0.9819

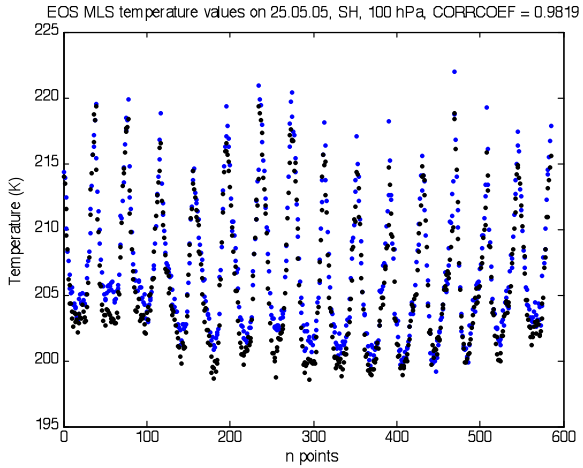

f) May PCC = 0.96

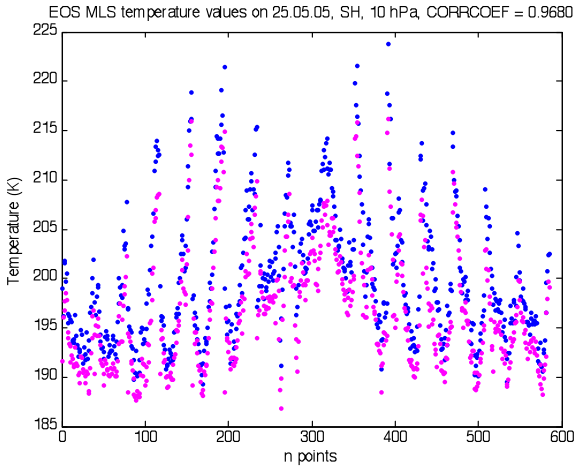

Figure 2.38. Continuation.

g) July PCC = 0.9902

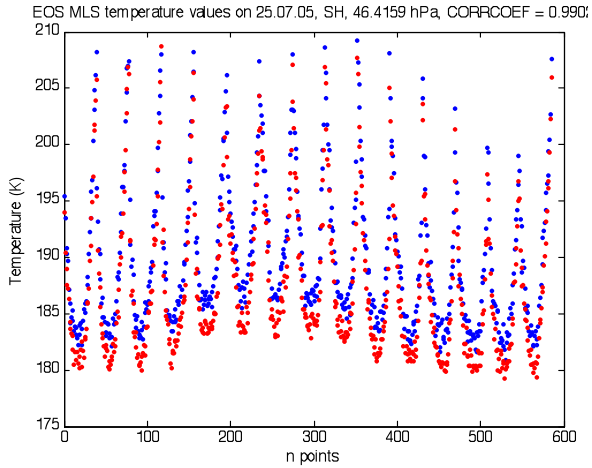

h) July PCC = 0.9827

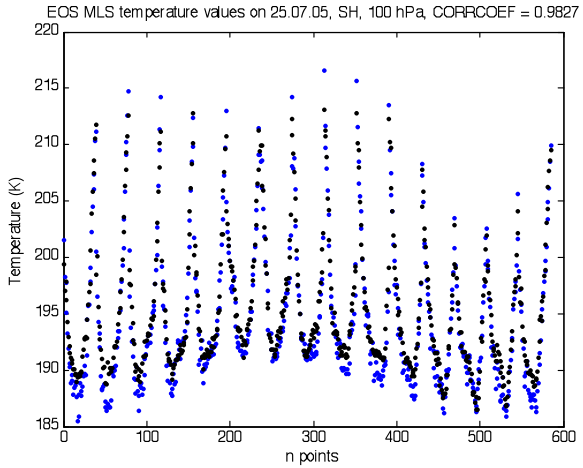

i) July PCC = 0.9596

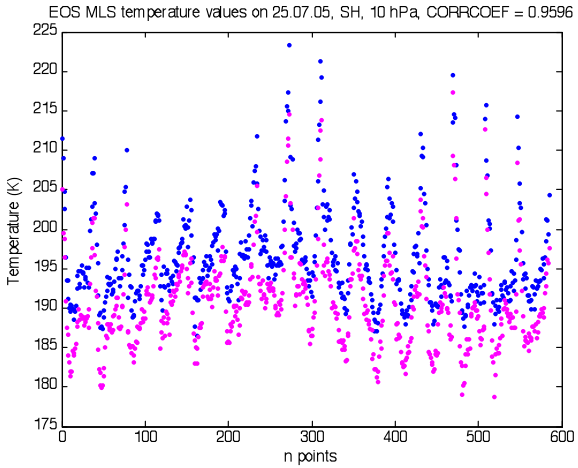

Figure 2.38. Continuation.

j) August PCC = 0.9920

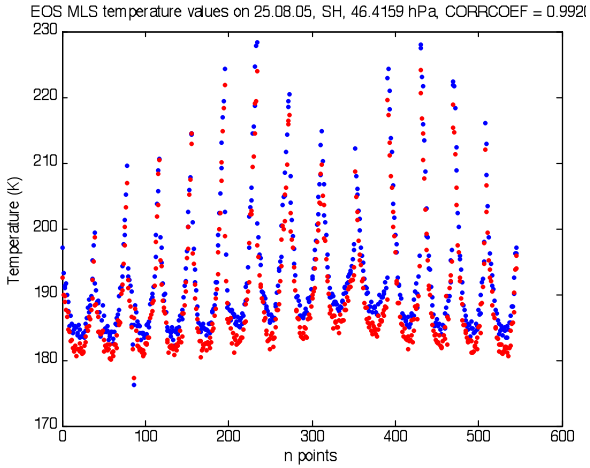

k) August PCC = 0.9672

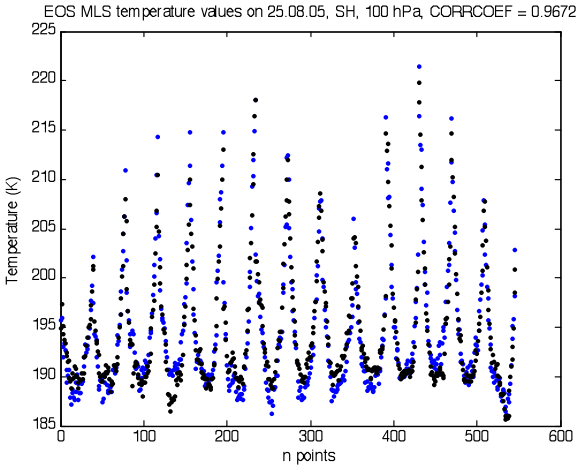

l) August PCC = 0.9935

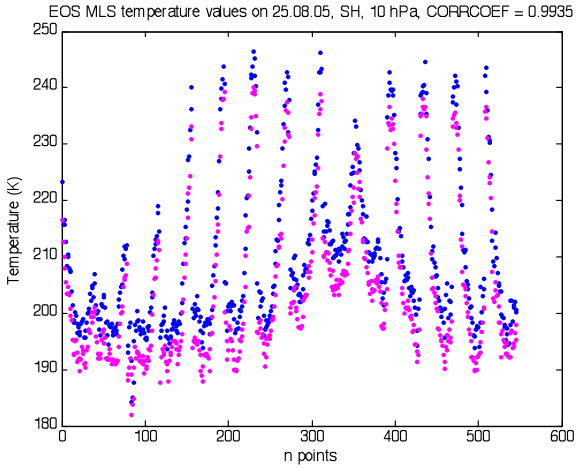

Figure 2.38. Continuation.

m) September CC = 0.9972

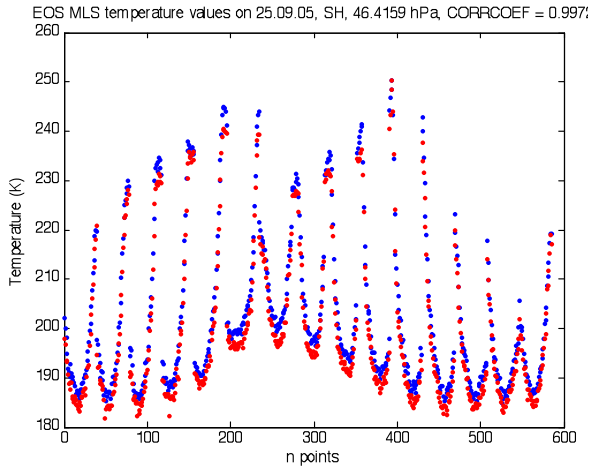

n) September CC = 0.9929

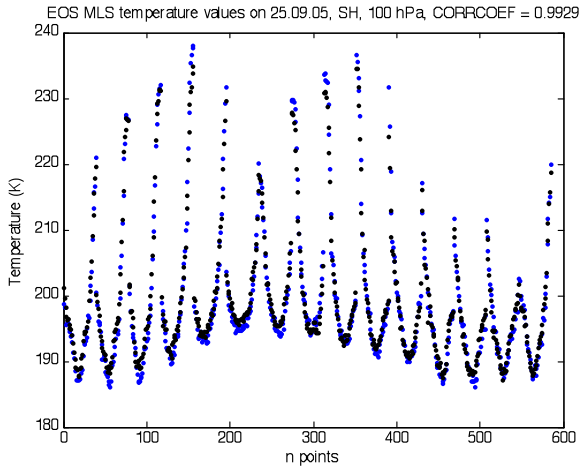

o) September CC = 0.9944

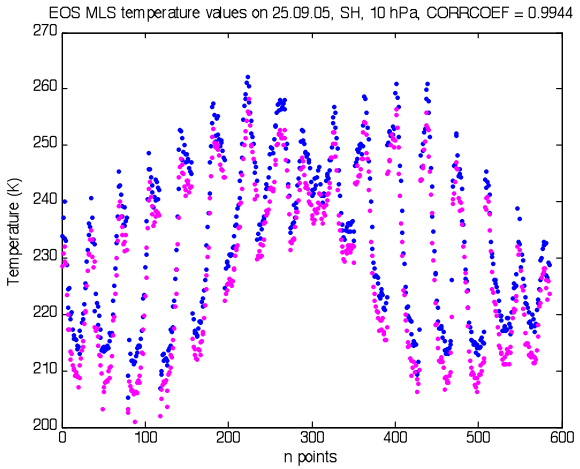

Figure 2.38. Continuation.

p) October PCC = 0.9959

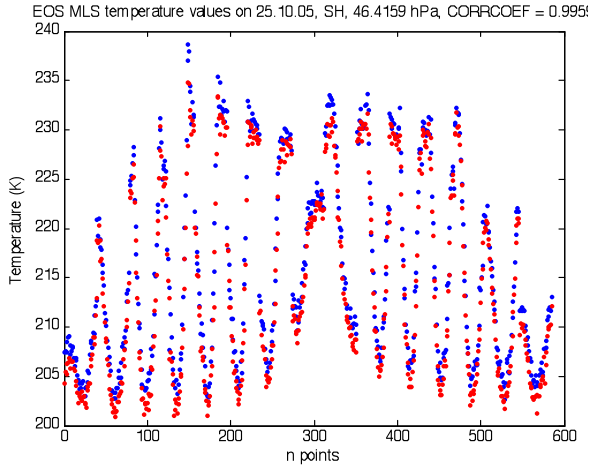

q) October PCC = 0.9926

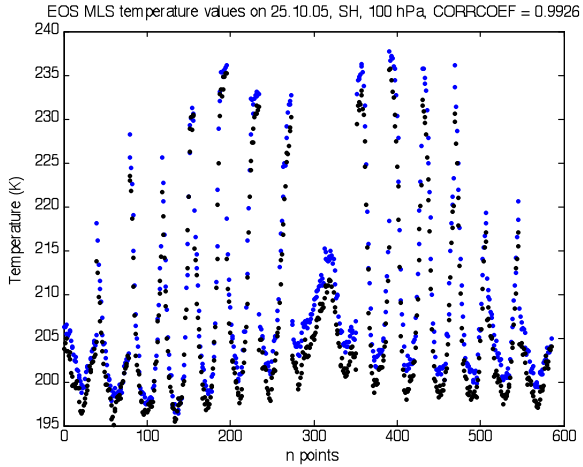

r) October PCC = 0.9889

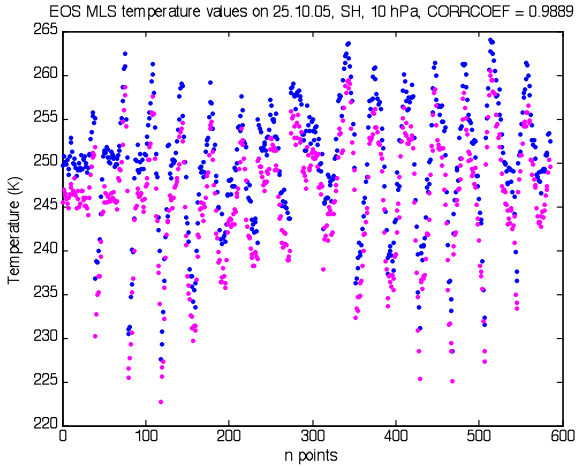

Chapter 3

POLAR STRATOSPHERIC OZONE CHEMISTRY: BACKGROUND

3.1. THE STRATOSPHERE

The Earth's atmosphere is commonly described as a series of layers defined by their thermal characteristics. Specifically, each layer is a region where the change in temperature with respect to altitude has a constant sign. The layers are called "spheres" and the boundary between connecting layers is the "pause". The lowest layer, called the troposphere, exhibits generally decreasing temperatures with increasing altitudes up to a minimum called the tropopause (see Figures 3.1 and 3.2).

The tropopause is associated with the minimum in the vertical temperature profile observed near 7-16 km altitude. Above the tropopause, the stratosphere exhibits increasing temperatures with the altitude up to a maximum of about 270 K at the level of the stratopause located near 50 km. The stratosphere is characterized by a rapid increase with height of the potential temperature in response to the strong heating produced by ozone absorption of solar ultraviolet radiation. As a result, the stratosphere is stably stratified with very slow vertical exchanges. At still higher altitudes, the temperature again decreases up to 85-100 km, where another temperature minimum is found. This layer is called the mesosphere, and its upper boundary is the mesopause. In all these layers, the major constituents, N_2 and O_2, make up about 80% and 20%, respectively, of the total number density, so that the mean molecular weight of air

varies little with altitude. Because of this common feature, the three layers are collectively referred to as the homosphere.

The region located above the mesopause is called the thermosphere. The temperatures there increase very rapidly with altitude, and can reach 500 to 2000 K above 500 km, depending on the level of solar activity. The composition of the thermosphere is very different from that of the lower regions. Atomic hydrogen (the lightest chemical element) becomes the most abundant compound in the upper thermosphere. In contrast to the homosphere, the mean molecular weight of air in this region varies with altitude; for this reason, the region above 100 km is also called the heterosphere. The major source of heat in the middle atmosphere is provided by absorption of ultraviolet radiation, particularly by ozone and, to a lesser extent, by molecular oxygen. In that way, the thermal structure of the atmosphere with its different layers is represented in Figure 3.1. Text Adapted from *Brasseur and Solomon* [2005].

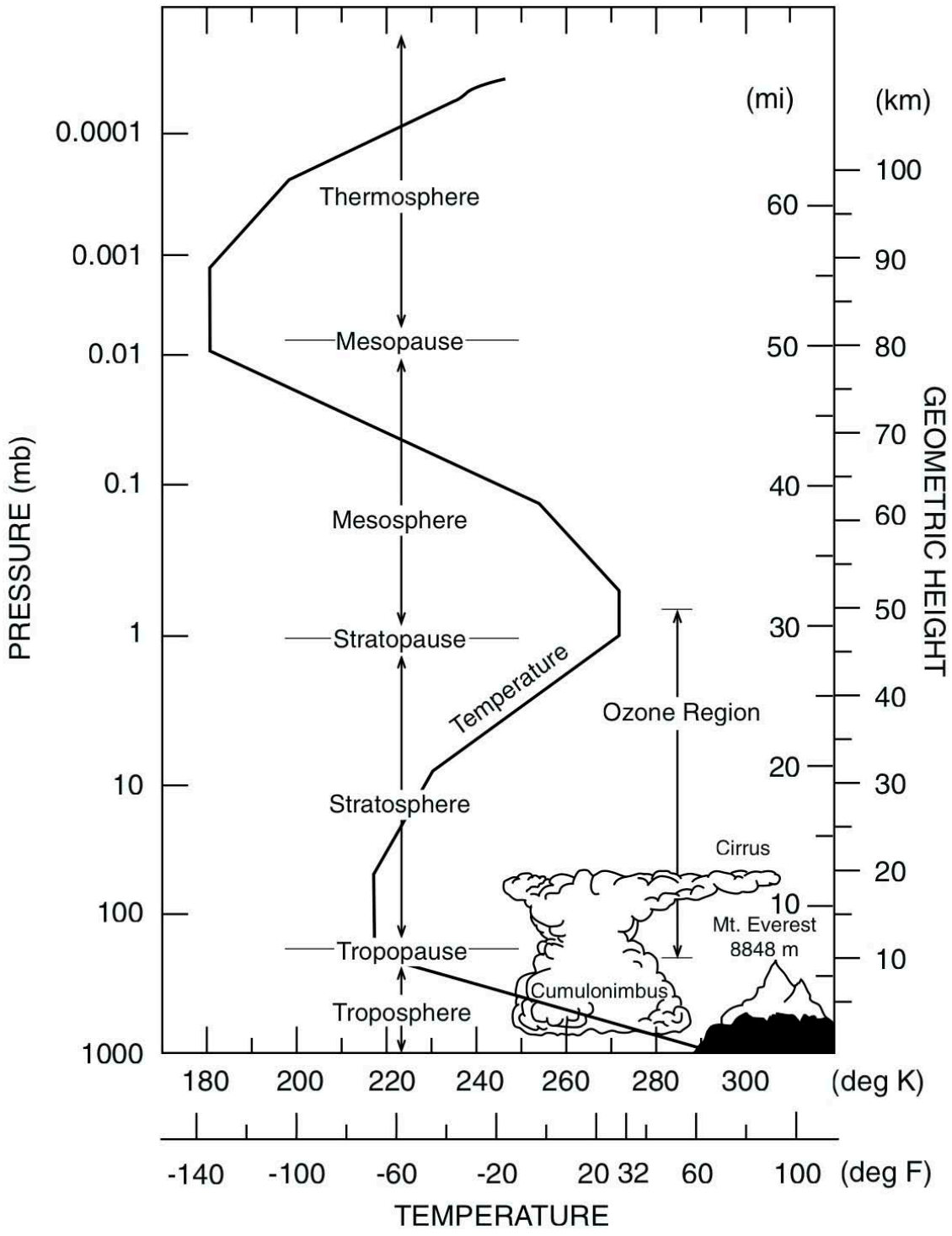

Figure 3.1. "Schematic representation of the thermal structure of the atmosphere with its different layers". From *Brasseur and Solomon* [2005].

In most parts of the stratosphere (above 20 km) and the mesosphere, the prevailing mean zonal winds are directed eastward (westerlies) during winter, and westward (easterlies) during summer, with maximum velocities of the order of 60-75 ms^{-1} near 70

km. Above this altitude the zonal flow becomes less intense. The strong westerly winds in the winter polar stratosphere form the so-called polar vortex, and partly isolate the polar region from low latitude influences. Text Adapted from *Brasseur and Solomon* [2005].

3.2 POLAR OZONE DEPLETION: HISTORY

Sydney Chapman was among the first researchers to examine ozone in the atmosphere and to define sets of chemical reactions that describe ozone production and destruction. As a result of the work of G. M. B. Dobson, historical records of ozone have been taken over Antarctica since the spring of 1956. The record began by Dobson was key in the discovery of the Ozone Hole in the 80's above the Antarctic.

In 1970, the Dutch Nobel prize winning atmospheric chemist Paul Crutzen showed that nitrogen oxides (NO and NO_2), stable reservoir species, react catalytically (without themselves being consumed) with ozone in a chemical cycle to destroy molecules of stratospheric ozone ultimately. Nitrogen oxides form in the atmosphere from the decomposition of chemically stable nitrous oxide (N_2O), that is produced by microbiological processes in the soil and provides the principal source of NO in the middle atmosphere and accelerates the destruction of ozone in the stratosphere [*Brasseur and Solomon*, 2005]. The catalytic cycle is known as the "Odd Nitrogen Catalytic Cycle" and evidences the connection between microorganisms at the ground and ozone depletion in the polar stratosphere. This link has motivated and enhanced the recent rapid development of research on global biogeochemical cycles [*http://www.nobelprize.org/nobel_prizes/chemistry/laureates/1995/press.html]*. The potential of nitrogen oxides to decompose ozone was also noted by the American researcher Harold S. Johnston in the 70's by pointing out that supersonic aircraft would

be capable of releasing nitrogen oxides at altitudes of 20 km, threatening to the stratosperic ozone layer.

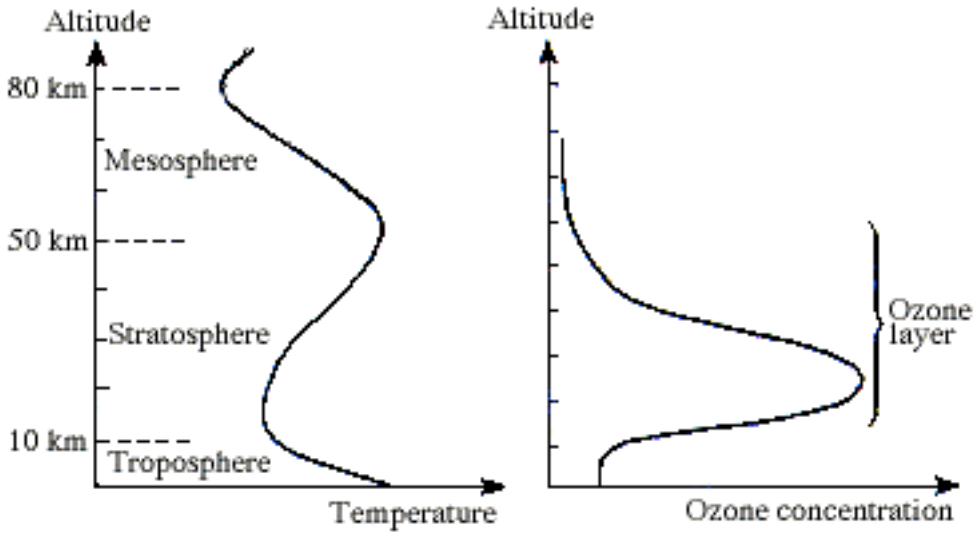

Figure 3.2. Variation in temperature and ozone concentration up through the atmosphere.

Source:http://www.nobelprize.org/nobel_prizes/chemistry/laureates/1995/press.html

The most obvious start of the Ozone Hole story perhaps began in 1974 when Mario Molina and Sherwood Rowland found that chlorine forms could take part in the catalytic destruction of ozone. Molina and Rowland also discovered that the main source of chlorine in the stratosphere came from man-made pollutants called chlorofluorocarbon (CFC) gases aka “freons”. Sunlight breaks down CFCs to produce atomic chlorine that cascades subsequently to catalytically destroy stratospheric ozone molecules in a cycle known as the Odd Chlorine catalytic cycle. The odd chlorine catalytic cycle was the first cycle associated with halogens, and highlighted the possibility of significant man-made ozone depletion.

Japan’s Shigeru Chubachi was the first to report anomalously low levels of ozone publicly in 1984. His results were obtained from February 1982 to January 1983 at the Syowa station in Antarctica and were presented during a conference in Greece [*Chubachi*, 1984]. Nevertheless, the British Antarctic Survey (BAS) received international recognition for the discovery of the Antarctic Ozone Hole in 1985 because, among other reasons, they published an article in Nature, the world's most cited interdisciplinary scientific journal, that showed a record of ozone measurements since 1957 at BAS stations in Antarctica [*Farman et al.*, 1985].

The discovery of the Antarctic Ozone Hole in 1985 by Joseph Farman, Brian Gardiner, and Jonathan Shanklin [*Farman et al.*, 1985] led to an intensive study of changes in the ozone layer. Measurements obtained from instruments at Antarctic stations, satellite measurements, and results from in-situ measurements made during high altitude aircraft campaigns allowed a vast amount of knowledge to be gained. The studies quickly allowed researchers to prove that the Antarctic Ozone Hole could only be explained in terms of man-made emissions of halogen containing chemical compounds. Halogens are non-metal elements from group 17 on the periodic table and consist of elements such as fluorine (F), chlorine (Cl), bromine (Br) and iodine (I), with the most important ozone depleting elements being chlorine and bromine. Through various measurements it became clear that sources of halogens in the stratosphere had been artificially increased by the man. As highlighted by Molina and Rowland, chlorofluorocarbons developed by Thomas Midgley, Jr. and Charles Franklin Kettering in 1928, and used as refrigerants and propellants for aerosols were particularly important in ozone depletion. In the stratosphere (between 15 and 50 km) ultraviolet light breaks the bond holding chlorine atoms (Cl) to the CFC molecule. Ultraviolet decomposition of chlorofluorocarbons in the stratosphere produces less stable chlorine

compounds that release chlorine atoms ($Cl^{\cdot}$) which destroy ozone. A timeline for some of the most relevant events associated with the Antarctic Ozone Hole is found in Figure 3.3.

The presence of halogens (e.g. chlorine, fluorine and bromine) in the middle atmosphere results from the upward diffusion from the troposphere of halocarbons which are released at the Earth's surface as a results of natural or anthropogenic processes. These compounds break up in the stratosphere and release halogen atoms.

Once released in the middle atmosphere, fluorine, chlorine and bromine atoms react rapidly with ozone to form $FO^{\cdot}$, $ClO^{\cdot}$ and BrO. Further reactions, which will be presented in the following sections, lead to efficient catalytic destruction of odd oxygen via $ClO^{\cdot}$ and BrO.

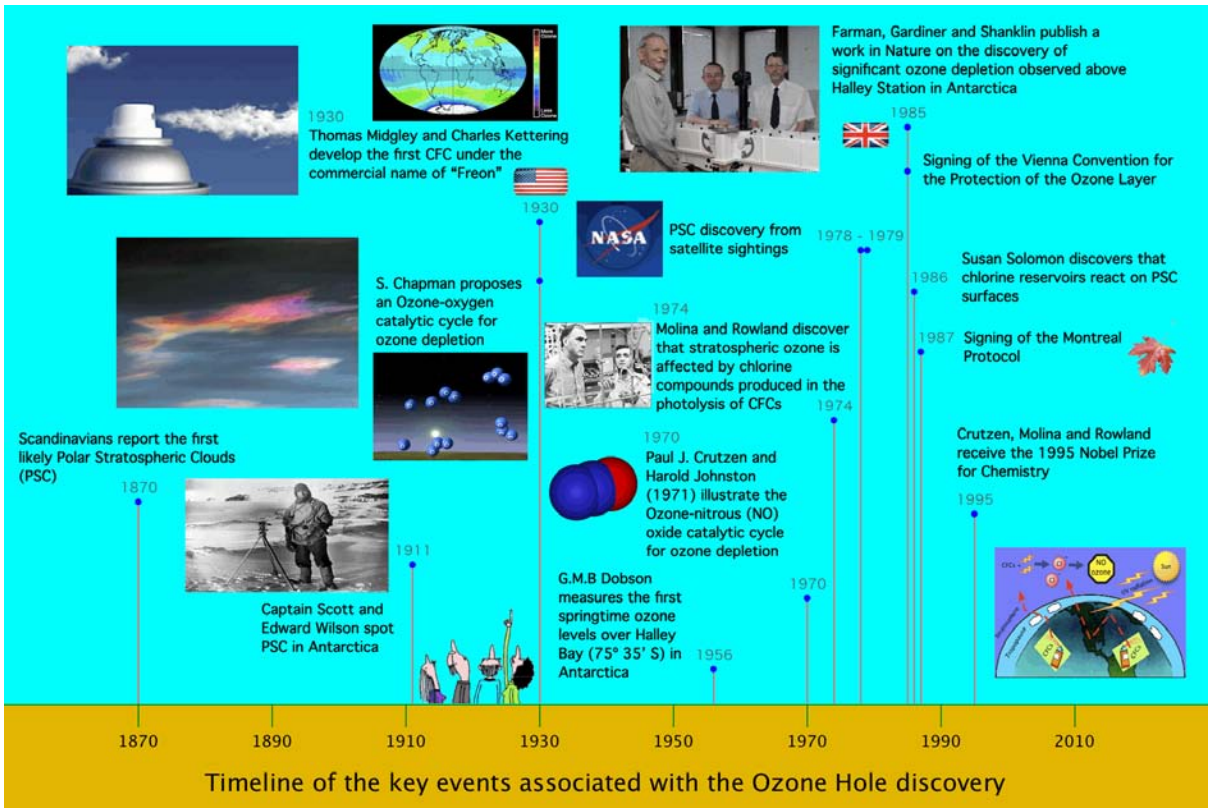

Figure 3.3. A timeline of key events associated with ozone chemistry and the Ozone Hole. Note: The public report of anomalously low levels of ozone at Syowa station, Antarctica in 1984 by the Japanese researcher S. Chubachi is not included in the timeline. © Diagram designed by A.A.-T.

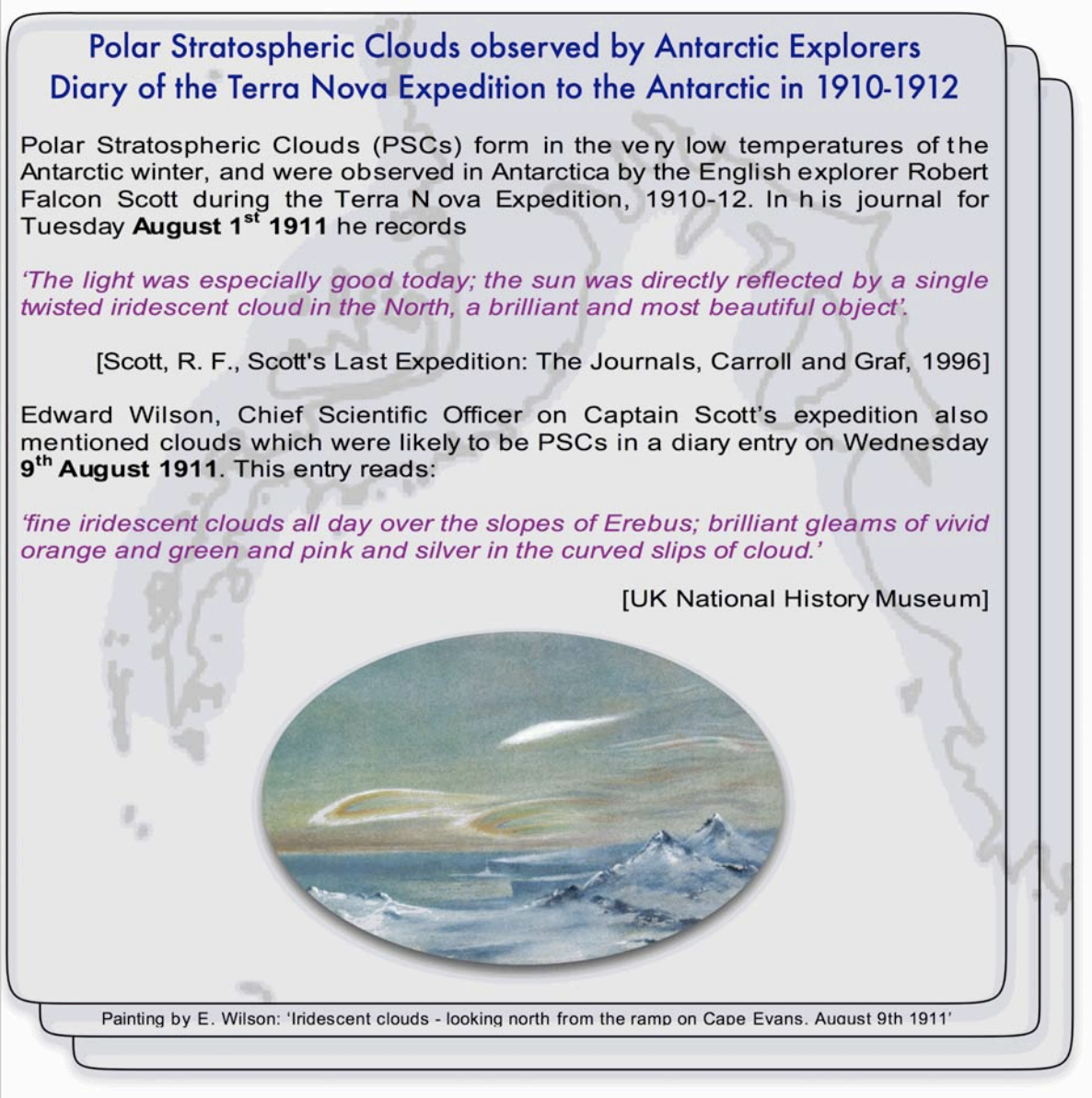

Figure 3.4. A historic depiction of the first reported sight (by eye) of polar stratospheric clouds by Captain Scott and Edward Wilson in the early 90's in Antarctica. © Diagram designed by A.A.-T..; Copyright © Scott Polar Research Institute, University of Cambridge, United Kingdom. Reprinted with permission.

3.3 THE MISSING LINK IN OZONE DEPLETION: PSC

Within a small period of time it became clear that the processes observed by Molina and Rowland could not explain the rate of ozone depletion observed. In particular, the rate of ozone depletion necessary for the Antarctic Ozone Hole to form could not be related to gas-phase chemistry alone.

Additionally, aircraft measurements made in 1987 demonstrated that chlorine monoxide levels were over one hundred times higher than those predicted by gas-phase models. Therefore, it was clear that some process was required to ensure that chlorine was active and that chlorine remained active also. The solution was a role for heterogeneous catalysis when chemical constituents interacted within or on the surface of particles. Catalytic reactions of this type could be used to explain the rapid and massive ozone depletion observed in the Antarctic stratosphere. However, polar ozone loss also required the release of reactive chlorine from the reservoir compounds hydrogen chloride (HCl) and chlorine nitrate ($ClONO_2$). How?

Based on experimental evidence and the altitude at which Antarctic ozone depletion occurred, ~12 to 22-25 km, it also became apparent that this altitude range was far below the altitudes where gas phase chlorine chemistry would predict major change [*Hofmann et al.,* 1992; *Solomon,* 1999]. After notable work, in 1986, Susan Solomon identified the potential importance of polar stratospheric clouds in chlorine activation [*Solomon et al.,* 1986]. She and co-authors also discovered that heterogeneous chemical reactions produce chlorine. The cycle can be written as follows:

$$HCl(solid) + ClONO_2(gas) \rightarrow Cl_2(gas) + HNO_3(solid)$$
$$Cl_2 + h\nu \rightarrow Cl + Cl$$
$$O_3 + Cl \rightarrow ClO + O_2$$

CYCLE 1

where $h\upsilon$ represents the energy of a photon of light. In this cycle, an ice surface allows the reaction of hydrogen chloride with another chlorine reservoir species, chlorine nitrate, that takes place at a much higher rate than in the gas phase. Cycle 1 is schematically explained in Figure 3.5.

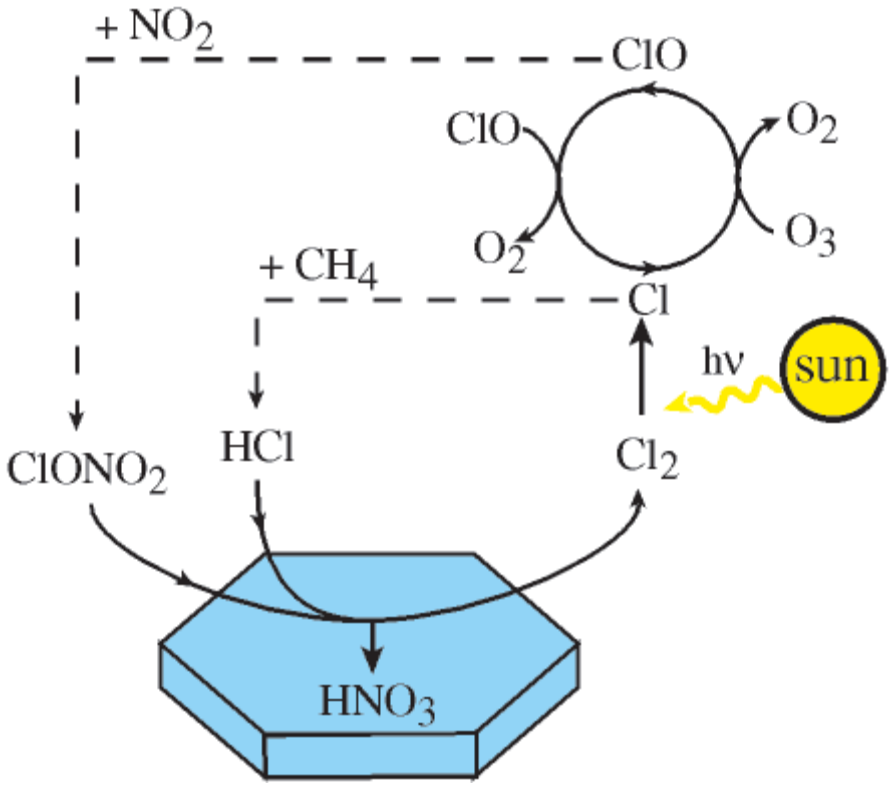

Figure 3.5. A schematic of the chemical reactions that occur on PSC particles in the stratosphere; taken from *Zondlo et al.* [2000].

Polar stratospheric clouds are also called Mother-of-Pearl or Nacreous (Iridescent) Clouds (see Figures 3.4 and 3.7) because of their opalescent feature caught by the eye. At least three types of PSCs are known to occur and each contains a mixture of water, nitric acid, and sulphuric acid; and can either be ice or liquid particles. Each of these cloud types forms only at very cold temperatures, while the formation temperature depends on the abundance of water vapor, nitric acid and/or sulfuric acid. For typical stratospheric conditions PSC formation occurs below -78^{o}C. For comparison, it is

helpful to note that the coldest temperature that has been recorded on the Earth's surface is -89.2^{o}C at the Vostok station located in Antarctica. Temperatures such as these occur most often in the stratosphere, and frequently between June and November at altitudes between 10 and 25 km in the Antarctic stratosphere. Globally, these temperatures are not observed frequently in the stratosphere. Very low temperatures during Antarctic winter generally lead to the growth of large PSC particles that are predominantly composed of ice (see Figure 3.6), with the incorporation of nitric acid (HNO_3). PSC particles can grow so large that they eventually fall out of the lower stratosphere as liquid droplets, irreversibly reducing concentrations of nitrogen oxides in the process often called 'denitrification'. Resultant low levels of nitric acid indicate that the reactive chlorine gas that forms remains chemically active for long periods, thereby increasing the probability of ozone depletion.

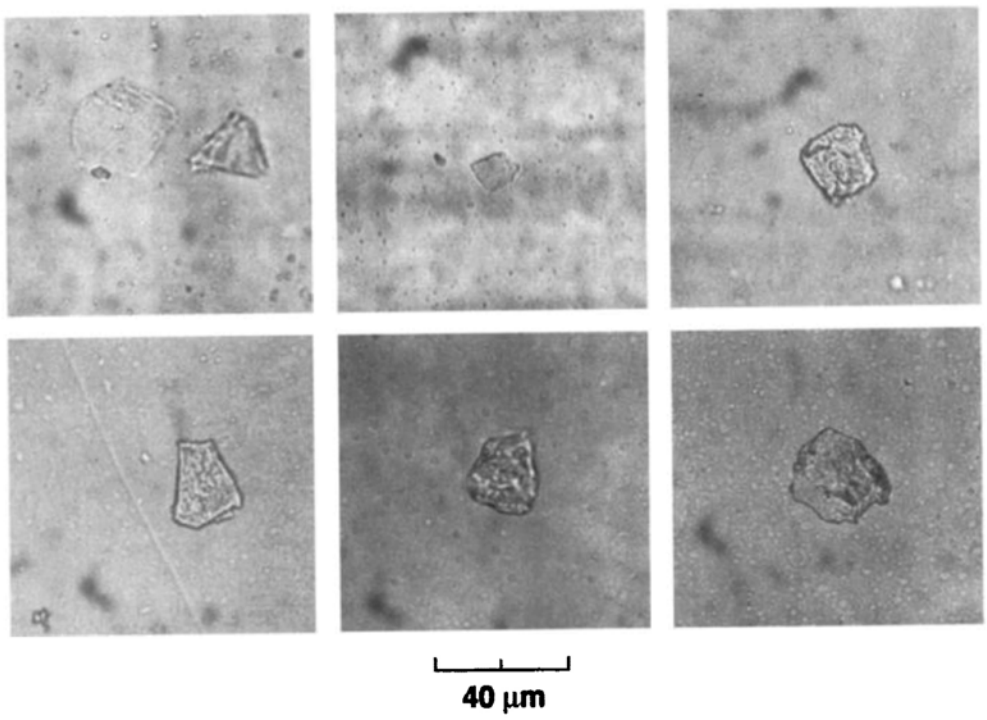

Figure 3.6. Microscopic images of ice crystal appearance, which show rounded corners (indicating evaporation). Crystals collected al 67.5ºS and 172ºE in 1994 at ~191 K. From *Goodman et al.* [1997].

Figure 3.7. A photograph of Polar Stratospheric Clouds near Ross Island, Antarctica. Source: Antarctica New Zealand Photo Collection. No copyright infringement.

However, these chemical reactions can only occur in a stratosphere that has been dehydrated and denitrified, or, in other words, in a stratosphere where water and nitrogen oxides have been removed. The reactions can also only occur on special cloud/aerosol particles, and this major discovery by atmospheric chemist Susan Solomon was one of the major challenges scientists had in understanding the cause of the Antarctic Ozone Hole.

In summary, without PSCs, solar UV light breaks down CFCs and the resultant chlorine exists either as chlorine monoxide (ClO^-), formed in a reaction with ozone (O_3), or as free chlorine (Cl^-). In the absence of PSCs, gases from the atmosphere, such

as nitrogen dioxide (NO_2) and methane (CH_4), react with chlorine monoxide and free chlorine to trap the chlorine in inert chemical species (often called reservoir species) such as chlorine nitrate ($ClONO_2$) and hydrogen chloride (HCl). For such a case, ozone destruction is relatively minimal since the chlorine needed to destroy ozone is stored in reservoir species. PSC particles allow heterogeneous chemical reactions that free molecular chlorine (Cl_2) from reservoir species. However, PSCs also prevent reservoir species from forming by removing nitrogen oxides from the atmosphere through the gravitational settling of nitric acid (HNO_3). Therefore, ozone depletion is significantly accelerated in regions of PSCs since chlorine remains active in UV light. Therefore, catalytic ozone destruction is likely to occur. However, the formation processes and the chemical composition of PSCs are, today, still poorly understood, nearly a quarter of a century after their importance was discovered. Gaps in understanding are at least partially associated with the inherent difficulty in measuring miniscule liquid or solid droplets that occur well above the normal flight level of most aircraft, as well as the difficultly in observing PSCs using satellite data and their independent role in chlorine activation for each kind of PSC. In the laboratory, simulations of the correct thermodynamic conditions for realistic PSC formation are also complicated.

3.4 CATALYTIC CHEMICAL REACTIONS

Two catalytic cycles dominate the destruction of ozone over Antarctica. The first cycle involves chlorine monoxide (ClO^-), often called the chlorine catalytic cycle, and can be written using chemical symbols as follows:

$$ClO + ClO + M \rightarrow Cl_2O_2 + M$$

$$Cl_2O_2 + h\nu \rightarrow Cl + ClO_2$$

$$ClO_2 + M \rightarrow Cl + O_2 + M$$

$$2 \times \left(Cl + O_3 \rightarrow ClO + O_2\right)$$

CYCLE 2

In the multi-phase cycle, M represents a third body that is required for collisional deactivation in order to remove excess energy, and $h\upsilon$ represents the energy of a photon of light. Cycle 2 is the catalytic set of reactions identified by Molina and Rowland.

A more intuitive representation of this cycle of interactions is shown in Figure 3.8. One important point clearly observable in Figure 3.8 is the cyclic nature of the set of reactions. Therefore, the reactions are catalytic once chlorine is activated (once the set of reactions has occurred chlorine is free to break up more ozone), and it is the catalytic nature of these reactions that makes them particularly efficient in massive ozone destruction.

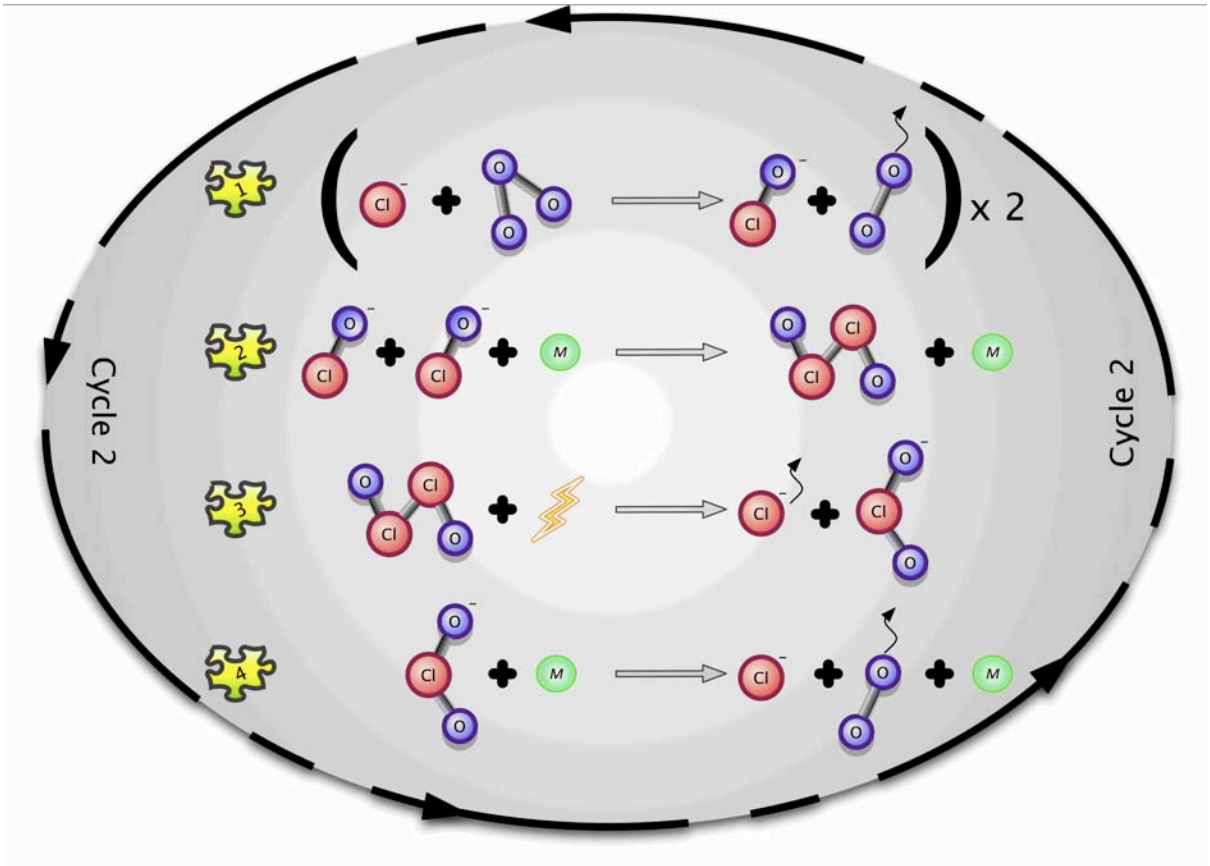

Figure 3.8. The catalytic chlorine ozone destruction cycle ClO¯ClO⁻ (aka Cycle 2). Note: The pictographic representation of chemical molecules does not necessarily map out the actual bonding geometry of the atoms to the molecules. The essence of the figure is to pictographically show catalytic Cycle 2. ©A.A.-T.

The second catalytic cycle involves ClO^- and BrO and can be written as follows:

$$ClO + BrO \rightarrow Cl + Br + O_2$$

$$Cl + O_3 \rightarrow ClO + O_2$$

$$Br + O_3 \rightarrow BrO + O_2$$

CYCLE 3

A schematic of this cycle is shown in Figure 3.9.

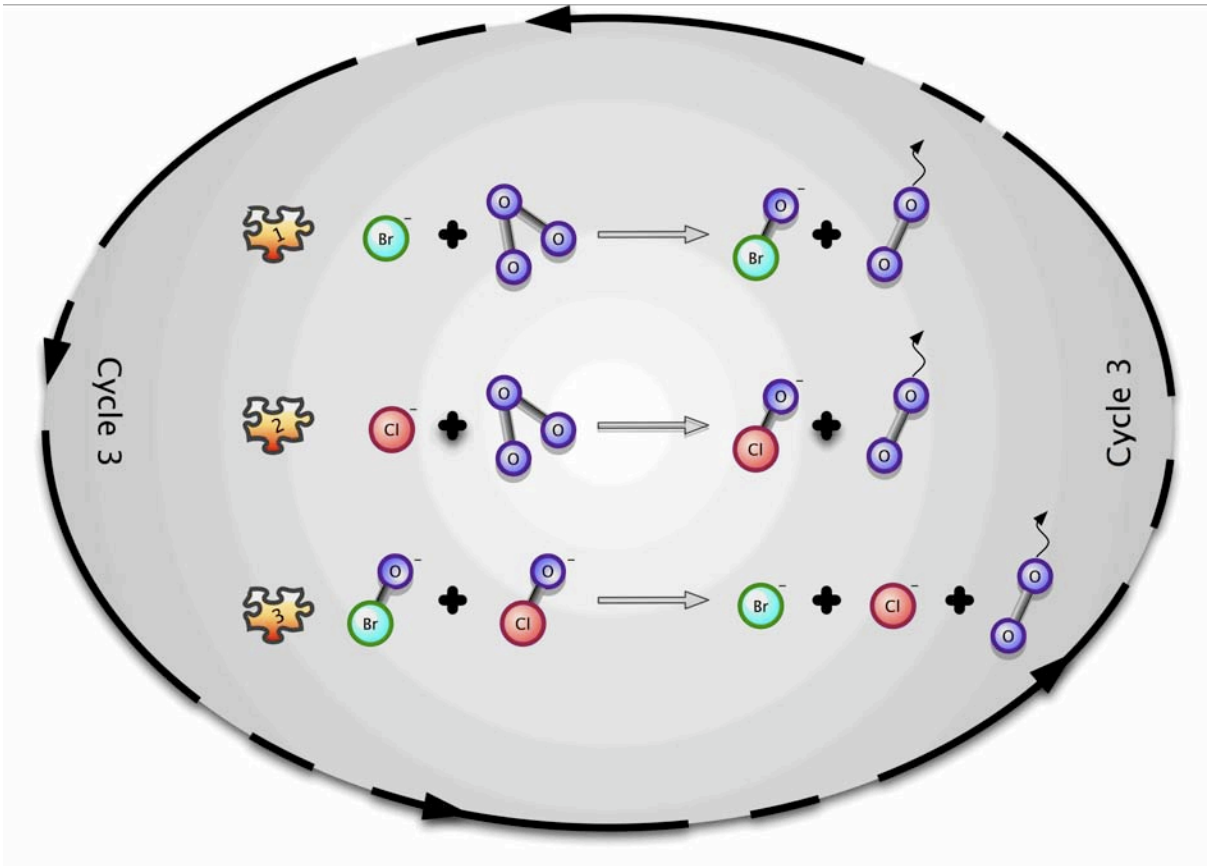

Figure 3.9. The catalytic chlorine ozone destruction cycle BrO-ClO^- (aka Cycle 3). Note: The pictographic representation of chemical molecules does not necessarily map out the actual bonding geometry of the atoms to the molecules. The essence of the figure is to pictographically show catalytic Cycle 3. ©A.A.-T.

Both of the cycles are associated with the group of chemicals called halogens (as previously indicated), and, therefore, other texts may refer to them as equations for 'halogen chemistry'. The inclusion of these catalytic cycles into numerical models is sufficient to explain most of the ozone decline during Antarctic spring. However, while these processes are the most important reactions that destroy ozone, a number of other processes can occur that have some impact on ozone depletion. Estimates indicate that 75% of Antarctic ozone depletion is associated with chlorine species that react

catalytically, while approximately 20% is associated with bromine species. A more detailed review is available in *Solomon* [1999].

The reader should note that Cycles 2 and 3 require visible sunlight for completion of the reaction cycles and to maintain chlorine monoxide abundance. Therefore, continuous darkness over Antarctica during winter limits sunlight dependent ozone destroying reactions. The return of sun to Antarctica in late winter/early spring provides the sunlight that initiates catalytic ozone destruction cycles and that partially explains the timing of maximum ozone depletion.

3.5 THE SEASONAL CYCLE OF OZONE DEPLETION

All we have learned regarding the processes that contribute to the formation of the Antarctic Ozone Hole can be gathered together to explain the timing of various aspects.

In June, Antarctic winter begins and the Antarctic Polar Vortex, which separates the Antarctic stratosphere from the rest of the stratosphere, is formed. Stratospheric temperatures fall and become cold enough for PSC formation.

During July, PSCs form and denitrify and dehydrate the stratosphere. Heterogeneous chemical processes, involving hydrogen chloride and chlorine nitrate that occur on PSC particle surfaces and free chlorine, also take place.

In August, heterogeneous chemical reactions continue to occur on PSC particle surfaces. Antarctic stratospheric temperatures also generally drop to a minimum during this month. If PSC formation temperature thresholds were independent of chemical concentrations, then PSC volume would be at a maximum during this period.

During September, sunlight returns to the center of the vortex and activates the ClO–ClO and ClO–BrO catalytic cycles that destroy ozone. As spring begins, temperatures begin to increase and the quantity of PSCs begins to decrease.

In October, temperatures continue to rise and PSCs become scarce. The lowest levels of stratospheric ozone are reached during this month.

During November, the temperature gradient between the pole and the equator is reversed and the polar vortex breaks down. The removal of this barrier to transport implies that ozone-rich air from mid-latitudes replenishes Antarctic ozone and ozone-poor air previously constrained to the region over Antarctica, and spreads across the Southern Hemisphere.

A timeline for the seasonal cycle of Antarctic ozone depletion that summarizes this section is shown in Figure 3.10.

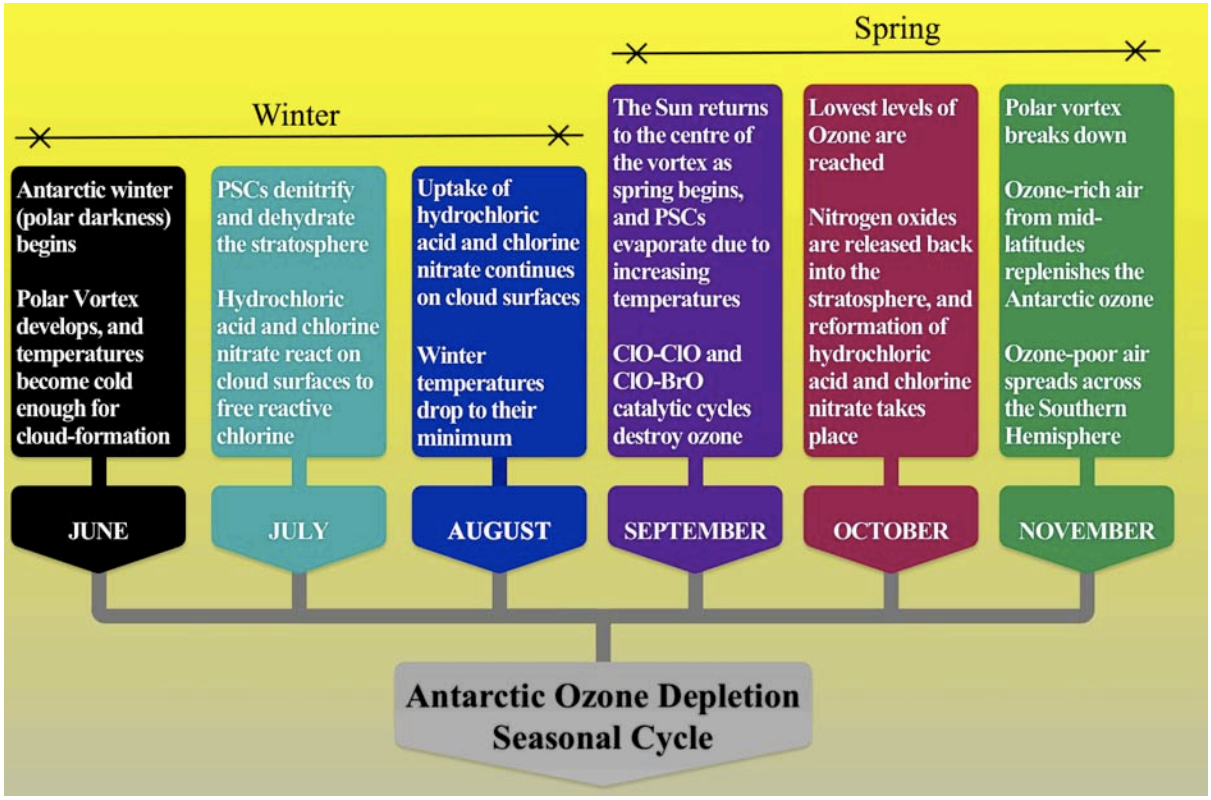

Figure 3.10. The seasonal evolution of Antarctic ozone depletion. ©A.A.-T.

Chapter 4

PSC MODELING AND ALGORITHM DEVELOPMENT I: ASSESSMENT

4.1. PSC CLASSIFICATION/DEFINITION

Generally speaking, PSCs occur during the polar winter over an (approximate) altitude range between 12 and 25 km [*McCormick et al.*, 1982; *Solomon*, 1999]. During this period, the temperatures are low enough for the condensation of Type Ia-b and Type II PSC particles. According to the first PSC classification originally presented by *Poole and McCormick* [1988], *Browell et al.* [1990], and *Toon et al.* [1990], Type Ia PSCs are formed of solid nitric acid trihydrates (NAT) at a molar ratio of 1:3 for HNO_3–H_2O [*Voigt et al.*, 2008 and references therein], and form at temperatures below the NAT saturation temperature (T_{NAT}) (between 192 and 197 K for typical partial pressures of water vapor and nitric acid in the lower stratosphere) [*Hanson and Mauersberger*, 1988; *Lowe and MacKenzie*, 2008]. Type Ib PSC particles are primarily composed of a supercooled ternary solution (STS) of $HNO_3/H_2SO_4/H_2O$ in the liquid phase, and their formation temperature is approximately 4 K lower than T_{NAT} [*Tabazadeh et al.*, 1994].

Type II clouds are believed to consist of H_2O ice crystals [*Turco et al.*, 1989] and have been observed at even colder temperatures near the stratospheric ice frost point (T_{ice}) of ~188 K, as measured by *Kent et al.* [1986] and *Fahey et al.* [1989], computed

using the analytical parameterizations of *Marti and Mauersberger* [1993] or *Murphy and Koop* [2005].

Given that the frost point of NATs is roughly 7 K higher than that of water ice (e.g. *Tabazadeh et al.*, [1994]), Type Ia particles are more widespread in the stratosphere [*Abbatt and Molina*, 1992]. However, because all possible NAT nucleation mechanisms and some aspects of PSC composition are not, yet, fully understood, the denitrification and chlorine activation simulations used to predict ozone losses may not be sufficiently robust or sensitive enough to the broader set of vertical applicable levels in both polar stratospheres [e.g. *Tolbert and Toon*, 2001; *Drdla and Schoeberl*, 2002; *Grooß et al.*, (2005a); *WMO*, 2006; *Pitts et al.*, 2009].

For this work, the year-to-year variations of PSC formation and chlorine partitioning derived from EOS Aura MLS measurements and NCEP/NCAR re-analyses in the Southern Hemisphere, for the 2005-2009 winter seasons, were examined concurrently.

4.2. PSC MODELING. ALGORITHM DEVELOPMENT: FIRST GENERATION

Algorithms and Computation of PSC formation surface area over the Earth using standard satellite temperature data. Development and Performance.

4.2.1 Literature recourse.

Literature available on PSC area calculation was, admittedly, rather scarce during the process of dealing with the problem of computing PSC-induced areas in the entire Antarctic stratosphere from standard temperature satellite observations.

Parrondo et al. [2007]'s Figures 6 and 7 report areas of potential Type I and Type II PSC formation based on the European Centre for Medium-Range Weather Forecasting (ECMWF) analysis fields during the Antarctic winter 2003 at different isentropic surfaces between 300 K and 700 K. Nonetheless, information about the PSC formation temperature thresholds utilized is presented; however, a description of the algorithms for calculation of this potential PSC formation area in the Antarctic stratosphere 2003 is not presented nor described in the paper.

Pitts et al. [2007] apply a PSC detection algorithm ("v1") as a function of altitude (km) to the Cloud-Aerosol Lidar and Infrared Pathfinder Satellite Observations CALIPSO spacecraft data. They define a *21 ×21-box grid in polar stereographic coordinates centered on the South Pole and extending to 55º at its sides* [*Pitts et al.* 2007]. On the other hand, *Pitts et al.* [2009] use the "second-generation" detection algorithm of *Pitts et al.* [2007]. *Pitts et al.* [2009] define a 25 ×25-box grid in polar stereographic coordinates *covering latitudes poleward of 50º* hereafter. Figure 3 of that study shows a comparison of the daily areal coverage of PSCs in the Antarctic stratosphere in 2006 using the two algorithms reported by *Pitts et al.* [2007, 2009]. Overall, their "second-generation" algorithm measures greater PSC area than the "v1" detection algorithm at around 20 km from June to August in 2006 in the Antarctic. Also, the "second-generation" algorithm detects more PSC area in October in the upper troposphere-lower stratosphere than v1 does in the same year[5].

[5] Whether further algorithms are developing by new express inclusion of data comparison from newcomers' PSC algorithms is beyond the scope of this thesis. A series of novel algorithms were developed and implemented at this stage for the present work.

In the present study, pressure surfaces are utilized in order to compare the results with *Pitts et al.* [2007, 2009], who used altitude surfaces (in km) rather than isentropic surfaces for PSCs. Since other studies of HCl depletion in 2006 in Antarctica and the Arctic were not available, pressure surfaces were utilized. The codes, functions, and analyses for the production of isentropic surfaces were provided to *Alexander et al.* [2011], but that study gathered PSC data, in contrast to this work. Therefore, the PSC areas in this work were compared to the relevant literature, and the ones available were *Pitts et al.* [2007, 2009]. For future studies, isentropic surfaces should be straightforward to incorporate (see Figures 8.7 to 8.34 in Chapter 8).

Using Aura MLS satellite data, it was calculated the daily surface area of Type I and II PSCs were calculated for the SH from 60º S to available EOS MLS South Pole standard temperature measurements from 2005 to 2010. Four methods were developed, implemented ultimately tested. One method in particular showed to be the most effective calculator of the PSC surface areas, and the motivation to rule out other algorithms will be described fully in subsequent sections of this chapter. PSC areas are considered as planar and/or spherical projection spots above the Earth, where PSC formation is observed in this work.

In order to present an analysis of the PSC area computation using algorithms designed to convert the location of a point on the earth's surface from geographic coordinates (latitude and longitude) to, e.g., Universal Transverse Mercator (UTM) Grid form (easting/northing) for computation of PSC area, in this particular case, a description of these algorithms is presented as per *Bernath* [1987] and the *Defense Mapping Agency Technical Manual 8358.2 (DMA TM 8358.2) [1989](see further below)*. It can be mentioned that the process to access the documentation on how these algorithms work was a devoted work, since some documents were part of, or actually

were, military files of the United States' respective agencies. The information gathered was freely acquired. In the following sections, it is described how the four algorithms developed work.

4.2.2 UTM-UPS Grid

Standard geographic to UTM coordinate conversion algorithm/Standard UTM to Geographic Coordinate Conversion Algorithm.

Regarding the position of a surface on the Earth, it was necessary to transform Latitude-Longitude to UTM-UPS standard coordinates. The Universal Transverse Mercator grid (UTM) works together with the Universal Polar Stereographic grid projection (UPS) when polar surfaces are involved, which is relevant at this stage. By utilizing plane projections of the Earth, a point of interest above the body in question, i.e. the Earth, is seen in a two-dimensional Euclidean space denoted $\Re^2$ (see Figure 4.1). Its resulting position is referred as rectangular coordinates (“Easting”,“Northing”), measured in distance units (e.g. metres).

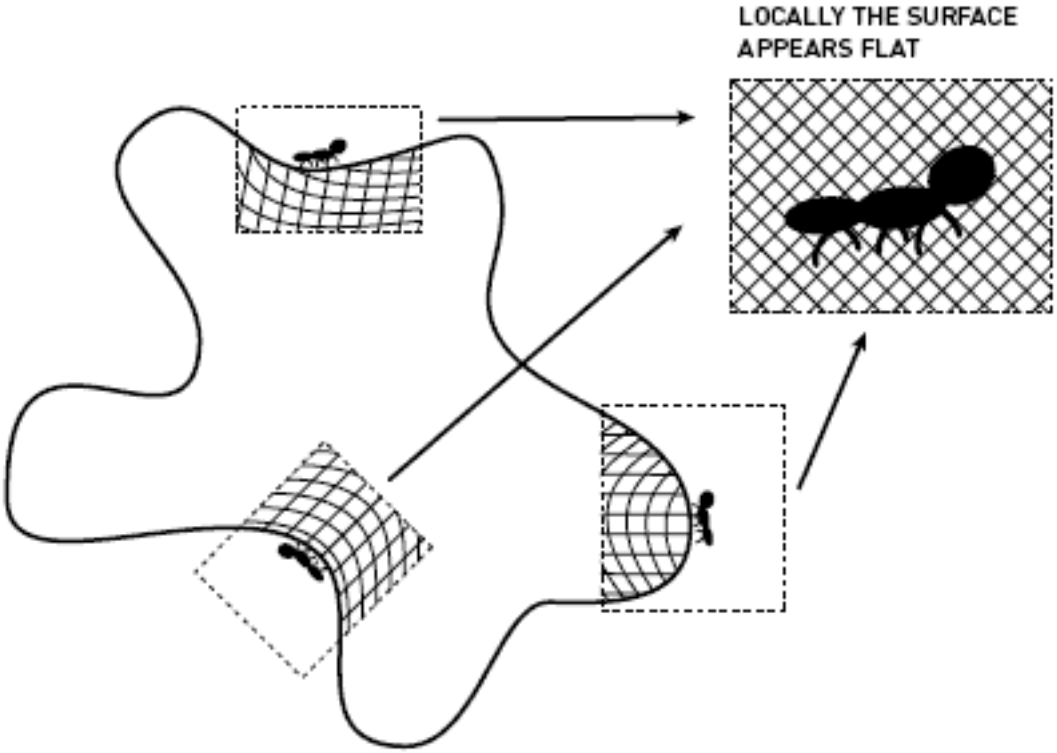

Figure 4.1. Map projection of the area of an irregularly curved surface showing transformation of the area, making it appear flat. Result is achieved in the Earth treating the problem of transforming Lat-Long to standard UTM-UPS coordinates, in essence.

4.2.2.1 UTM Grid Specifications.

This section provides the specifications of the parameters that define the Universal Transverse Mercator (UTM) Grid, the system upon which some of the algorithms in this document were initially based.

Projection: Universal Transverse Mercator (Gauss-Kruger type)

Longitude of Origin: Central meridian of each zone (cmz).

Latitude of Origin: 0º (the Equator)

Zone numbering: starting with 1 for the zone from 180º W to 174º W, and increasing eastward to 60 for the zone from 174º E to 180º E.

Zone limits and overlap: The zones are bounded by meridians whose longitudes are multiples of 6º west or East of Greenwich.

Polar region overlap: The UTM overlaps 30' onto the UPS grid, which extends from the poles to 83º30'N or 79º30'S respectively.

Unit of measurement: Meter

Conversion of Geographic coordinates to grid coordinates. High Level Outline of the UTM algorithm and Mathematical Development.

The general formulae for the computation of N ("Northing") and E ("Easting") are:

$$N = FN + \left(T1 + \Delta\lambda^2 T2 + \Delta\lambda^4 T3 + \Delta\lambda^6 T4 + \Delta\lambda^8 T5\right)$$

$$E = FE + \left(\Delta\lambda T6 + \Delta\lambda^3 T7 + \Delta\lambda^5 T8 + \Delta\lambda^7 T9\right)$$

where,

E = grid easting

N = grid northing

FN = False Northing $\begin{cases} 0 \text{ for the Northern Hemisphere} \\ 10000000 \text{ for the Southern Hemisphere} \end{cases}$

FE = False Easting (500000)

$\Delta\lambda = \lambda - \lambda_0$ = difference of longitude from the central meridian of the projection

$$T1 = Sk_0$$

$$T2 = \frac{\upsilon \sin\phi \cos k_0}{2}$$

$$T3 = \frac{\upsilon \sin\phi \cos^3 k_0}{24}\left(5 - \tan^2\phi + 9e'^2\cos^2\phi + 4e'^4\cos^4\phi\right)$$

$$T4 = \frac{\upsilon \sin\phi \cos^5 \phi k_0}{720}\begin{pmatrix} 61 - 58\tan^2\phi + \tan^4\phi + 270e'^2\cos^2\phi \\ -330e'^4\tan^2\phi\cos^2\phi + 445e'^4\cos^4\phi \\ +324e'^6\cos^6\phi - 680\tan^2\phi e'^4\cos^4\phi \\ +88e'^8\cos^8\phi - 600\tan^2\phi e'^6\cos^6\phi \\ -192\tan^2\phi e'^8\cos^8\phi \end{pmatrix}$$

$$T5 = \frac{\upsilon \sin\phi \cos^7 \phi k_0}{40320}\left(1385 - 3111\tan^2\phi + 543\tan^4\phi - \tan^6\phi\right)$$

$$T6 = \upsilon\cos\phi k_0$$

$$T7 = \frac{\upsilon \cos^3 \phi k_0}{6}\left(1 - \tan^2\phi + e'^2\cos^2\phi\right)$$

$$T8 = \frac{\upsilon \cos^5 \phi k_0}{120}\begin{pmatrix} 5 - 18\tan^2\phi + \tan^4\phi + 14e'^2\cos^2\phi \\ -58\tan^2\phi e'^2\cos^2\phi + 13e'^4\cos^4\phi \\ +4e'^6\cos^6\phi - 64\tan^2\phi e'^4\cos^4\phi \\ -24\tan^2\phi e'^6\cos^6\phi \end{pmatrix}$$

$$T9 = \frac{\upsilon \cos^7 \phi k_0}{5040}\left(61 - 479\tan^2\phi + 179\tan^4\phi - \tan^6\phi\right)$$

where, UTM projection parameters are:

ϕ = latitude

λ = longitude

λ_0 = the central meridian of the projection

k_0 = central scale factor. For the UTM, k_0 = 0.9996

Ellipsoid Parameters. By convention, ellipsoid parameters are defined as follows:

a = semi-major axis of the ellipsoid

b = semi-minor axis of the ellipsoid

f = flattening or ellipticity = (a-b)/a

e^2 = (first eccentricity)^2 = $(a^2 - b^2) / a^2$

e'^2 = (second eccentricity)^2 = ($a^2 - b^2$) / b^2

n = (a – b) / (a + b) = f / (2 – f)

υ = normal to the ellipsoid terminating at the minor axis = $\upsilon = \dfrac{a}{\left(1 - e^2 \sin^2 \phi\right)^{1/2}}$

S = meridional arc (the true meridional distance on the ellipsoid from the equator)

$= A'\phi - B' \sin 2\phi + C' \sin 4\phi - D' \sin 6\phi + E' \sin 8\phi$

where:

$$A' = a\left[1 - n + \frac{5}{4}\left(n^2 - n^3\right) + \frac{81}{64}\left(n^4 - n^5\right) + \cdots\right]$$

$$B' = \frac{3}{2} a\left[n - n^2 + \frac{7}{8}\left(n^3 - n^4\right) + \frac{55}{64} n^5 + \cdots\right]$$

$$C' = \frac{15}{16} a\left[n^2 - n^3 + \frac{3}{4}\left(n^4 - n^5\right) + \cdots\right]$$

$$D' = \frac{35}{48} a\left[n^3 - n^4 + \frac{11}{16} n^5 + \cdots\right]$$

$$E' = \frac{315}{512} a\left[n^4 - n^5 + \cdots\right], \; E' \approx 0.03\text{mm}$$

4.2.2.2 Projection: Universal Polar Stereographic grid (UPS). Description.

The stereographic projection is best known in its polar form and is frequently used for mapping polar areas where it complements the UTM used for lower latitudes. The coordinate transformation from geographical to projected coordinates is executed via the distance and azimuth of the point from the centre point or origin [*POSC*, 2008], see Figure 4.2. It is defined on the WGS-84 Ellipsoid (6,378,137 meters).

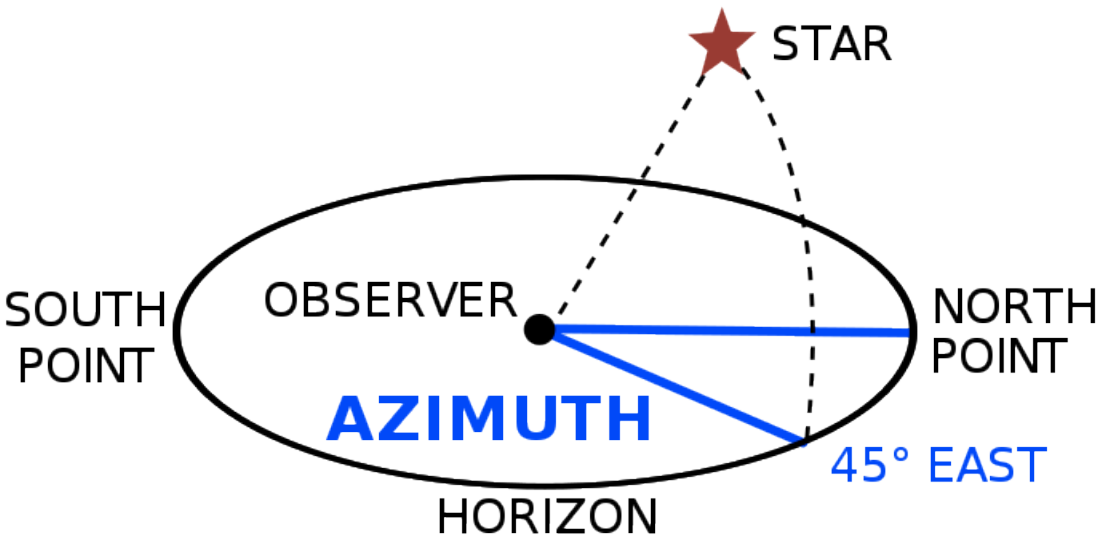

Figure 4.2. Illustration of azimuth angle. The azimuth is the angle that starts from North direction, indicated here as 45º. From *Pearson Scott Foresman* [2011].

Specifications:

Unit of Measurement: Meter

Ellipsoid: WGS-84

False Northing (FN) = False Easting (FE): 2,000,000 meters

Scale factor at the Origin: 0.994

Limits of system:

North zone: The north polar area 84º – 90º

South zone: The south polar area 80º – 90º

Overlap with the UTM: The UPS grid will be extended to 83º30'N and 79º30'S to provide a 30' overlap with the UTM Grid System.

The general formulae for the computation of N and E are:

$N = FN - R \cos \lambda \rightarrow$ for the North Zone

$N = FN + R \cos \lambda \rightarrow$ for the South Zone

$E = FE + R \sin \lambda \rightarrow$ for Both Zones

where λ is longitude (radians) and *R* is the radius of the parallel of latitude from the pole (obtained from tables).

*NOTE: False Easting is either added or subtracted dependent on the location of the point relative to the central meridian.

4.2.3 *LUNAR* METHOD

Also, it is possible to calculate regions or "surface bands" on the Earth by knowing two values of latitude and a pair of longitude values too. Thus, what we have is a region delimited by four points. This method is utilized for calculation of areas above the Moon. By doing on the Earth calculations similar to those that could be made on the surface of the Earth's moon, for those same four-points enclosed regions instead, we can calculate their terrestrial surface areas using Equation 4.2.1 [*lunarpedia*].

$$A_{lunar\_surfaces} = \frac{\pi r^2}{180}(\sin\phi_2 - \sin\phi_1)(\lambda_1 - \lambda_2) \qquad (4.2.1)$$

where ϕ_1, ϕ_2 are latitude values, λ_1, λ_2 longitude and r the radius of the body--in this case, the Earth's. For obvious reasons, we nicknamed this method the "Lunar Method."

4.2.4 TRIANGULATION METHOD

There exists as well the Triangulation Method, which can be used to measure a surface made up of a certain number of points. It consists of the division of the surface into a set of triangles [*Mathworld*] connecting each point to each natural neighbour (to see how Matlab Delaunay triangulation works, see Figure 4.3) to get all the points

connected in a “triangulated grid,” at the end. Then, if we sum up all the triangular surfaces, it would be obtained the total area of the original regular or irregular surface.

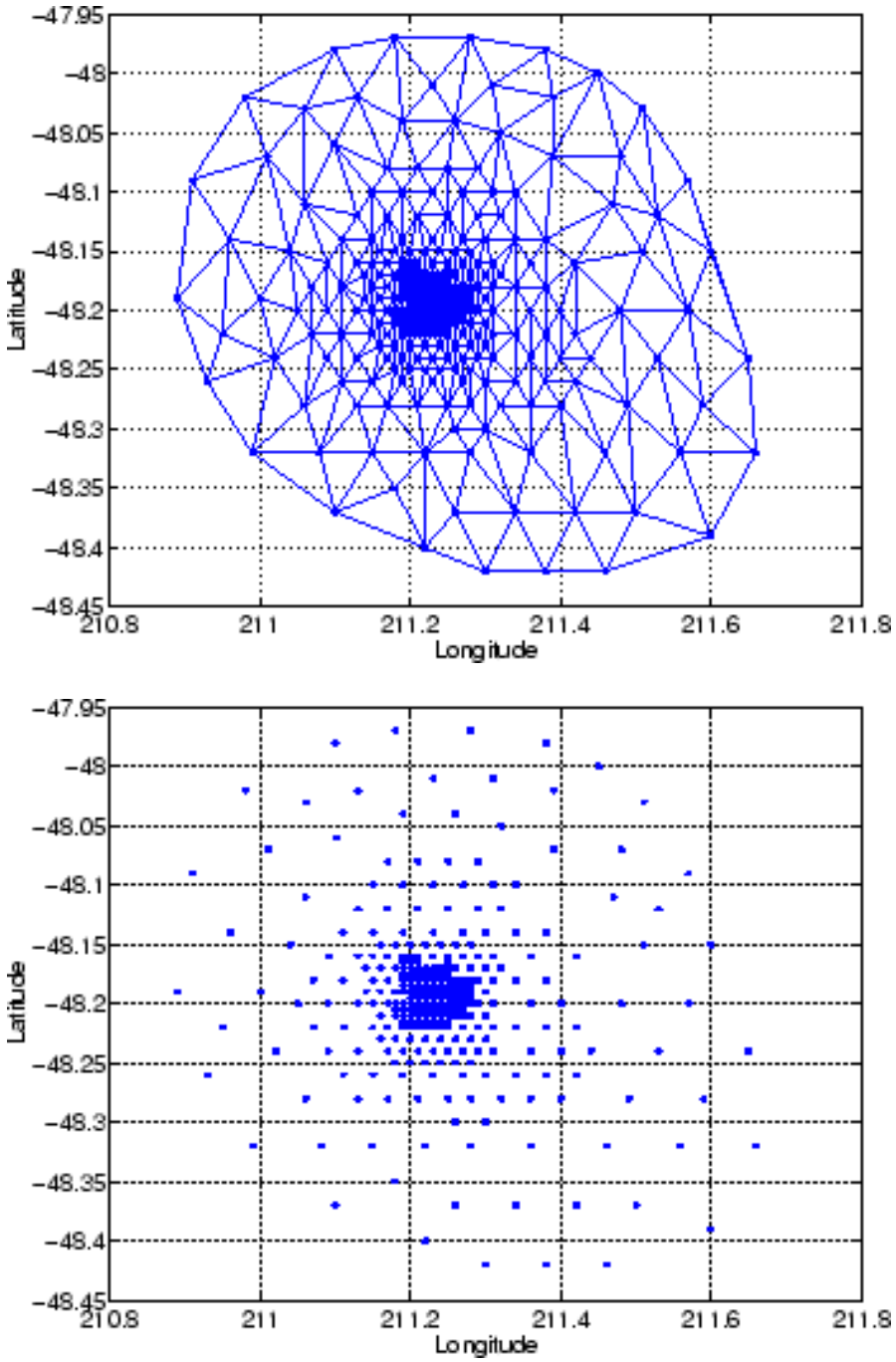

Figure 4.3. Implementation of a Delaunay Matlab refinement algorithm to construct conforming triangulations and 2D mesh (Upper) from a random original set of points between ~ -47ºS and ~ -49ºS (Bottom).

For example, Figure 4.4 shows the triangulation of data points of irregular and regular terrestrial bodies such as North America conformed by Canada, the United States, Mexico, and the Caribbean, and a half spheroid representing the Earth from the Equator poleward in Figure 4.6.

Figure 4.4. Implementation of a Delaunay refinement algorithm to construct conforming triangulations and 2D meshes over North America. From [*Laurent Rineau*, 2011]. This can be easily proven when triangulate four points which draw a square, resulting in two triangles after triangulation and, by calculating both areas and summing them up, it is acquired the total surface area of the square, which is exactly

the same as the calculated without subdividing the square up into triangles. This method is perfect when it is necessary to calculate the surface area of an unknown-shaped body where, if it is a sphere, then it may be use spherical trigonometry to calculate the surface area of each, in this case, spherical triangle (see Figure 4.9).

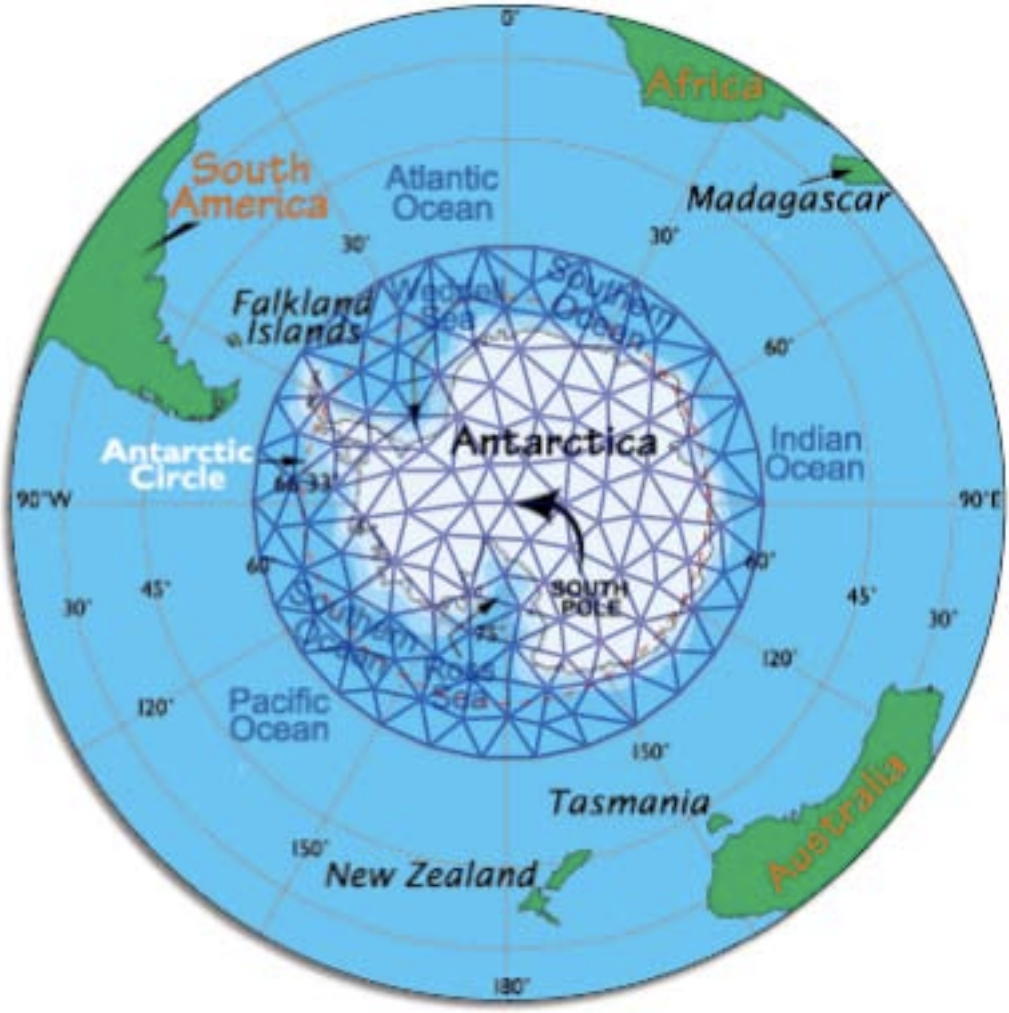

Figure 4.5. As per Figure 4.4 but for the Antarctic region 60ºS poleward.

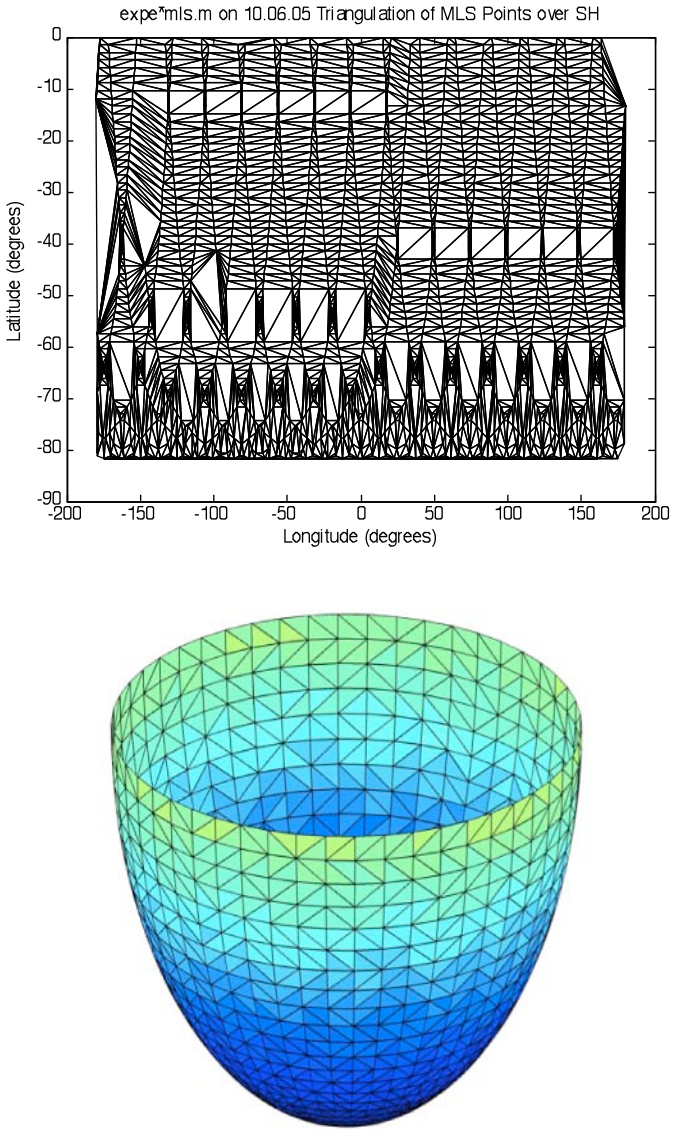

Figure 4.6. [Top] Delaunay triangulation applied to the dataset of EOS MLS longitude and latitude points available on 10.06.05 covering the SH shown in a planar projection. [Bottom] As per Figure 4.6 Top, but for 3D mesh and for half the Earth, seeing its shape as a spheroid.

4.2.5 PROPORTIONS APPROACH

The exception to the triangulation method (mentioned above) was the use of a very rough method at some point (as a result of examining all possible sides of our scenario), to calculate the surface area of the SH on a random day (19.07.05). It was

obtained the number of points obtained for temperature over the SH (equal to 1760 points for that day) and then it was done an approximation, considering that that amount was equivalent to a half of the Earth previously calculated (using the area of a sphere formula) less south pole surface area, and we came up with ~$2.5x10^8$ km^2. Doing something similar to find the number of points with PSCs temperature formation (below 195 K) equal to 259, we saw it as just a proportion, so those points had an equivalence of $3.7x10^7$ km^2, a rough result, but if it is compared to Figure 4.14b, it seems to be a rough but good approximation indeed. However, this method was not chosen because it may lack accuracy in the long run.

There were written different Matlab codes for each method that it was tested for calculation of PSC surface areas. Figure 4.7 shows how the EOS MLS temperature data points are distributed on the SH for a specific day in 2005 below a PSC formation threshold of 195 K. As it can be seen, it is not a well-organized grid and, for different days, there are different distributions, depending upon the daily amount of points below PSC temperature formation thresholds.

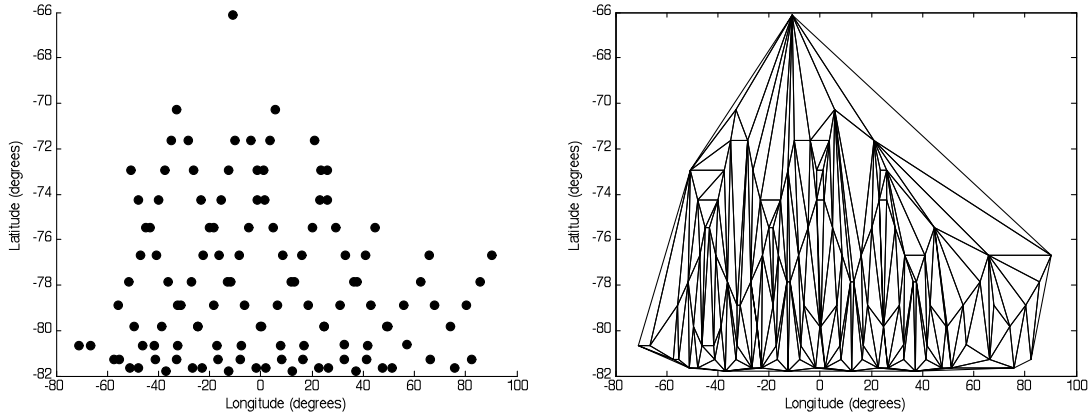

Figure 4.7. [Left] EOS MLS dataset points on the SH with PSC Temperature formation on 10.06.05. [Right] Delaunay triangulation applied to Fig. 4.7(left) sample.

4.2.6 Spherical Trigonometry

The shortest path between two points on a sphere, also known as an orthodrome, is a segment of a great circle [*Weisstein*, 2011] (see Figure 4.8).

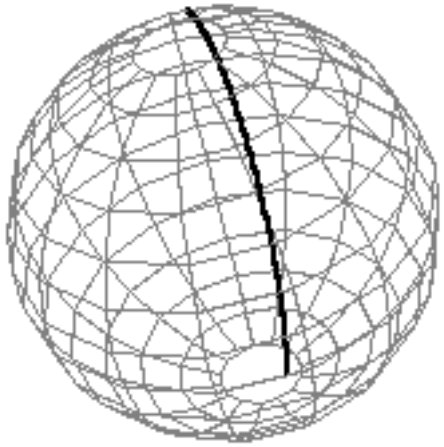

Figure 4.8. Illustration of an orthodrome in the Earth.

A great circle is a section of a sphere that contains a diameter of the sphere [*Kern and Bland*, 1948, p. 87]. Sections of the sphere which do not contain a diameter are called small circles. To find the great circle distance or geodesic distance between two points located at latitude ϕ and longitude λ of (ϕ_1, λ_1) and (ϕ_2, λ_2) on a sphere of radius *a* the great circle distance is

$$d = a \cos^{-1}\left[\cos \phi_1 \cos \phi_2 \cos(\lambda_1 - \lambda_2) + \sin \phi_1 \sin \phi_2\right]$$

where the *equatorial* radius is a = 6378.137 km (spheroid NAD83/WGS8), for the Earth. For the rest of Spherical trigonometric formulations relevant to this thesis, request the author**.**

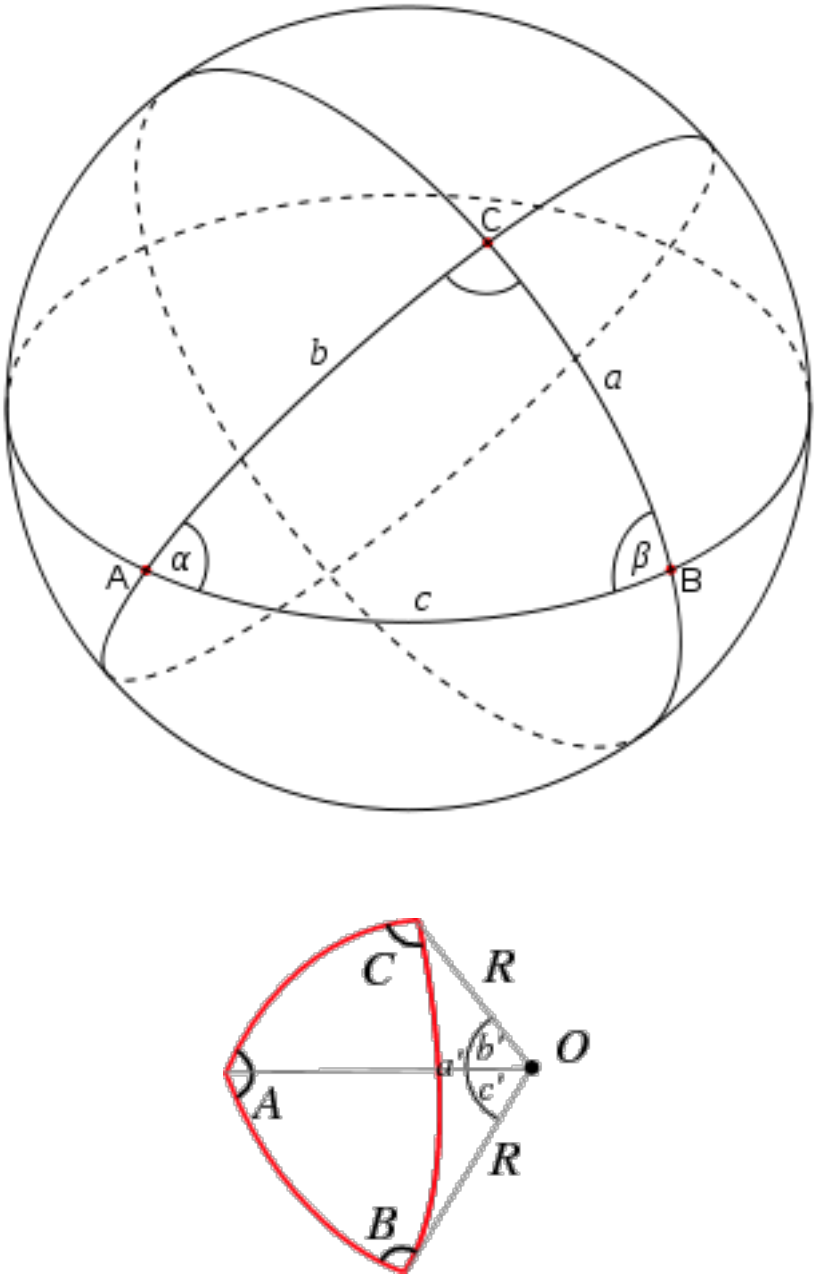

Figure 4.9. (Top) Schematic of a spherical triangle of vertices A, B, and C. (Bottom) Spherical triangle drawn on the surface of a sphere of radius R, centered at a point *O* = (0,0,0), with vertices A, B, and C. From [*Weisstein*, 2011–bottom figure].

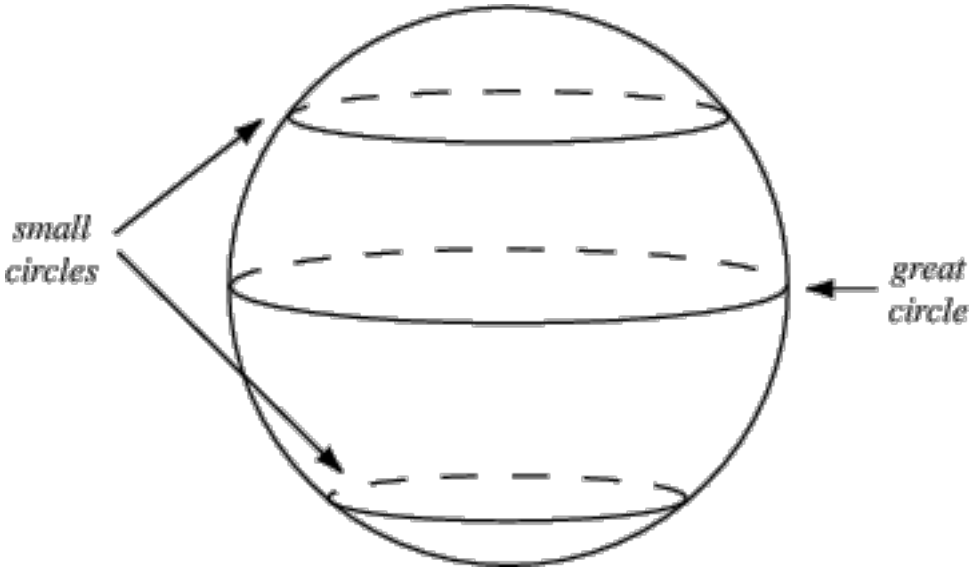

Figure 4.10. A schematic diagram of a great circle. From *Weisstein* [2011].

Continuing on, the first approach in the calculation of PSCs surface areas was converting the original longitude-latitude dataset into points measured in distance units through the UTM-UPS map projection. Since the UPS grid system covers the south polar area from 79.5° to 90°, with a 30° overlap with the UTM system [*DMA TM 8358.2*], and we were modelling the SH with daily EOS MLS measurements from points very close to the equator up to ~82°S, it was decided to consider them together to have a more accurate cover. Both systems have scale factors as function of latitude and they were also included in our calculation programming codes. Thus, having a plane projection of the Earth we used Triangulation of points and Lunar Method as well. However, the results obtained were not accurate enough when it was checked reliability of both algorithms calculating the SH surface area. Figure 4.11 shows the results from June to October 2005 using triangulation on the UTM-UPS grid (figure 4.11a) with values for the SH surface area between ~2.3×10^8 km^2 and ~0.3×10^8 km^2. Using the Lunar Method (Figure 4.11b), the values acquired were between ~1.2×10^8 km^2 and ~0.2×10^8 km^2.

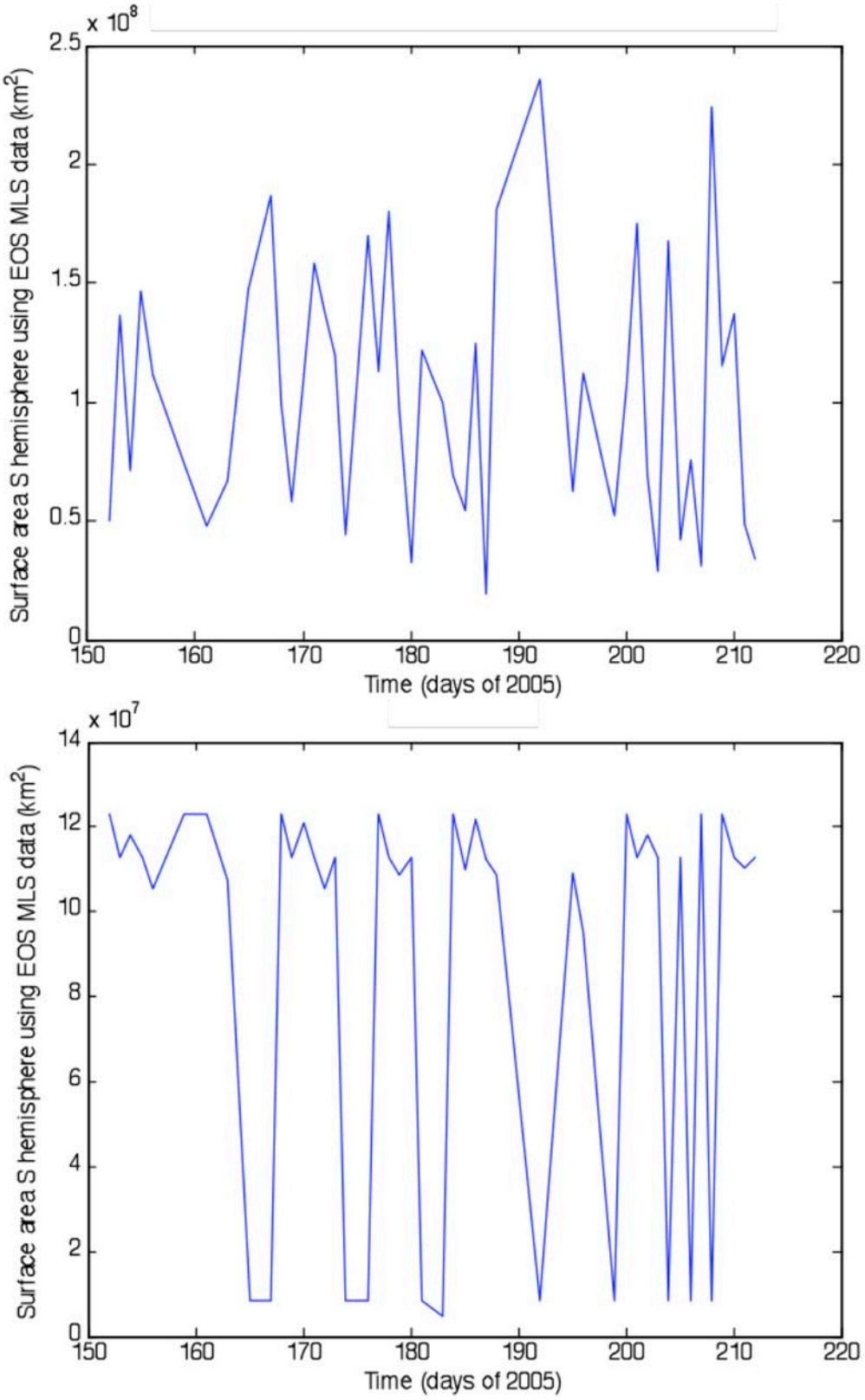

Figure 4.11. Calculation of SH surface area from June to October 2005 with two different methods: [a] Triangulation applied to a converted UTM-UPS grid. [b] Lunar Method applied directly on EOS MLS original geographic grid.

Finally, the way we worked out the solution to our launched scenario was by doing a triangulation of the EOS MLS longitude-latitude points (see Figure 4.7b), using the Matlab Delaunay function--(deliberately it is not explained before just to emphasize here the description of our successful algorithm) which returns a set of triangles containing indices into x and y of the vertices of each triangle. Then, for each spherical triangle, it was worked with spherical trigonometry equations to find the area of each triangle, which consists of calculating the excess magnitude in radians of each triangle times the squared radius of the Earth.

Figure 4.12 shows the expected results of the SH surface area using the algorithm described above, from June to October 2005. Note that on 15.07.05, the EOS MLS satellite instrument measured less points than on any other day from that period of time, which can imply that it was not a not well-organized grid of points for that day, and then a poor surface area calculation. To fix these problems, there were added some extra points covering the equator, and also latitudes beyond the EOS MLS available measurements. The results are shown in Figure 4.13.

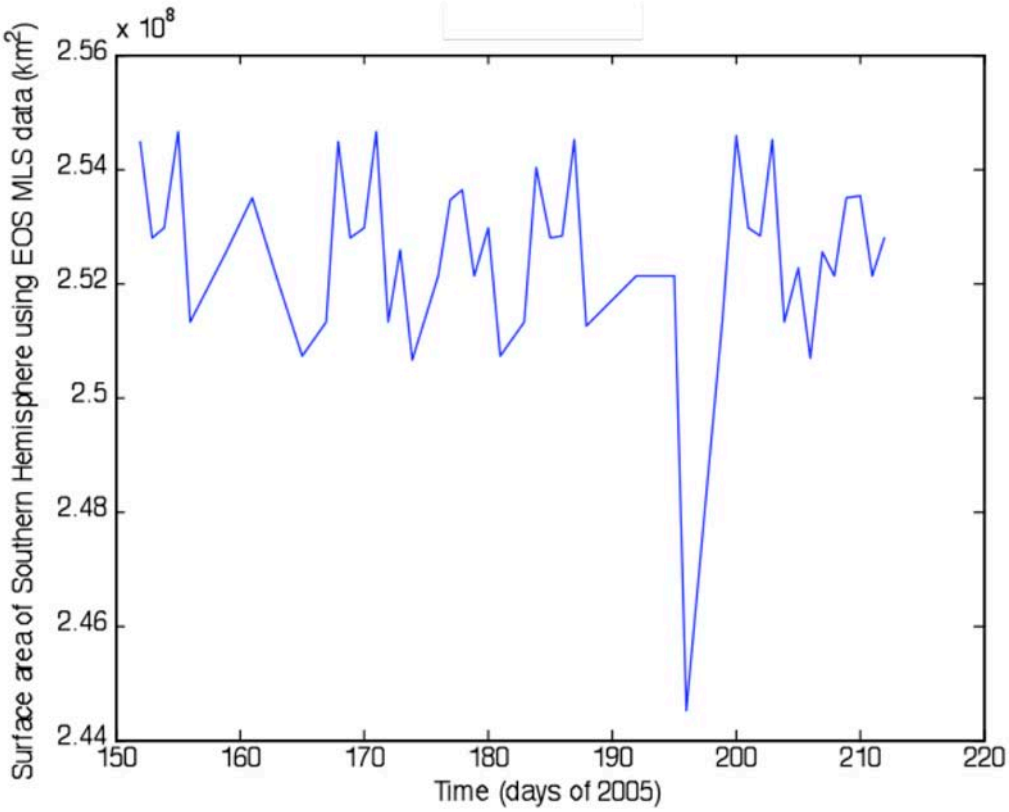

Figure 4.12. Calculation of SH surface area by Jun-Oct 2005 using triangulation and spherical trigonometry.

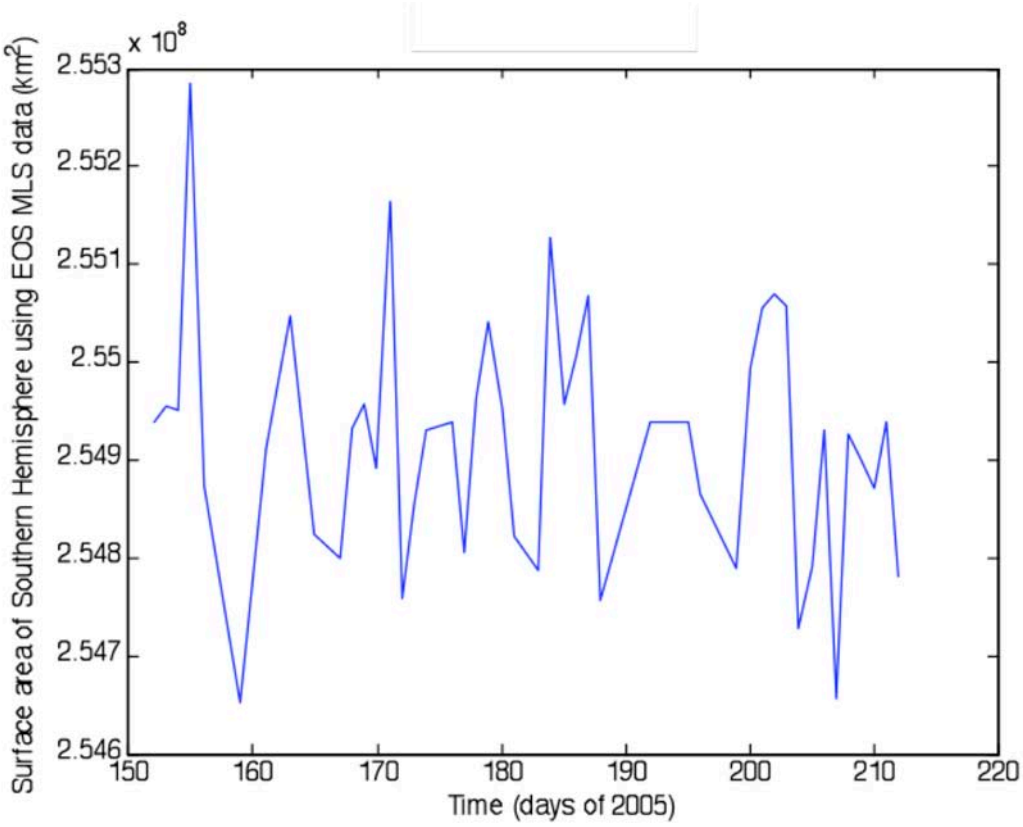

Figure 4.13. Like figure 4.12, but extra points were added to reduce variations in the area calculations along with the time.

Once the scenario was cleared up with the implementation of a good algorithm, next step was to calculate PSCs surface areas at different pressure levels and along periods of time in 2005 in which PSCs were observed. The set of Figures 4.14a-g shows those results.

Figure 4.14[a-g]. PSC surface areas measured in 2005 using our best algorithm implemented (triangulation and spherical trigonometry):

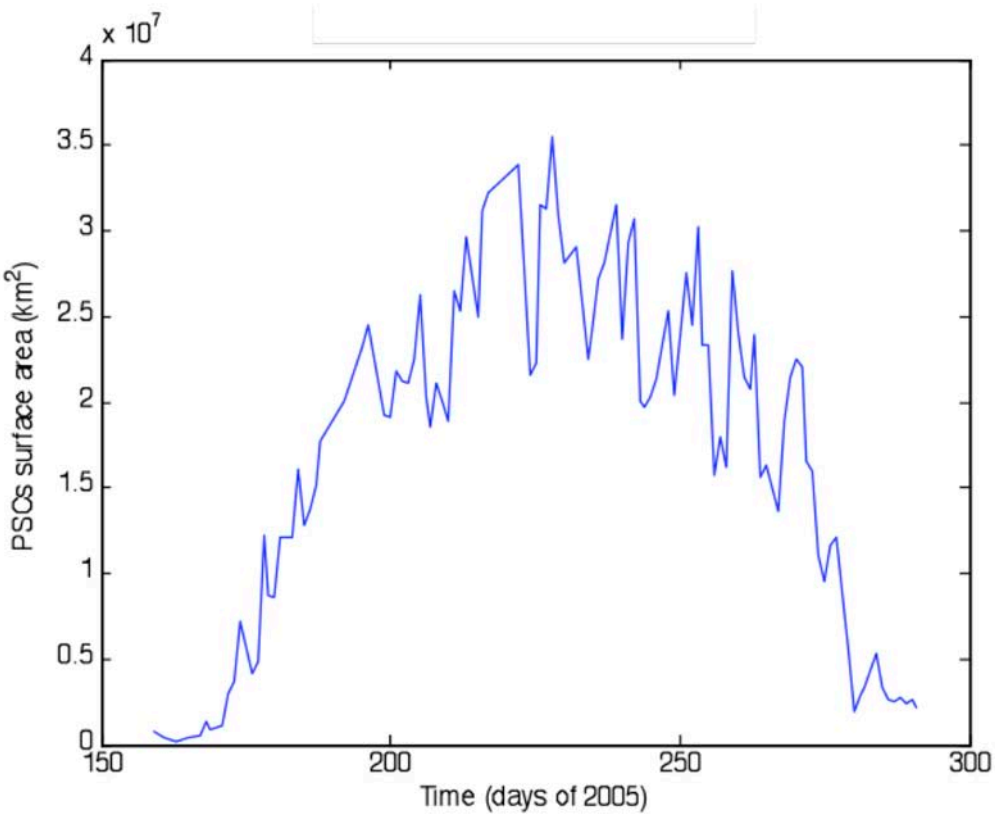

4.14[a] pressure level: 100 hPa

isentropic level: 425 K → height: 16 km.

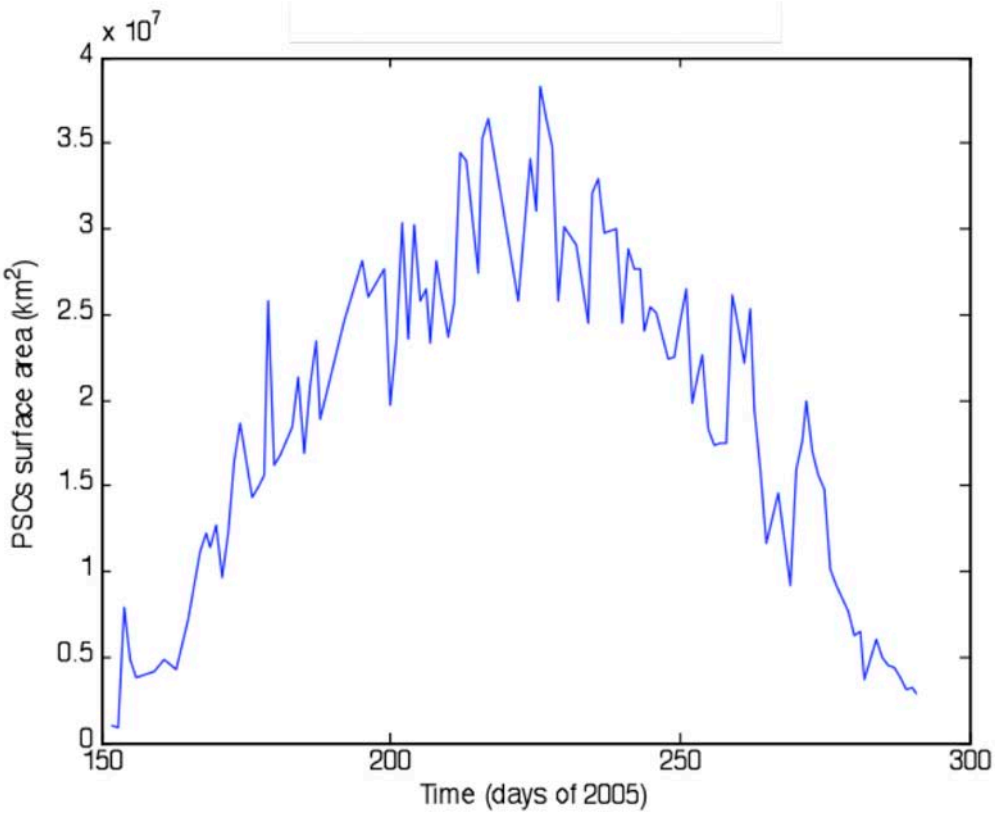

4.14[b] pressure level: 68.1292 hPa

isentropic level: ~475 K → height: ~18.5 km.

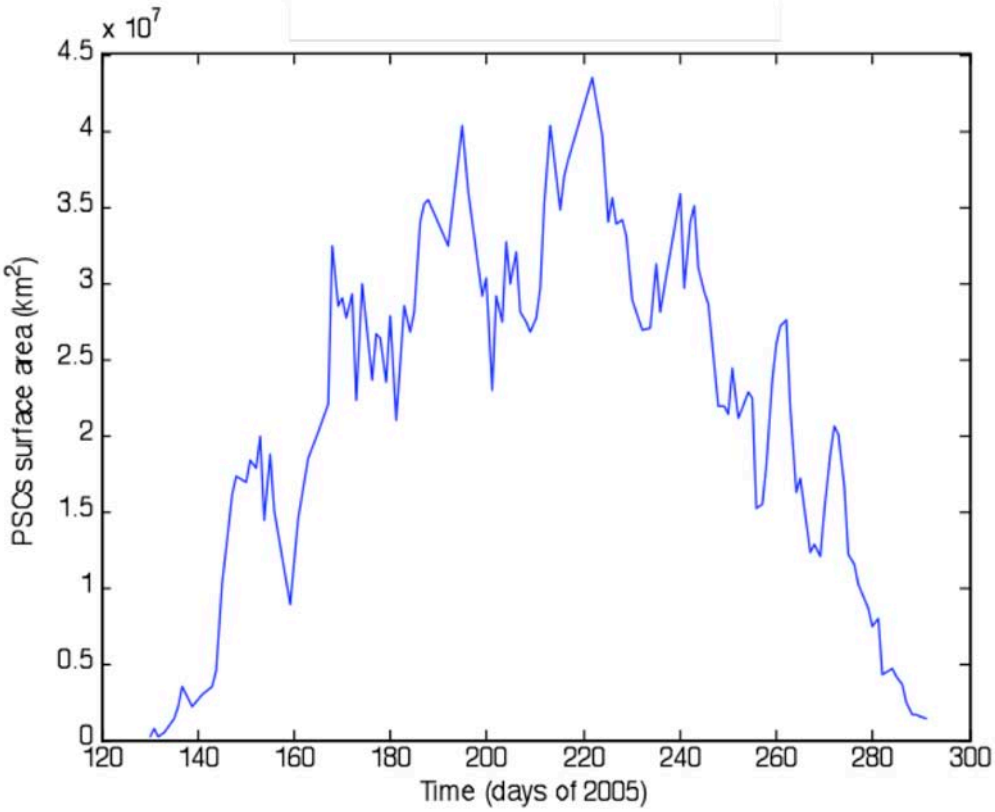

4.14[c] pressure level: 46.4159 hPa

isentropic level: ~525 K → height: ~20.5 km.

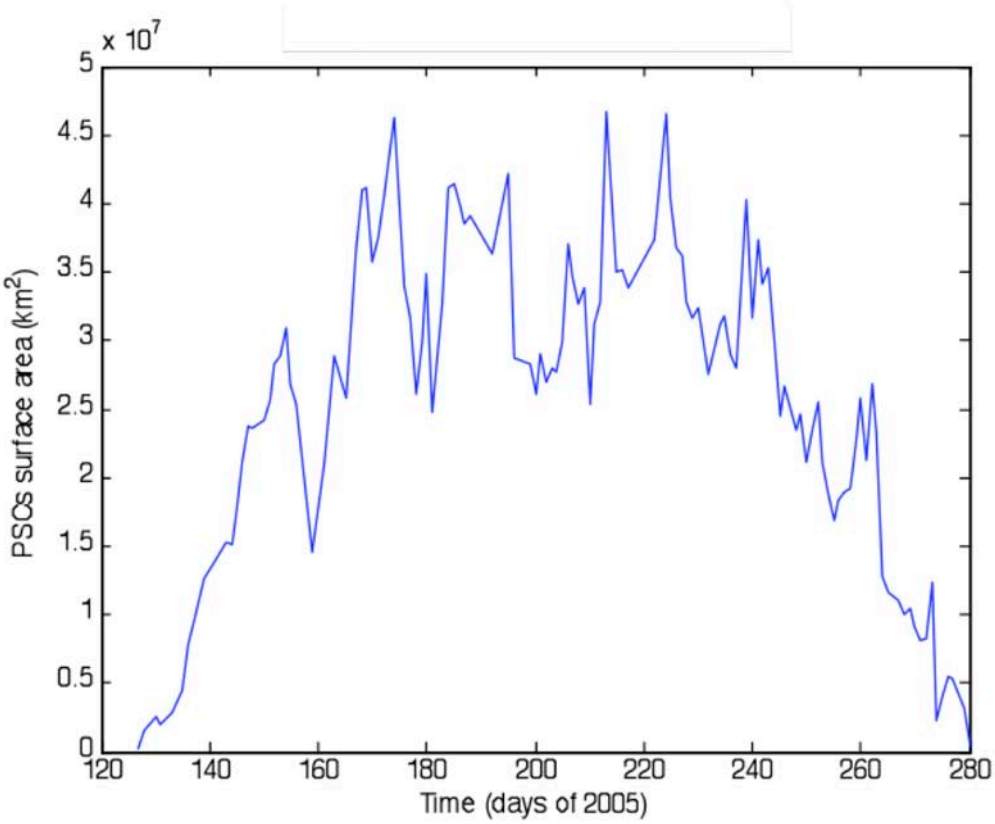

4.14[d] pressure level: 31.6228 hPa

isentropic level: ~600 K → height: ~24 km.

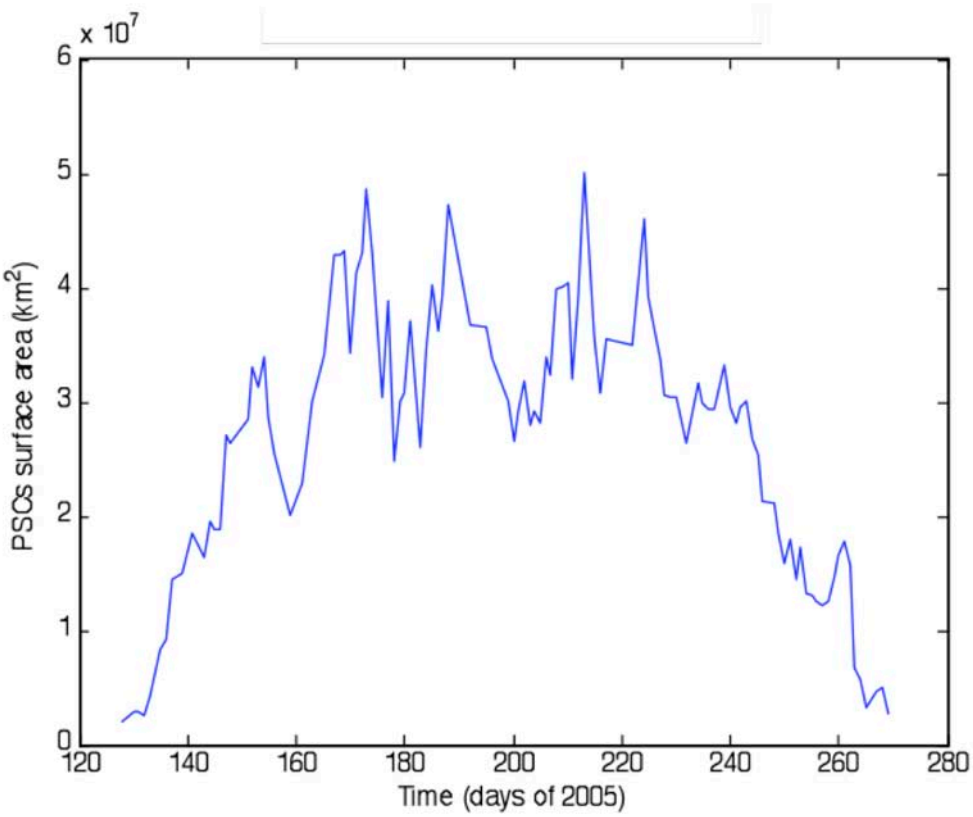

4.14[e] pressure level: 21.5443 hPa

isentropic level: ~750 K → height: ~27 km.

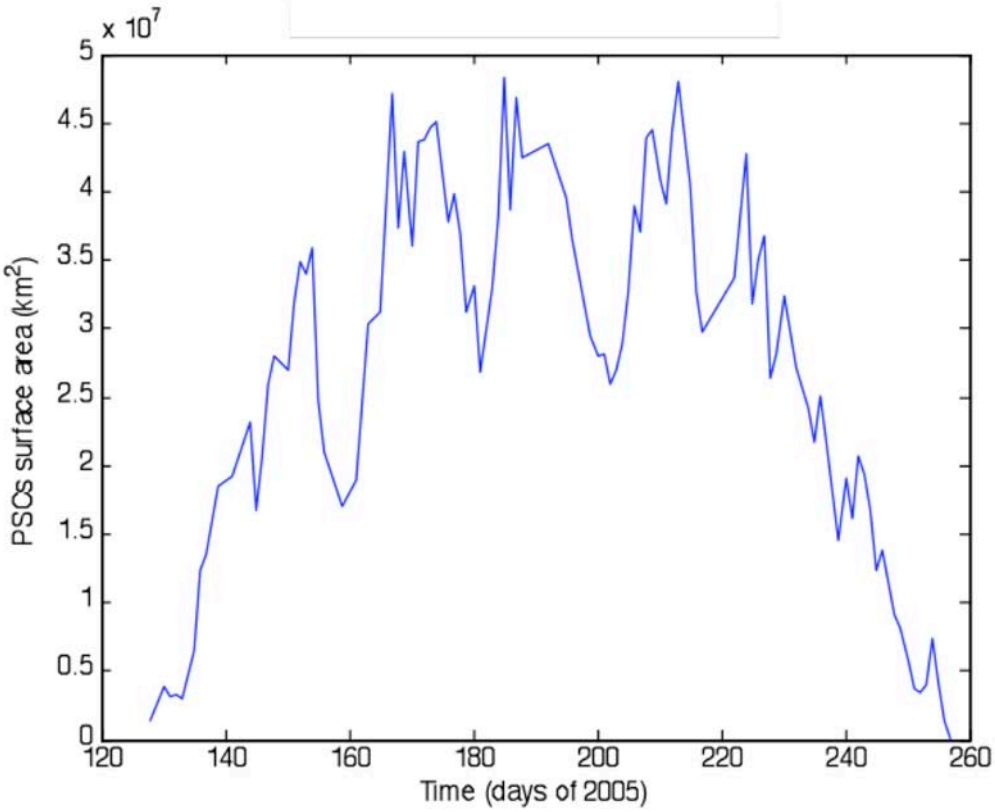

4.14[f] pressure level: 14.678 hPa

isentropic level: ~850 K → height: ~29.5 km.

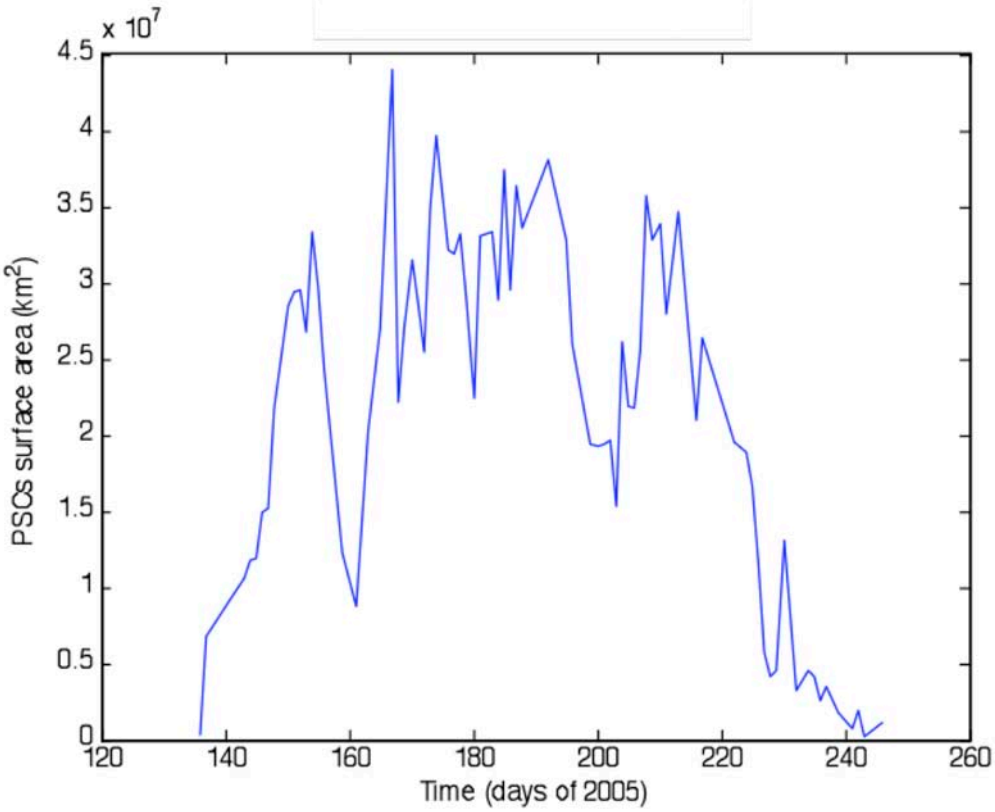

4.14[g] pressure level: 10 hPa

isentropic level: 900 K → height: 31 km.

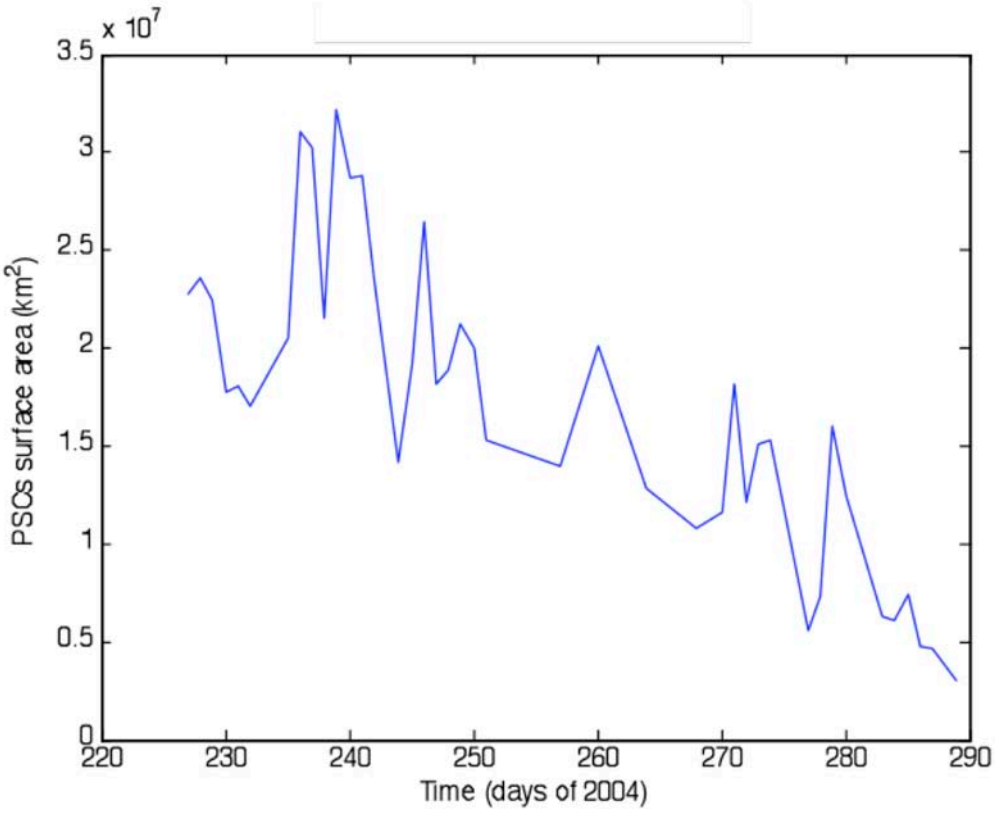

Figure 4.15. PSCs surface areas observed at a pressure level of 100 hPa, given limited available EOS MLS data in 2004.

4.2.7 Discussion

We started solving our problem by converting the original geographic coordinates from the EOS MLS dataset into a UTM-UPS grid system since it was considered that working on a plane projection would allow us to work in a more convenient (or better known) environment. However, it demanded an exhaustive research of both grid systems when it became evident that the result of the distance between two random points of our xy-plane was further away from the “real” value calculated by using the spherical distance formula.

Even though (it was seen that those discrepancies varied depending on the latitude), in some cases the results had just small inaccuracies instead of considerable ones, we were not getting the expected results. So it was added to the Matlab codes the respective scale factor considerations for each grid system, improving the results obtained--but still they were lacking accuracy. Looking through Figure 4.11a, it is clear that on only for one day did it was get a good estimation of the SH surface area.

That is when we switched then to using the Lunar Method, but it showed in our tests a bad performance working on a non-squared grid. So we started analyzing about how to add some special features in the programming code which was testing the Lunar Method, to make it able to work well with the random EOS MLS points distributions. However, as we were still confident that the triangulation method could work properly, it was planned to avoid dealing with map projections to be directly working on the Earth.

The first results of the new Matlab code allowed us to calculate the SH surface area, getting a max value of 2.4×10^{11} km^2 and a min one equal to 2.15×10^{11} km^2, both values bigger than our expected value (2.56×10^{8} km^2) by an evident and interesting 3 orders of magnitude.

We were able to include the final touches to our code to start getting the expected results (see Figures 4.12 and 4.13).

As it can be seen in Figure 4.13 how, after adding some points to our datasets, the variations on the areas calculations were fixed. It should be noted here that Figure 4.13 does not show a constant straight line because the y-axis has a very accurate scale and the variations shown are actually very small. Also, the results of PSC formation and existence areas (Figures 4.14 and 4.15) at different pressure levels are good enough,

and they should be compared in the near future with other results using different datasets, and hopefully using the same areas calculator algorithm successfully used here.

Finally, it is required to add to the results now the threshold PSCs temperature formation (T_PSCs) in order to obtain the actual temperature (during this work it was considered T_PSCs below to 195 K, in some cases) on each day of the EOS MLS measurements.

We included to the algorithm the threshold PSC temperature formation, calling the Matlab function *nat_equilib,* whose input values are the H_2O and HNO_3 concentrations in ppbv units and also pressure measured in hPa units. In the meantime, we are considering H_2O = 3.0 ppbv and HNO_3 = 10.0 ppbv, and the value for the pressure depends on the EOS MLS pressure level we select every time we run our code.

Previously, it was described how successfully we were calculating the PSC surface areas using EOS MLS level-2 version 1.5 data.

In the last algorithm, we first found the temperature points below 195 K and over that grid the triangulation was done. In the improved algorithm, we are doing first triangulation over all the available EOS MLS level-2 version 2.2 temperature points, and then we find the vertices of the triangles which satisfy the condition that the average temperature of those three vertices in each triangle is below the PSC threshold temperature (see Figures 4.17 and 4.18). Then all of them are summed up to get the total PSC surface area, as it was explained before. Note that before considering the average temperature in the triangles, we started looking for those triangles which satisfied the condition that each single vertex had a temperature below the PSC threshold (see Figure 4.16).

Here is important to mention that when it is said *all the available EOS MLS level-2 version 2.2 temperature points,* we mean that we first selected the good points, according to the EOS MLS level-2 version 2.2 quality reference manual. According to it, we should discard temperature profiles with an EOS MLS Quality flag lower than 0.6, and we should discard as well those temperature profiles with a Convergence flag higher than 1.2, so “good” means, in this case, something that satisfies what it was mentioned above (2 flags criterion). (The values, 0.6 and 1.2, are known as Quality threshold and Convergence threshold, respectively).

We should mention here, in order to improve the already written Matlab codes organization, that:

area10b_expe_version2.m is the code which uses the area calculator based on EOS MLS v2.2 data with a very simple quality control: only removing points with a latitude value of -999 degrees.

area10c_expe_version2.m is as described above but with what we called “quality-control” (see appendix A). It uses 2 quality flags: convergence and quality flags.

area10cc_expe_version2.m is the code which uses the area calculator based on EOS MLS v2.2 data using 4 quality flags: convergence, quality, status, and precision flags (status and precision flags were described in Sect. 2.1.4).

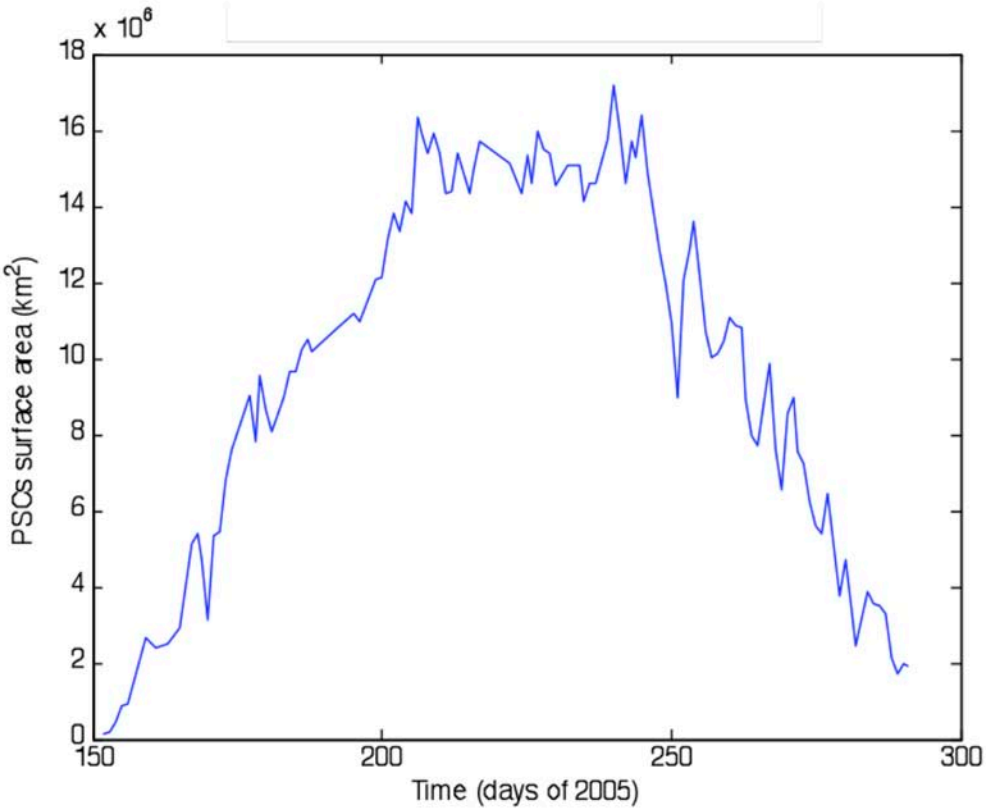

Figure 4.16. PSC surface area vs. time in 2005 using EOS MLS data level-2 version 1.5, Pressure = 68.1292 hPa and considering each of the three vertices of each triangle after triangulation with a temperature below PSC threshold.

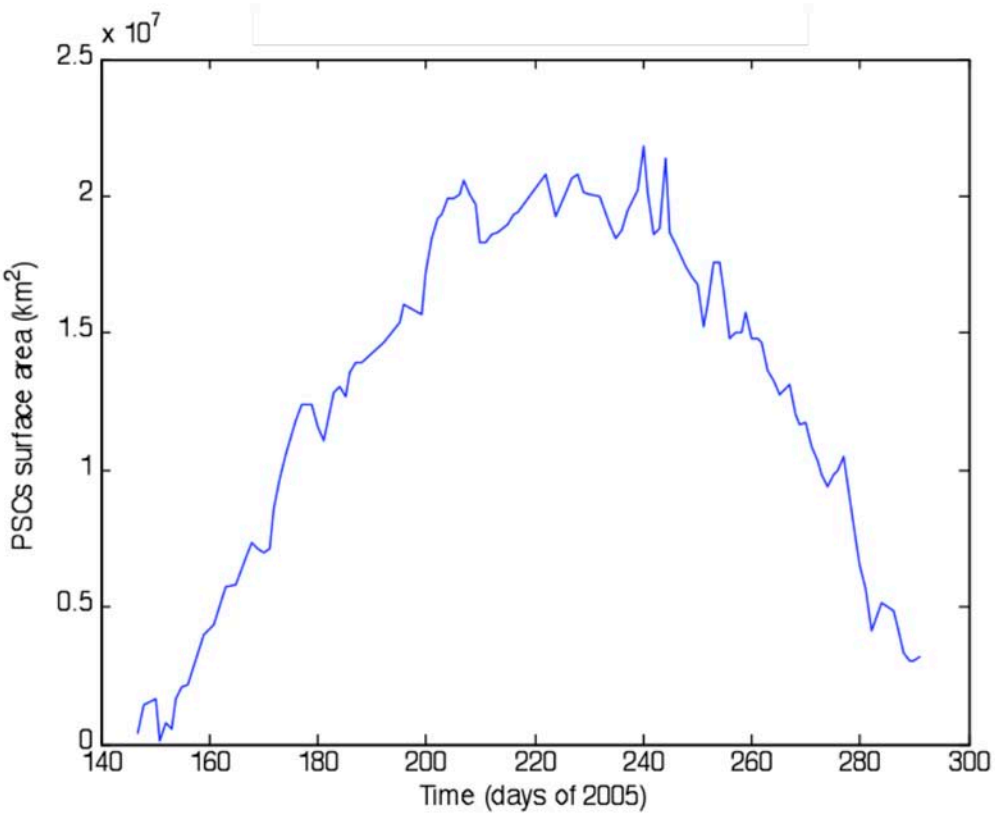

Figure 4.17. As in Figure 4.14, but in this case considering that the average temperature of all the vertices for each triangle is below the PSC threshold.

EOS MLS data level-2 v2.2 data set has 47 pressure levels, whereas EOS MLS data level-2 version 1.5 has 37, so the respective coincidences in pressure levels for both versions (see Table 2.1) were found, in order to make a good comparison of plot results when the algorithm for each different EOS MLS data set version is run.

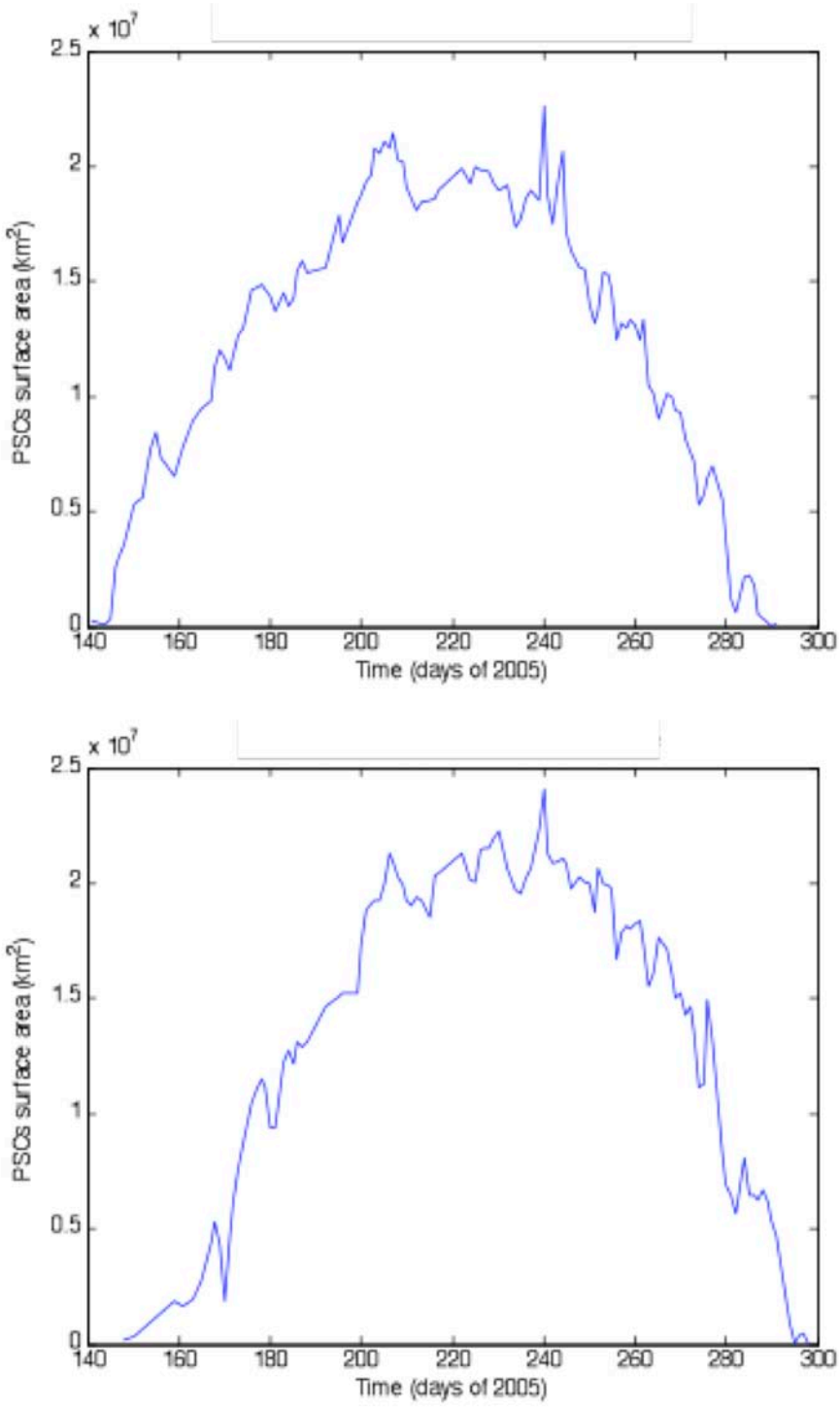

Figure 4.18. Consideration described in Figure 4.17 showing PSC surface area vs. time in 2005 using EOS MLS data level-2 version 1.5, Pressure = 46.4159 hPa (upper plot) and Pressure = 100 hPa (lower plot).

In order to determine how different was the EOS MLS version 2.2 when compared to the EOS MLS version 1.5, correlation coefficients were computed (see Figure 2.38 with correlation coefficients plots).

As it can be seen, the different correlation coefficients show good matching between both data set versions. For all studied cases, the first decimal position is always 9, which gives to have correlation coefficients great than 0.9.

PSC surface area versus time using EOS MLS level-2 version 2.2 for different years were calculated in: 2004, 2005, 2006, 2007, and 2008. Here it should be noted that 2004 data set is incomplete, so only part of the trend for the profile is actually seen.

As a way to check results, the PSC area calculator algorithm using NCEP/NCAR is used covering the SH in order to measure the reliability of the PSC area values, getting a value of 2.5382×10^8 km^2 for the SH surface area--which means that we can trust the results, if we compare this value to 2.56×10^8 km^2, the actual area of half the Earth.

In this case, employing the EOS MLS v2.2 data products, Temperature is considered, and for that, the suggestion from the *EOS MLS Version 2.2 Level 2 Data Quality and Description* document is that “profiles for which Status is an even number should be used in scientific studies”, whereas “values at altitudes where the estimated precision is flagged negative should not be used.” This was done, observing almost the same trend between using 2 and 4 quality flags. Here it is important to mention that for each value of temperature (3496 values on each of the 47 pressure levels), it is obtained its respective quality flag value, for each of the 4 quality-control flags.

For example, on October 1, 2005, it was seen that (naming Flag 1: Quality, Flag 2: Convergence, Flag 3: Precision, Flag 4: Status and aux1: all 4 flags) Flag 1 removed

2.95% points, Flag 2: 0.6%, Flag 3: 0%, Flag 4: 0% and aux1: 3.1%. For a more general analysis, see Appendix A.

Furthermore, the percentage of points removed was calculated using EOS MLS v2.2 data and 2 flags or 4 flags following the simple calculation described by Eq. 4.2.2.

$$removed\_data = \left[1 - \left(\frac{good\_data}{total\_data}\right)\right] \times 100\% \qquad (4.2.2)$$

where *good_data* is the number of temperature points after applying 2 or 4 flags filters, and *total_data* = 3496.

Once the total removed data was calculated using 2 and 4 quality flags, the respective correlation factors were computed for different number of qualiy flags. We noticed that there was not such an important difference between considering 2 and 4 quality flags (see Figures 4.19, 4.20 and 4.21).

From Figure 4.19, it can be seen that the difference in pressure level is not important in the calculation of those correlation coefficients and that the highest percentages of removed points in all plots of Figures 4.19–4.21 correspond to a poorly calculated surface area value, since the number of points available for that matter is not sufficient. For example, from Figure 4.21, it can be seen that roughly the highest peak of *removed points* is in a day near to the day 200 in 2007 and, going to look at previous calculations (not shown), a bad quality *area* calculation value is actually observed for the same day.

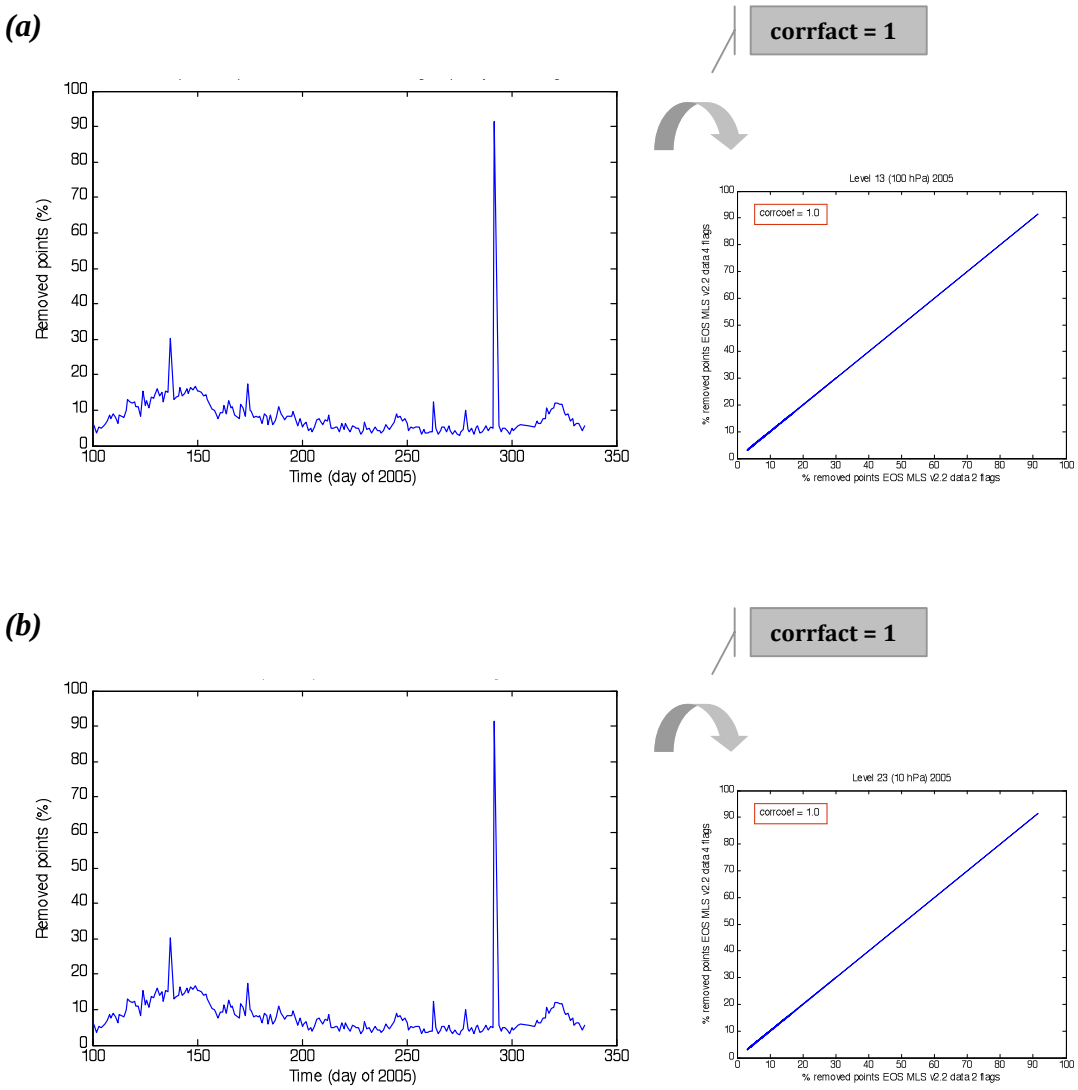

Figure 4.19. Percentage of temperature removed points considering 2 and 4 quality flags on PSCs surface area calculation using EOS MLS v2.2 data in 2005 for pressure = 100 hPa (Fig. 4.19a) and pressure = 10 hPa (Fig. 4.19b) and their respective correlation factor values.

4.3 NCEP/NCAR and EOS MLS v2.2 data sets.

(a)

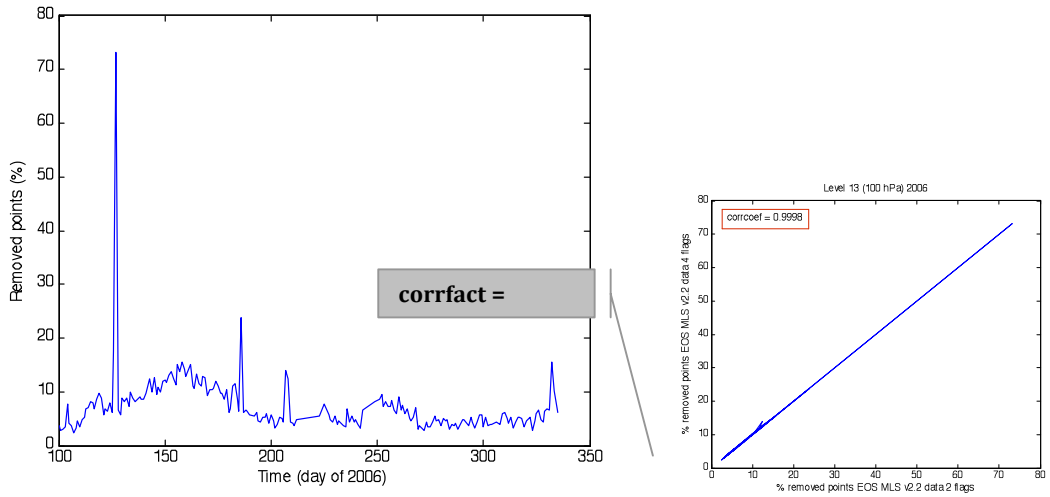

(b)

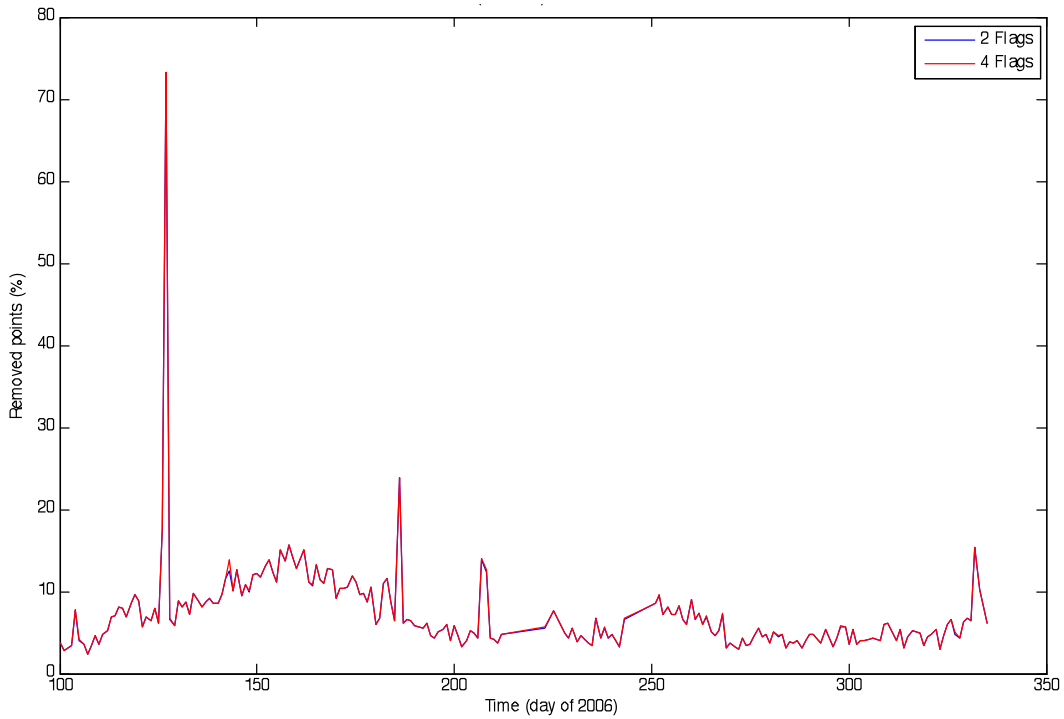

Figure 4.20. Percentage of temperature removed points considering 2 and 4 quality flags on PSCs surface area calculation using EOS MLS v2.2 data in 2006 for a pressure of 100 hPa and the correlation factor calculation (Fig. 4.20a). Holding on area calculation plots using 2 and 4 quality flags (Fig. 4.20b).

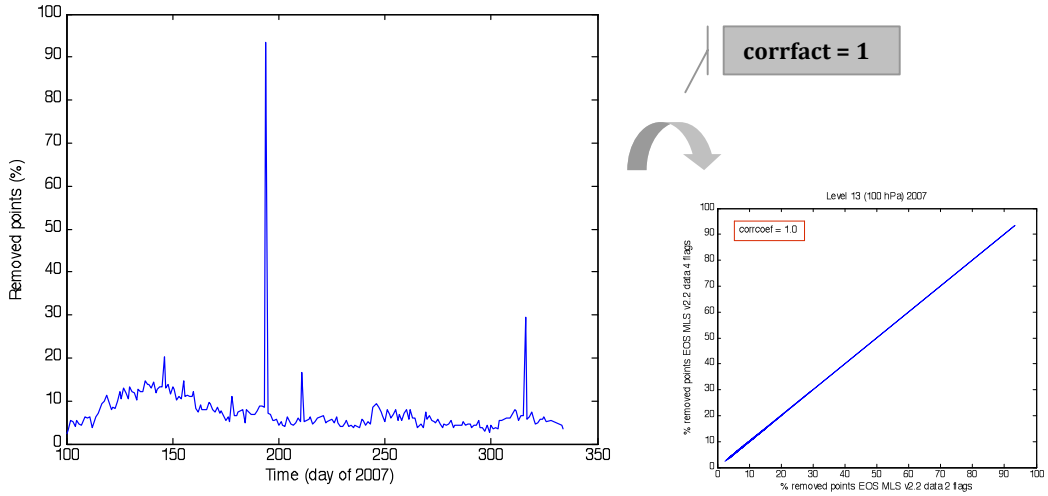

Figure 4.21. Percentage of temperature removed points considering 2 and 4 quality flags on PSC surface area calculation using EOS MLS v2.2 data in 2007 for a pressure of 100 hPa and the correlation factor calculation.

NCEP/NCAR data set has 17 pressure levels from 1000 hPa to 10 hPa. The matrix of temperature (ncep_data.ho) has a size of 17x73x144, the matrix of latitude: 73x1 and longitude: 144x1, whereas the EOS MLS v2.2 data set has temperature, latitude and longitude matrices as follows: 47x3496, 3496x1 and 3496x1, respectively, so for each value of temperature on each pressure level we have its respective values of latitude and longitude, which it is not the same in the case of NCEP/NCAR.

For EOS MLS, we considered latitudes from below to -60° up to ~ -82° (the last available latitude in the SH for this satellite-based data set). For NCEP/NCAR latitudes from -60° to -82.5° are considered, since -82.5° is the closest NCEP/NCAR latitude value to EOS MLS's -82°.

Thus, latitude and longitude matrices were created in order to have a data structure similar to EOS MLS data (all values are actual NCEP/NCAR latitude and longitude values):

$$NCEP/NCAR\_lat\_matrix = \begin{bmatrix} -60 & -60 & -60 & \dots \\ -62.5 & -62.5 & -62.5 & \dots \\ \vdots & \vdots & \vdots & \vdots \\ -82.5 & -82.5 & -82.5 & \cdots \end{bmatrix} \text{ size: 10x144}$$

$$NCEP/NCAR\_lon\_matrix = \begin{bmatrix} 1 & 2 & \cdots & 360 \\ 1 & 2 & \cdots & 360 \\ \vdots & \vdots & \vdots & \vdots \\ 1 & 2 & \cdots & 360 \end{bmatrix} \text{ size: 10x144}$$

4.4 PSC surface area calculation error analysis [using EOS MLS v2.2 data]. In order to calculate the error values for each PSC surface area value on each day of the PSC surface area vs. time plots, for each good temperature value (T) in the SH zone it is obtained that:

$$T' = T + \left[(T_{precision}) \times (\text{random number}) \right] \qquad (4.2.3)$$

where *T'* is the temperature value with its error associated and *T_precision* corresponds to the Precision flag for each value of temperature, as it was explained before.

So, using values of T' the PSC area calculator was used for computation of the PSC surface area errors, generating first 100 different area error values for each area value for each day of each specific year and pressure using a Monte Carlo simulation. From the matrix of area errors statistical information on the mean, max, min, median and standard deviation values were obtained.

4.5 T_{NAT} and PSC area

As we started studying a connection between PSC formation temperature (T_{NAT}) and PSC area, we did then some quick reading through some of the publications that cite *Hanson & Mauersberger* [1988]'s paper for calculation of PSC T_{NAT} based on pressure, nitric acid and water vapour mixing ratios. We found out that those authors use different values for $T_{NAT,}$ following different criteria. For example, [*Campbell and Sassen*, 2008] use H_2O and HNO_3 concentrations of 4 ppmv and 10 ppbv, respectively on their calculations for $T_{NAT\ ,}$ while *Nedoluha et al.* [2003] use for these same mixing ratios: 5 ppmv and 10 ppbv.

Pitts et al. [2007]: *we chose a value of T_{PSC} =198 K. This value is warm enough to exclude most if not all clouds from the background ensemble. We found that changing T_{PSC} by +1–2_ changes the total number of PSCs identified by about 1%.* […] *We have found that 198K is sufficient in all cases.*

In our previous results, we kept calculating PSC area at T_{NAT} = 195 K and, when we were using *Hanson & Mauersberger* [1988]'s algorithm, we used H_2O and HNO_3 concentrations of 3 ppmv and 10 ppbv.

Now, using EOS MLS v2.2 temperature profiles in 2005, we calculated PSC area for three different T_{NAT}'s over what we call "PSC region," which in terms of pressure covers from 100 hPa to 10 hPa (pressure values in which PSCs are potentially observed). Those temperatures are T1: 195 K, T2: 197.48 K (H_2O and HNO_3 concentrations of 3 ppmv and 10 ppbv) and T3: 199.66 K (H_2O and HNO_3 concentrations of 5 ppmv and 10 ppbv.). On Figure 4.23 the PSC area results are shown, where T1 is in blue, T2 in red, and T3 in black.

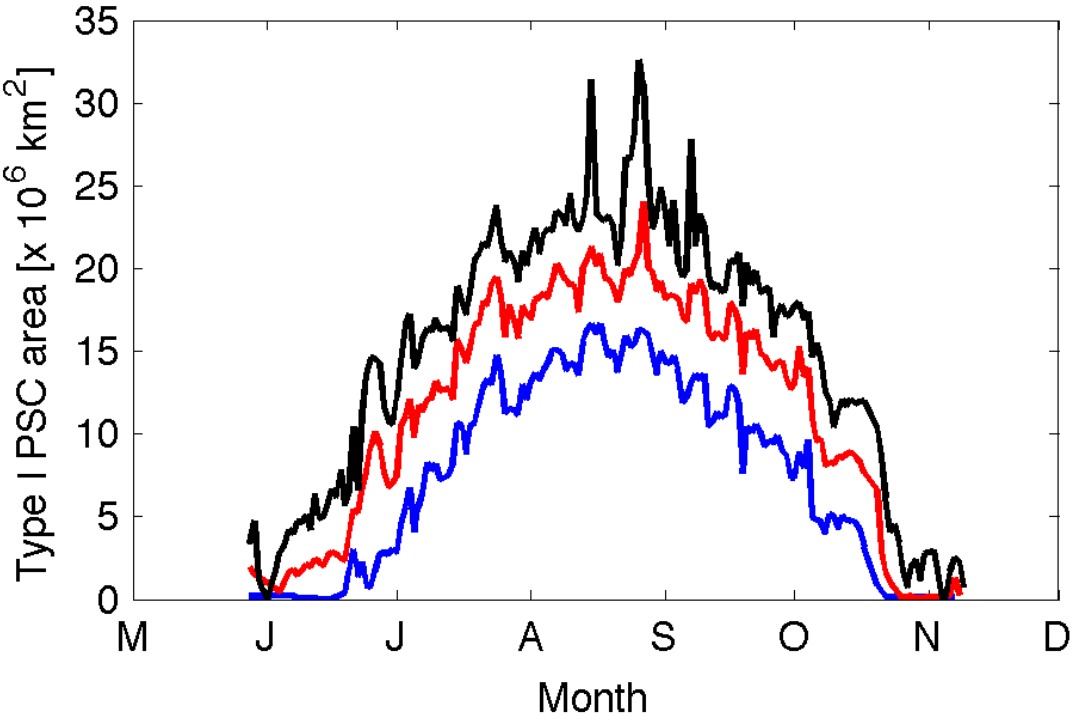

Figure 4.23. Type I PSC area at different T_{NAT} (corresponding to different H_2O and HNO_3 concentrations) derived from EOS MLS in 2005 at 17.5 km. Blue line: 195 K, Red line: 197.5 K (3 ppmv H_2O and 10 ppbv HNO_3) and Black line: 199.7 K (5 ppmv H_2O and 10 ppbv HNO_3).

Note: in order to be able to make comparisons between years, and not only portions of them, the Figures 4.29 to 4.31 are from those years in which the available data on Atmos *data_store* covers whole years. Thus, even though plots for incomplete years (e.g. 2004), were also generated, these are not included in this thesis.

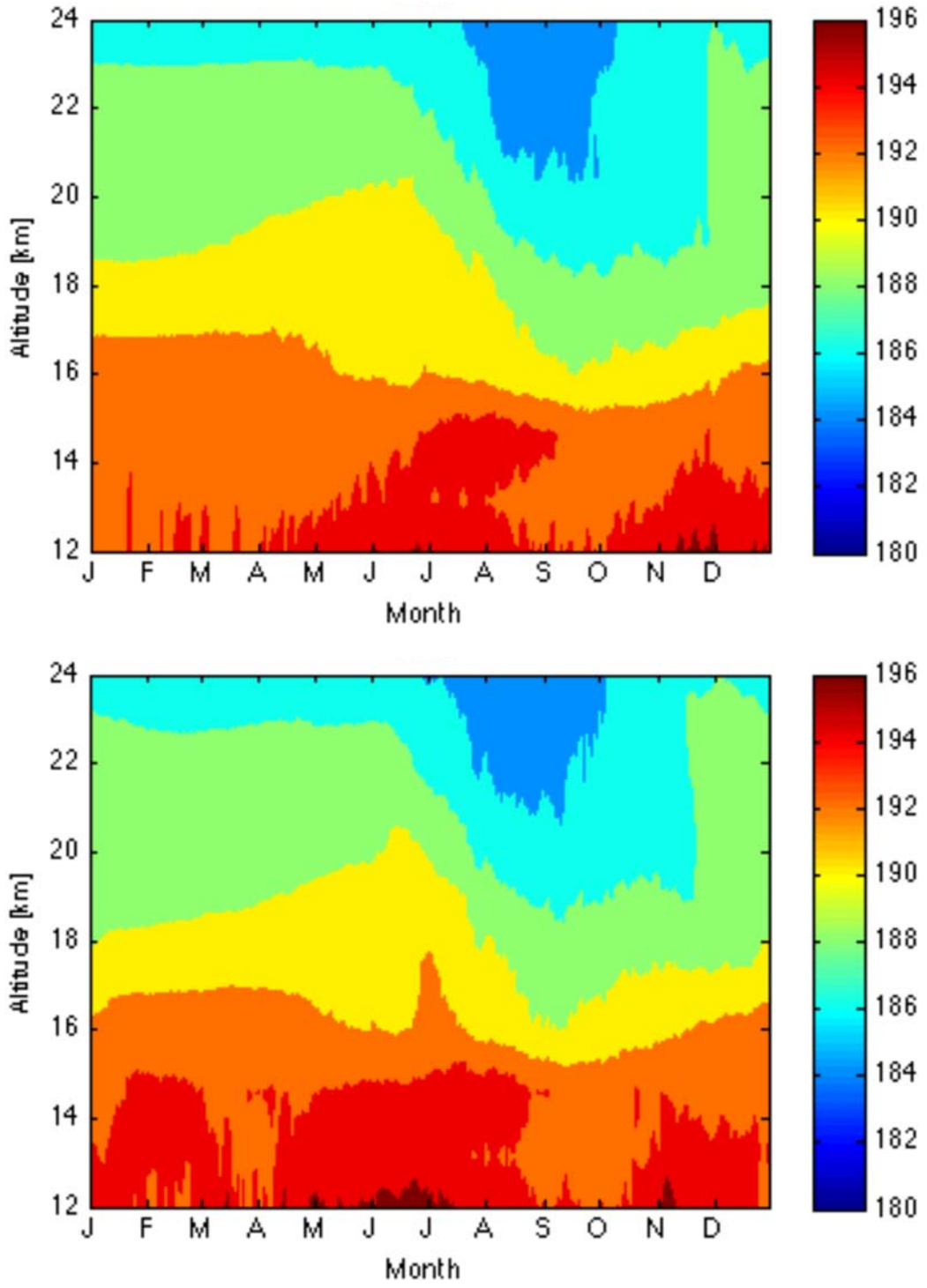

Figure 4.24. Computation of mean T_{ice} using *Marti and Mauersberger* [1993] derived from Aura MLS water vapor concentrations in 2006 (Top) and 2007 (Bottom) from 12 km to 24 km over the Antarctic region [60º S– 82ºS].

Further Analysis on EOS MLS v2.2 Temperature

Given the results from using different *levels* of quality control on nitric acid and water vapour profiles, we went back for a while to Temperature in order to see how it was affected by those quality controls. In the past, we were using for the Temperature profiles only the quality flags suggested by our documentation, without any additional improvement. Our results for different years and different pressure levels are described in Appendix A.

Here it is important to say that from the work on studying the quality of the data, we observed a relationship between the number of discarded points and our calculations of PSC area.

The Figures 4.25 and 4.26 show how PSC area is affected. For the calculations, we chose a day on the satellite dataset in which the number of temperature points after and before applying the maximum of quality control remained constant, in order to work in a day with the mean number of points available. The day we chose was 29.09.05, and we selected a pressure of 100 hPa. The algorithm is based on the PSC area calculator and removes points randomly. For Figure 4.25, we used 20 random points following a Monte Carlo statistical analysis.

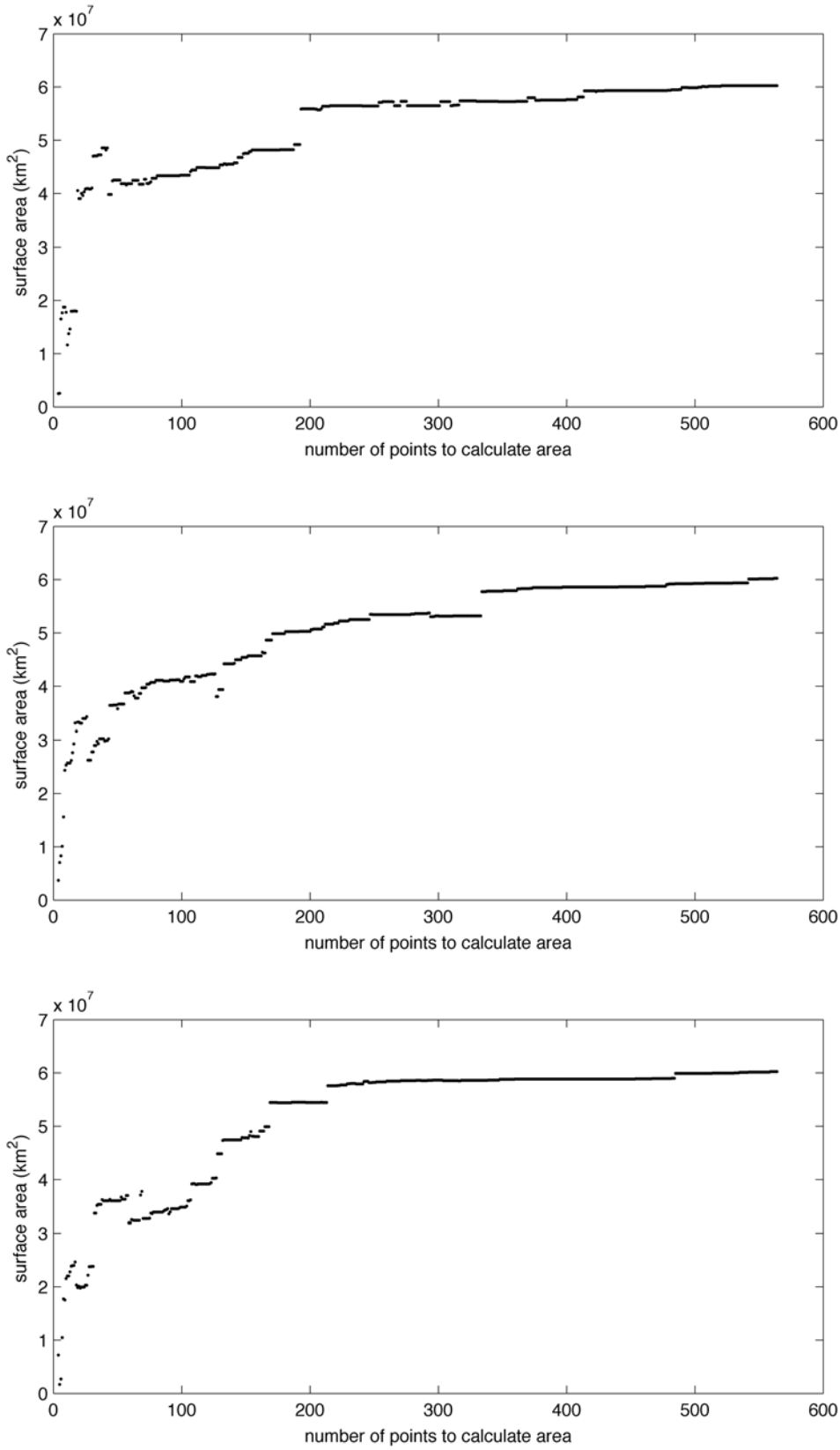

Fig 4.25. Random variations in area calculation by removing points randomly from the temperature dataset on 29 July, 2005.

In Figure 4.26, it is shown the same analysis as in Figure 4.25, but using 1E03 and 1E04 random points. In terms of speed calculation, we can say here that using the algorithm working with a huge number of random points (e.g. 1E04) requires more than three days without a pause to finish the calculations.

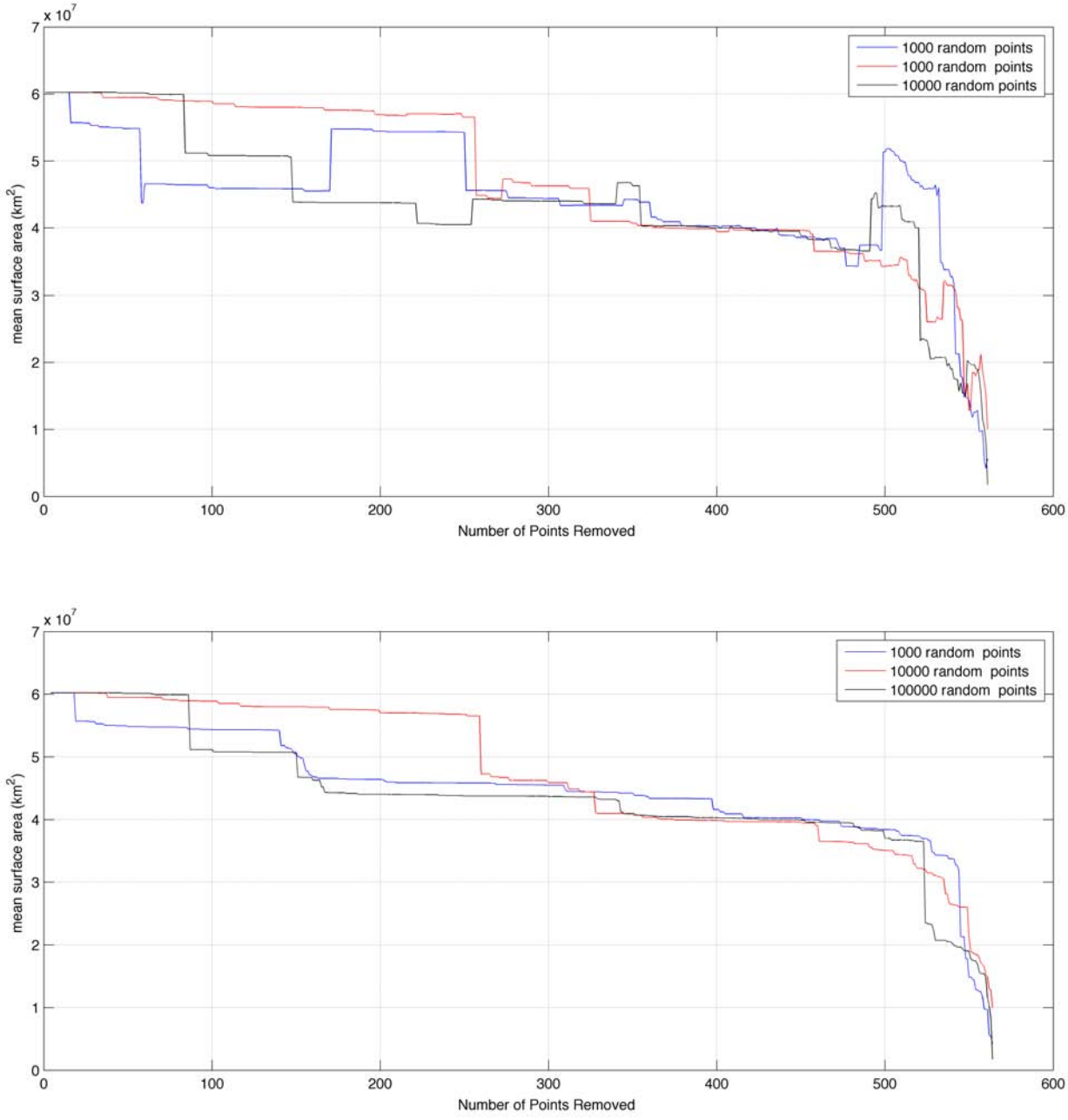

Fig 4.26. Mean variation in area calculation by removing points randomly from the temperature dataset on July 29, 2005.

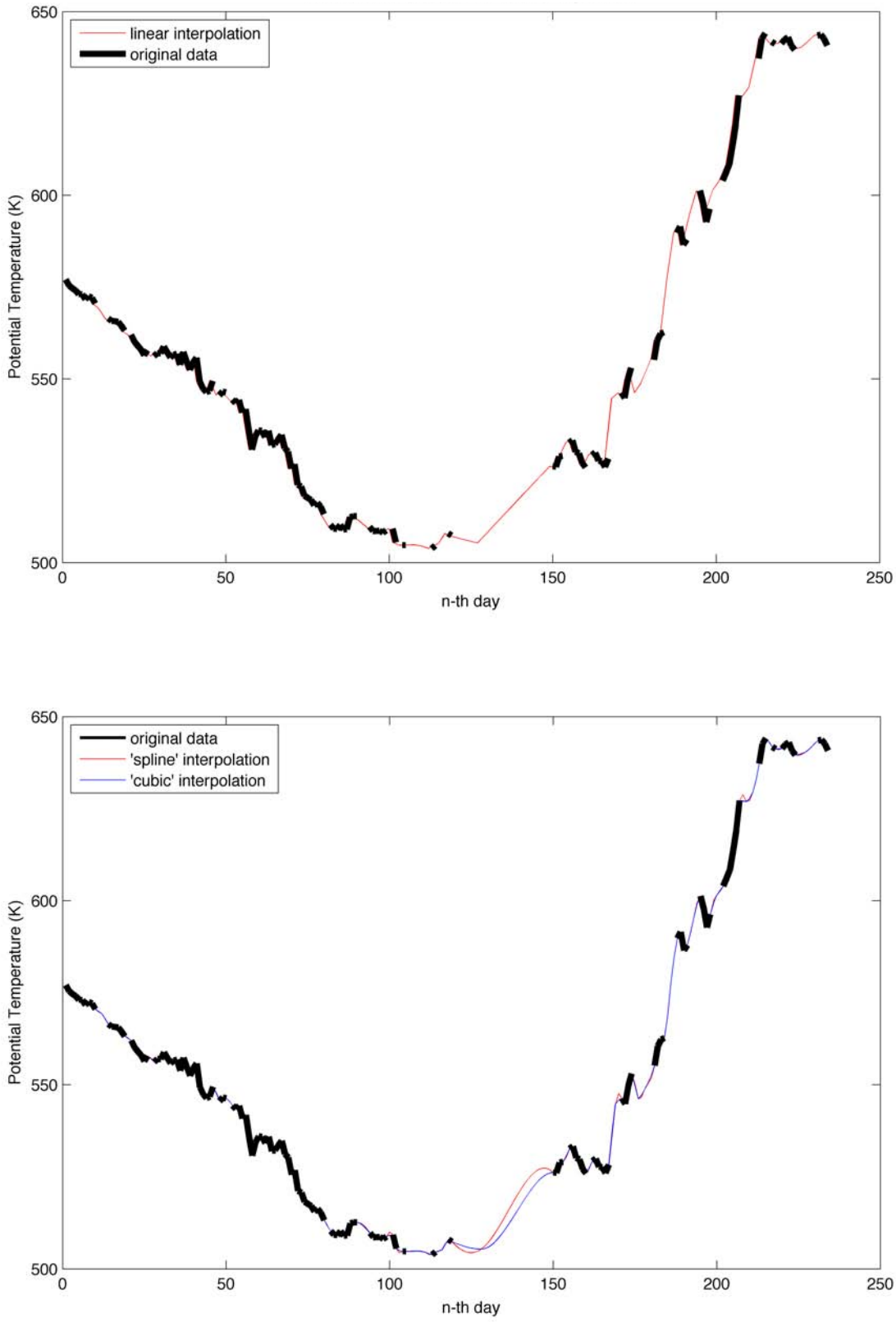

Fig 4.27. Linear interpolation [top] on the temperature data on a random day. Spline and Cubic interpolations [bottom] on that same data.

Figure 4.27 [top] shows how a linear interpolation works on the temperature data on a random day, level 19, in 2005. Figure 4.27 [bottom] shows how a cubic and a spline interpolation work on the same day and under the same pressure conditions.

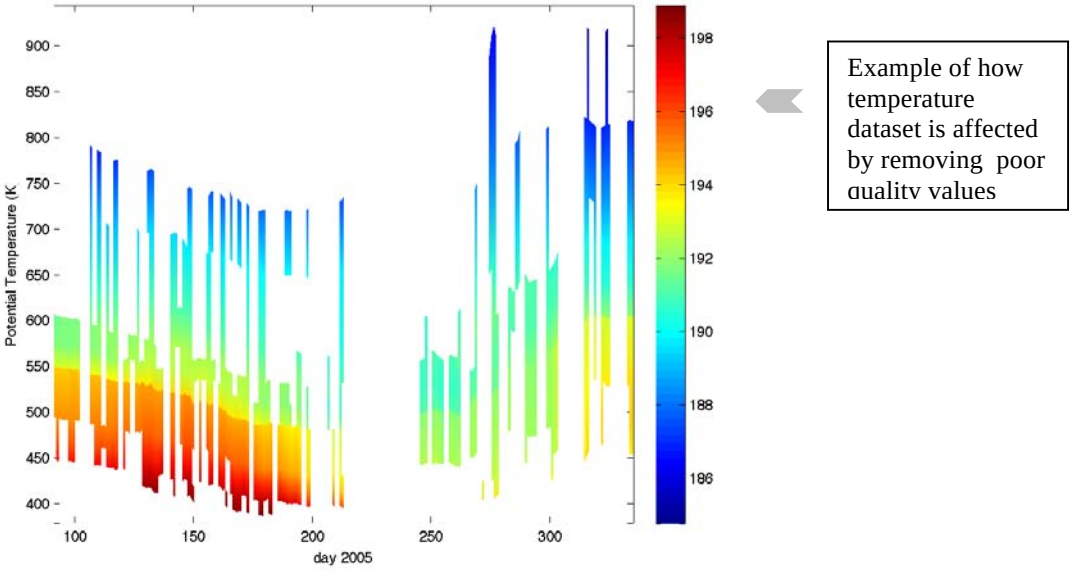

Fig 4.28. An example of how temperature dataset is affected by removing the 'bad' values.

T_{NAT} calculated from EOS MLS v2.2 H_2O and HNO_3 values

T_{NAT} was calculated using *Hanson and Mauersberger* [1988]'s algorithm for different pressures and H_2O and HNO_3 concentrations in ppmv and ppbv units, respectively, directly from the EOS MLS v2.2 dataset, for calculation of PSC area below this threshold. Results are shown in Figure 4.29.

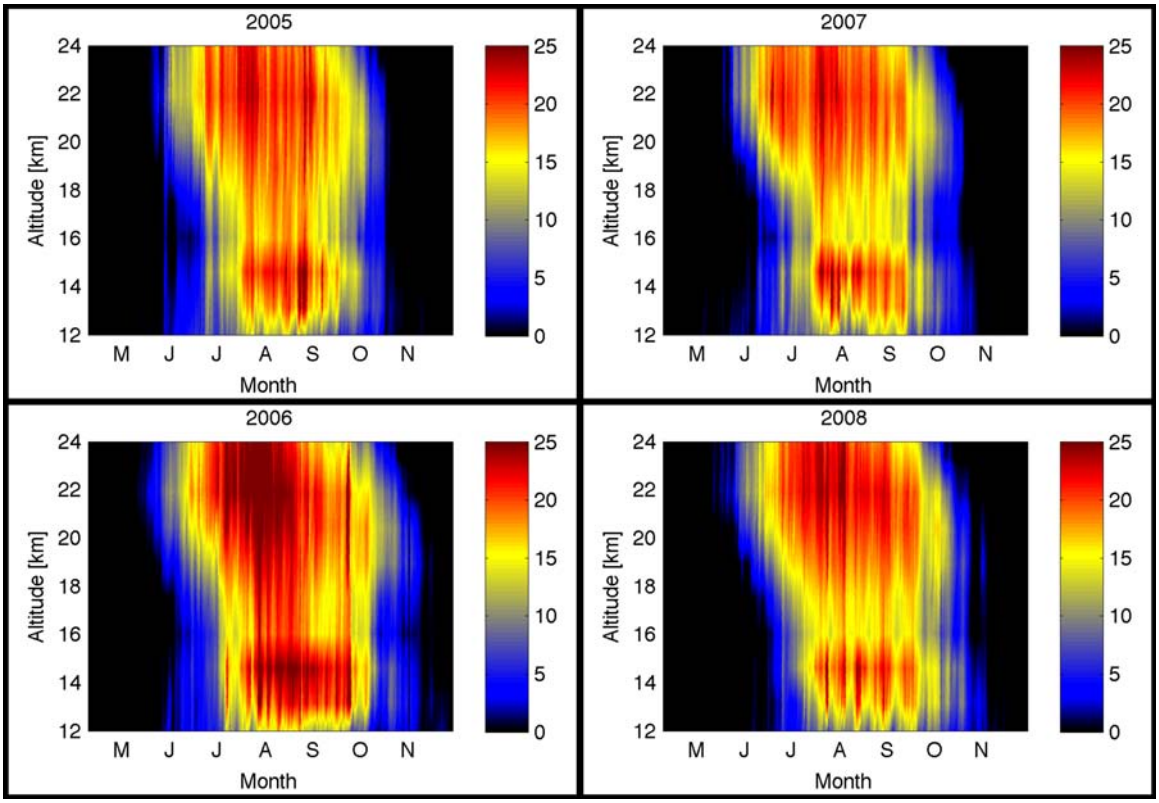

Figure 4.29. Inferred Type I PSC area [millions of km^2] from EOS MLS v2.2 over APVR for 2005 to 2008 and altitude range of 12-24 km. T_{NAT} threshold is derived from the dataset using *Hanson and Mauersberger* [1988] formulation, where HNO_3 mixing ratio was set at 100 hPa and the H_2O concentration as a function of pressure and time. The mean T_{NAT} value was found to be 196.5 K over that period of time and altitudes.

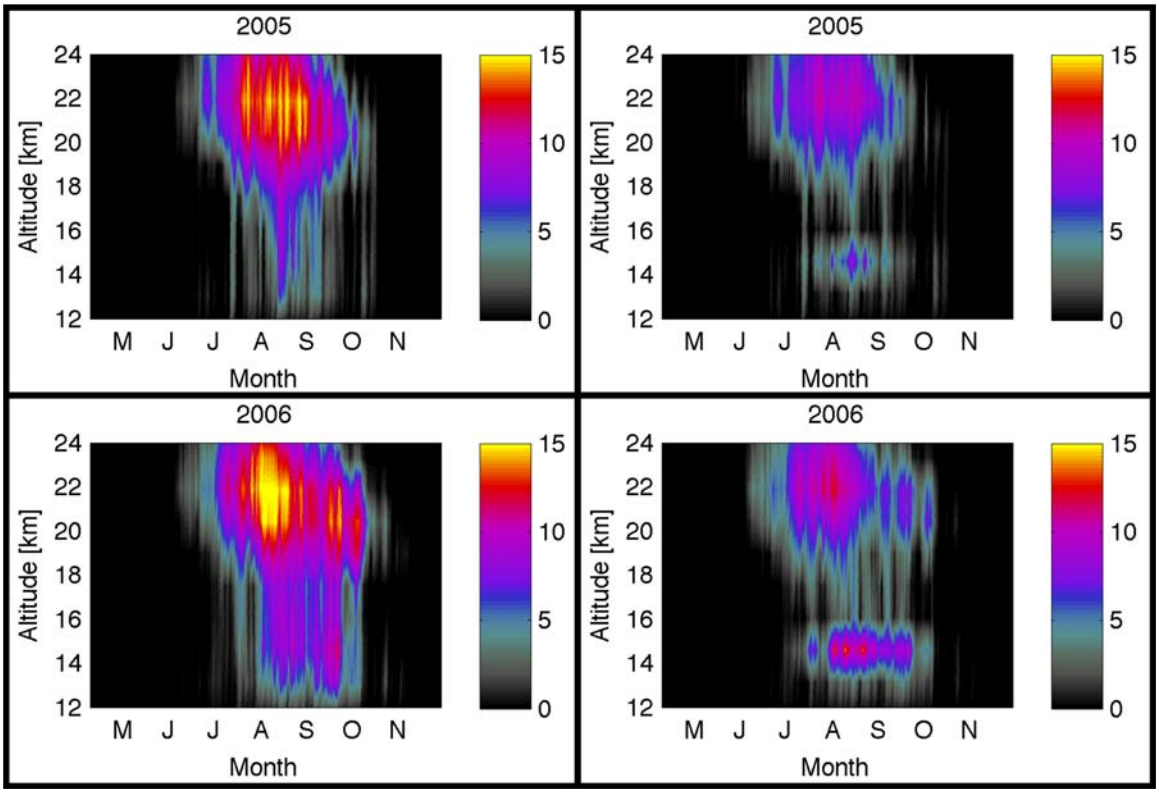

Figure 4.30. Type II PSC area [millions of km^2] from EOS MLS v2.2 over APVR in 2005-06 and altitude range of 12-24 km. In the left column, we show results for T_{ICE} threshold derived from a constant value of H_2O concentration and on the right side, those from T_{ICE} threshold derived from H_2O measured daily by EOS MLS data.

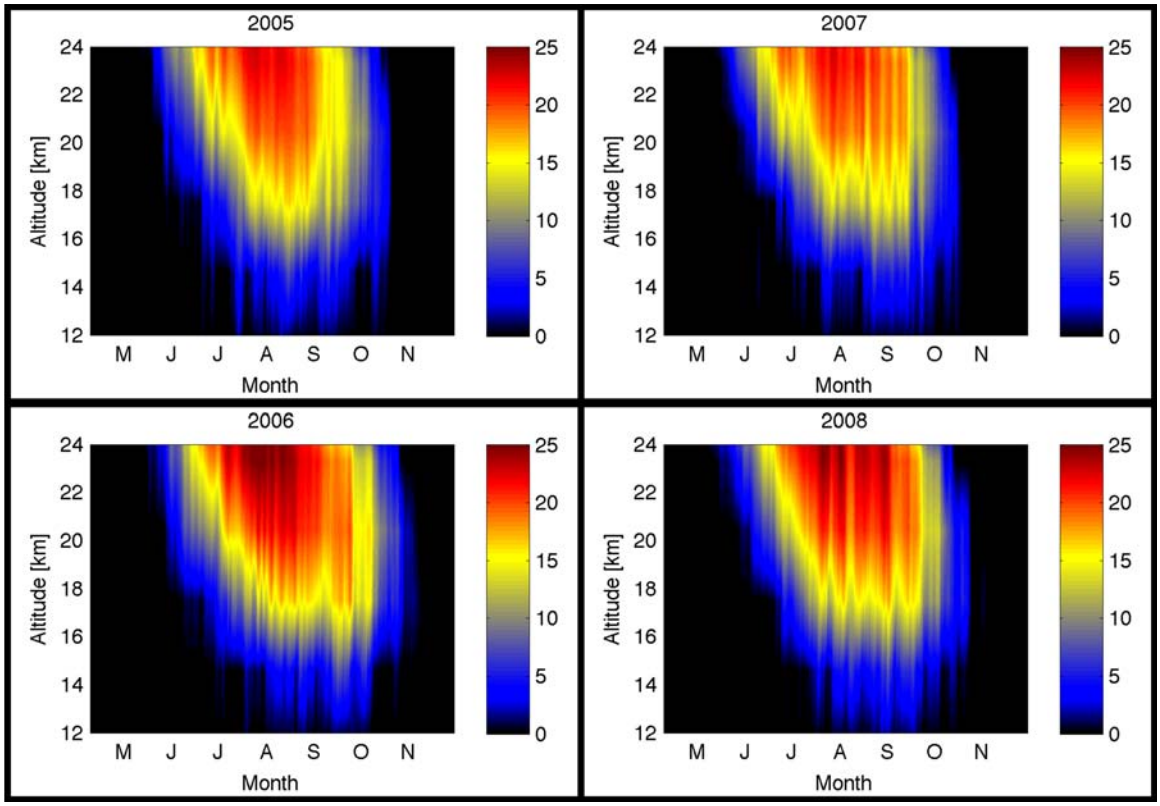

Figure 4.31. Type I PSC area [millions of km^2] from NCEP/NCAR analyses over APVR for 2005 to 2008, and altitude range of 12–24 km with T_{NAT} threshold set constant at 195 K.

Comparison of Aura MLS Type I PSC-induced areas and NCEP/NCAR areas (see Figures 4.29 and 4.31) suggests that at some altitudes, the Type I PSC area derived using these independent datasets is overestimated at higher altitudes by NCEP/NCAR and underestimated at lower altitudes.

However, good agreement overall using EOS MLS dataset compared to NCEP/NCAR (see Figure 4.32) was found.

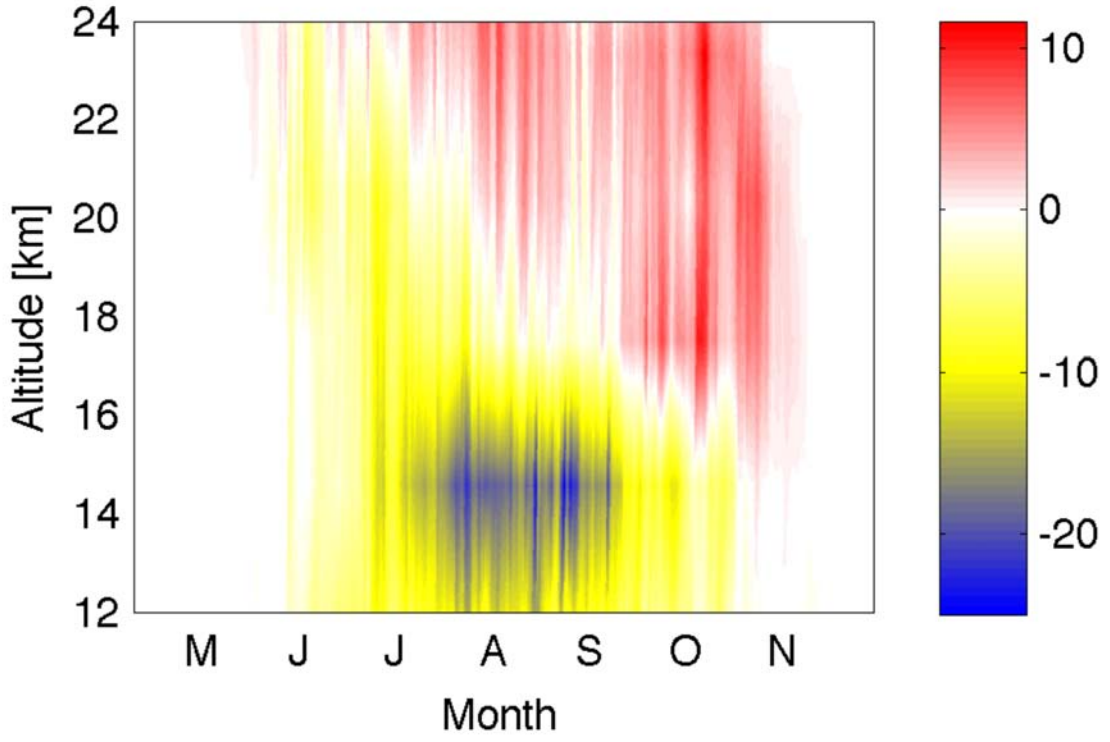

Figure 4.32. Difference in Type I PSC area [millions of km^2] over APV region between NCEP/NCAR reanalysis and EOS MLS dataset observations in 2006, over different altitudes.

PSC area and chlorine activation: Part I

Further analysis on this topic will be presented in the next chapters. Here it is presented a group of five plots aim to show all PSC, Temperature, ClO, and HCl changes in the same picture (see Figures 4.33–4.37).

Three different NAT PSC Temperature thresholds were chosen (197.5 K, 195 K and 192.5 K) for NAT PSC surface area calculation. As in some studies 195 K is usually a first start; for that matter we chose 2.5 K greater than 195 K and 2.5 K lower than this 195 K threshold too. (Note that 197.5 K corresponds to NAT temperature derived from *Hanson and Mauersberger* [1988]'s formulation using 3 ppmv and 10 ppbv water vapour and nitric acid concentrations,

respectively at 100 hPa (~17 km). In red and orange in Figures 4.33 to 4.37 it is shown APVR Average Temperature and Mean HCl vmr (volume mixing ratio) calculated over APVR Latitudinal means. Dots in light green symbolize daytime ClO data points.

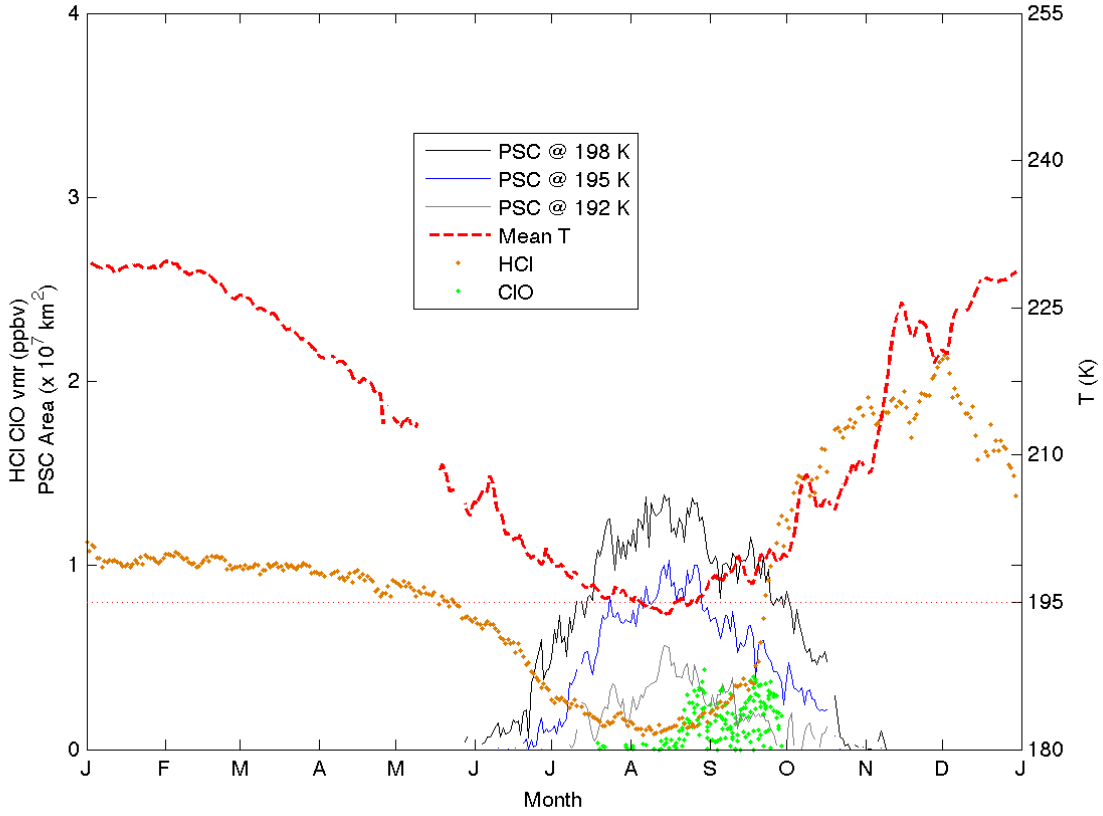

Figure 4.33. Year: 2005 and approximate altitude: 17 km.

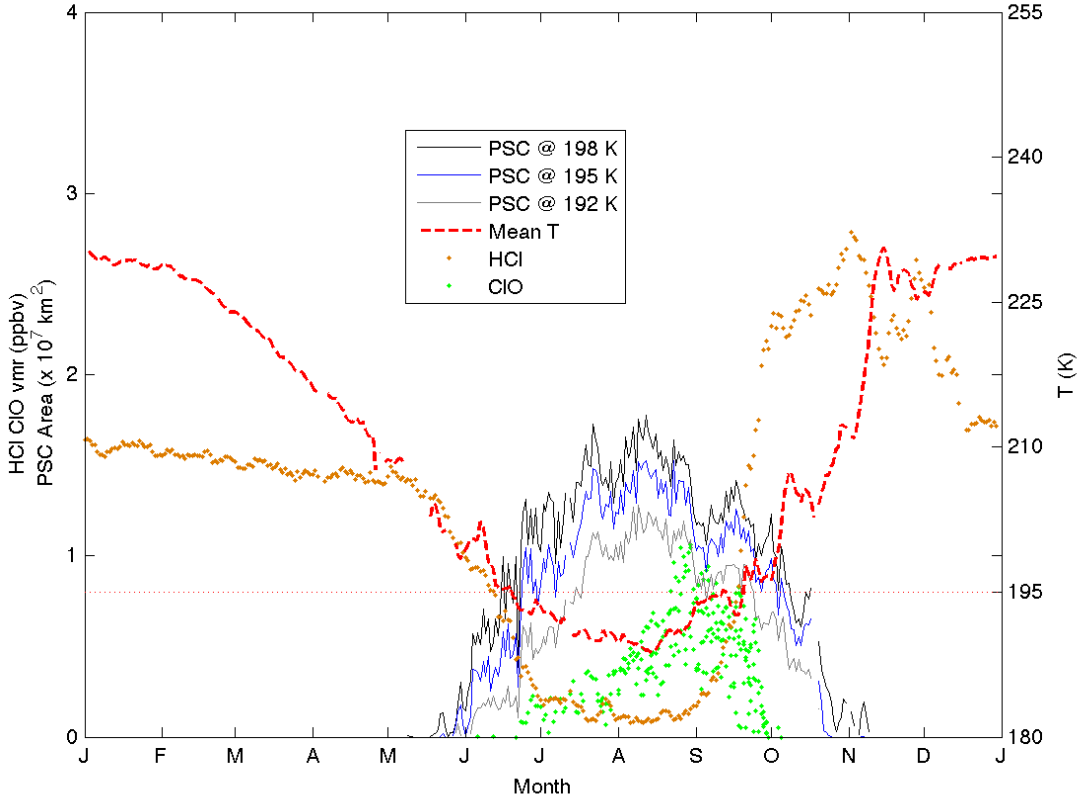

Figure 4.34. Year: 2005 and approximate altitude: 20 km.

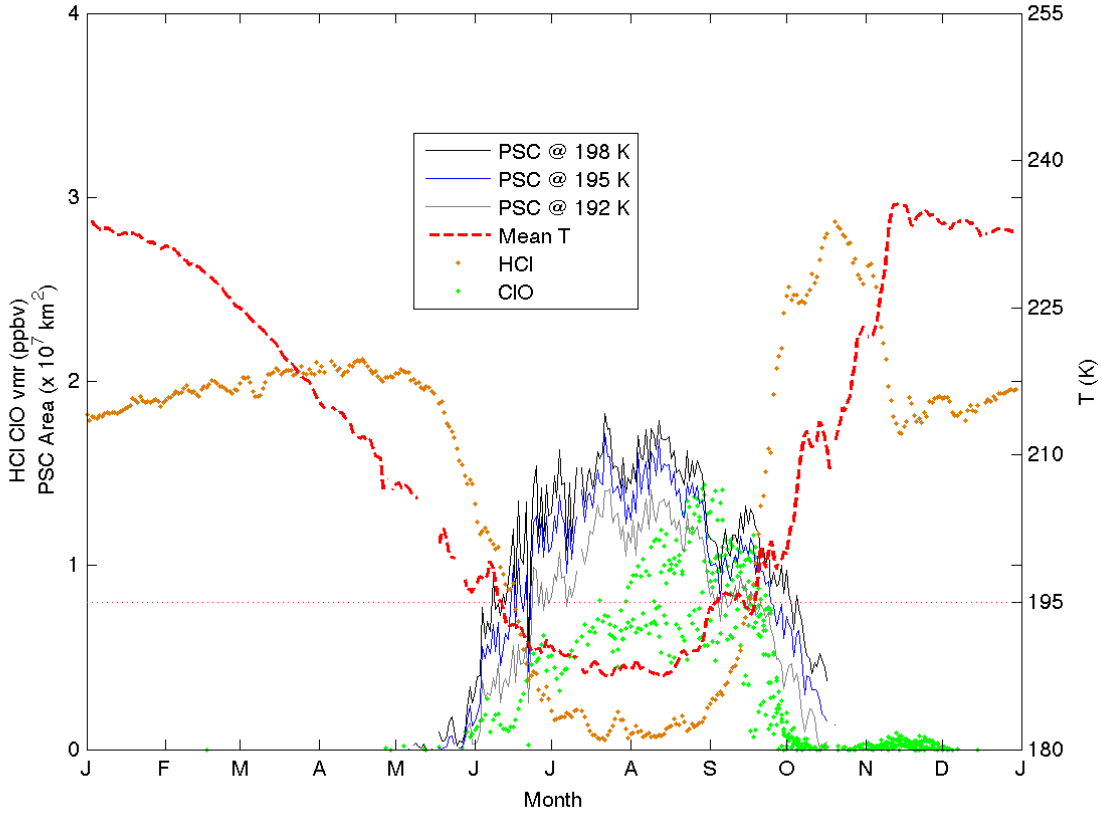

Figure 4.35. Year: 2005 and approximate altitude: 23 km.

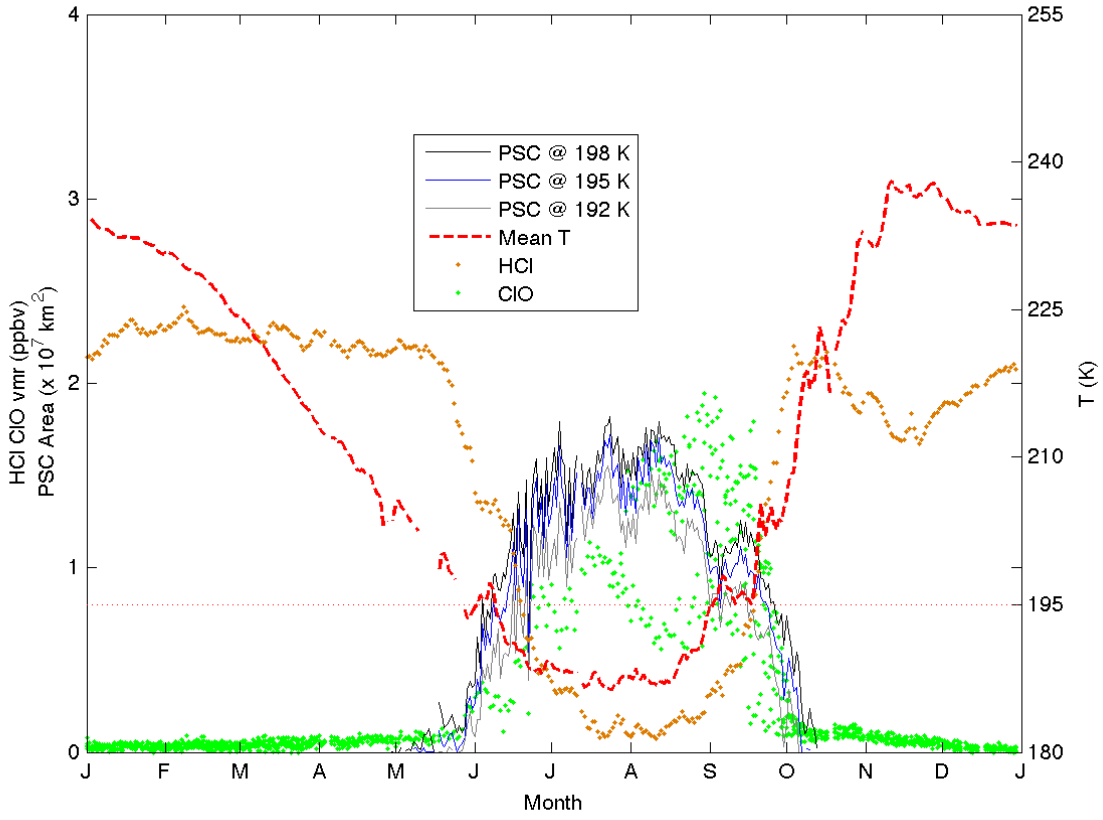

Figure 4.36. Year: 2005 and approximate altitude: 26 km.

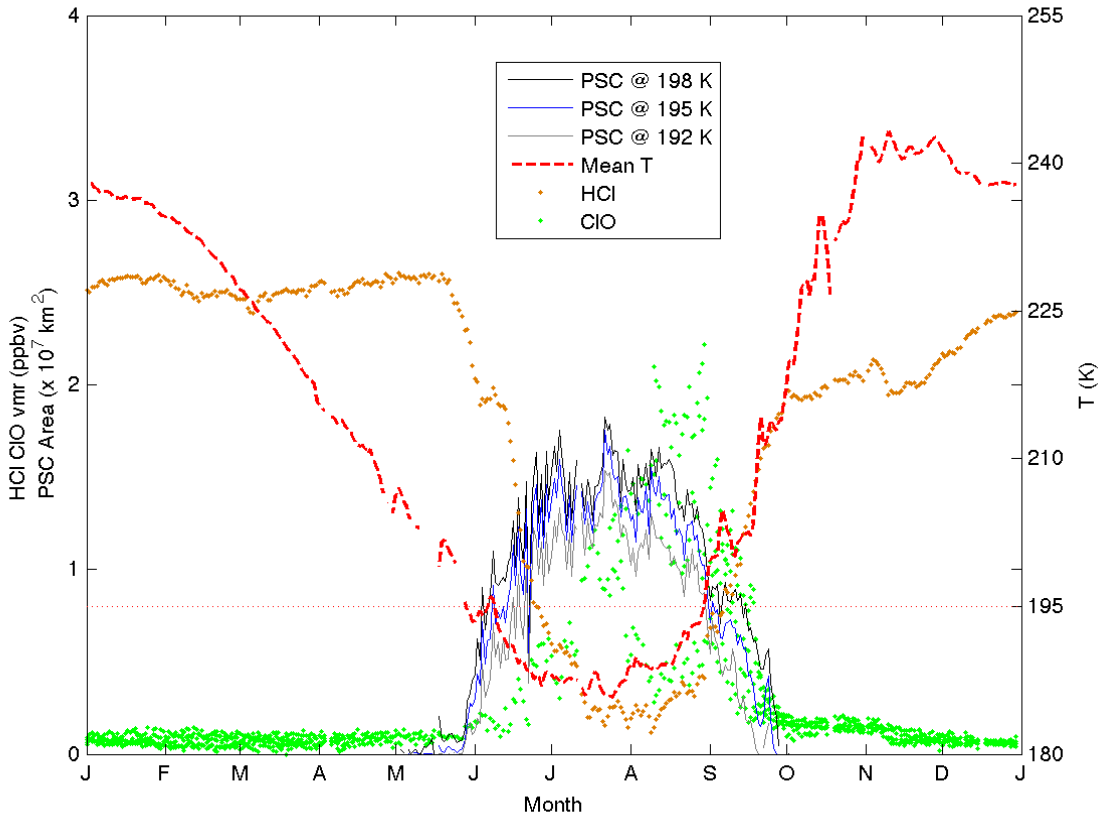

Figure 4.37. Year: 2005 and approximate altitude: 29 km.

Figure 4.33 to 4.37: Temporal evolution of Type Ia and Type Ib PSC area [x10^7 km^2] and changes in chlorine partitioning [ppbv] over the Antarctic Polar Vortex region (APVR) derived from MLS measurements in 2005 at ~17-29 km is displayed.

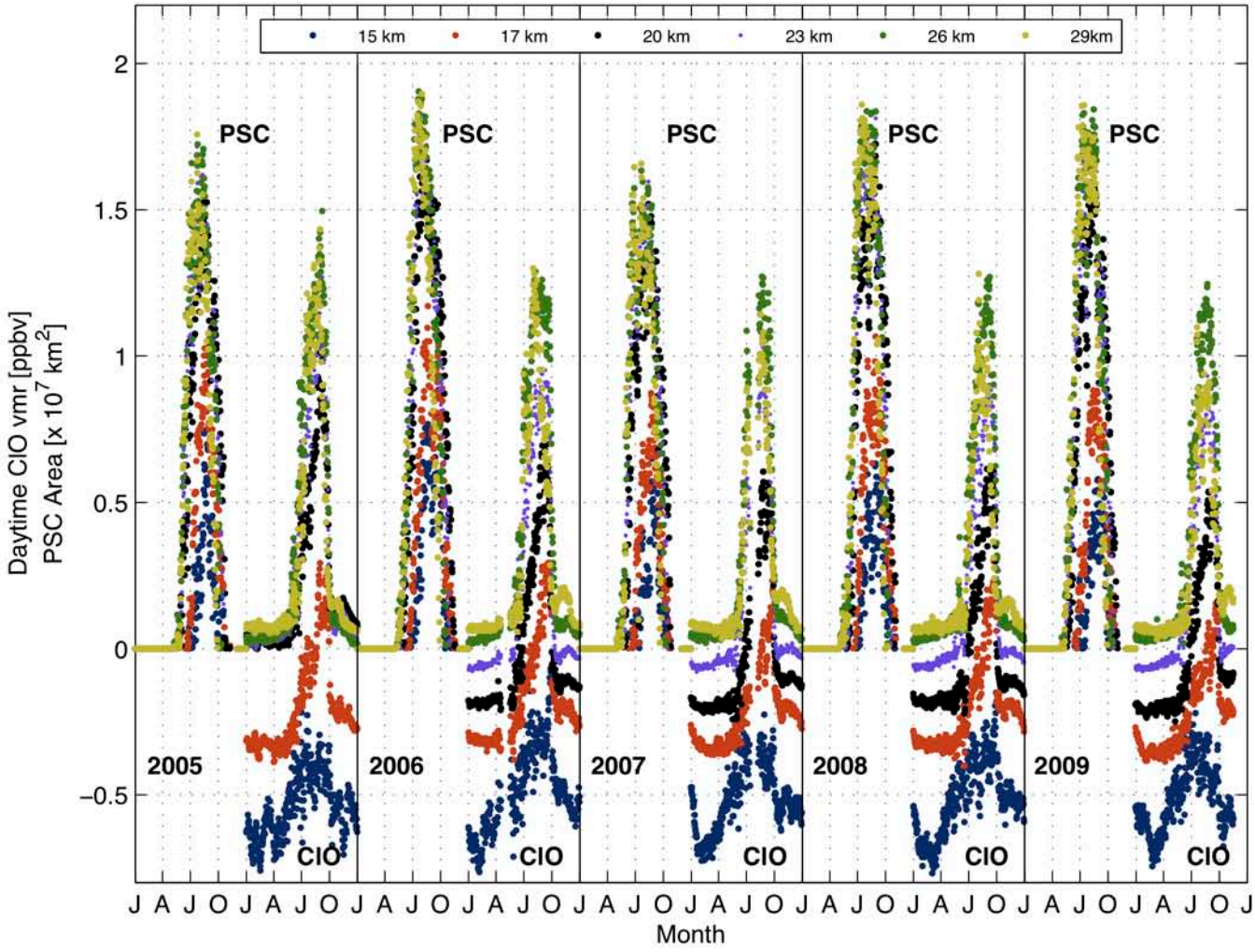

Figure 4.38. Timeseries of Type I PSC area at 195 K inferred from MLS temperatures and uncorrected daytime ClO data at six different stratospheric altitudes in 2005-2009.

Chapter 5

PSC Modeling and Algorithm Development II: Validation

5.1 PSC algorithm development (inclusion).

As defined in the previous chapter, PSC areas were chosen to be derived using Delaunay triangulation of temperature observations below PSC formation thresholds. Delaunay triangulation [available from The MathWorks, Inc., (http://www.mathworks.com/); *Barber et al.*, 1996] derives a set of lines connecting each data point to its natural neighbour (see Figure 5.1) and then it is applied the convex hull algorithm in order to determine the area of spherical sections employing spherical trigonometry. The total PSC area $A_{PSC_{Total}}$ in this region is defined as follows:

$$A_{PSC_{Total}} = \sum_{i=1}^{m} A_{PSC_{bin_i}} \qquad (5.1.1)$$

where $A_{PSC_{bin_i}}$ is the total *PSC area* in each geographic *bin* computed as follows:

$$A_{PSC_{bin}} = \left\{ \left(\sum_{j=1}^{n} A_{SpT_j} \right), \forall \left[SpT \right] \ni \overline{T} < T_{NAT} \right\} \qquad (5.1.2)$$

where A_{SpT} is the area of the j^{th}-spherical triangle, denoted as [*SpT*], which is enclosed by the m^{th}-bin. $\overline{T}$ symbolizes the average temperature obtained from the

temperature data vertices of each [*SpT*] under investigation. The symbols ∀ and ∋ indicate, respectively, “for all” and “such that”.

Areas were computed in 20º x 20º geographic bins spanning Antarctica between 60ºS and 80ºS (adapted from *Alexander et al.*’s, [2011], grid definition). The reader should note that the grid was defined in order to bin a larger number of satellite data points that would not be captured utilizing a smaller bin-sized grid (not shown) for triangulation. If the grid definition looks coarse to some readers, the definition was used for the calculation of PSC and for HCl-depletion areas. Therefore, every area result is based on the same grid, and efficient data triangulation is guaranteed for every data set and for all of the areas in exactly the same grid using different data. Using this definition, the global percent error of the PSC algorithm was 0.5% [*The World Factbook*, 2010]. The chemical study did not use a potential vorticity (PV) or an equivalent latitude (EqL) to bin the data, since during a collaborative analysis [*Alexander et al.*, 2011] it was revealed that analyzing the data relative to the vortex edge provided no advantage to the standard co-ordinate system as a result of non-constant dynamics. In addition, *Manney et al.* [2007] suggested that using EqL or PV as a vortex-centered coordinate did not alleviate all of the sampling problems, including those in studies using “vortex averages”, and in analyses of localized features (such as polar stratospheric clouds) and other fields that did not correlate well with PV. A future part of the present study will introduce Derived Meteorological Products (DMPs) for a comprehensive dynamics analysis.

The derivation of geographically binned PSC areas was used by *Pitts et al*. [2007, 2009] for CALIPSO observations of PSCs. Therefore, this methodology allowed a comparison of the order of the values obtained in this work with previous studies. One of the differences in *Pitts et al.*’s [2007, 2009] algorithms was a change of bin sizes

using stereographic coordinates, thus PSC algorithms may be sensitive to the grid definition. A comparison of the PSC area data for 2006, shown here, with the work of *Pitts et al.* [2007, 2009] shows values on the order of those reported by *Pitts et al.* [2009] (see Figure 5.2 for PSC-induced areas derived from NCEP/NCAR 2.5º assimilations as per Scheme 3 in the present study) in five Antarctic PSC seasons in the climatological region between 60ºS and 80ºS. Inclusion of the region poleward of 80ºS revealed that approximately 90% of the total NAT area was then measured (not shown).

5.1.1 Monte Carlo Simulation

Uncertainties in the inferred PSC area were derived from Aura MLS temperature errors using a Monte Carlo algorithm that produced 1e+2, 1e+3, and 1e+4 iterations of the temperature field, with randomly selected uncertainties for each selected measurement point. Only the 1e+2 iteration analysis is shown here due to the rank of CPU intensive simulations. In addition, selecting a larger number of iterations did not dramatically improve the results (not shown). The total PSC area and the variance information were then derived from the resulting distribution.

5.2 PSC temperature threshold integration

Three different schemes for examining NAT cloud formation threshold temperatures were defined. In the first scheme, NAT cloud areas were inferred from MLS temperature observations below a T_{NAT} threshold set at 195 K and specified on a latitude-longitude grid. When using the formulation of *Hanson and Mauersberger* [1988], the value corresponds to an unperturbed stratosphere at 50 mbar. Since 195 K

also corresponds to a value that has been defined as a threshold input for chlorine activation in chemistry-climate models (CCMs) [e. g. *Shindell et al*., 1998; *Austin et al*., 2003], and since other studies such as *Toohey et al* [1993], *Webster et al* [1993], and *Lowe and MacKenzie* [2008] have identified that the onset of chlorine activation occurred at ~195 K, the main aim of choosing a 195K threshold for Scheme 1 was to compare HCl depleted areas with inferred PSC areas (using 195 K at different levels) in order to corroborate findings.

The second scheme involved a computation of the mean T_{NAT} specified on a geographic latitude-longitude grid via the formula of *Hanson and Mauersberger* [1988], and the calculated PSC surface areas from Aura MLS standard temperature observations. The resulting T_{NAT} values inherited the one-day temporal resolution feature of MLS data and varied conformably as a function of location, pressure level, water vapor (H_2O), and nitric acid (HNO_3) abundance in the bin of the grid. Scheme 2 used Aura MLS pressure-dependent H_2O and HNO_3 VMRs. The species abundance was averaged over each 20º wide longitude bin, defined within the region from [60ºS–80ºS]. As a result, for one of the selected days and at one specified pressure level, eighteen T_{NAT} values were evaluated respective to the bin in the Antarctic grid as defined in this study. The changing and the exclusive value of 195 K, as defined in Scheme 1 for actual T_{NAT}, was performed with a diagnostic in order to compare what the models may be doing relative to chlorine activation.

Regarding the models, *Morgenstern et al.* [2009] reported that for their CCM (the UK Chemistry and Aerosols model in the stratosphere (Strat-UKCA)) the formula of *Hanson and Mauersberger* [1988] was used to define the formation of PSCs, as part of the stratospheric chemistry description of heterogeneous chlorine-activating processes on PSCs used for assessing the ozone hole. Generally speaking, *Morgenstern* [2011]

suggested that the present generation of chemistry-climate models do not typically have a hard-wired chlorine activation temperature. Rather, PSCs are formed when HNO_3 is saturated over NAT, and when H_2O is saturated over ice [*Hanson and Mauersberger* 1988]. Thus, the inclusion of a second scheme that evaluated T_{NAT} directly from relevant standard satellite measurements was of interest for roughly modelling what actual CCMs do when using T_{NAT} as a threshold for chlorine activation.

In the third scheme, PSC areas were derived from NCEP/NCAR temperatures, while keeping T_{NAT} constant at 195 K in order to compare NAT cloud coverage inferred from both MLS and NCEP/NCAR datasets. The work presented here focused on the calculation of the maximum possible area of induced PSCs, and corresponds to NAT PSCs ($T_{NAT} > T_{STS} > T_{ice}$), despite the fact that *Carslaw et al.* [1998] suggested that Type II PSC particles can provide ~100 times more surface area than liquid aerosols since ice-clouds require very low stratospheric temperatures in order to form. However, temperatures below ~188 K are generally not observed synoptically in early winter.

Figure 5.3 shows the computed average NAT equilibrium temperature frequency in Antarctica using *Hanson and Mauersberger's* [1988] formulation from the initial period of PSC formation [*Höpfner et al.*, 2006] until mid-winter in the Southern Hemisphere polar stratosphere at 46 hPa (~23 km). For five years, as per the second scheme, both Aura MLS H_2O and Aura MLS HNO_3 data were zonally averaged. The average T_{NAT} values obtained are shown in Figure 5.3 and are in agreement with those provided by *Lowe and MacKenzie* [2008] between 192 K and 197 K (see Sect. 4.1); the frequency peak corresponds to a value of ~195 K. By employing the data sets presented in Chapter 2, the local analysis validated the use of 195 K as one of the temperature thresholds for PSC-induced computations.

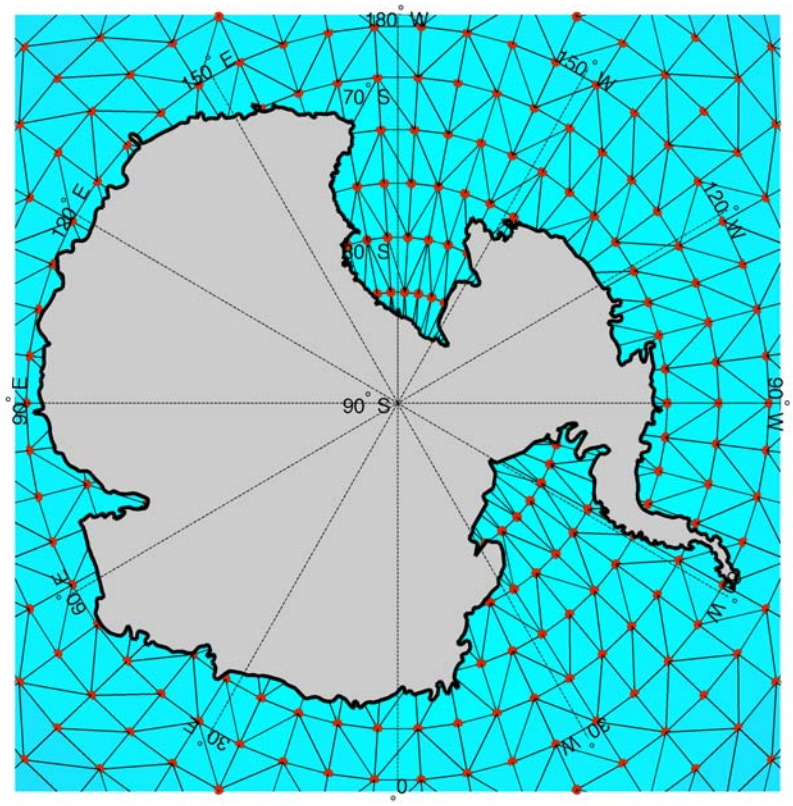

Figure 5.1. Triangulated mesh of data points (red filled dots) in a random day in Antarctica.

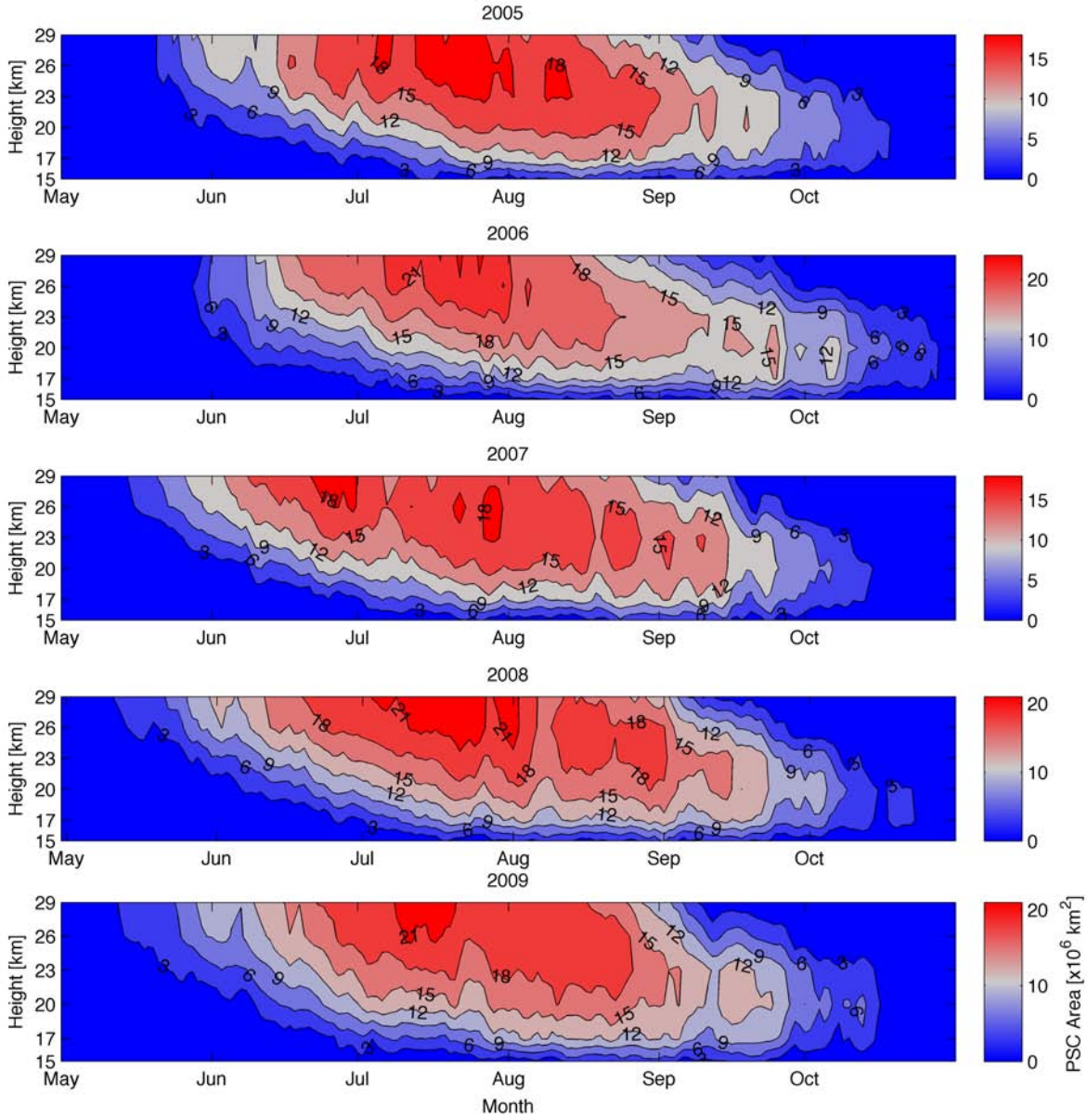

Figure 5.2. PSC-induced areas as a function of altitude (km) and time (e.g. *Pitts et al.*, [2009]) for the 2005-2009 Antarctic seasons using the algorithm developed, and employing Scheme 3 described in Sections 5.1 and 5.2, respectively.

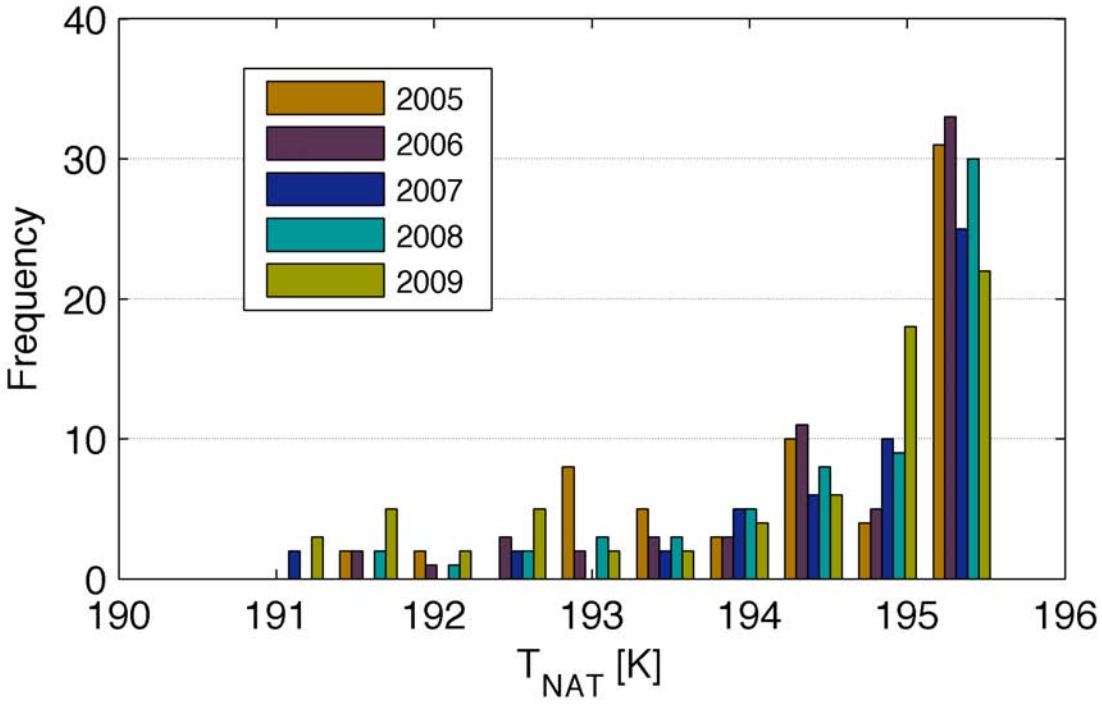

Figure 5.3. 2-D histogram of zonal mean NAT saturation calculated temperatures at the 46 hPa pressure surface (~23 km) from 1 May to 1 August in the Antarctic polar region [60ºS–80º], as per Scheme 2 (see Section 5.2) from 2005 to 2009 in the Southern Hemisphere polar middle stratosphere.

Chapter 6

Polar stratospheric chlorine-chemistry - Primary study case: Antarctica

6.1. Chlorine Activation via surface reactions

PSC formation leads to chlorine activation in Antarctica via heterogeneous reactions on the surface of PSC particles [*Solomon et al*., 1986]. As indicated in Equation 1.1.1, the key reaction involves two main chlorine reservoirs in the stratosphere: HCl + $ClONO_2$ → Cl_2 + HNO_3. Based on experimental results, the reaction shown in Equation 1.1.1 occurs quite efficiently on ice surfaces at stratospheric concentrations of $ClONO_2$ and HCl. However, depending on the thermodynamic state of the surface, the reaction is also effective on NAT surfaces [*Abbatt and Molina*, 1992]. The reaction can also occur on frozen sulfate aerosols at temperatures below 200 K [*Zhang et al.*, 1994], but is significantly more readily observed during periods of enhanced volcanic sulfate loading as reported by, for example, *Cox et al*. [1994], *Zhang et al*. [1994], and *Webster et al*. [1998, 2000]; although *Bonne et al*. [2000] and more recently *Harris et al.* [2010] suggest that cold background aerosol activation in the stratosphere may also impact the seasonal evolution of polar chlorine partitioning. Previously, *Portmann et al.* [1996] had reported the role of background aerosol in polar ozone depletion.

Based on model results, *Drdla and Müller* [2010] defined a parameterization of the threshold temperature for chlorine activation (T_{ACL}), and ultimately ozone loss in the polar stratosphere that depended on the water vapor atmospheric concentration, the surface area, the densities of liquid sulfate aerosol, and the altitude. The model-based

study presented in that study reports that, under different conditions, the onset of chlorine activation does not occur at T_{NAT} or 195 K.

Using ERA Interim reanalyses data, *Harris et al.* [2010] reported that the correlation of ozone loss and PSC areas deduced from NAT existence in the Arctic improved with altitude. At lower altitude levels (400 K), when cold aerosol activation is assumed in the place of NAT the relationship is more compact.

Employing satellite-based and reanalysis observations, the reaction shown in Eq. 1.1.1, as well as how the reaction explicitly links changes in chlorine partitioning to PSC aerosol formation, is the focus of the work presented.

For this thesis, measurements of hydrogen chloride (HCl), as retrieved by the Aura Microwave Limb Sounder (MLS) instrument, were the main focus since HCl plays an important role in the reaction shown in Equation 1.1.1. Previous studies have shown that HCl and $ClONO_2$ reservoirs make up more than 95% of inorganic chlorine (Cl_y = HCl + $ClONO_2$ + HOCl + Cl_x) in the Antarctic lower stratosphere before the onset of chlorine activation, whereas reactive chlorine species (Cl_x = ClO + Cl_2 + 2 Cl_2O_2 + OClO) represent the predominant forms inside the activated vortex [*Wilmouth et al.*, 2006]. Based on aircraft measurements, *Jaeglé et al*. [1997] suggested that 60-75% of Cl_y was HCl at the beginning of Antarctic winter, while *Michelsen et al*. [1999] suggested that nearly 80% of Cl_y was HCl at the beginning of Antarctic winter. *Santee et al*. [2008b] also indicated that HCl made up the majority of the total chlorine in the polar stratosphere, and existing evidence supports the supposition that HCl is the principal reservoir of inert chlorine in the middle and upper stratosphere (e.g. *Morgenstern et al.*, [2009]). Therefore, HCl plays an important role in ozone depletion.

The fraction of HCl/Cl_y is altitude dependent and, therefore, variations in the abundance of HCl provide a useful proxy for chlorine partitioning in the stratosphere. In particular, the roles of NAT particle formation namely, [7]T_{NAT} and sulfate aerosol, aka [8]T_{ACL}, in chlorine activation in the Antarctic winter 2006 season were quantified. The Antarctic winter 2006 season was chosen as the focus since PSC formation was particularly extensive, as observed by CALIOP and pointed out by *Pitts et al.* [2009], and since 2006 was a particularly interesting year, with a record-breaking ozone hole. Therefore, peculiar conditions for PSC formation and ozone depletion in the Antarctic stratosphere were observed in 2006 and offered a good scenario for concurrently analyzing HCl depletion.

6.2 The HCl depression algorithm and the HCl threshold definition (ΔHCl)

A new chemical algorithm adapted from that described in section 5.1 was implemented in modelling areas depleted of HCl over Antarctica. A HCl-depletion threshold (ΔHCl) was defined by computing the mean and the standard deviation of the pressure-dependent HCl concentrations over the 3-month period from 30 Jan to 1 May, 2005-2009, at different altitudes over the Antarctic stratosphere. As discussed in Sect. 2, the period was selected because it occurred well before the period for which temperatures were cold enough for PSC formation. The procedure is a valid criterion for steady-state HCl loading measured at each pressure level before the onset of the chlorine activation and deactivation periods [e.g. *Douglass et al.*, 1995; *Michelsen et al.*, 1999].

[7] $T_{NAT} \equiv f(H_2O_{[ppmv]}, HNO_{3[ppbv]}, \text{pressure})$ [*Hanson and Mauersberger*, 1988].

[8] $T_{ACL} \equiv f(H_2O_{[ppmv]}, SA_{[\mu m^2 cm^{-3}]}, \text{pressure})$ [*Drdla and Müller*, 2010].

In order to examine the sensitivity of the derived HCl depletion area to the HCl threshold, three different HCl threshold-attained areas were utilized. The areas were compared with PSC modelled-areas obtained from the algorithm, as described in the previous section. Calculation of HCl depleted areas allowed the identification of chlorine activation areas. The characterization of the HCl-depletion threshold is presented in Equation 6.2.1, as follows:

$$\Delta HX(n) = \mu - 2n\sigma \text{ for } n = 2,3,4 \qquad (6.2.1)$$

where ΔHX is the HCl-depletion threshold, μ is the mean HCl nominal value derived from MLS HCl measurements, *n* is the number of standard deviations (σ), and, for this case, HX represents HCl. Using this approach, Threshold 1 ΔHX(2) is the least conservative threshold with results four standard deviations below the nominal mean value being identified as a HCl depleted region. The most conservative HCl-depletion threshold is ΔHX(4).

In Figure 6.1, the seasonal evolution of the ratio of HCl/Cl_y is outlined. Here, the reader should note that the Cl_y was derived from climatologically averaged HCl and daytime ClO species (SZA < 92º), measured from Aura MLS satellite observations in 2006 at an approximate 23 km altitude over the geographic region from 60ºS–80ºS, inclusive. The simple relationship obtained from available chemical satellite data in this work presented a clear picture that partitioning between chlorine species could be approximately characterized by these two species in Antarctica, and only in Antarctica. The timings of chlorine activation in late May and in deactivation in early September were also identified. Figure 6.1 also shows near constant HCl nominal conditions before the onset of chlorine activation, and clearly demonstrates the expected negative

correlation between chlorine reservoir HCl and ClO. The data also shows HCl at peak production by mid-October-November during 2006.

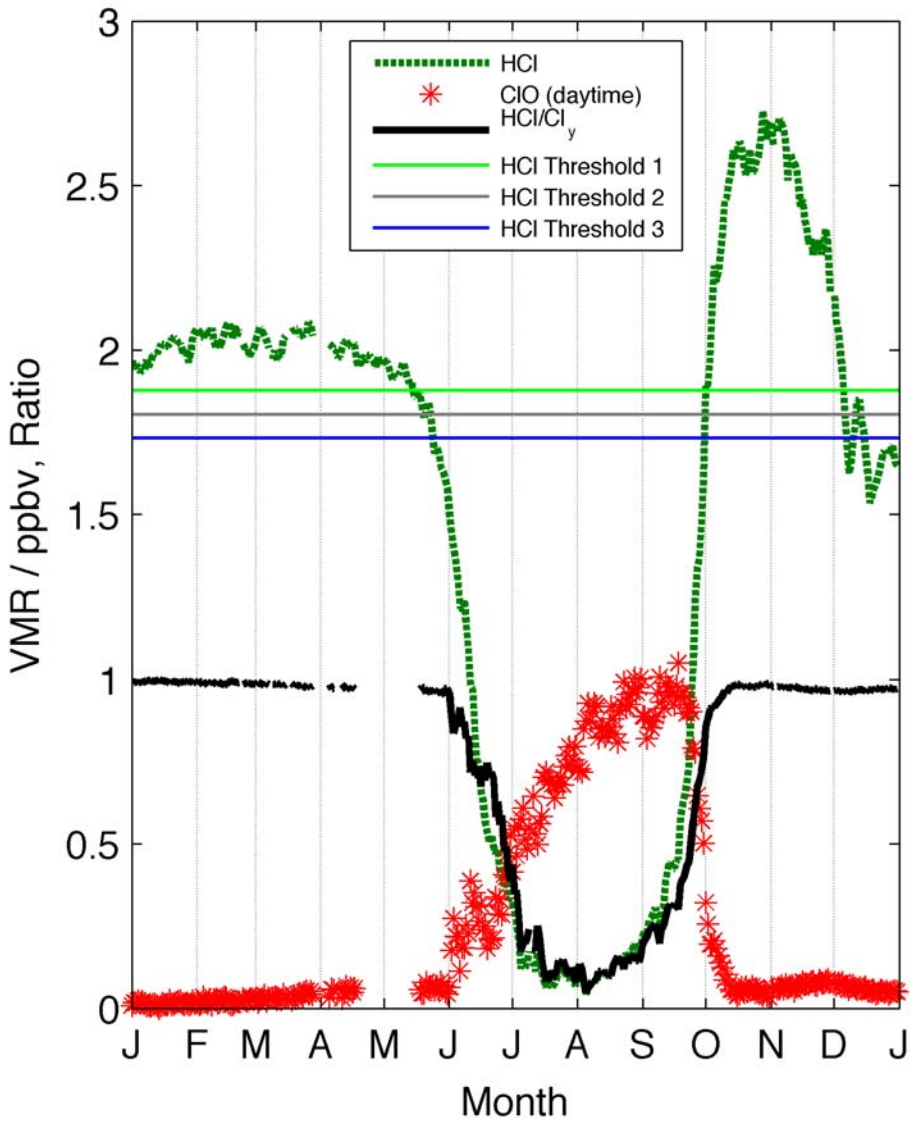

Figure 6.1. The seasonal evolution of HCl/Cl_y roughly estimated from available MLS HCl and ClO in 2006 at 46 hPa. The three horizontal lines identify the HCl depletion thresholds defined in this work. The HCl is higher during November than during January because HCl undergoes a recovery phase in depleted O_3. As ozone abundance falls below a critical value, 0.5 ppmv, [*Douglass et al.*, 1995], the net production of HCl is dominant, since the reaction Cl + CH_4 takes place rapidly [*Crutzen et al.*, 1992;

Prather and Jaffe, 1990; *Mickley et al.*, 1997; *Michelsen et al.*, 1999]. The sudden rise in HCl effectively shuts down chlorine catalytic processes that deplete ozone.

The computed HCl-depletion thresholds investigated for this pressure level (~46 hPa) are also shown in Figure 6.1. A comparison of the thresholds with HCl mean values indicated that even the least conservative threshold identified the start of HCl depletion, and that the second and third thresholds were more conservative estimates for the start date of HCl depletion in the Antarctic region.

PSCs are observed, each year, during Antarctic winter, and the heterogeneous reaction (Equation 1.1.1), which involves the two main chlorine reservoirs available in the polar stratosphere, likely commences soon after PSC formation [*Molina et al*., 1987; *Tolbert et al*., 1987; *Drdla and Schoeberl*, 2002]. The total area of HCl-depletion measured during early winter when the uptake of HCl is primarily believed to occur in or on PSCs was of particular interest for this study. HCl depletion was observed by the Aura MLS at the 147 hPa surface over the period identified. However, due to the limited quality of MLS HCl data at this pressure level [*Froidevaux et al*., 2008], this data is not discussed.

6.3 The extent of HCl depletion

In Figure 6.2, the mean HCl concentrations during 2006 over two latitude bands, one at higher polar latitudes [75º–80º] and the other at lower polar latitudes [60º–65º], in the Southern Hemisphere are presented. Figure 6.2 also provides the minimum temperatures observed in each latitude band at two selected PSC altitudes (e.g. *Santee et al*., [2005]). The climatological mean synoptic temperature for the Antarctic region [60ºS–80ºS] during 2006 is also provided.

(a)

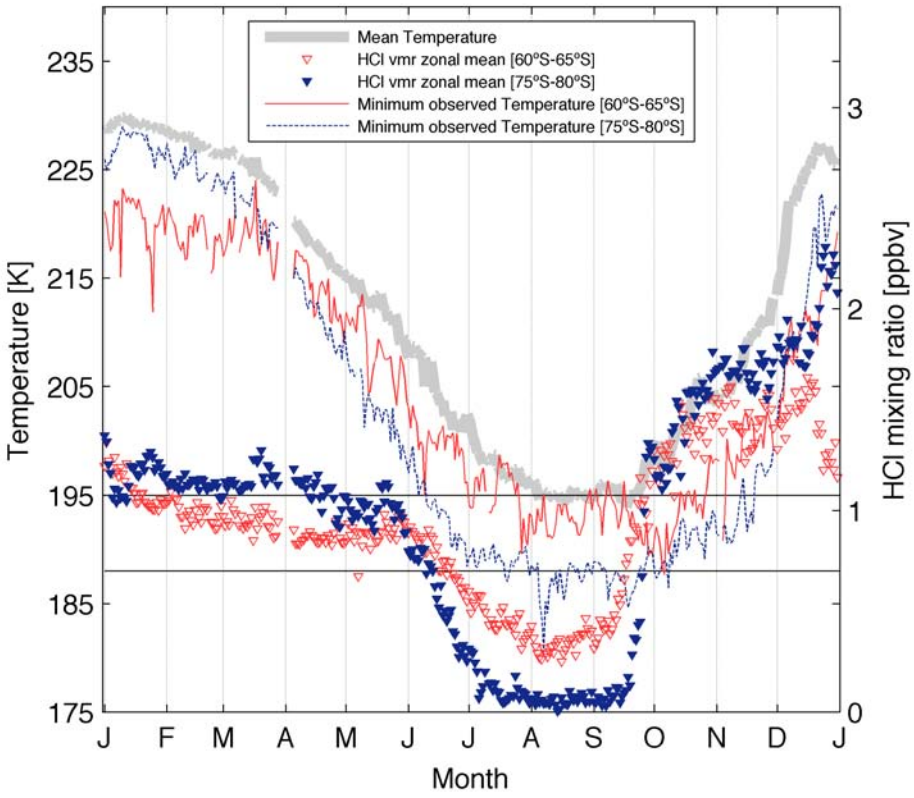
Mean Temperature
HCl vmr zonal mean [60°S-65°S]
HCl vmr zonal mean [75°S-80°S]
Minimum observed Temperature [60°S-65°S]
Minimum observed Temperature [75°S-80°S]
Temperature [K]
HCl mixing ratio [ppbv]
Month
J F M A M J J A S O N D J
175 185 195 205 215 225 235
0 1 2 3

(b)

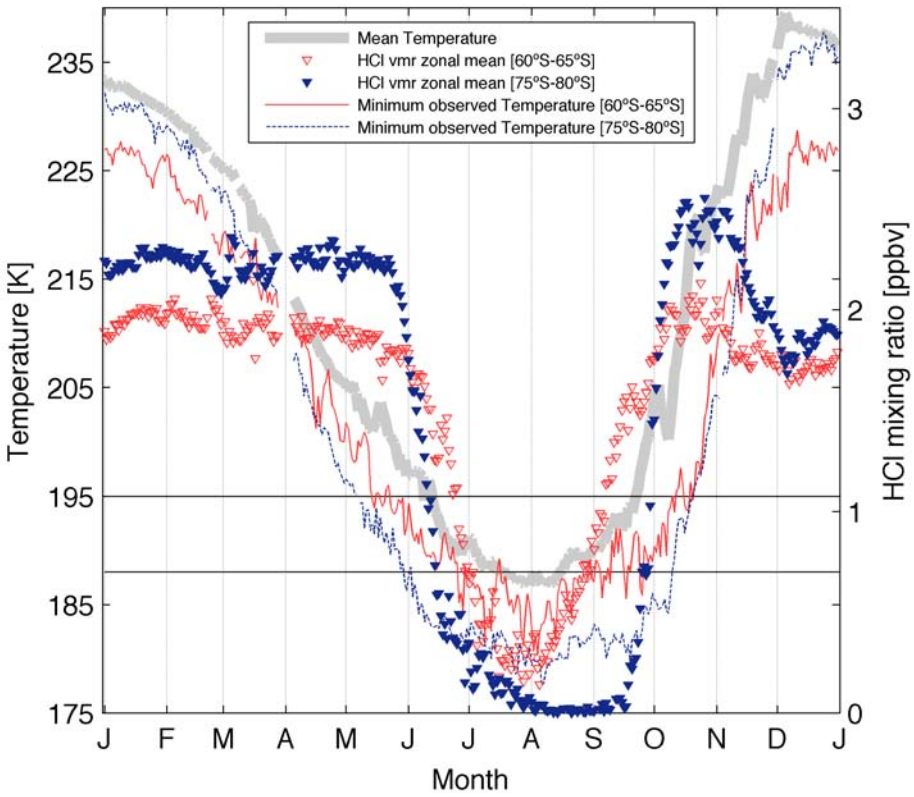
Mean Temperature
HCl vmr zonal mean [60°S-65°S]
HCl vmr zonal mean [75°S-80°S]
Minimum observed Temperature [60°S-65°S]
Minimum observed Temperature [75°S-80°S]
Temperature [K]
HCl mixing ratio [ppbv]
Month
J F M A M J J A S O N D J
175 185 195 205 215 225 235
0 1 2 3

Figure 6.2. Changes in chlorine partitioning (ppbv) and minimum observed temperatures (K) (e.g. *Santee et al*., [2005]) over the Antarctic polar region in 2006 at approximately 17 km (a) and 26 km (b). Daily means were calculated by binning MLS HCl (triangles) data into 5º bands and by averaging [60ºS - 65ºS] (blue) and [75ºS - 80ºS] (red). The daily minimum temperature observed in each latitude band is represented by solid lines from the same color scheme. The thick gray line denotes the APV region-averaged temperature measured daily using Aura MLS data. The black horizontal lines demark T_{NAT} = 195 K and T_{ice} = T_{NAT} – 7 K (e.g. *Nedoluha et al*., [2003]).

Figure 6.2 shows a clear relationship between temperatures below PSC formation threshold values and the onset of decreases in HCl concentration during winter at approximately 17 km (100 hPa) and 26 km (31.6 hPa) (Figures 6.2-a- and 6.2-b-, respectively). At high polar latitudes [75ºS–80ºS], HCl depletion was larger and lasted longer than at lower polar latitudes [60ºS–65ºS], where HCl recovery appeared to begin much faster than at higher latitudes. Figure 6.2 also suggests that HCl depletion began at mean temperatures higher than the PSC formation temperature at the levels shown in Figures 6.2--a and 6.2--b[9]. However, a close examination of Figure 6.2 indicates that a minimum temperature was observed when HCl depletion began to occur in latitude bands that dropped below PSC formation thresholds, within the uncertainties associated with Aura MLS temperature data. Since a comparison of Panel 6a (c) with Panel 6a (a) demonstrates that significantly larger areas of HCl depletion appeared earlier at higher stratospheric altitudes than at the lowest level examined in this study, the likely role of

[9] Using the formulation by *Hanson and Mauersberger* [1988] for T_{NAT}, and assuming constant water vapor and nitric acid mixing ratios of 5 ppmv and 10 ppbv, respectively; the T_{NAT} at the lowest (highest) level shown in Figure 5 is ~199.7 K (~193 K).

cold sulfate [*Portmann et al.*, 1996] in reconciling the temperature vs. HCl depletion issue at different levels is worth examination and may explain why large areas of HCl depletion begin earlier higher up, as compared to lower, in the stratosphere. According to *Portmann et al.* [1996], if frozen aerosols are more important in heterogeneous processing at higher altitudes, whereas liquid aerosols play a more effective role at lower altitudes, then the results provided here for the HCl depletion areas shown in Panel 6a may imply that HCl depletion, through frozen aerosol, is more efficient and massive than liquid aerosol. However, such an assumption can only be determined after the role of aerosol in chlorine activation is assessed at different stratospheric altitudes, and for different conditions. In order to determine this result, the formula of *Drdla and Müller* [2010] which considers the role of aerosol in chlorine activation was applied. The results are provided in Sect. 7.2.1.

6.4 HCl depletion and PSC surface areal coverage

HCl depleted areas over the Antarctic stratosphere are shown in Panel 6a and were derived using the three HCl-depletion thresholds described in Section 6.2 for 2006. Panel 6a also shows the corresponding PSC areas derived at four different altitudes in 2006 from standard Aura MLS observations and from NCEP/NCAR assimilations. Worth noting is that the three different T_{NAT} scenarios, previously described in Section 5.2, were used for the PSC-induced areas shown in Panel 6a. Therefore, they provide an explicit comparison for the two sets of chemical and PSC-induced areas, along with the scenario cases comparison.

(a) ~17 km

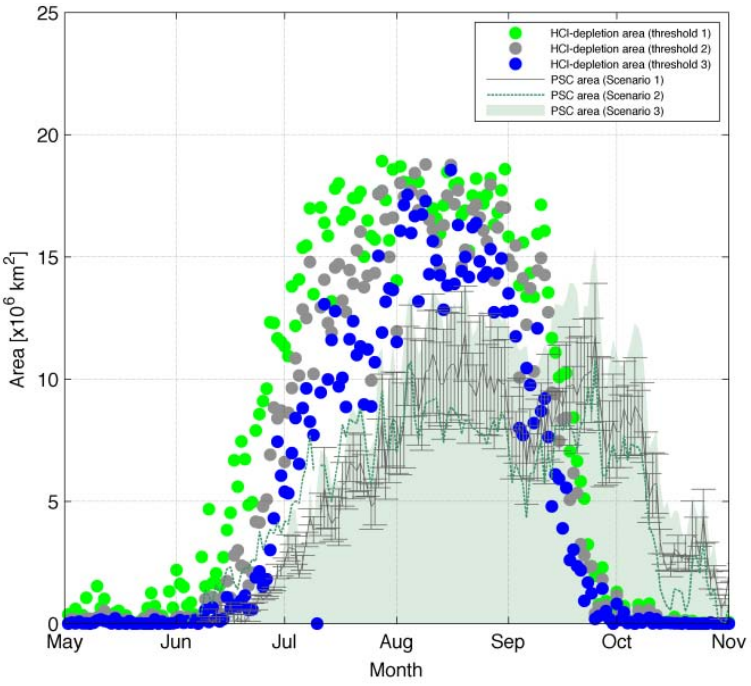
HCl-depletion area (threshold 1)
HCl-depletion area (threshold 2)
HCl-depletion area (threshold 3)
PSC area (Scenario 1)
PSC area (Scenario 2)
PSC area (Scenario 3)
Area [x10^6 km^2]
0
5
10
15
20
25
May
Jun
Jul
Aug
Sep
Oct
Nov
Month

(b) ~20 km

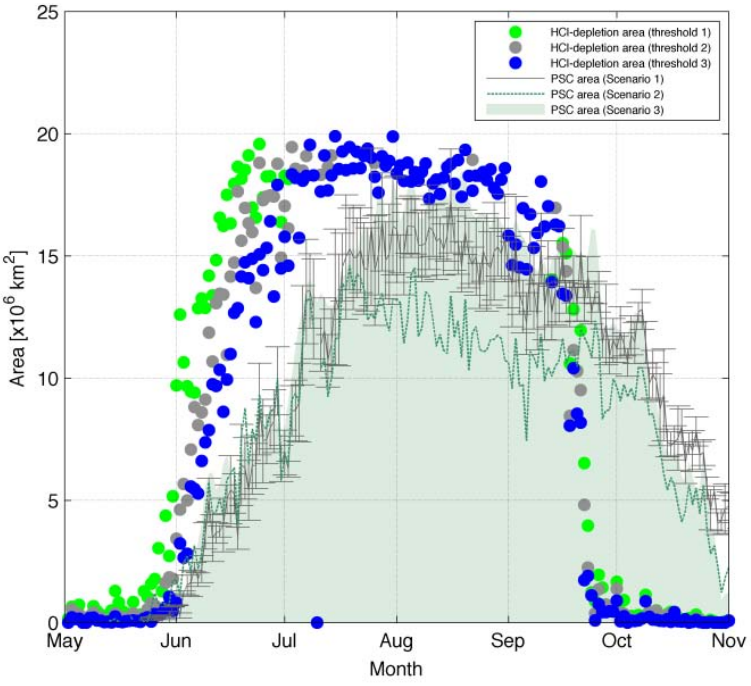
HCl-depletion area (threshold 1)
HCl-depletion area (threshold 2)
HCl-depletion area (threshold 3)
PSC area (Scenario 1)
PSC area (Scenario 2)
PSC area (Scenario 3)
Area [x10^6 km^2]
0
5
10
15
20
25
May
Jun
Jul
Aug
Sep
Oct
Nov
Month

(c) ~23 km

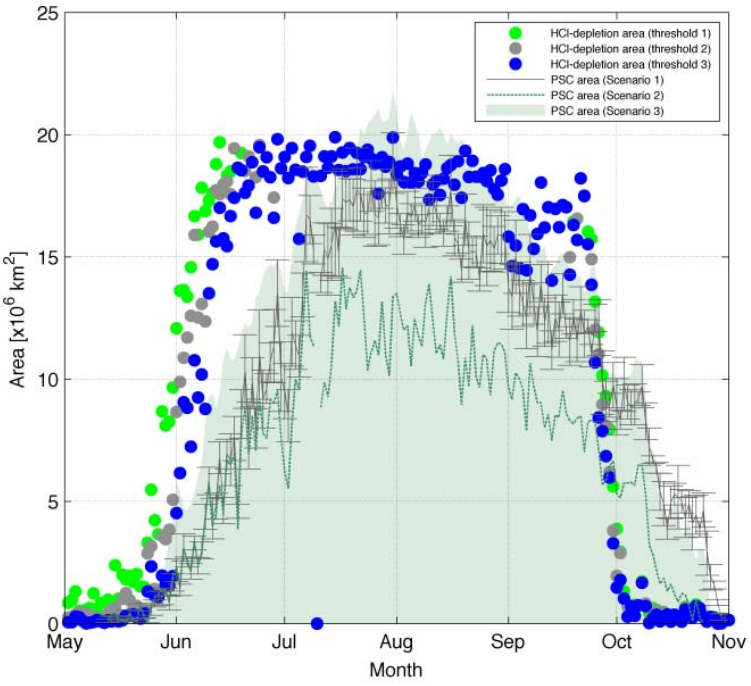

(d) ~26 km

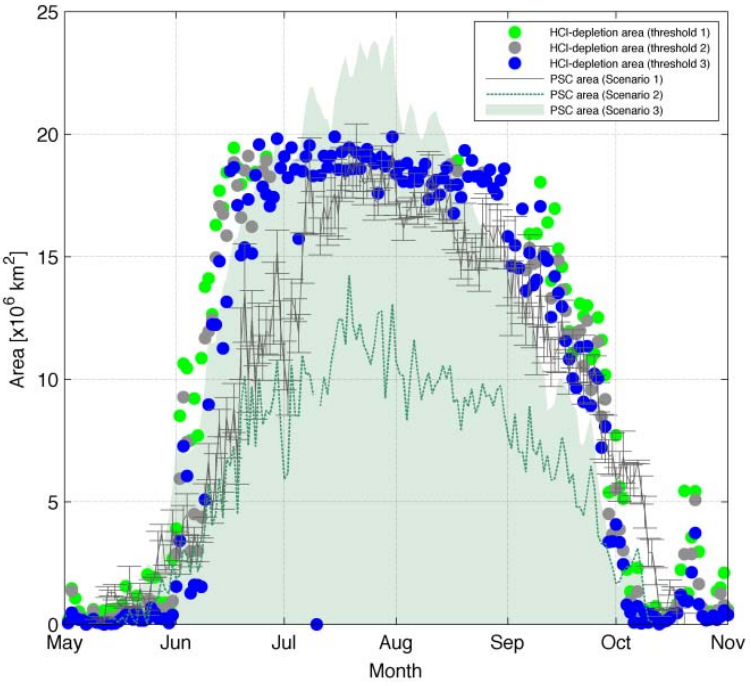

Panel 6a. HCl depleted areas versus PSC inferred areas over the Antarctic region [60ºS - 80ºS] in 2006, at approximately 17 km [a], 20 km [b], 23 km [c], and 26 km [d] for

three different HCl-depletion thresholds and PSC formation temperature threshold scenarios.

A comparison of HCl-depleted areas and the PSC area (derived from temperature data) over the Antarctic region at 100 hPa (~17 km), as shown in Panel 6a, indicates that both PSC and HCl-depleted areas increased in early June (earlier at 46 hPa (~23 km)) and were reduced after September. However, the HCl-depleted area was larger than the area potentially covered by PSC from June to the beginning of September. The finding represents the first time, in the literature, that this discrepancy has been determined for 2006. The increase and the decrease in the HCl-depleted area in June and September, respectively, were more rapid than changes in the inferred PSC area at approximately 17 km, 20 km, and 23 km. The result is independent of the HCl depletion criteria and the method for calculating the PSC formation temperature, even when uncertainties in the measurements were taken into account. Thus, the area for which the distribution of HCl changed is larger than the area associated with PSCs for which chlorine activation could have occurred using T_{NAT} as a threshold. The pattern could be related to parcels of air being depleted of HCl as they pass through fixed areas of PSC [*Cariolle et al*., 1989; *Webster et al*., 1993]. Another possibility, as pointed out by *Portmann et al*. [1996], is a role for sulfate aerosol, since the emergence of Antarctic ozone hole polar ozone depletion is profoundly influenced by liquid sulfate aerosol. In particular, *Hofmann and Oltmans et al*. [1992] and *Portmann et al*. [1996] found that liquid aerosols are relatively more effective in heterogeneous processing at lower altitudes, while frozen aerosols are potentially more effective at higher altitudes.

Panel 6a (b) shows that at approximately 20 km, both PSC and HCl-depletion began to increase in late May and decreased after September. Earlier in June, HCl-depleted areas increased more rapidly than PSC areas, until early July, when HCl-depleted areas were similar to the PSC area. Panel 6a (b) also indicates that HCl depleted areas were considerably larger than the corresponding PSC areas during the early season, even when both patterns began to develop simultaneously in late May. Panel 6a shows a sustained peak in HCl depletion (the maximum of HCl areas shown in this Panel) during the PSC season in Antarctica (May-October), as identified by *Pitts et al*. [2009]. The time when HCl depleted areas began to decrease also represents the period before the onset of the HCl recovery phase. As indicated by *Portmann et al.* [1996] the timing of HCl reformation directly influences the length of ozone loss.

The altitude for which HCl remained depleted for the longest length of time occurred at approximately 46 hPa (~23 km) (for ~3 months). As compared to other levels in the stratosphere, at this level, HCl depletion also began earlier. In an opposite manner, HCl depletion had less duration and began later at the lowest altitude. An inspection of Panel 6a (b, c, and d) shows that for lower pressures HCl depletion began earlier (by mid-June) than for higher pressures (Panel 6a (a)).

Jaeglé et al. [1996, 1997] suggested that the excursion of air parcels to low polar latitudes allowed the formation of NO_x in sunlight conditions. These species combined with ClO^- to form $ClONO_2$ providing an oxidation partner for HCl. Hence, this mechanism allowed a further loss of HCl at lower latitudes. However, an examination of these types of excursions is not presented in this study.

6.4.1 Pearson's r correlation coefficients (PCCs) computation

Table 6.1 displays Pearson correlation coefficients (PCCs) (significant at the 5% level) between the two measurements for the seasonal patterns of PSC and HCl depleted areas, as well as the differences between the two areas based on data spanning the entire PSC season and for an earlier portion of the PSC season (1 June 2006 – 1 August 2006). The data presented in Table 6.1 shows values for all of the combinations of the three possible PSC thresholds used, as well as two of the HCl thresholds (corresponding to the most and the least conservative HCl thresholds used for this study) at each altitude shown in Panel 6a.

Table 6.1. PCCs** and the differences calculated between the HCl depleted area and the PSC area ($A_{HCl\text{-}depleted} - A_{PSC}$). The values reported are based on two HCl thresholds (ΔHCl(n), n = 2,4) and three different PSC formation temperature threshold scenarios (see Sect. 5.2) derived from observed temperatures and MLS chemical data in the Antarctic polar stratosphere.

The first numbers in each box of the table are correlation coefficients spanning the Antarctic full PSC season (1 May – 31 Oct) [*Pitts et al*., 2009], the second (light gray box) represents area differences (x 10^6 km^2) averaged over the full season and the last value (dark gray row) is the area differences (x 10^6 km^2) averaged only during the winter between 1 Jun and 1 Aug in 2006.

Height (approximate)	Type I PSC Area					
	PSC formation temperature threshold (*Hanson & Mauersberger* [1988])					
	Scenario 1 MLS 195 K		Scenario 2 MLS T_{NAT}		Scenario 3 NCEP 195 K	
	HCl Depletion Area					
	HCl-depletion threshold (this thesis' Equation 6.2.1)					
	ΔHCl(2)	ΔHCl(4)	ΔHCl(2)	ΔHCl(4)	ΔHCl(2)	ΔHCl(4)

17 km	0.38	0.56	0.64	0.70	0.58	0.65
	+4.21	+0.73	+4.30	+0.96	+1.73	-1.06
	+8.89	+3.52	+6.34	+1.53	+6.63	+1.93
20 km	0.42	0.61	0.60	0.72	0.65	0.75
	+1.83	+0.42	+3.33	+1.97	+0.86	-0.38
	+8.13	+5.45	+8.37	+5.69	+7.08	+4.40
23 km	0.72	0.81	0.79	0.86	0.85	0.90
	+2.85	+1.89	+6.00	+4.99	+0.64	-0.31
	+7.04	+5.63	+9.58	+8.16	+3.67	+2.25
26 km	0.89	0.92	0.91	0.94	0.94	0.95
	+2.28	+1.20	+6.77	+5.66	0.53	-0.51
	+4.69	+3.16	+8.69	+7.15	-0.75	-2.28

**These correlation coefficients are significant at the 5% level.

The PCCs between the two sets of areas identified in Table 6.1 are higher for higher altitudes. The combination of Scenarios 2 and 3 for PSC thresholds and the most conservative HCl threshold, ΔHCl (n = 4), were generally slightly higher than other permutations. An examination of the HCl-depleted and inferred PSC difference in areas over the entire Antarctic vortex period indicated that large differences between the two areas (determined by summing all of the values of the second row in Table 6.1) were observed at 23 km (16.06×10^6 km^2) and 26 km (15.93×10^6 km^2). Small differences were found at 20 km (8.03×10^6 km^2) and at 17 km (10.87×10^6 km^2). However, the largest contribution to these values at higher altitudes came from Scenario 2 values where T_{NAT} areas, during the winter, were much smaller than 195 K; or were HCl depleted areas, compared to those at lower levels.

The consistently positive values of the area difference that were identified in Table 6.1 correspond to consistently larger HCl depleted areas than the PSC areas, suggesting that the choice of different PSC formation threshold values and HCl depletion are unlikely to explain these differences.

An examination of Table 6.1 also reveals that the differences between PSC and HCl depletion areas are the largest early during the PSC season, suggesting that only small

volumes of PSC's were required to produce the observed chlorine activation early in the season and that this gap in areas gave rise to other factors in addition to PSCs for chlorine activation, as follows: 1) heterogeneous processing via liquid aerosols, and 2) large eddy temperature fluctuations sufficiently cold enough for PSC formation that standard Aura MLS products and NCEP/NCAR assimilations do not consider.

6.5 Other Aura MLS products linked to chlorine activation

In order to examine chlorine activation more thoroughly, Aura MLS chlorine monoxide (ClO) observations were used for investigating the efficiency of chlorine activation in Antarctica and for simultaneously comparing these estimates with the PSC areas inferred from the NCEP/NCAR reanalysis in the Antarctic polar stratosphere between 60ºS and 80ºS from 2005 to 2009.

In Figure 6.3, calculated Type Ia PSC areas for the T_{NAT} threshold that were set constant at 195 K are presented, together with the average daytime ClO concentration (SZA < 92º) in the Antarctic region [60ºS–80ºS]. Figure 6.3 presents regions where ClO was present and that were enclosed by areas where PSCs could form. ClO abundances were observed earlier at high levels (by early June in 2006). Later, the highest concentrations of ClO were also observed at high levels. Additionally, given the formation of the ClO dimer and its well-known role in ozone depletion [*Molina and Molina*, 1987; *Sander et al*., 1989; *Solomon*, 1999; *WMO*, 2006], the period for which ClO remains available in the stratosphere is critical for ozone depletion. Panel 6a shows that the period of time for which HCl was depleted longer (at high levels) corresponded to periods of high ClO values (Figure 6.3, year 2006).

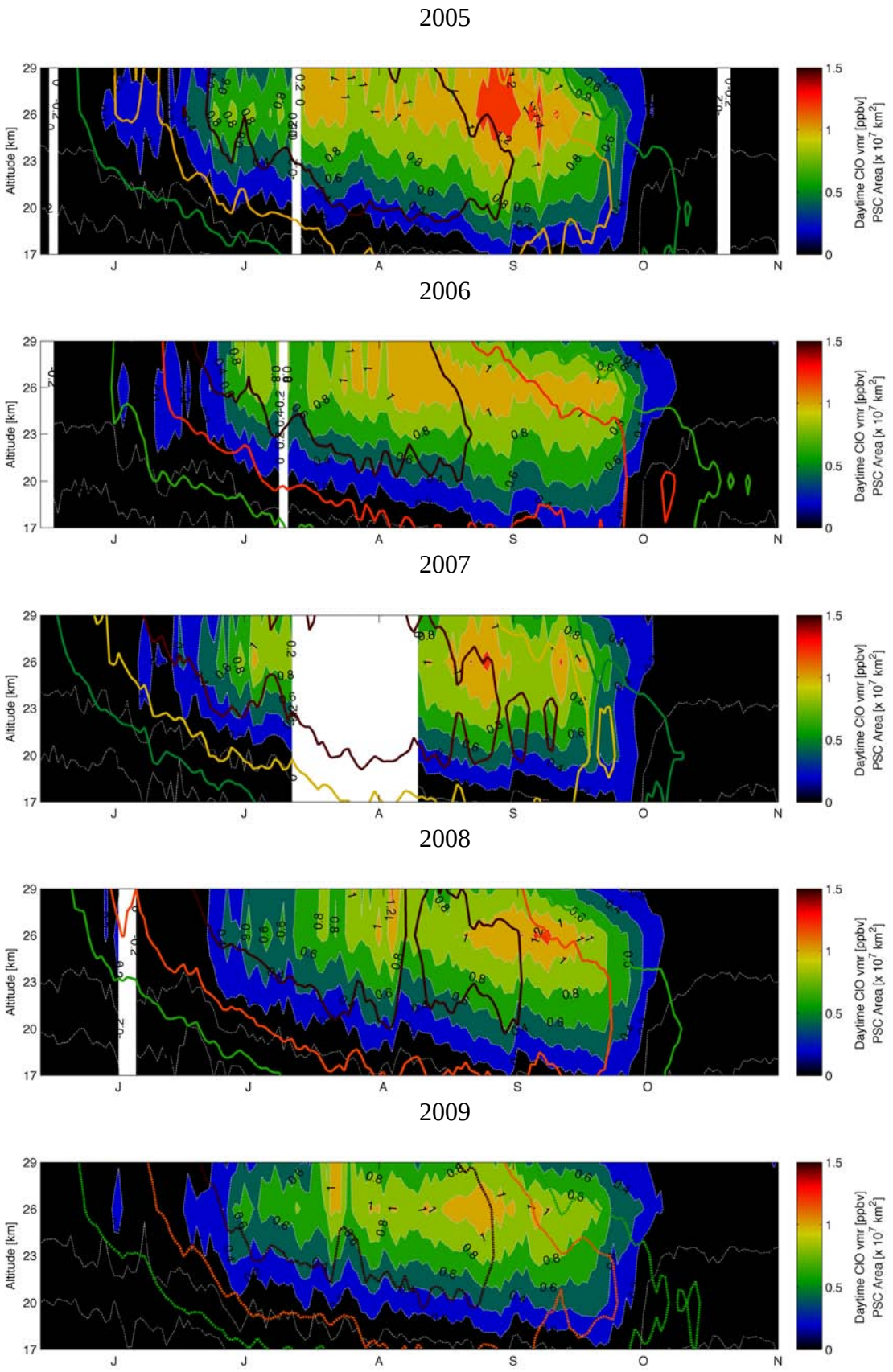

Figure 6.3. The time-height contour plot of the daytime ClO mixing ratio (filled colors) [ppbv]. The PSC area for Type Ia PSCs (dotted contour lines [x 10^7 km^2]), as

inferred from NCEP/NCAR temperatures observed in the APV region over the Southern Hemisphere polar stratosphere in 2006 are also displayed. The color scale depicted for PSC area contour lines [x 10^7 km^2] is the same as per the color scale used for filled contours [ppbv]. For simplicity, each PSC line has been scaled by a factor of $1x10^{-7}$ for representing the PSC area values. The ClO data shown here have not been corrected for their bias. White vertical gaps correspond to missing satellite data.

In order to examine the vertical transport in the stratosphere in 2006, one of the passive tracers of air motion in the stratosphere that the Aura MLS measures (N_2O) was employed. Previous studies such as *Santee et al*. [1996], *Jaeglé et al*. [1997], and more recently *Hayashida and Sugita* [2007] have related Cl_y and N_2O in order to produce estimates of chemical chlorine changes; and for the examination of the likely impact of air motion on chemical transport at different levels in the stratosphere. In the present study, a polynomial fit of N_2O to the inferred Cl_y derived for data from day 1 to day 121, over the altitude range from 17 km to 29 km in 2006 in Antarctica, was calculated, as follows:

$$[Cl_y]\ (ppbv) = -5.6x10^{-7}[N_2O]^3 + 0.00021[N_2O]^2 - 0.037[N_2O] + 5.6 \qquad (6.5.1)$$

where the climatological bulk of the total inorganic chlorine concentration $[Cl_y]$ was calculated using the approximation $Cl_y \approx HCl + ClONO_2$, and was assumed to be distributed as 70% HCl and 30% $ClONO_2$ at the start of the Antarctic winter, an approximation used in the model-based study by *Drdla and Schoeberl* [2002] before the onset of chlorine activation. In equation 6.5.1, $[N_2O]$ represents the N_2O mixing ratio in ppbv. The derivation of Equation 6.5.1 employs a methodology adapted from *Bonne et al*. [2000].

The volume mixing ratio (VMR) of the measured H_2O from the Aura MLS is shown in Figure 6.4, and represents area averaged between the Antarctic region [60ºS–80ºS] in 2006 in the south polar stratosphere.

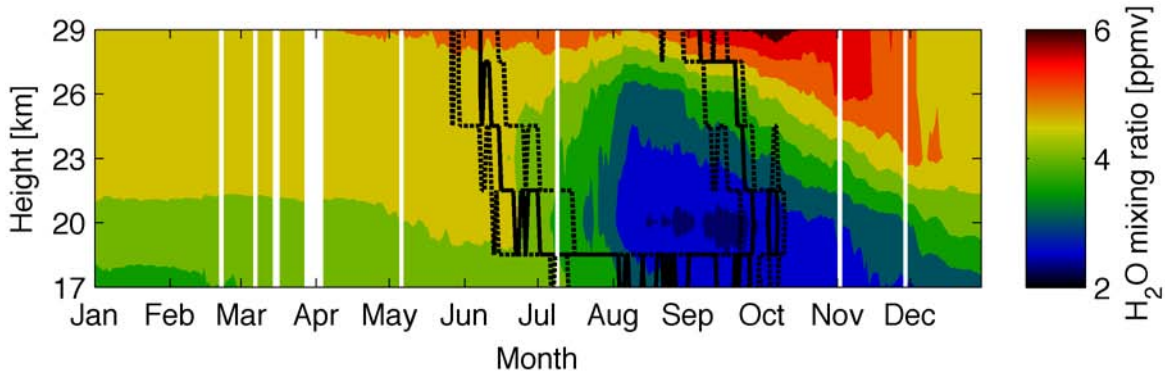

Figure 6.4. The time-height contour plot of H_2O volume mixing ratios derived from Aura MLS species in the Antarctic polar stratosphere in 2006 at different pressure surfaces (altitudes). The full (dotted) black contour lines indicate MLS temperatures below 195 K (± 3 K). White vertical gaps correspond to missing data.

Chapter 7

Temperature vs HCl depletion Issue Reconciliation

7.1 Inter-annual variability

Panel 7a displays year-to-year changes in Aura MLS HCl depletion areas for three HCl depletion thresholds, as well as the Aura MLS and NCEP/NCAR PSC-induced areas for two different threshold schemes (Scheme 2: T_{NAT} and Scheme 3: 195 K) from 2005 to 2009 for four pressure surfaces (see Table 7.1 for equivalent altitude) in the Antarctic lower-middle stratosphere. The diagrams shown in Scenarios 2 and 3 show a poorer correlation of areas at low stratospheric altitudes, whereas correlation coefficients are improved at higher altitudes with respect to 100 hPa (~17 km). Additionally, in the years 2006 and 2008, the correlations slightly dropped, particularly at the lowest level, which may be due to the fact that 2008 and 2006 were two of the coldest years in the Antarctic stratosphere [*Pitts et al.*, 2009], so chlorine activation was due to more PSC formation and to more cooling of liquid aerosols at the lowest levels. For this reason, PSC formation alone in the lower altitudes is not sufficient for explaining the amount of chlorine activation or for showing better correlations during the slightly colder winters of 2006 and 2008 and deserves further analysis.

Table 7.1. The equivalence of pressure level to pressure (in hPa), as per the Aura MLS v2.2 Level 2 dataset for ClO, HCl, O_3, and HNO_3. An estimation of the height values (in km) is provided* for reference.

Aura MLS Pressure Level	Equivalent Pressure (hPa)	Equivalent Height (km)
7	100.00	17.50
8	68.13	20.42
9	46.42	23.33
10	31.62	26.25
11	21.54	29.17

* Assuming a scale height (H) of 7.6 km.

Another explanation is the role of large eddy temperature perturbations not observed using standard MLS or not included in NCEP/NCAR temperature products, during these years, for total chlorine activation through HCl [*Murphy and Ravishankara*, 1994]. Further work on this thesis extracted stratospheric gravity waves from satellite temperature data [e.g. *Wright et al.*, 2010, 2011] in order to quantify their role in chlorine activation. However, no conclusive data was determined.

7.2 The Role of Frozen Aerosol

7.2.1 HCl depletion, T_{NAT}, and T_{ACL}

The formulation of *Drdla and Müller* [2010] was defined using satellite data in order to calculate areas of chlorine activation below the temperature threshold as proposed in this study (T_{ACL}) and previously used in model-based studies, such as the *Tilmes et al.*

[2007] and *SPARC CCMVal* [2010] report that used this threshold for chlorine activation, rather than T_{NAT} or plain 195 K. T_{ACL} was utilized in order to examine the role of liquid aerosols in heterogeneous processing for ozone depletion. Thus, Aura MLS corrected H_2O data was employed (see Section 2.1.3.4) and the algorithm described in Section 5.1 for the computation of surface areas $T < T_{ACL}$ was enclosed by the climatological region [60ºS–80ºS] at four different pressure surfaces between 100 hPa and 21.6 hPa (see Table 7.1 for equivalent approximate altitude levels). Based on that work, the areal coverage below T_{ACL} in 2006 was computed and compared with HCl depletion and T_{NAT} area data derived from v2.2 MLS observations, and is presented in Panel 7b.

T_{ACL} was derived from MLS v2.2 H_2O zonal means in the geographic latitude-longitude grid, as defined per Scheme 2 and as described in Sect. 5.2 (except for the dependency upon HNO_3) using constant values of the sulfate surface area (SA) within the range defined by *Drdla and Müller* [2010].

At 17 km, similar areas below T_{ACL} for SA = 0.1 $\mu m^2 cm^{-3}$ (as displayed in Panel 7a(a)) to the T_{NAT} areal coverage for Scheme 2 were determined. Furthermore, T_{ACL} for SA = 1 $\mu m^2 cm^{-3}$ areas matched well with HCl threshold 3 during the early season, whereas T_{ACL} (SA = 11 $\mu m^2 cm^{-3}$) areas aligned with HCl thresholds 1 and 2 over the same period, at the same altitude (not shown). Although areas below T_{ACL}, calculated at the lowest level using *Drdla and Müller* [2010]'s formulation, did not show the timing for chlorine deactivation, their pattern before this process matched with the HCl depletion results presented for the lowest defined level.

However, at higher stratospheric pressure levels, particularly above 20 km, the T_{ACL} areas matched with HCl depleted areas during the season, when different constant

values of SA were utilized and even when defining a more conservative HCl-depletion threshold (n = 6, Equation 6.2.1) (see Panel3 (c-d)) could not be determined.

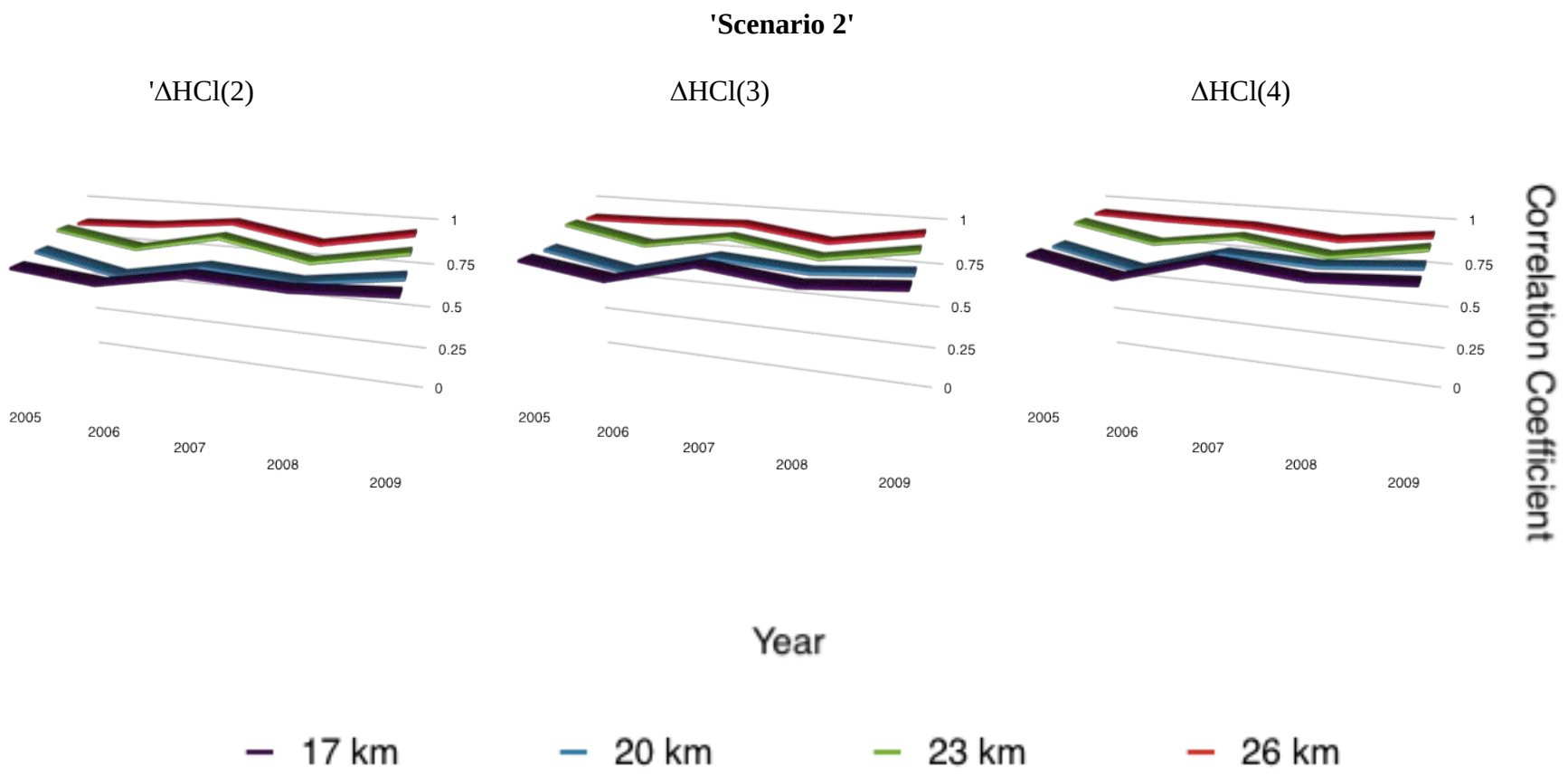

Panel 7a.1. PPCs as a function of year (2005 to 2009) for PSC and HCl depletion areas and at four Antarctic stratospheric altitudes (see Table 7.1 for the corresponding pressure surface). Panel figures correspond to the correlations for T_{NAT} and the data set of Scenario 2 (see Sect. 5.2) and three HCl depletion thresholds.

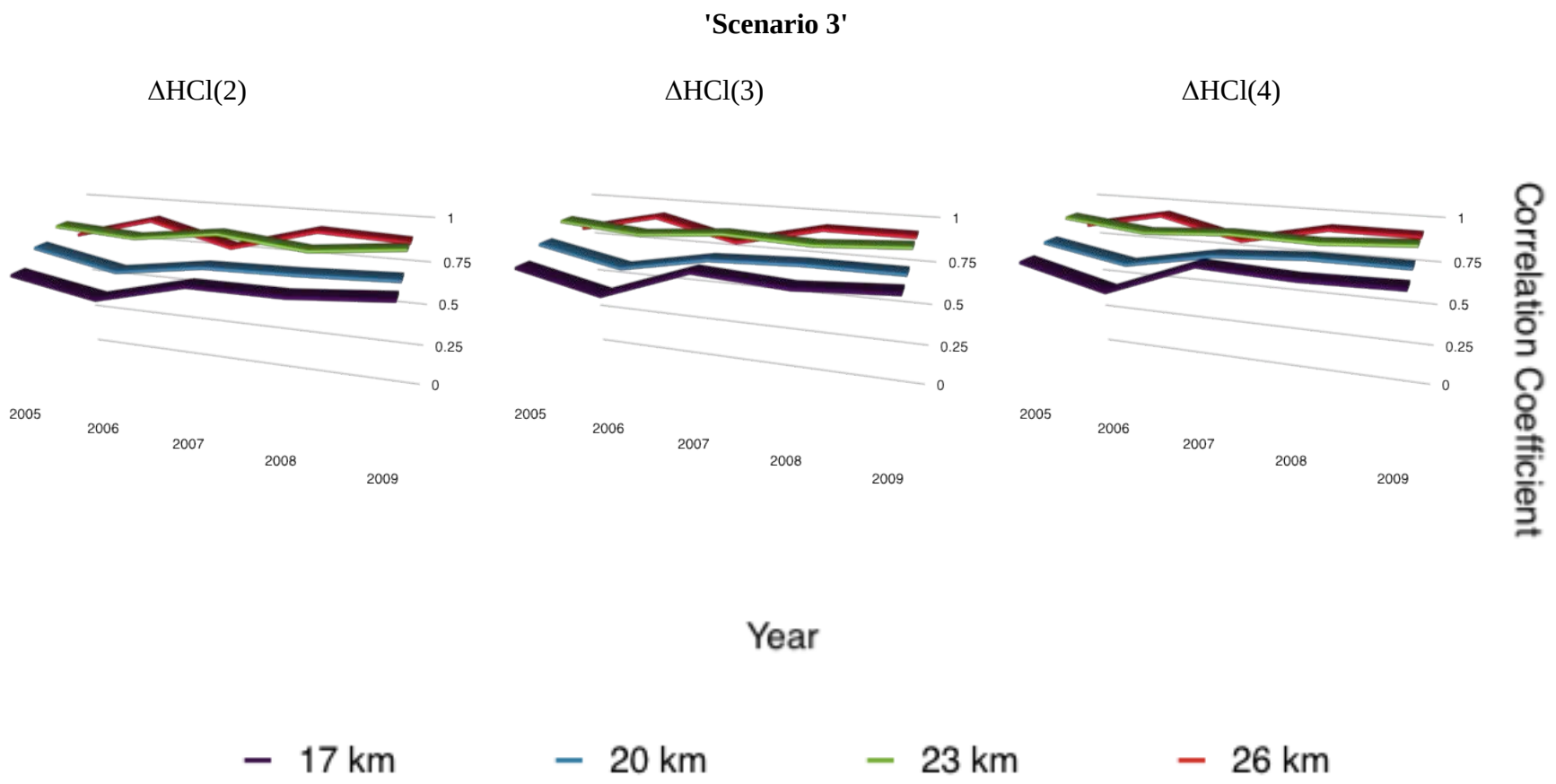

Panel 7a.2. PPCs as a function of year (2005 to 2009) for PSC and HCl depletion areas and at four Antarctic stratospheric altitudes (see Table 7.1 for the corresponding pressure surface). The Panel figures: as for previous panel but for T_{NAT} and the database in Scenario 3 (See Sect. 5.2).

Panel 7b.1. (a) ~17 km

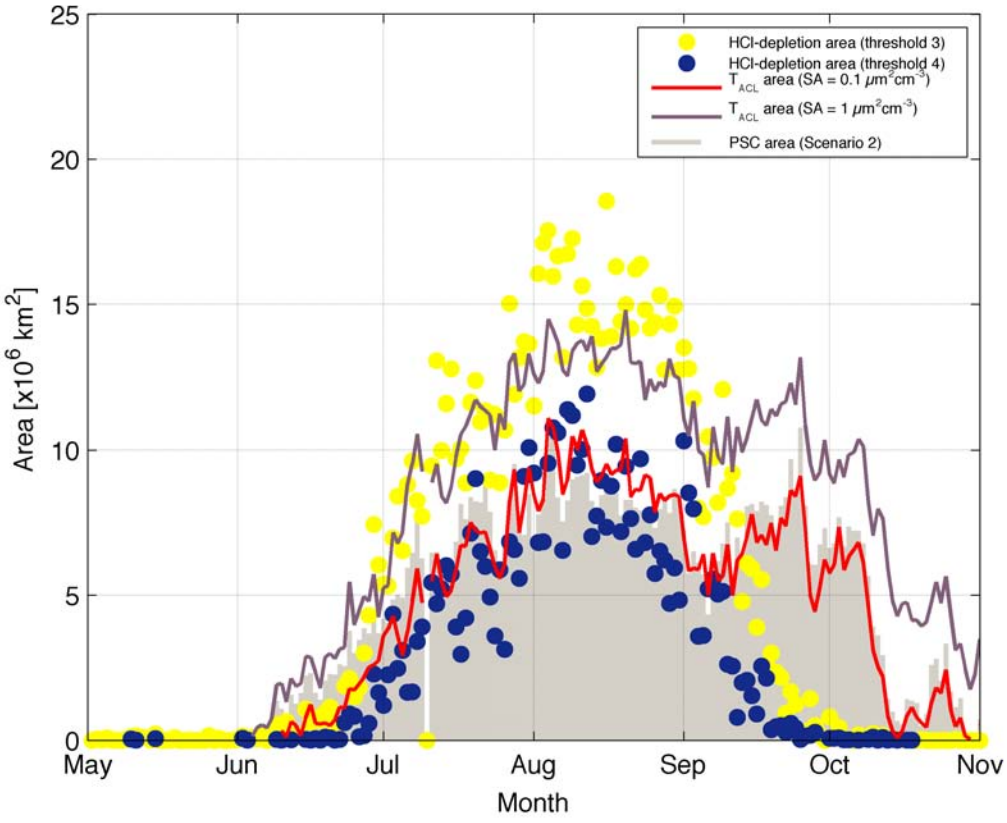

Panel 7b.2. (b) ~20 km

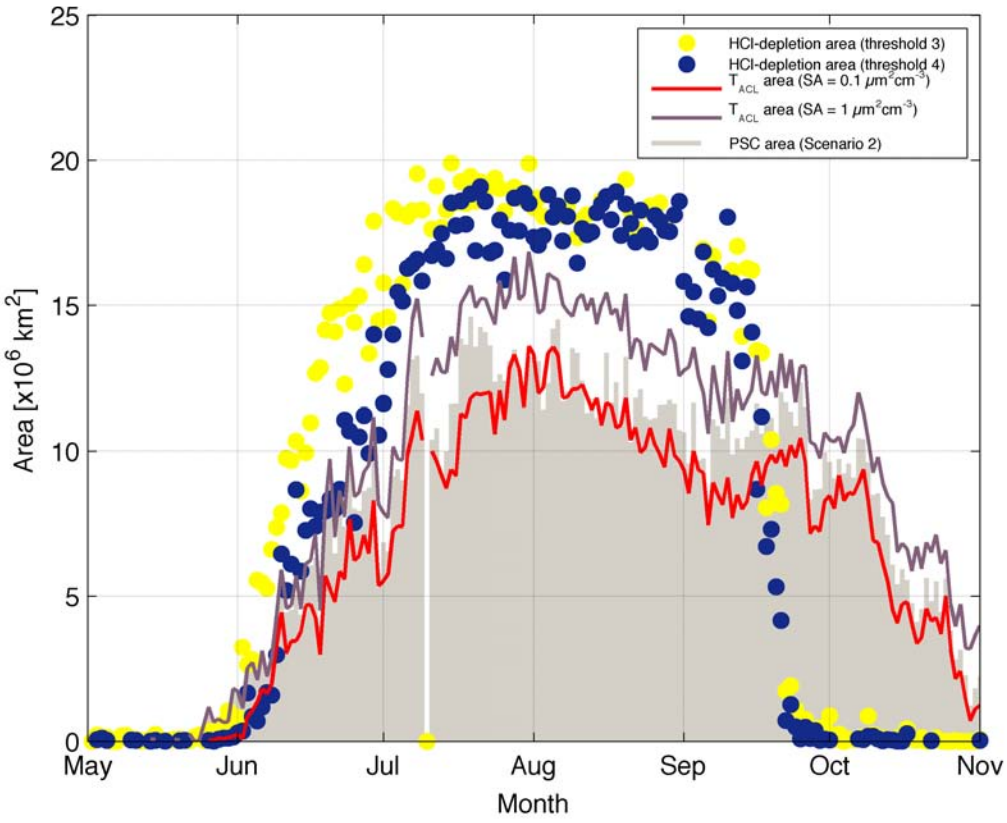

Panel 7b.3. (c) ~23 km

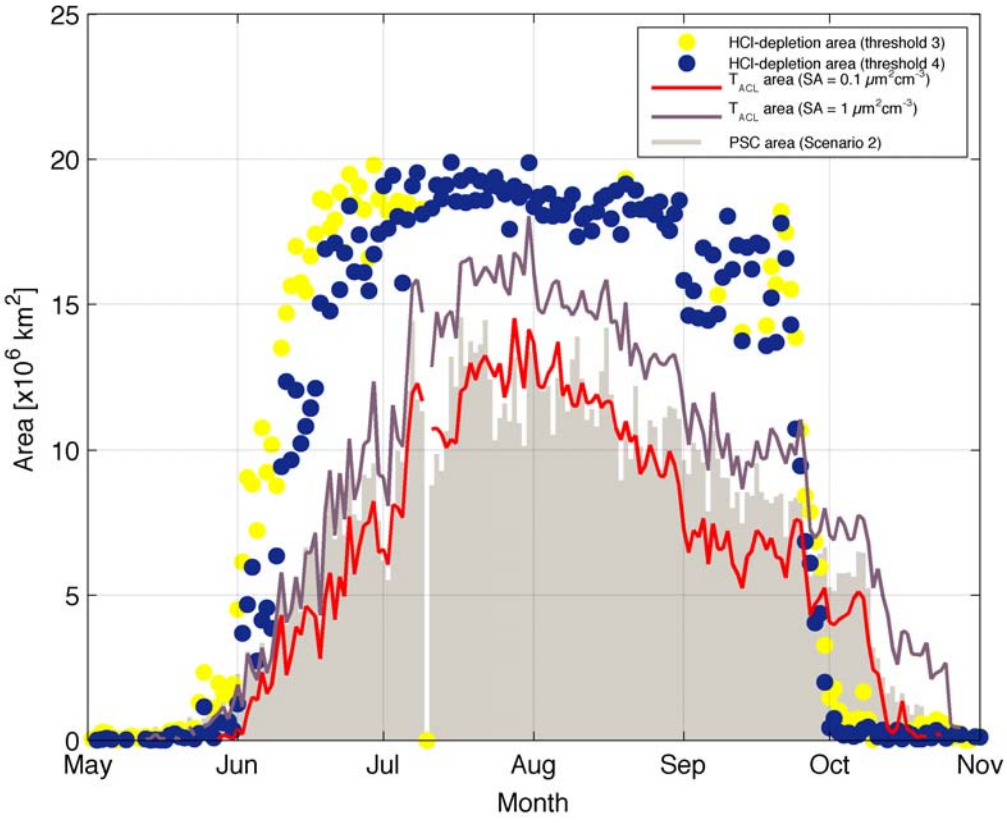

Panel 7b.4. (d) ~26 km

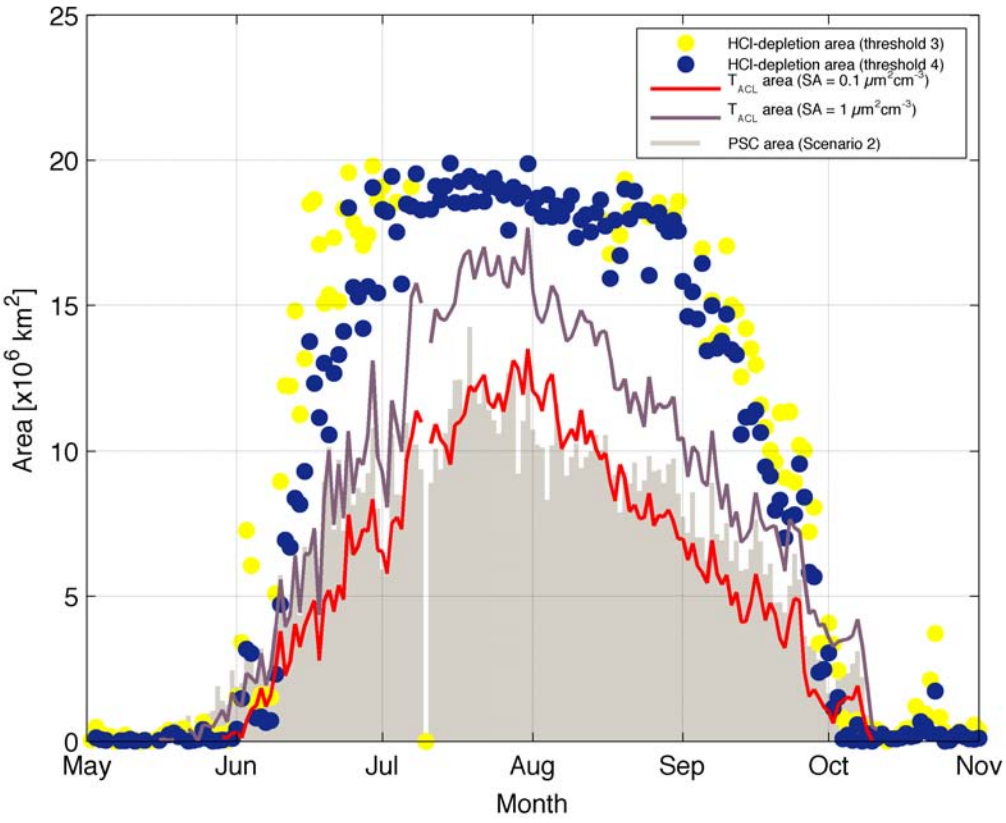

Panel 7b. HCl depleted areas versus T_{ACL} areas over the Antarctic region [60ºS - 80ºS] in 2006 at approximately 17 km [a], 20 km [b], 23 km [c], and 26 km [d]. Yellow dots represent HCl depleted areas using the most conservative HCl-depletion threshold as defined for this study (n = 4, Equation 6.2.1), and dark blue dots represent the same areas but for an extremely conservative HCl-depletion threshold (n = 6, Equation 6.2.1). Red (dark violet) lines are the chlorine activation areas using *Drdla and Müller*'s [2010] formulation for SA = 0.1 $\mu m^2 cm^{-3}$ (SA = 1 $\mu m^2 cm^{-3}$). The gray background area shows the PSC area, as per Scenario 2, as defined in this study.

7.3 HCl depletion and PSC surface areal coverage: Second generation

We have implemented a similar algorithm as described above for examination of HCl depleted areas over the Antarctic, where a HCl-depletion threshold has been determined by calculating the mean and standard deviation of pressure-dependent HCl concentrations over a two month period from day 30^{th} to 90^{th} in 2006. This steady state HCl period was selected because it occurs well before the period in which temperatures cold enough for PSC formation are observed as this was previously discussed in section 2.1.3.1.

Results shown indicate that HCl depletion areas are generally larger than PSC area derived from different T_{NAT} thresholds, especially during the HCl uptake phase during the Antarctic winter at lower stratospheric altitudes (17 and 20 km). This lack of correspondence maybe due to air mass processing by PSC and is an area for further work.

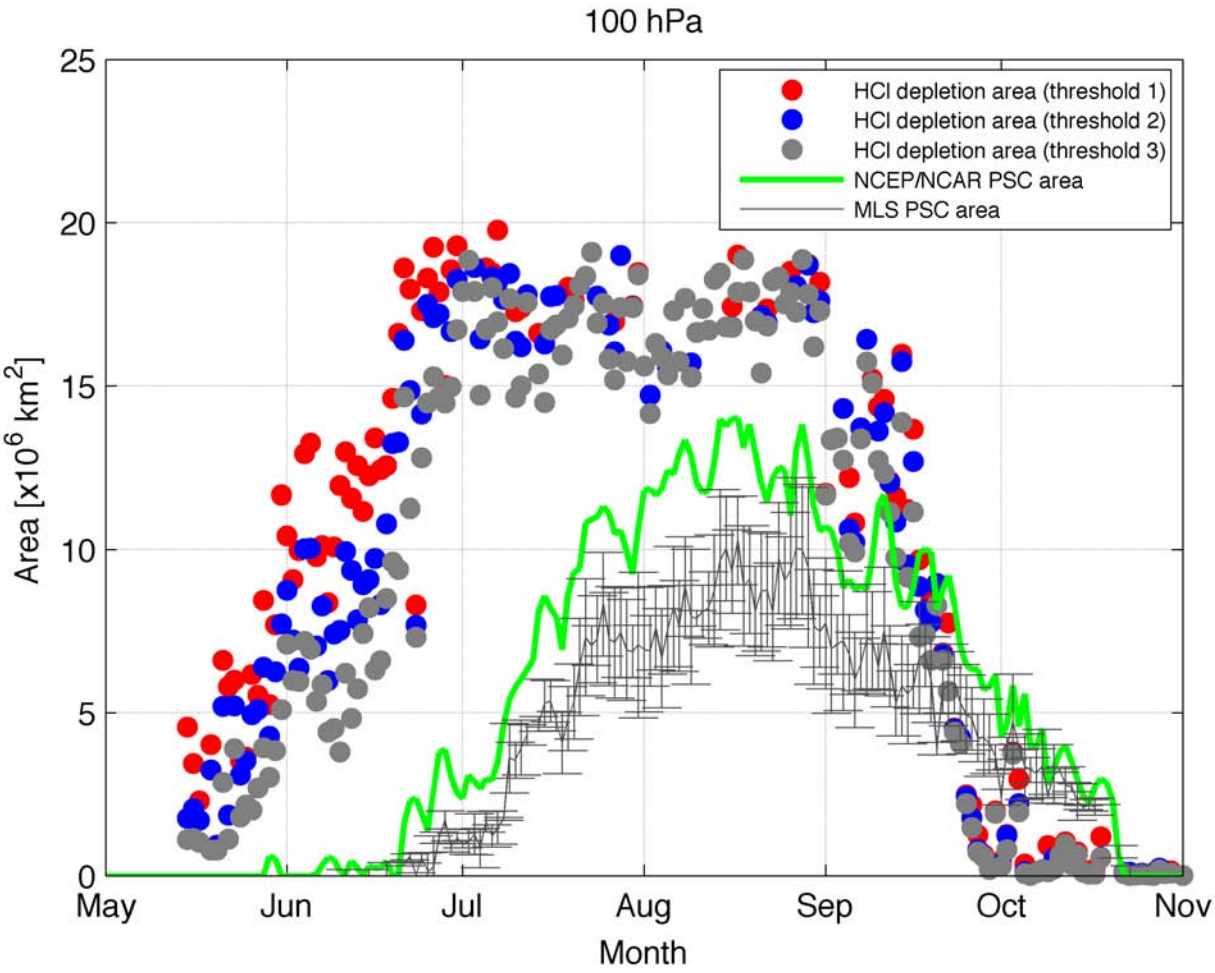

Figure 7.1. HCl depleted areas over APVR in 2005 at different pressure surfaces for different HCl uptake phase thresholds and corresponding with PSC areas. PSC area calculations are derived from temperatures below 195 K using NCEP/NCAR reanalysis and EOS MLS satellite-based data using the algorithm described in section 5.1.

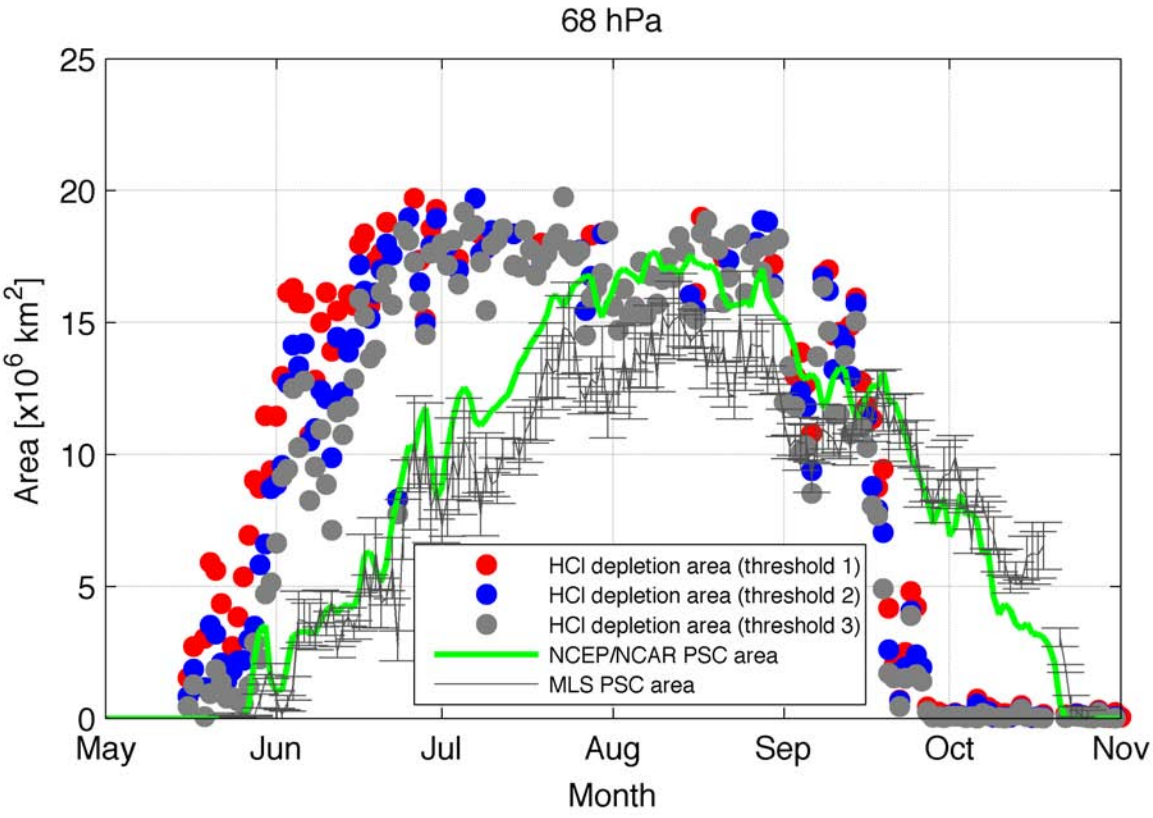

Figure 7.1. HCl depleted areas over APVR in 2005 at different pressure surfaces for different HCl uptake phase thresholds and corresponding with PSC areas. PSC area calculations are derived from temperatures below 195 K using NCEP/NCAR reanalysis and EOS MLS satellite-based data using the algorithm described in section 5.1.

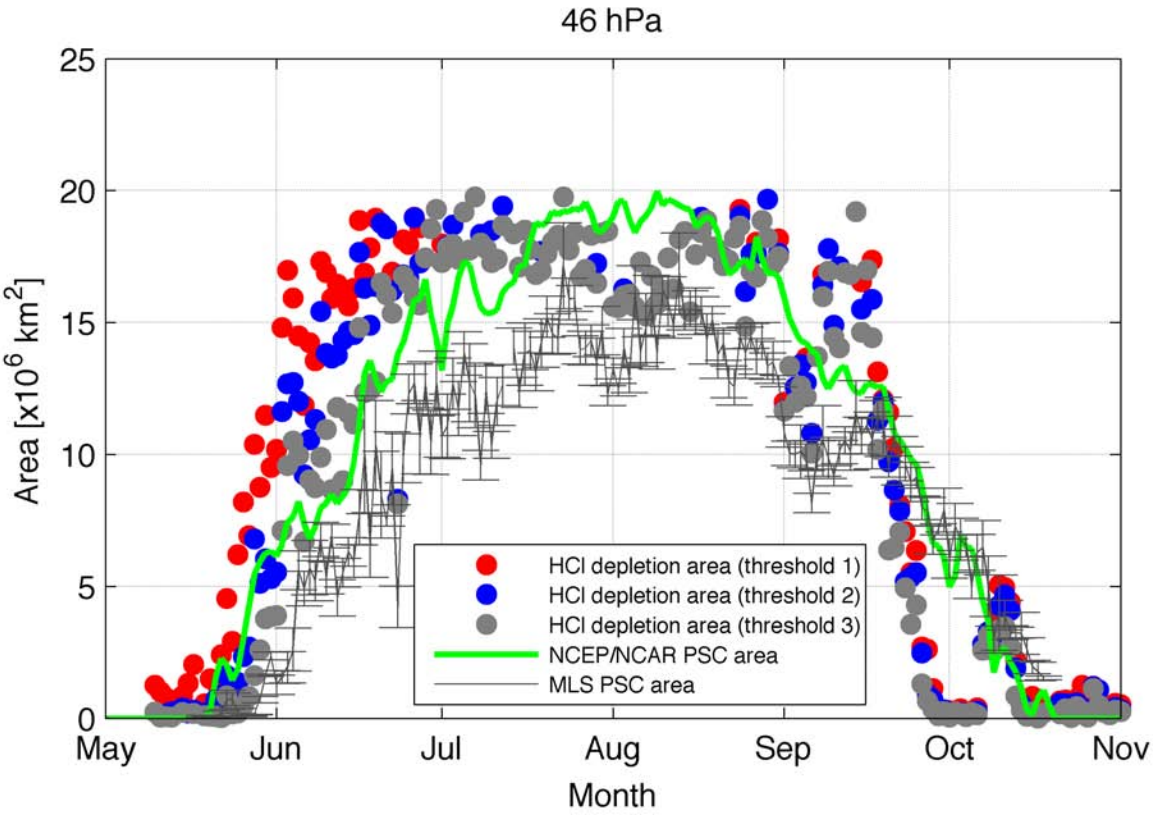

Figure 7.1. HCl depleted areas over APVR in 2005 at different pressure surfaces for different HCl uptake phase thresholds and corresponding with PSC areas. PSC area calculations are derived from temperatures below 195 K using NCEP/NCAR reanalysis and EOS MLS satellite-based data using the algorithm described in section 5.1.

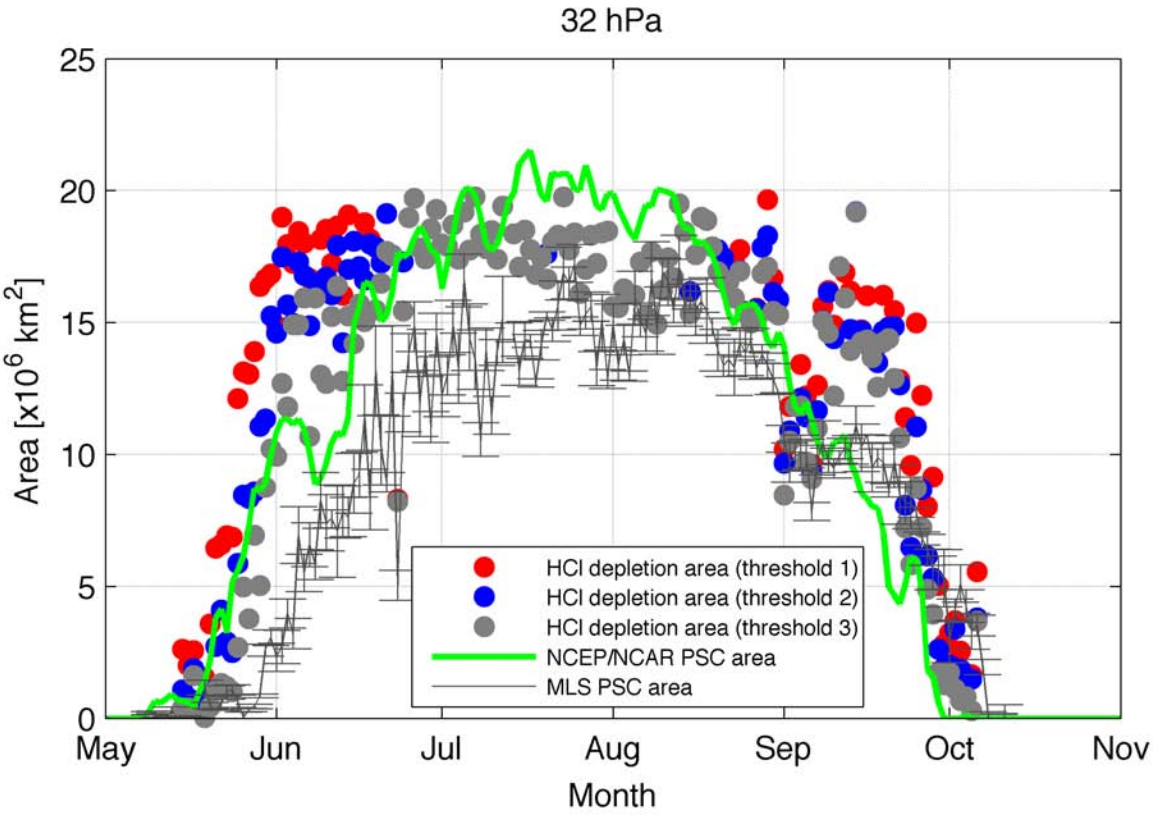

Figure 7.1. HCl depleted areas over APVR in 2005 at different pressure surfaces for different HCl uptake phase thresholds and corresponding with PSC areas. PSC area calculations are derived from temperatures below 195 K using NCEP/NCAR reanalysis and EOS MLS satellite-based data using the algorithm described in section 5.1.

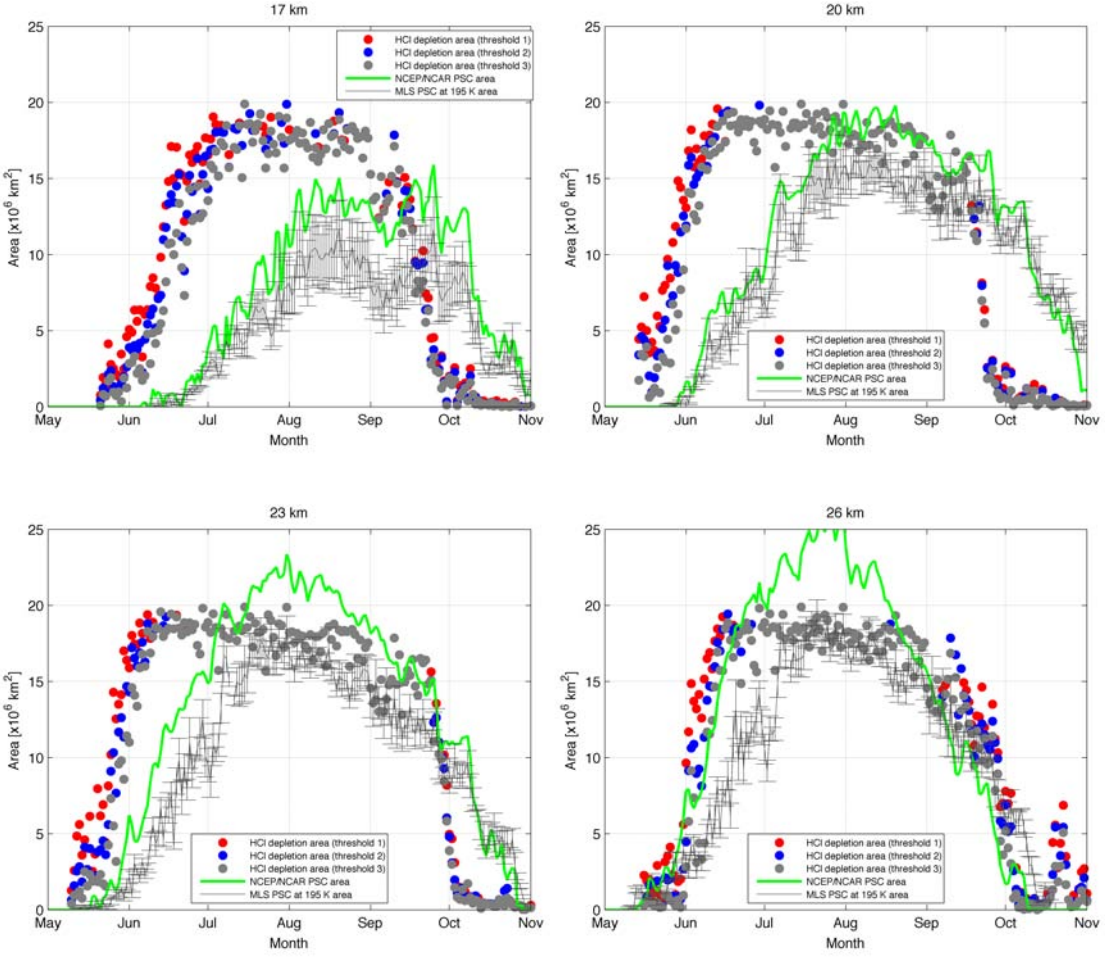

Figure 7.2. HCl depleted areas over APVR in 2006.

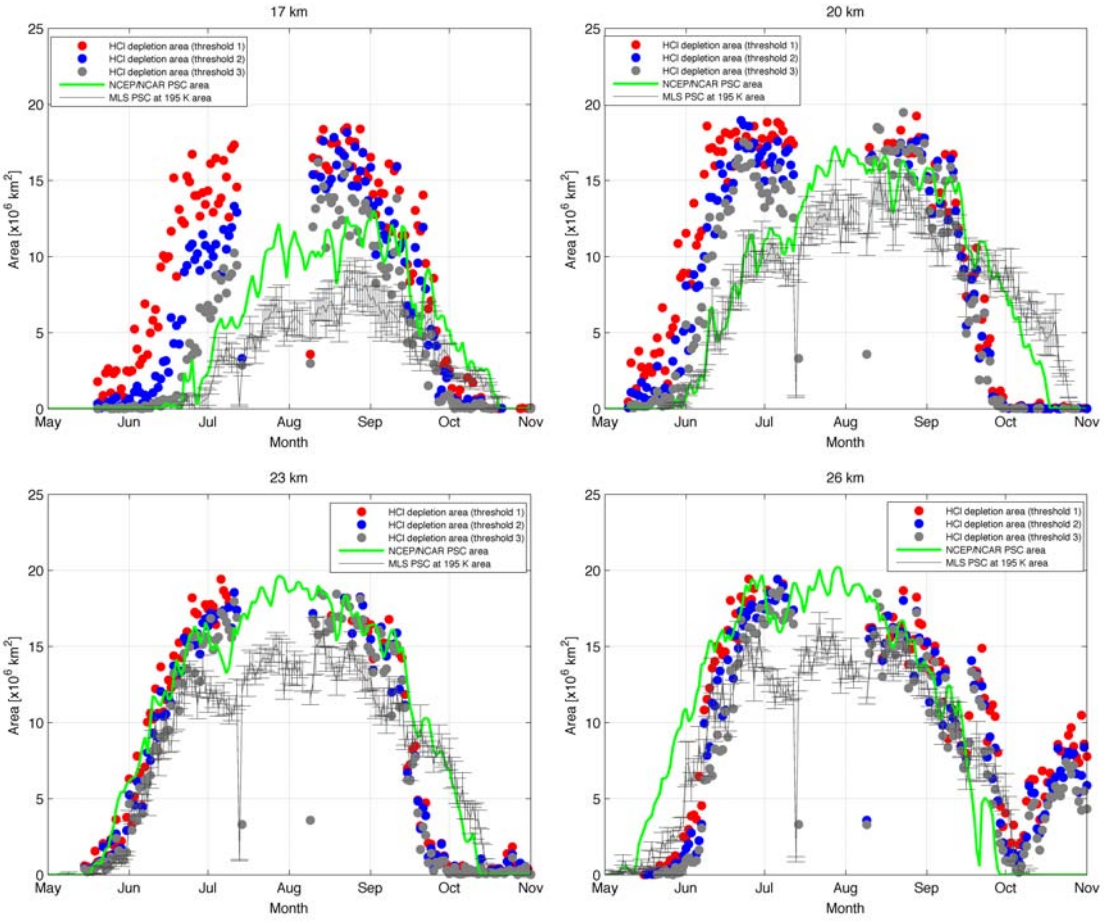

Figure 7.3. HCl depleted areas over APVR in 2007.

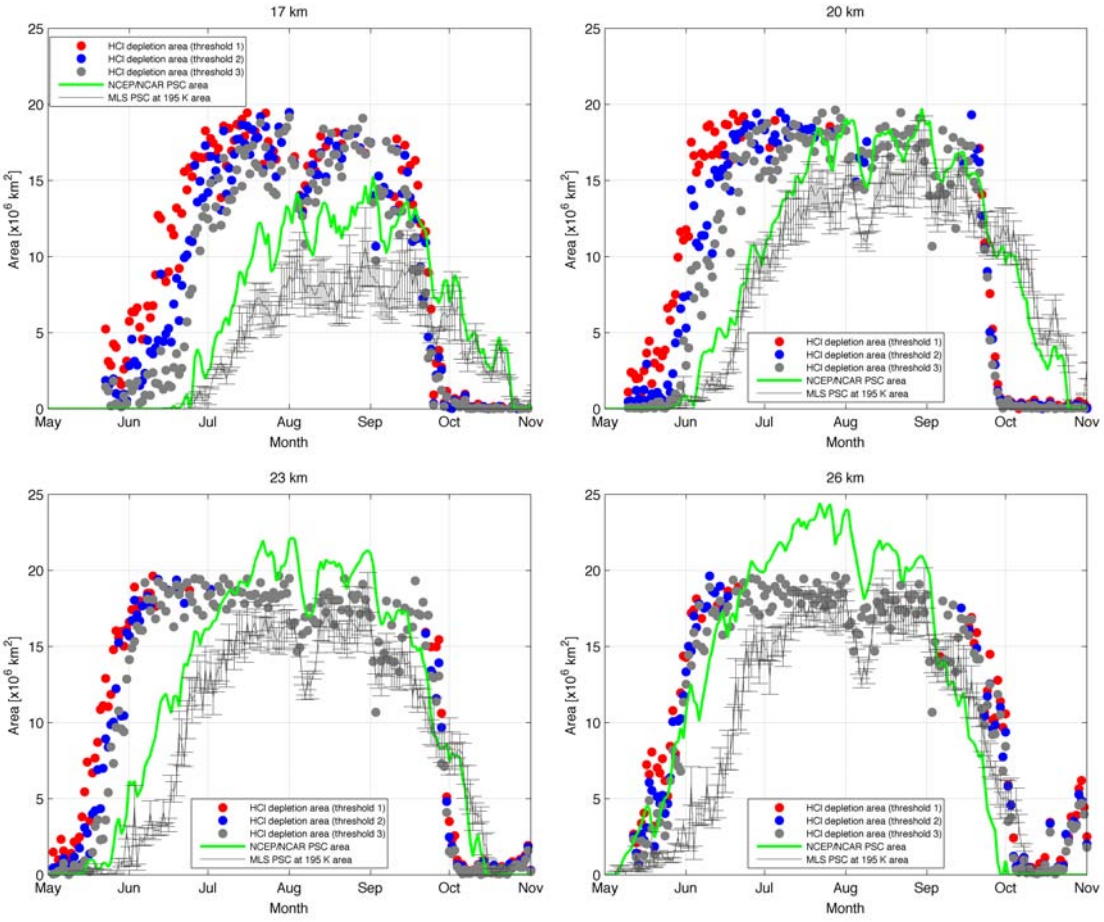

Figure 7.4. HCl depleted areas over APVR in 2008.

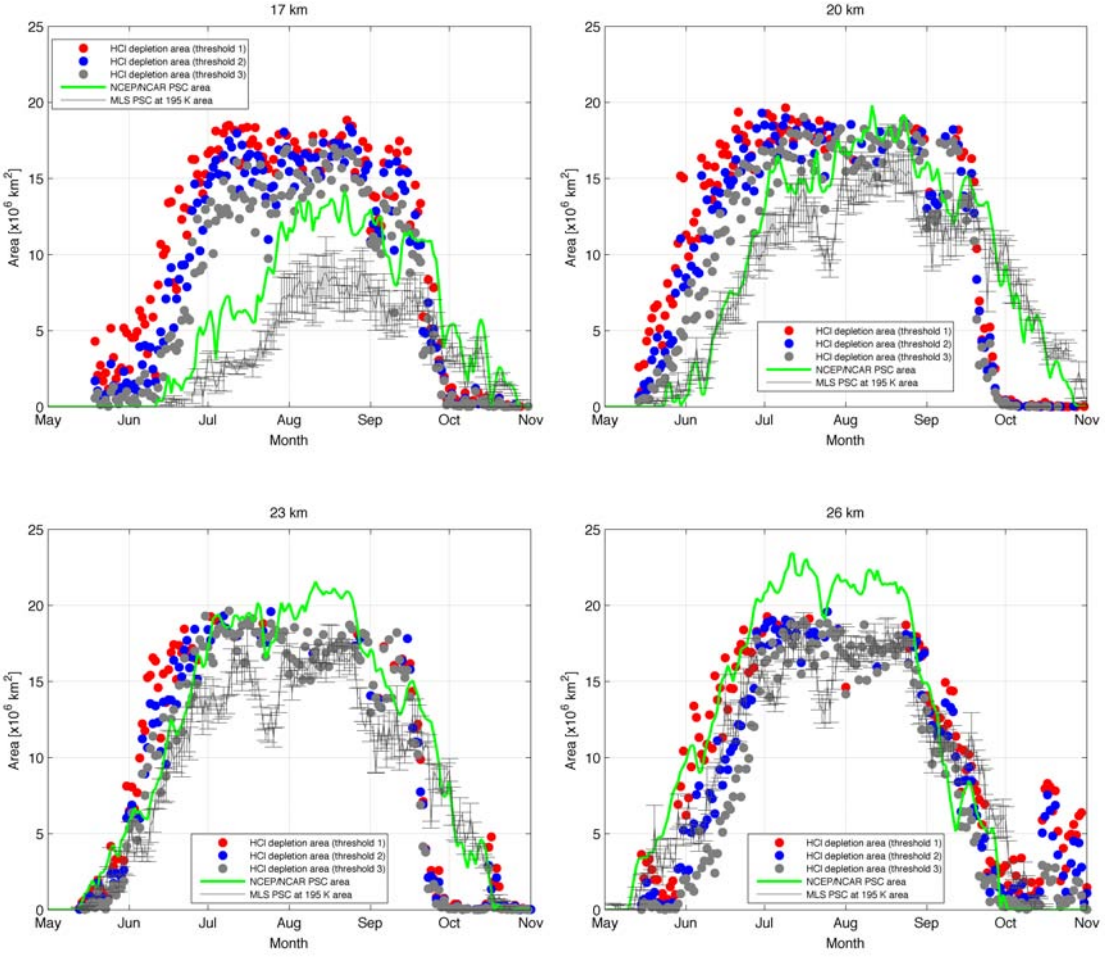

Figure 7.5. HCl depleted areas over APVR in 2009.

	Altitude	NCEP/NCAR PSC Area (T_{NAT} = 195 K)					EOS MLS PSC Area (T_{NAT} variable)					EOS MLS PSC Area (T_{NAT} = 198 K)				
		Year					Year					Year				
		2005	2006	2007	2008	2009	2005	2006	2007	2008	2009	2005	2006	2007	2008	2009
HCl depletion area (HCl Threshold 1)	17 km	0.75 +2.87 +11.35	0.67 +1.87 +10.79	0.79 +1.95 +8.89	0.79 +2.20 +9.66	0.83 +2.23 +9.00	0.80 +3.75 +11.71	0.76 +2.63 +10.91	0.85 +2.81 +9.72	0.83 +3.29 +11.38	0.86 +3.54 +10.91	0.77 +2.35 +10.36	0.73 +1.29 +9.31	0.82 +1.65 +8.50	0.76 +1.76 +9.61	0.84 +1.98 +8.73
	20 km	0.84 +1.16 +7.15	0.75 +0.67 +7.47	0.82 +1.21 +8.54	0.83 +1.16 +7.31	0.85 +1.09 +6.13	0.83 +2.14 +8.47	0.74 +1.67 +9.02	0.83 +1.71 +8.37	0.80 +2.32 +9.30	0.87 +2.01 +7.70	0.82 +0.87 +6.51	0.73 +0.48 +7.27	0.82 +0.55 +6.62	0.77 +0.77 +7.16	0.86 +0.46 +5.36
	23 km	0.91 +1.04 +2.94	0.88 +0.28 +2.79	0.94 -0.37 +0.65	0.89 +0.93 +3.19	0.94 -0.28 +1.65	0.90 +2.67 +7.66	0.83 +2.60 +8.14	0.93 +1.15 +4.35	0.84 +3.32 +8.78	0.93 +1.78 +6.06	0.90 +1.26 +5.18	0.84 +1.09 +6.02	0.91 -0.19 +1.80	0.84 +1.53 +5.85	0.93 +0.08 +2.91
	26 km	0.81 +2.64 +0.98	0.93 +0.41 -1.57	0.81 +1.04 -1.76	0.94 +0.43 -1.12	0.92 +0.23 -1.99	0.89 +3.65 +8.19	0.91 +2.71 +7.06	0.96 +1.92 +4.84	0.88 +3.68 +8.42	0.97 +2.05 +5.48	0.91 +2.04 +4.91	0.93 +0.66 +4.29	0.95 +0.16 +1.24	0.92 +1.22 +4.52	0.96 -0.18 +1.43
HCl depletion area (HCl Threshold 2)	17 km	0.79 +2.48 +10.00	0.69 +1.58 +9.76	0.86 +0.92 +4.42	0.83 +1.57 +7.45	0.86 +1.53 +6.74	0.84 +3.40 +10.44	0.78 +2.40 +9.94	0.90 +1.77 +4.98	0.85 +2.78 +9.57	0.89 +2.89 +8.74	0.80 +2.00 +9.09	0.74 +1.05 +8.31	0.88 +0.60 +3.70	0.79 +1.21 +7.58	0.86 +1.33 +6.49
	20 km	0.86 +0.80 +6.35	0.77 +0.48 +7.23	0.86 +0.69 +6.52	0.88 +0.75 +6.10	0.88 +0.73 +5.00	0.84 +1.78 +7.67	0.76 +1.52 +8.78	0.88 +1.23 +6.34	0.85 +2.01 +8.13	0.89 +1.88 +6.57	0.84 +0.52 +5.71	0.75 +0.29 +7.03	0.86 +0.11 +4.60	0.82 +0.44 +5.95	0.89 +0.46 +4.23
	23 km	0.94 +0.44 +2.07	0.90 +0.07 +2.63	0.94 -0.64 -0.31	0.92 +0.64 +3.06	0.95 -0.58 +0.82	0.93 +2.27 +6.78	0.85 +2.42 +7.98	0.93 +0.88 +3.39	0.86 +3.13 +8.65	0.94 +1.48 +5.23	0.93 +0.83 +4.30	0.85 +0.87 +5.86	0.91 -0.46 +0.83	0.86 +1.24 +5.72	0.93 -0.22 +2.08
	26 km	0.85 +2.05 +0.61	0.95 +0.01 -2.28	0.84 +0.34 -3.05	0.95 +0.20 -1.27	0.95 -0.83 -3.99	0.92 +3.22 +7.82	0.93 +2.40 +6.35	0.95 +1.46 +3.55	0.89 +3.51 +8.28	0.97 +1.27 +3.48	0.94 +1.57 +4.54	0.93 +0.34 +3.58	0.94 -0.31 -0.05	0.92 +1.03 +4.38	0.95 -0.96 -0.57
n area (HCl Threshol	17 km	0.82 +2.08 +8.62	0.71 +1.28 +8.51	0.89 -0.10 +1.51	0.87 +1.03 +5.27	0.88 +0.85 +4.58	0.87 +3.00 +9.07	0.79 +2.11 +8.69	0.92 +0.65 +1.45	0.88 +2.30 +7.42	0.91 +2.15 +6.44	0.82 +1.63 +7.71	0.76 +0.78 +7.04	0.89 -0.51 +0.30	0.83 +0.72 +5.37	0.88 +0.62 +4.24

20 km	0.87 +0.50 +5.44	0.79 +0.29 +6.98	0.88 +0.24 +4.43	0.91 +0.29 +4.48	0.91 +0.24 +3.30	0.86 +1.48 +6.76	0.77 +1.33 +8.53	0.90 +0.86 +4.26	0.88 +1.57 +6.58	0.92 +1.37 +4.87	0.85 +0.24 +4.80	0.77 +0.09 +6.78	0.89 -0.20 +2.51	0.86 -0.03 +4.33	0.91 -0.01 +2.53
23 km	0.96 -0.18 +0.83	0.91 -0.15 +2.38	0.94 -0.87 -1.25	0.93 +0.40 +2.87	0.96 -0.86 -0.07	0.94 +1.80 +5.55	0.86 +2.21 +7.72	0.93 +0.64 +2.45	0.87 +2.97 +8.47	0.95 +1.20 +4.34	0.93 +0.37 +3.06	0.87 +0.65 +5.60	0.91 -0.70 -0.11	0.88 +1.01 +5.53	0.93 -0.49 +1.19
26 km	0.87 +1.43 -0.23	0.96 -0.43 -3.15	0.85 -0.30 -4.47	0.95 0.00 -1.53	0.95 -1.76 -5.92	0.95 +2.75 +6.98	0.94 +2.05 +5.48	0.94 +1.03 +2.13	0.90 +3.33 +8.02	0.96 +0.53 +1.54	0.95 +1.08 +3.70	0.94 -0.02 +2.71	0.92 -0.75 -1.47	0.93 +0.85 +4.12	0.92 -1.71 -2.51

Table 7.2. Correlation coefficients and differences between HCl depleted area based on three thresholds versus the PSC area. Values derived at four stratospheric altitudes

from 2005 to 2009. First row in each altitude: are correlation coefficients, area differences third row in each altitude for full year and from 01 June to 01 August, respectively. T_{NAT} variable values are derived via *Hanson and Mauersberger* [1988] formulation derived from H_2O measured daily by EOS MLS data and MLS HNO_3 as the mean value in every year. The mean T_{NAT} values were found to be 195.9 K, 194.5 K, 193.6 K and 192.1 K over the period of time 2005-2009 at 17 km, 20 km, 23 km and 26 km respectively.

7.3.1 Antarctic winter 2010: a closer chemical look

Temperatures in 2010 were higher than in other recent Antarctic winters, and as a consequence slightly less chlorine activation occurred, but HCl depletion was still observed. The following Figures show PSC area vs. HCl depleted areas. It should be noted that on the charts, T_{NAT} *'var1'* refers to PSC area calculated using T_{NAT} threshold derived from daily vortex region average H_2O, daily vortex region average HNO_3 and pressure following the formulation of *Hanson and Mauersberger* [1988]; whereas T_{NAT} *'var2'* means as in T_{NAT} *'var1'* but T_{NAT} is in this case as function of daily bin region average H_2O, daily bin region average HNO_3 and pressure i.e. T_{NAT} calculated over each bin (latitude-longitude) dependent) every day --and each bin size is 20ºx20º over the region (60ºS–80ºS) at ~26 km.

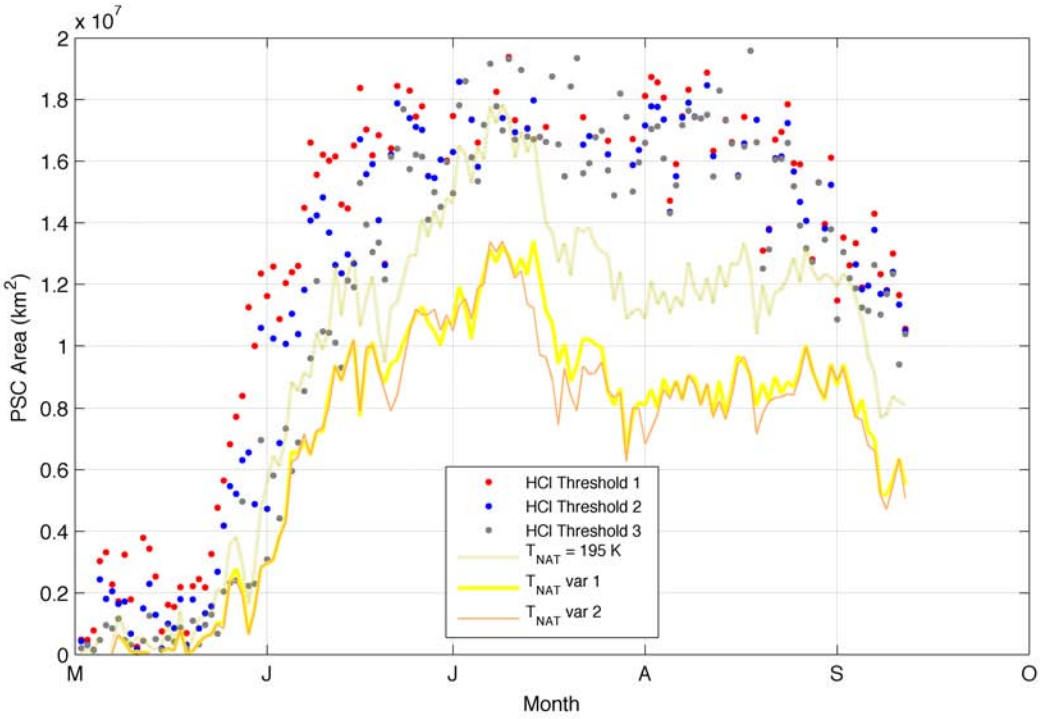

Figure 7.6. HCl depleted areas over APVR in 2010 at ~26 km.

Chapter 8

OROGRAPHIC GRAVITY WAVES AND PSC

8.1 INTRODUCTION

This chapter is a summary of the author's collaborative article, which is relevant to this thesis:

I. Alexander, S. P., Klekociuk, A. R., Pitts, M. C., McDonald, A. J., and Arevalo-Torres, A. (2011), The effect of orographic gravity waves on Antarctic Polar Stratospheric Cloud (PSC) occurrence and composition, *J. Geophys. Res.*, *116*, D06109, doi:10.1029/2010JD015184.

My contribution to this article is as follows: I took part in collecting, preparing and validating Aura MLS data for the whole paper in 2007 in Antarctica. I participated in providing T_{NAT} and T_{ICE} used in this paper. I was responsible for the complete Aura MLS data analysis in the paper, and partially responsible for the analysis of GW data that were not presented, but discussed, to complement conclusions. I collaborated in discussing the final version of the manuscript for submission using the contents of the present thesis.

In the following sections the work developed for Paper I will be shown and discussed. A good part of Paper I was being prepared in parallel to this thesis, therefore 'article I' represented a niche of opportunity for the present work.

A summary of this article is as follows:

A seasonal analysis of the relationship between mesoscale orographic gravity wave activity and polar stratospheric cloud (PSC) composition occurrence around the whole of Antarctica is presented. Gravity wave variances are derived from temperature measurements made with the Constellation Observing System for Meteorology, Ionosphere and Climate (COSMIC) Global Positioning System Radio Occultation (GPS-RO) satellites. Data from the Cloud-Aerosol Lidar with Orthogonal Polarization (CALIOP) instrument onboard the Cloud-Aerosol Lidar and Infrared Pathfinder Satellite Observations (CALIPSO) satellite are used to determine the PSC composition class distribution and spatial volume. The results show intermittent large wave activity above the Antarctic Peninsula which is coincident with large volumes of H_2O ice PSCs. These ice PSC volumes advect downstream, where increases in nitric acid trihydrate (NAT) PSC volumes occur, supporting the mountain wave seeding hypothesis. During winter 2007 in the latitude range 60°S–70°S, near the edge of the vortex and where temperatures are close to PSC formation thresholds, 30% of all PSCs are attributable to orographic gravity waves. In the separate composition classes, around 50% of both H_2O ice PSCs and a high NAT number density liquid–NAT mixture class of PSCs are due to these waves. While we show that planetary waves are the major determinant of PSC presence at temperatures close to the NAT formation threshold, we also demonstrate the important role of mesoscale, intermittent orographic gravity wave activity in accounting for the composition and distribution of PSCs around Antarctica. [*Alexander et al.*, 2011].

Given that MLS Data are shifted in longitude from [0, 360º] to [-180º, 180], we started converting COSMIC/CALIPSO grid cells into equivalent MLS longitudes as indicated below:

COSMIC/CALIPSO grid cell 1 → [300º E, 65º S] → [(290º - 310º E, 60º - 70º S)]

Equivalent MLS grid cell → [120º, 65º S] → [(110º - 130º, 60º - 70º S)]

COSMIC/CALIPSO grid cell 2 → [285º E, 75º S] → [(270º - 300º E, 70º - 80º S)]

Equivalent MLS grid cell → [105º, 75º S] → [(90º - 120º, 70º - 80º S)]

8.2 Aura MLS Validation. Results: T_{ICE} and T_{NAT} calculations above Alexander's Peninsula grid cells derived from MLS H_2O and MLS HNO_3.

Calculations for T_{ICE} are shown in Figure 8.3. *Marti and Mauersberger*'s [1993] formulation was used for this, using daily mean water vapor concentrations measured by MLS in 2007 over Peninsula grid cells 1 and 2.

Similarly, calculations for T_{NAT} are presented in Figure 8.5. Those were derived from *Hanson and Mauersberger*'s [1988] formulation using mean water vapor and nitric acid mixing ratios measured by MLS in 2007 at 15-26 km. Note that MLS HNO_3 data have a vertical resolution of roughly 3 km, whereas MLS water vapor profiles' resolution is ~1.5 km. This explains the differences (in resolution) between both ICE and NAT plots. Similarly, Figure 5-Bottom does not show any T_{NAT} data at roughly 20 km-higher in Jul.-Aug. due to likely cloud contamination of the MLS HNO_3 data at and below 100 hPa. Given that this may produce negative mean MLS concentrations, *Hanson and Mauersberger*'s [1988] formulation cannot give any T_{NAT} value, given that it uses logarithms of H_2O and HNO_3 concentrations to ultimately find T_{NAT}.

MLS H_2O concentrations and MLS temperatures above the two Peninsula grid cells in 2007.

Figures 8.1 and 8.2 show MLS water vapor concentrations and MLS temperatures averaged over Peninsula grid cell 1 (Figure 8.1) and Peninsula grid cell 2 (Figure 8.2). Figure 8.4 shows mean MLS H_2O mixing ratios over Peninsula grid cell 1 and 2 in 2007. Note that vertical data gaps in Figures 8.3 to 8.5 represent unavailable MLS data on some particular days.

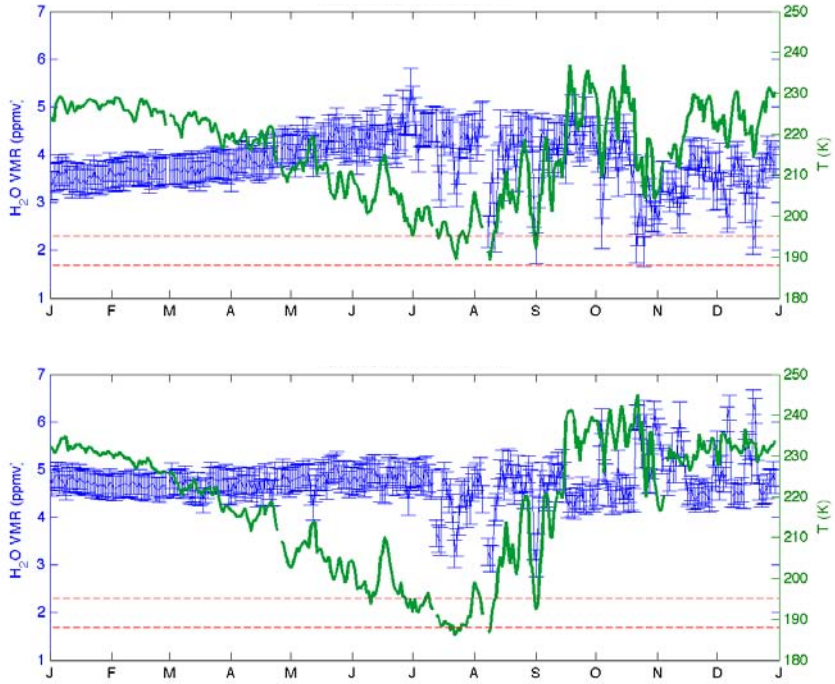

Figure 8.1. Mean water vapor measurements (blue) and mean temperatures (green dots) over Peninsula grid cell 1 at 19 km [Top] and 25 km [Bottom] derived from MLS observations in 2007.

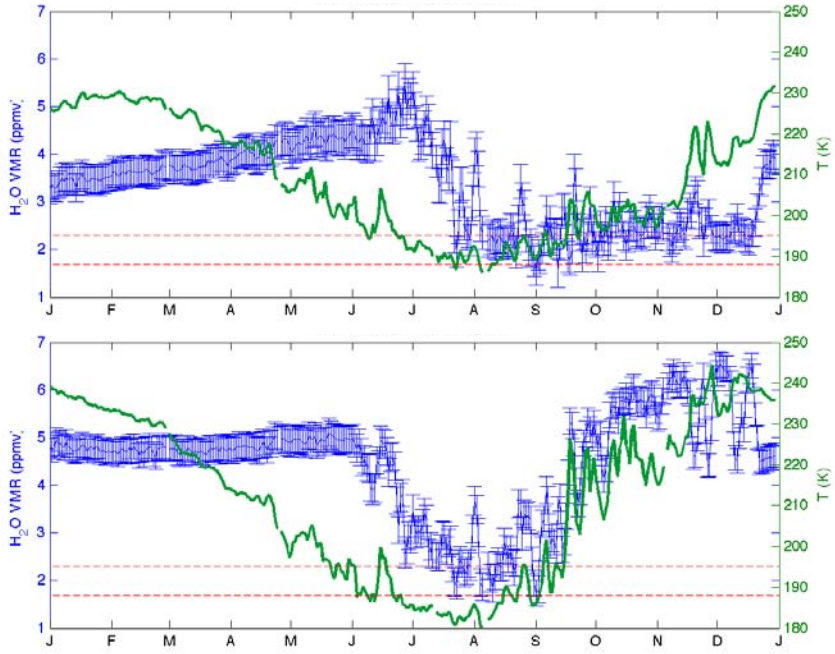

Figure 8.2. Mean water vapor measurements (blue) and mean temperatures (green dots) over Peninsula grid cell 2 at 19 km [Top] and 25 km [Bottom] derived from MLS observations in 2007.

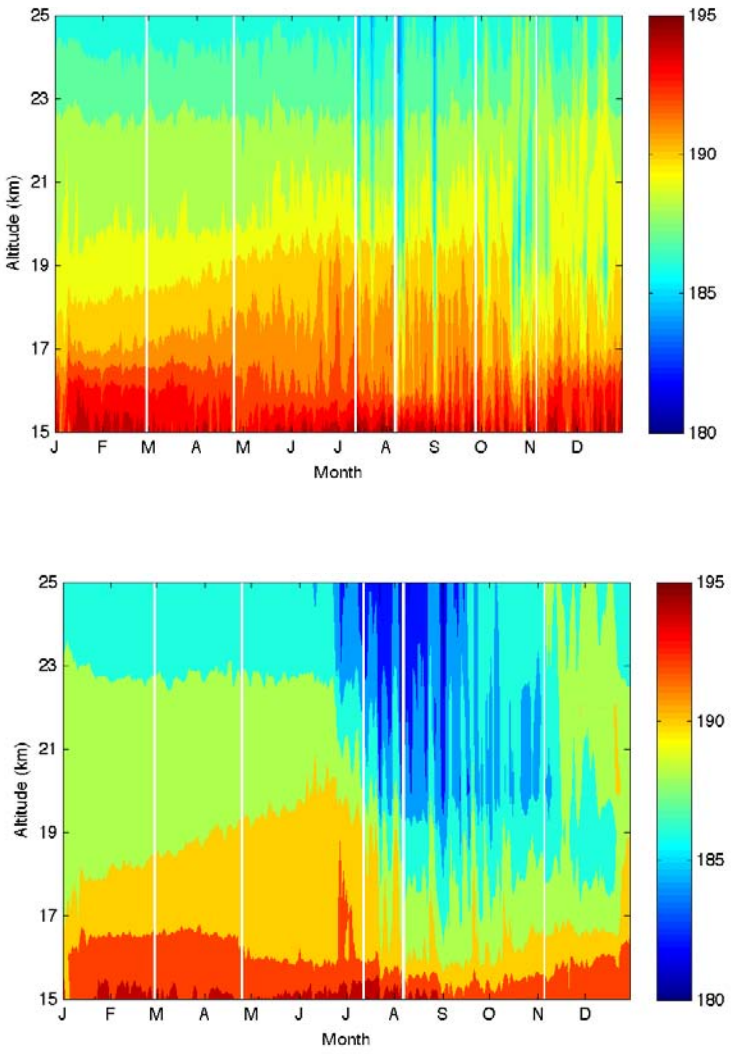

Figure 8.3. T_{ICE} calculations derived from mean MLS water vapor concentrations in 2007 over Peninsula grid cell 1 [Top] and Peninsula grid cell 2 [Bottom], using *Marti and Mauersberger*'s [1993] formulation.

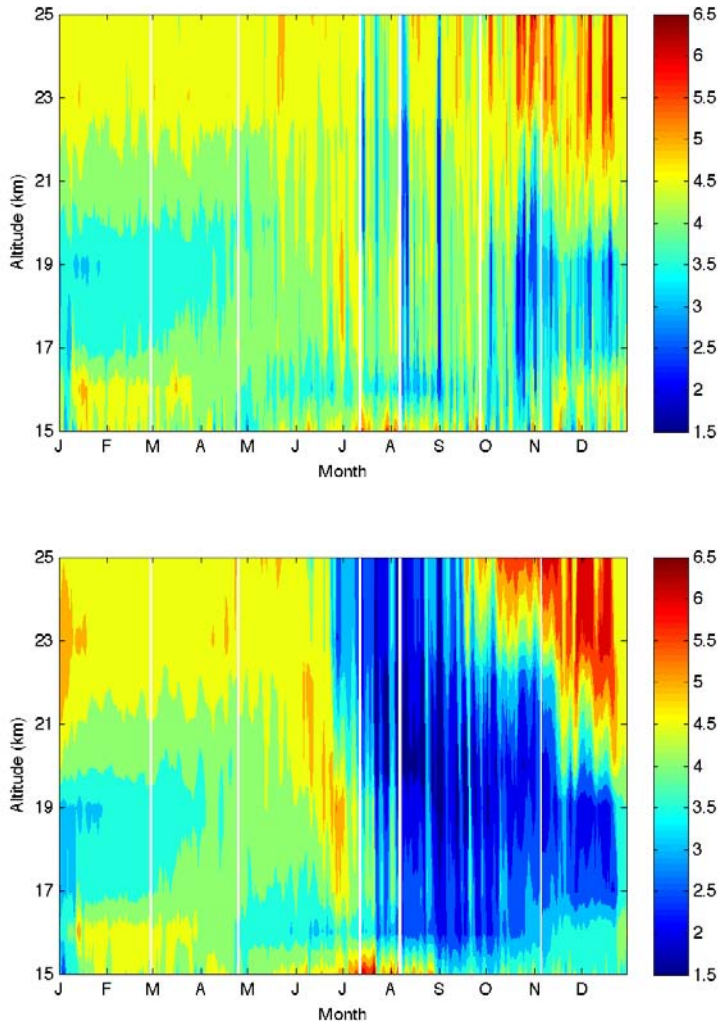

Figure 8.4. Mean MLS H_2O mixing ratio (ppmv) over Antarctic Peninsula grid cell 1 [Top] and grid cell 2 [Bottom].

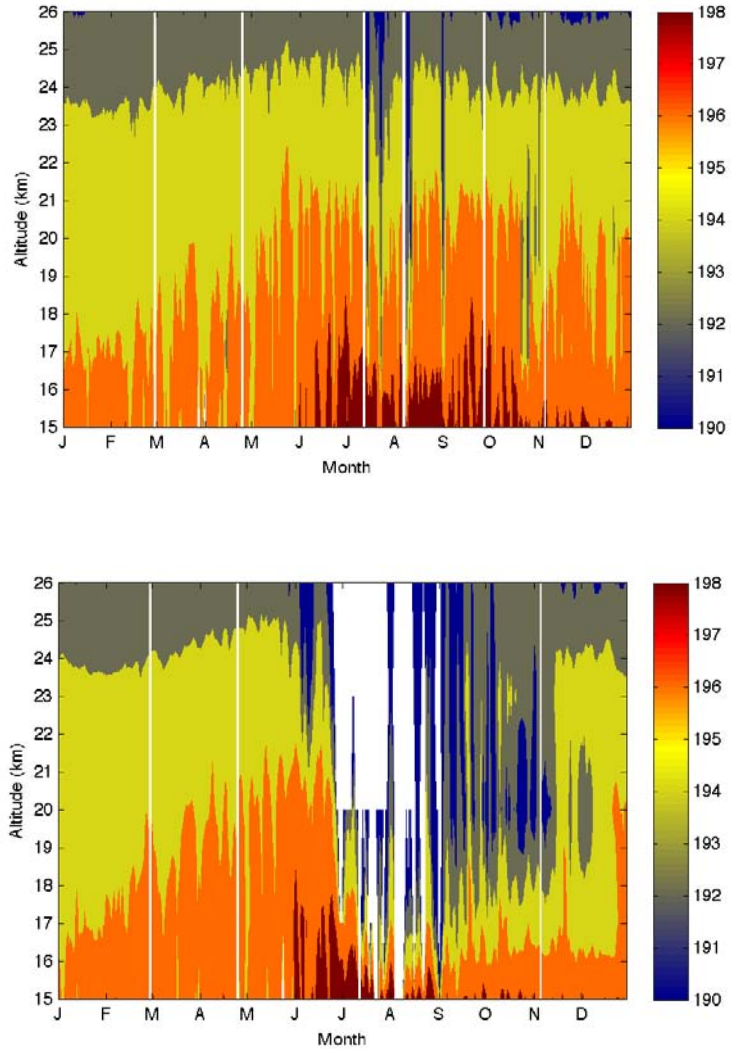

Figure 8.5. T_{NAT} calculations derived from mean MLS H_2O and HNO_3 concentrations in 2007 over Peninsula grid cell 1 [Top] and Peninsula grid cell 2 [Bottom], using *Hanson and Mauersberger*'s [1988] formulation.

Alexander's Antarctic Grid Cell Definitions

Grid Cell #	Longitude (°) COSMIC/CALIPSO	Aura MLS
1	[10, 30]	[-170, -150]
2	[30, 50]	[-150, -130]
3	[50, 70]	[-130, -110]
4	[70, 90]	[-110, -90]
5	[90, 110]	[-90, -70]
6	[110, 130]	[-70, -50]
7	[130, 150]	[-50, -30]
8	[150, 170]	[-30, -10]
9	[170, 190]	[-10, 10]
10	[190, 210]	[10, 30]
11	[210, 230]	[30, 50]
12	[230, 250]	[50, 70]
13	[250, 270]	[70, 90]
14	[270, 290]	[90, 110]
15	[290, 310]	[110, 130]
16	[310, 330]	[130, 150]
17	[330, 350]	[150, 170]
18	[350, 10]	[170, -170]
All 1-18th Cells have Latitude Coordinates [-60°, -70°]		
All 19-30th Cells have Latitude Coordinates [-70°, -80°]		
19	[0, 30]	[-180, -150]
20	[30, 60]	[-150, -120]
21	[60, 90]	[-120, -90]
22	[90, 120]	[-90, -60]
23	[120, 150]	[-60, -30]
24	[150, 180]	[-30, 0]
25	[180, 210]	[0, 30]
26	[210, 240]	[30, 60]
27	[240, 270]	[60, 90]
28	[270, 300]	[90, 120]
29	[300, 330]	[120, 150]
30	[330, 360]	[150, 180]

Table 8.1. Auxiliary table produced for *Alexander et al.* [2011] (not shown in the paper) in order to divide up the Antarctic region [60°–80°]S into grid cells of different size using both COSMIC and Aura MLS datasets.

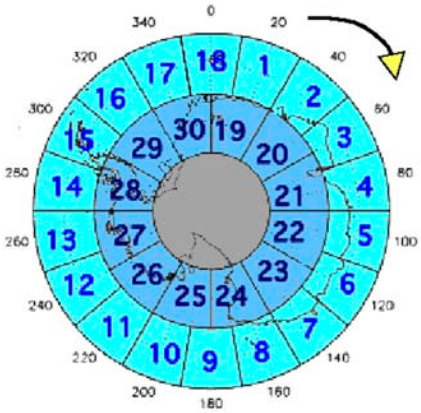

Figure 8.6. Illustrated version of Table 8.1 showing the grid definition used in *Alexander et al.* [2011], which aided in producing the Aura MLS information presented in this article.

Potential Temperatures (θ) were calculated using the equation

$\theta = T(P_o / P)^{2/7}$ [*Wohltmann and Rex*, 2008] (8.1.1)

where T was derived from mean temperature measured by MLS on each day at each pressure surface over each Grid Cell (GC). P is pressure and P_o reference pressure (e.g. 1000 mbar).

Subsequently we interpolated the data to 7 isentropic surfaces (400, 450, ... 650, 700). We chose cubic spline interpolation as the most accurate way to do this. See Figures 8.7 to 8.9, where you can see the data plotted against θ on two selected days over GC 15, and using in those cases both linear and cubic interpolation methods for comparison of results.

Once the cubic spline interpolation method was selected, we interpolated T, T_{ICE} and T_{NAT} data from 18 pressure surfaces onto the 7 isentropes. Please note that the pressure range 215-21 hPa was chosen in order to cover a isentropic region larger than 400-700

K and ensure that interpolation of data was made on a 'central' region (the 400-700 K region actually) of this θ larger region (~300-1000 K); that is to say, just to avoid doing extrapolation of data, which was actually never the case.

Sets of Figures from 8.10 to 8.17 and 8.18 to 8.24 show mean T_{ice} and T_{NAT}, respectively, as function of time and potential temperature in 2007 derived from Aura MLS H_2O zonally averaged over Antarctic GCs 1 to 30 and HNO_3 set constant at 10 ppbv. These data are presented in *Alexander et al.* [2011] as Hövmoller diagrams along with gravity wave and PSC data.

Mean Temperature as function of time and potential temperature in 2007 derived from Aura MLS measurements zonally averaged over GC 1 to GC30 are shown in Figures 8.25 to 8.34. These data are shown in Figures 2.13 and 2.14-left- for comparison to COSMIC temperatures in the present work as Hövmoller diagrams.

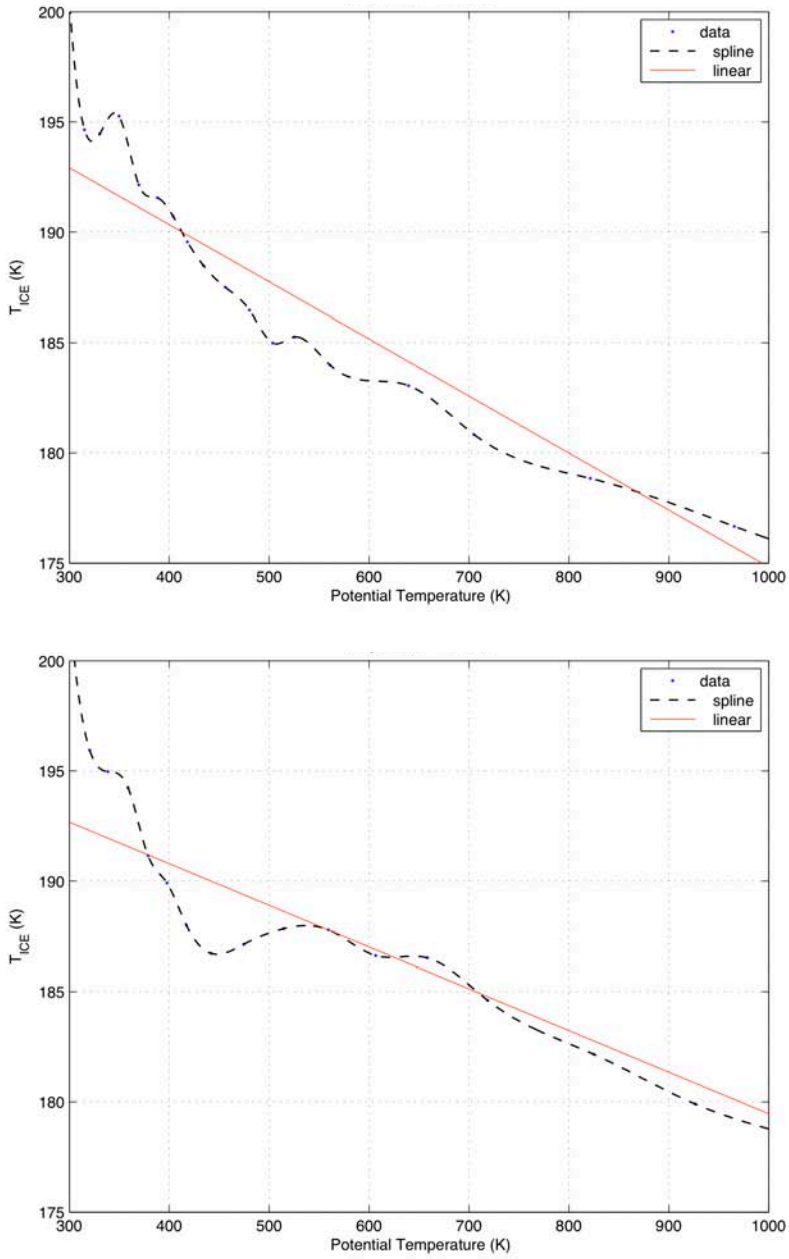

Figure 8.7. Interpolation of zonally averaged T_{ice} versus Potential Temperature information derived from Aura MLS over the Antarctic Grid Cell 15 on day 200 [Upper] and 300 [Bottom] in 2007.

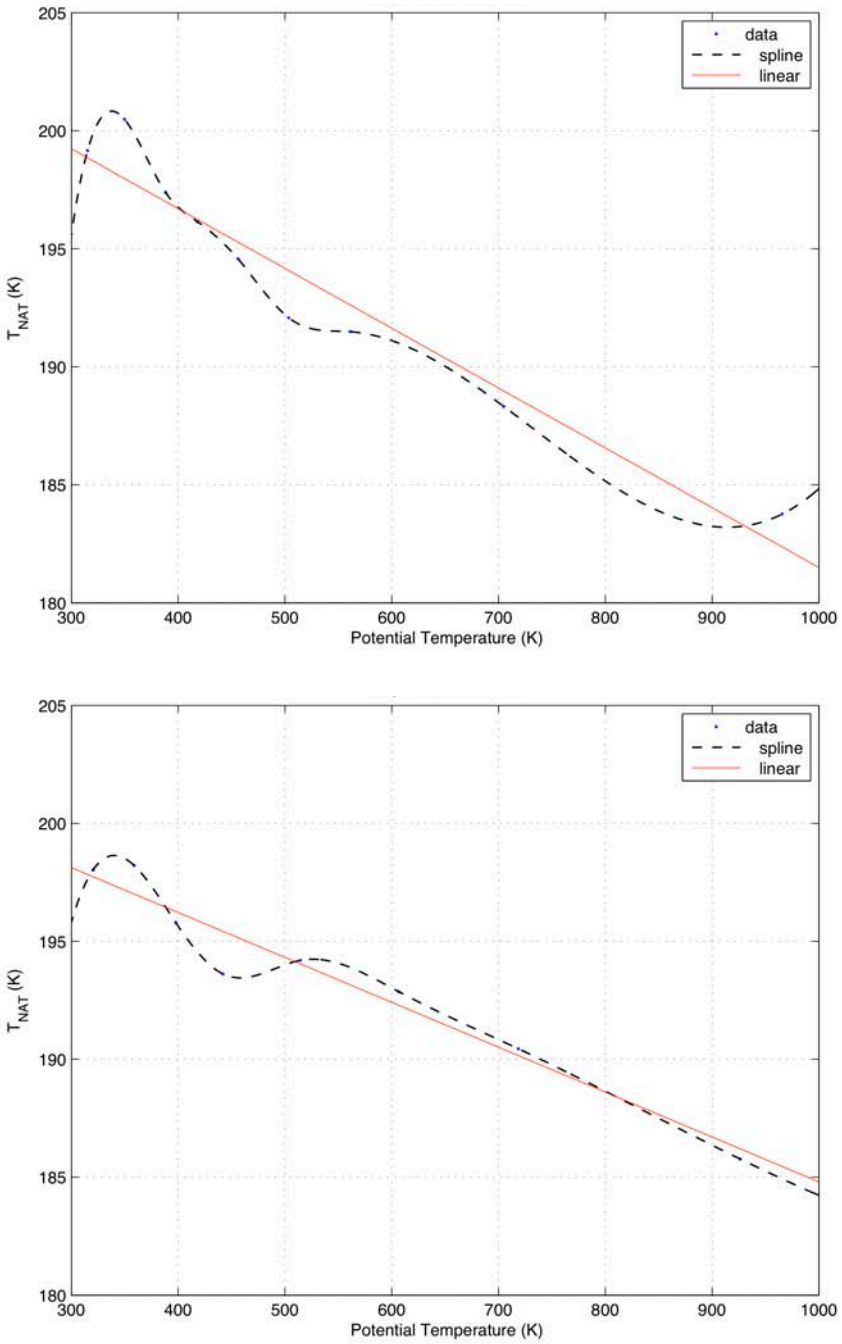

Figure 8.8. Interpolation of zonally averaged T_{NAT} versus Potential Temperature information derived from Aura MLS over the Antarctic Grid Cell 15 on day 200 [Upper] and 300 [Bottom] in 2007.

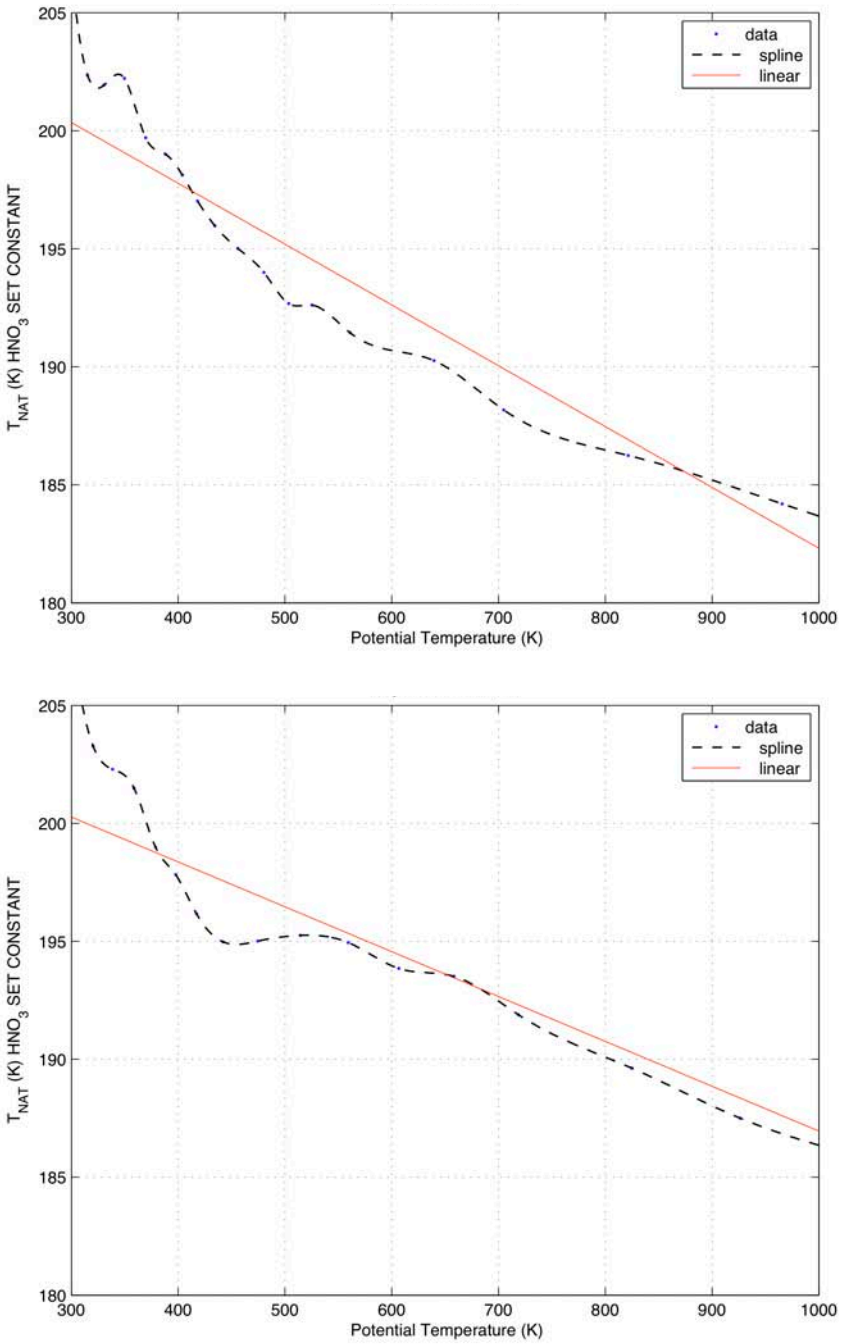

Figure 8.9. Like Figure 8.8, but for T_{NAT} as function of Aura MLS HNO_3 set constant (10 ppbv) instead of zonally averaged over the same grid cell.

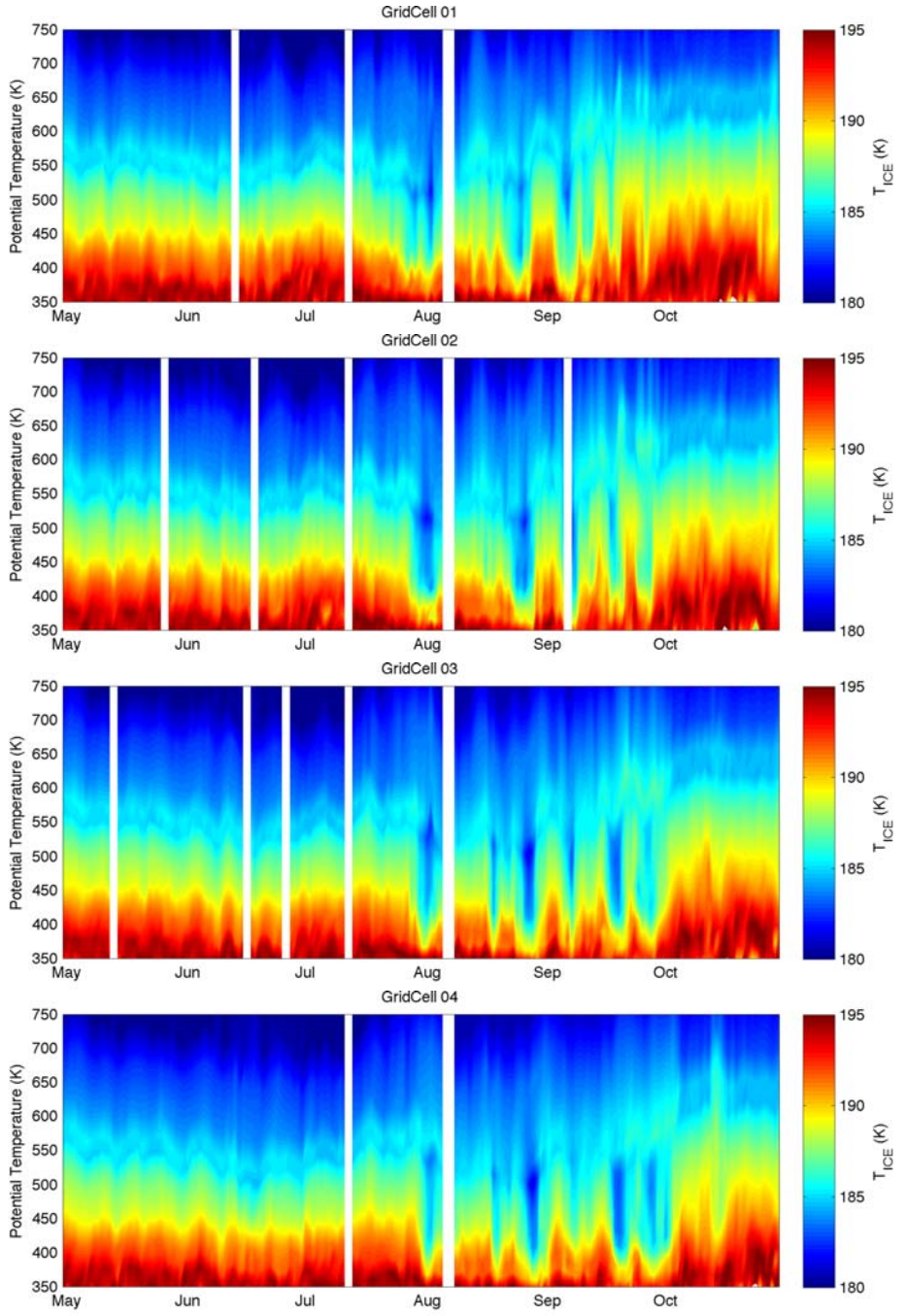

Figure 8.10. Mean T_{ice} as function of time and potential temperature in 2007 derived from Aura MLS H_2O zonally averaged over Antarctic grid cells 1, 2, 3 & 4 (from Top to Bottom).

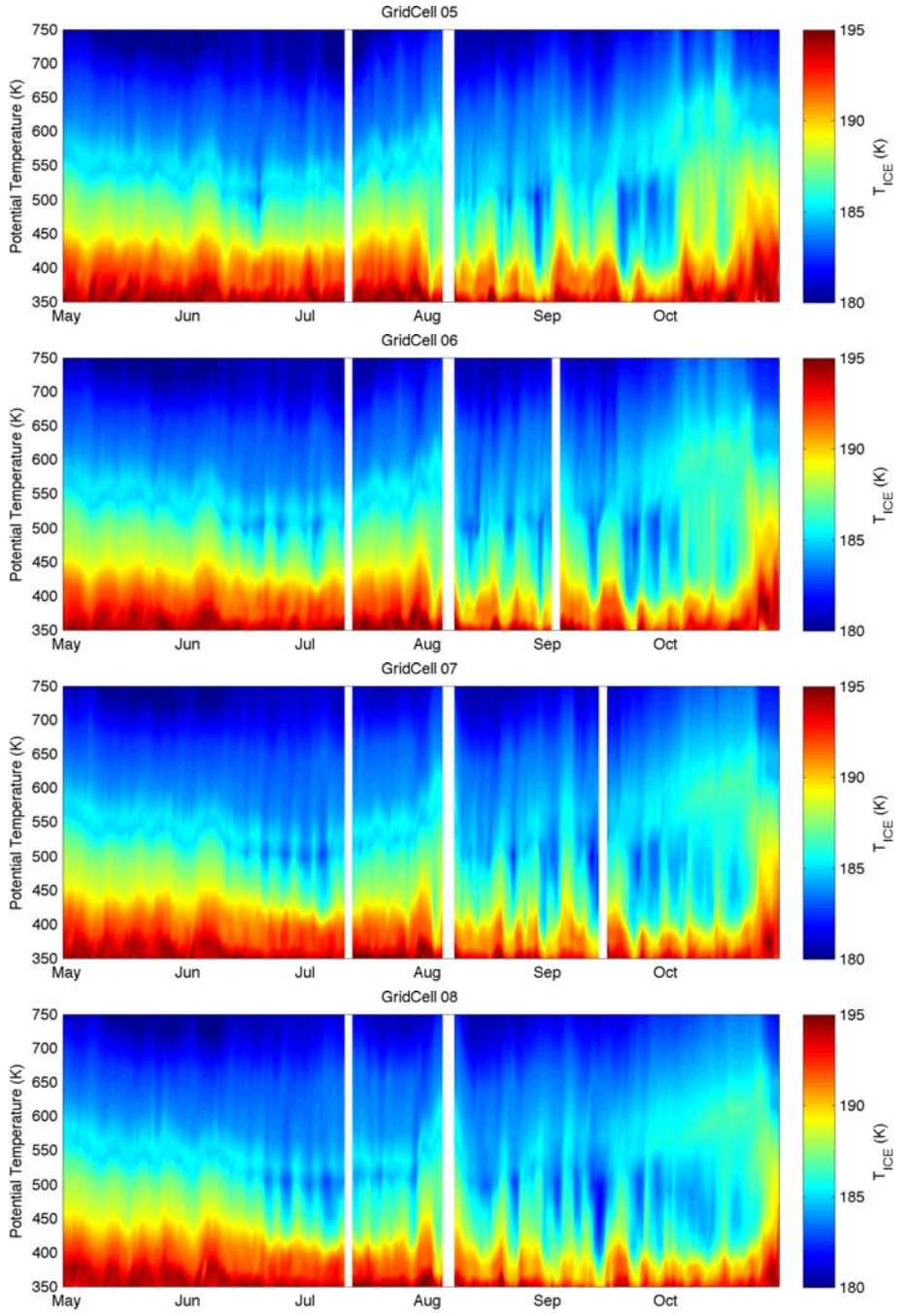

Figure 8.11. Like Figure 8.10, but for Antarctic Grid Cells 5, 6, 7 & 8.

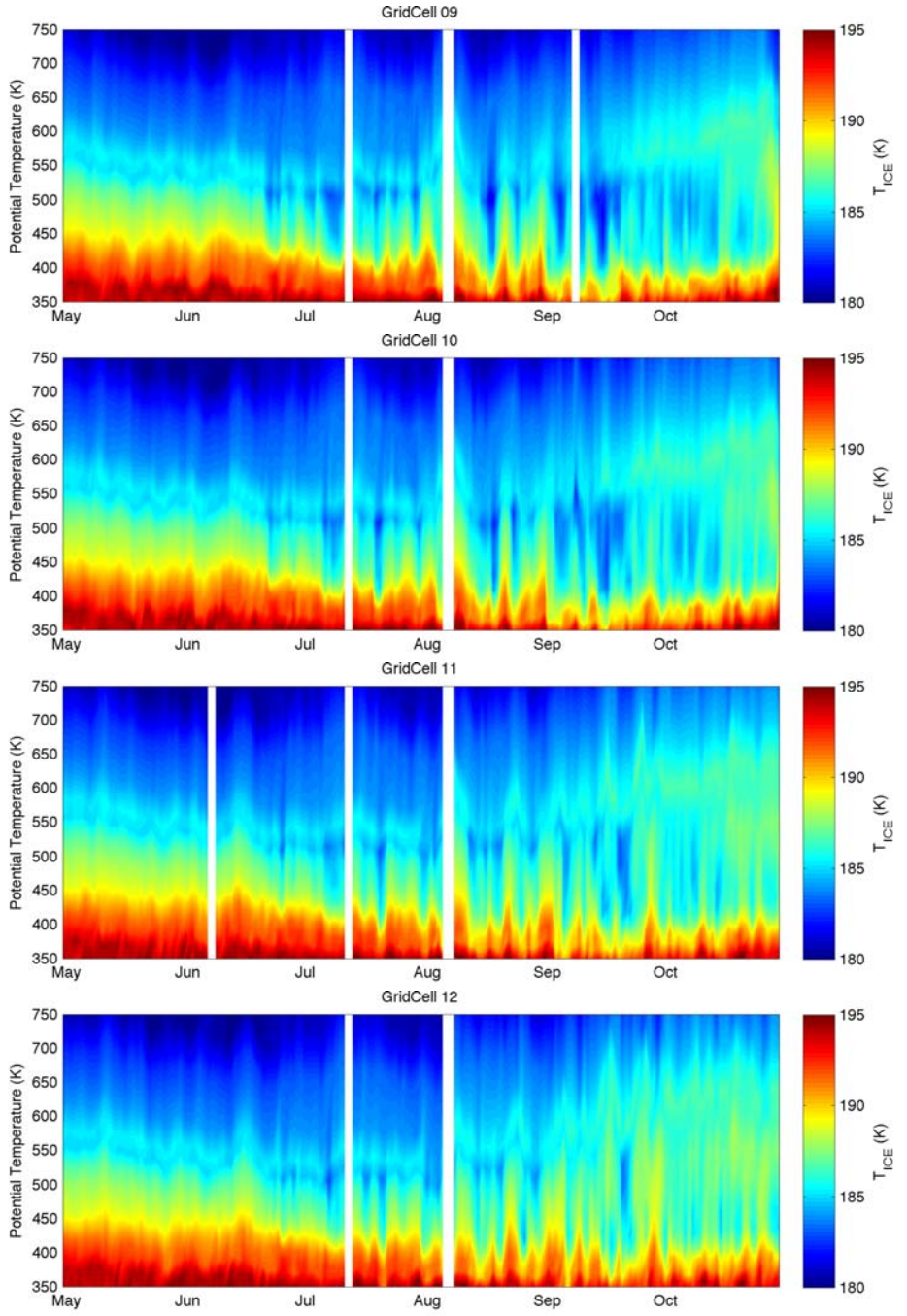

Figure 8.12. Like Figure 8.10, but for Antarctic Grid Cells 9, 10, 11 & 12.

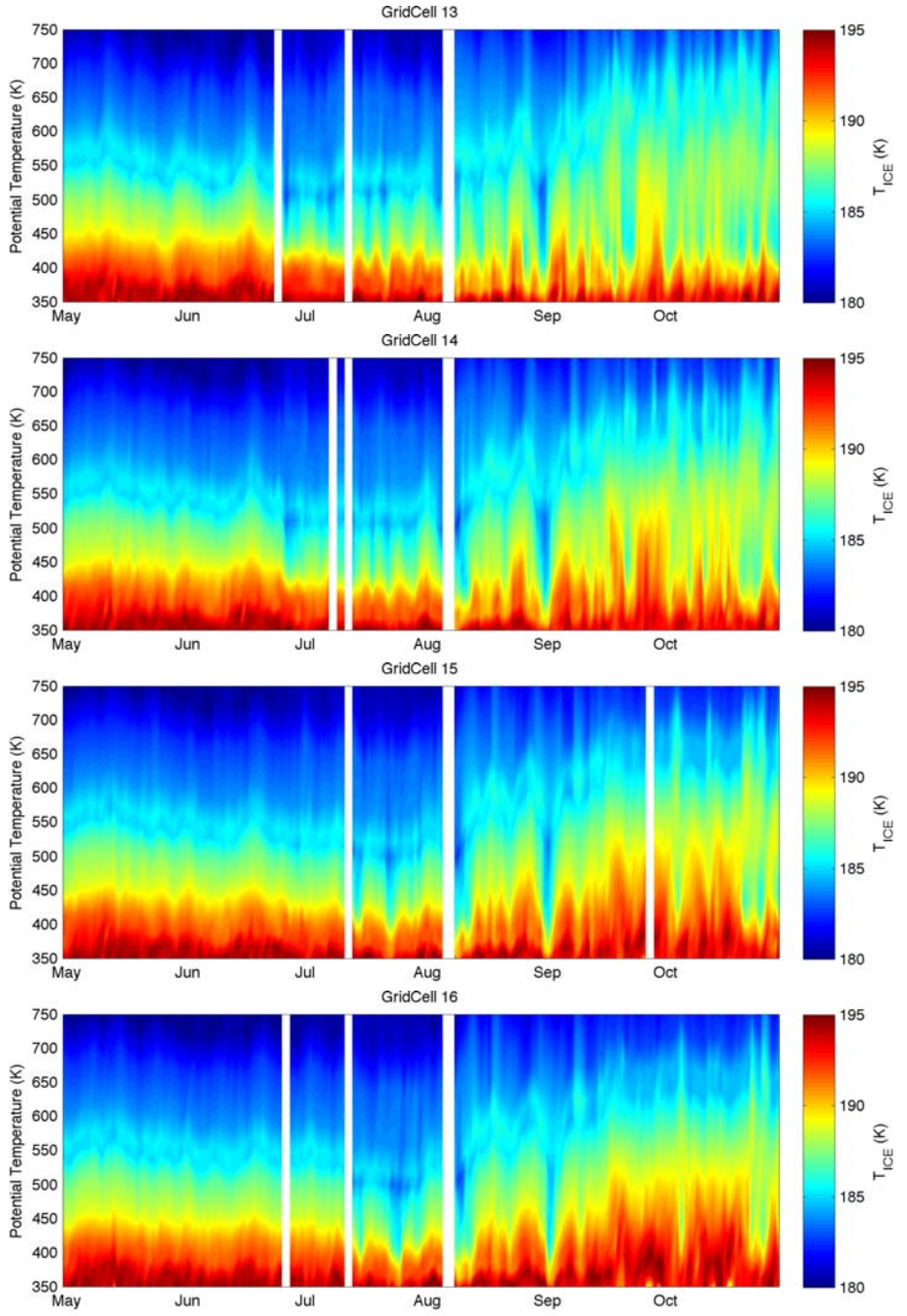

Figure 8.13. Like Figure 8.10, but for Antarctic Grid Cells 13, 14, 15 & 16.

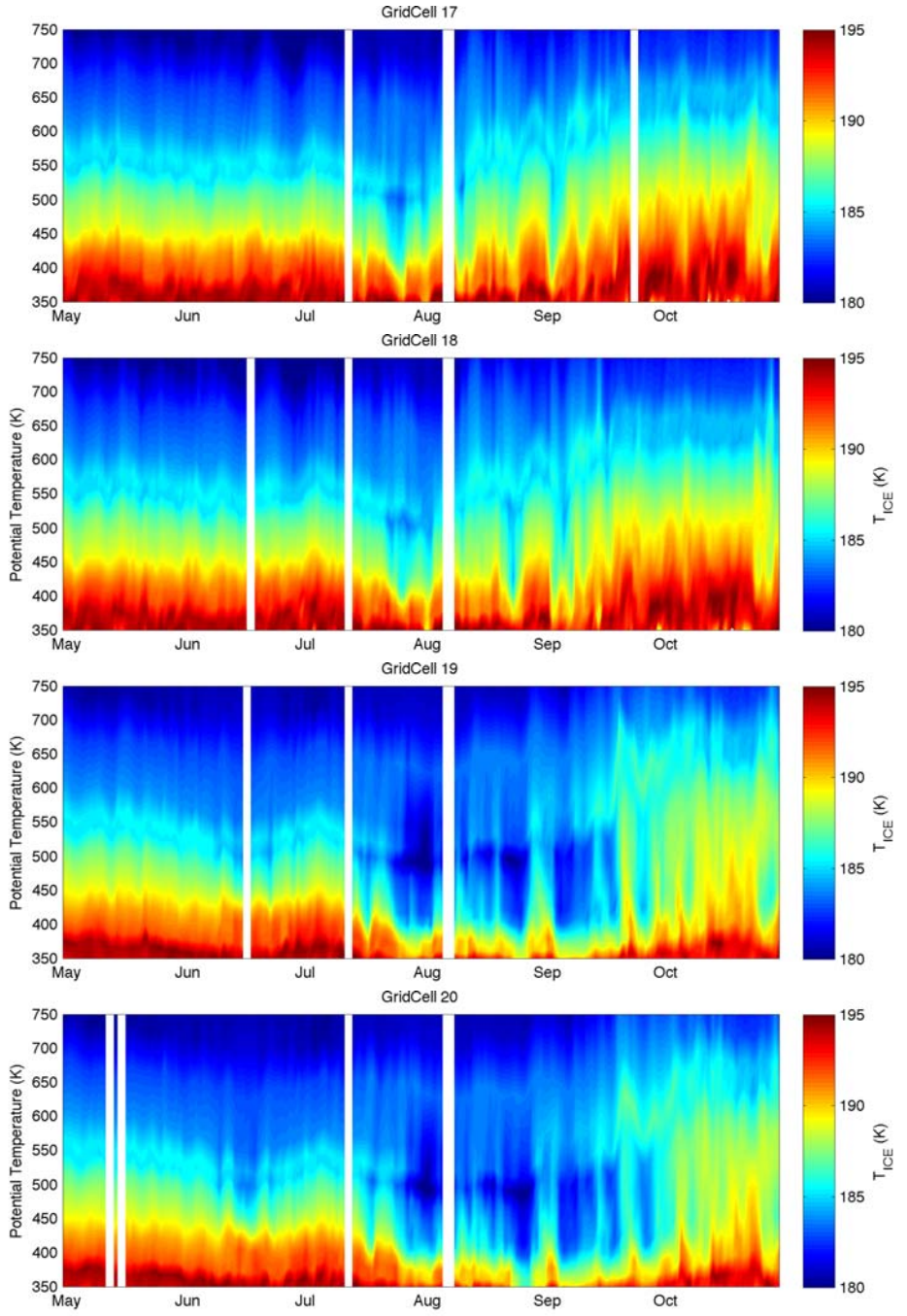

Figure 8.14. Like Figure 8.10, but for Antarctic Grid Cells 17, 18, 19 & 20.

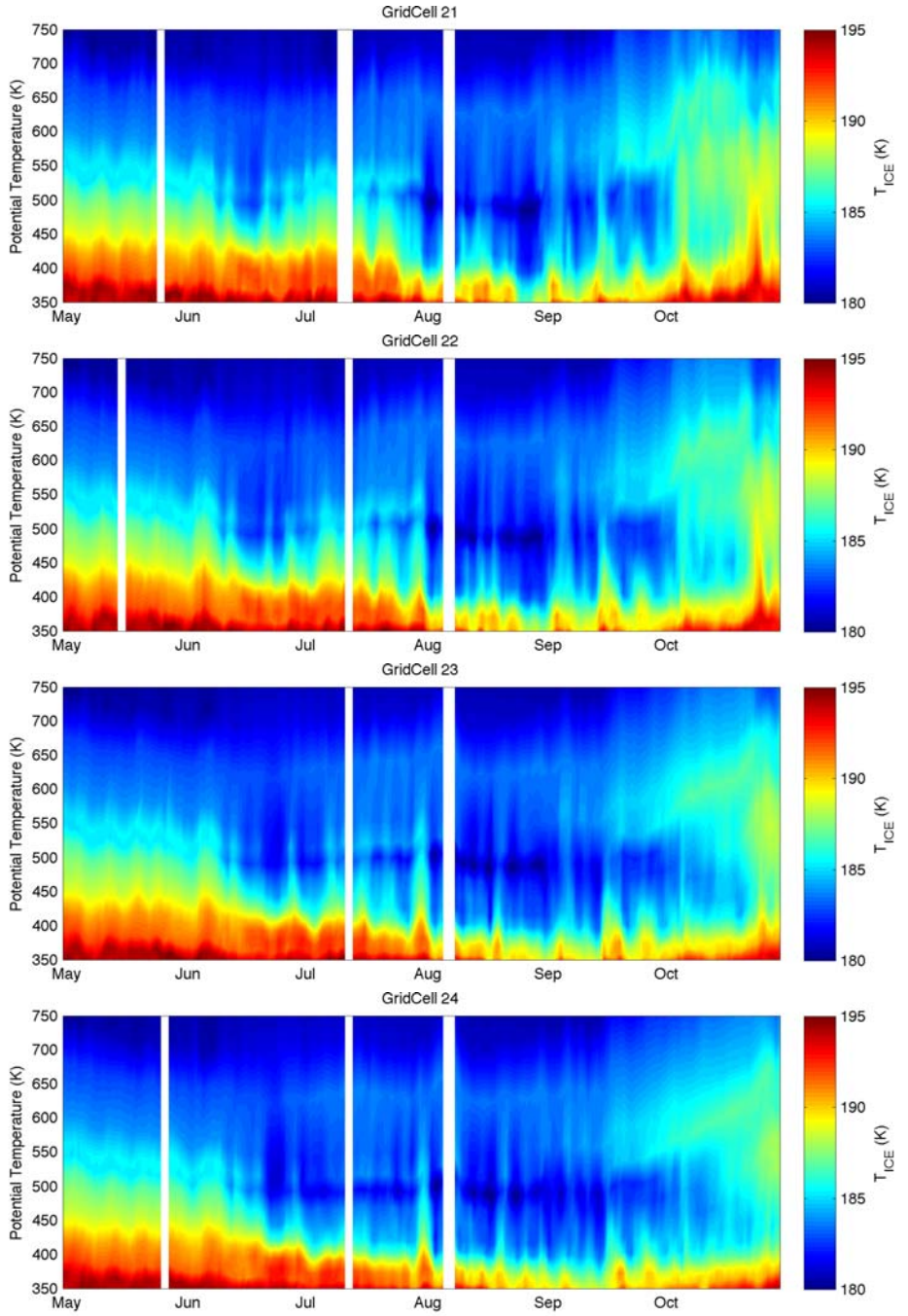

Figure 8.15. Like Figure 8.10, but for Antarctic Grid Cells 21, 22, 23 & 24.

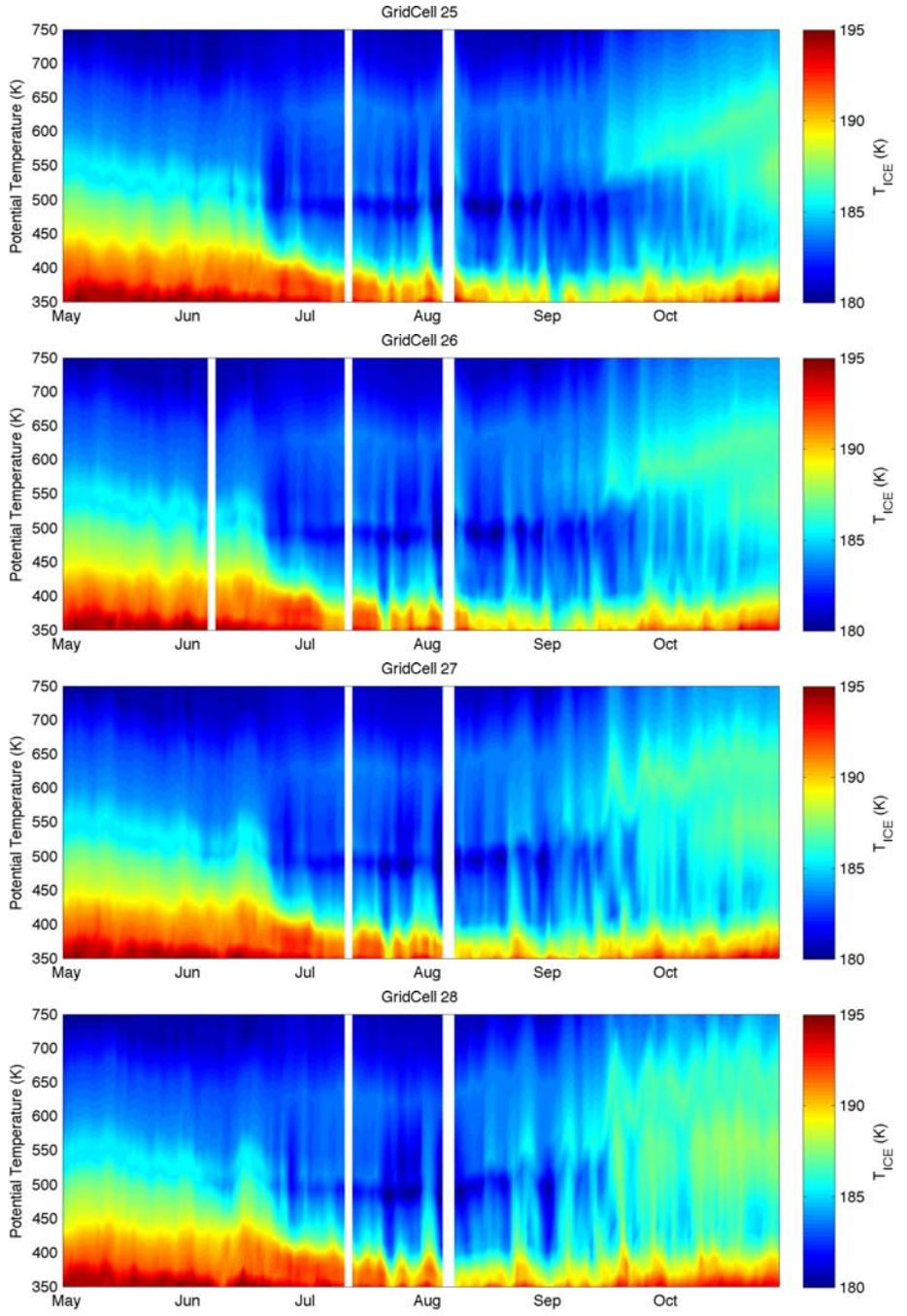

Figure 8.16. Like Figure 8.10, but for Antarctic Grid Cells 25, 26, 27 & 28.

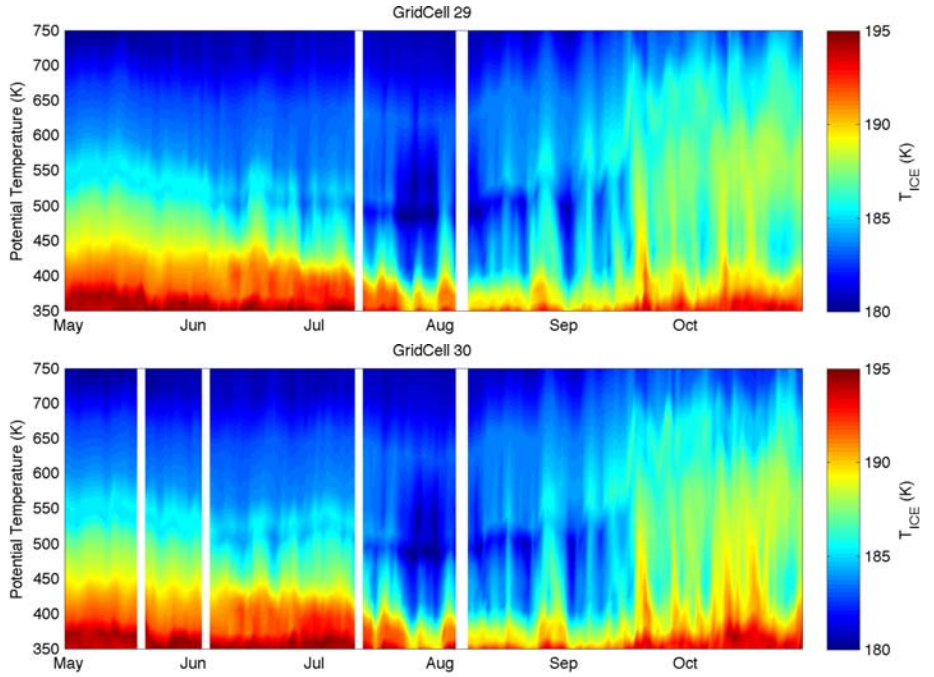

Figure 8.17. Like Figure 8.10, but for Antarctic Grid Cells 29 & 30.

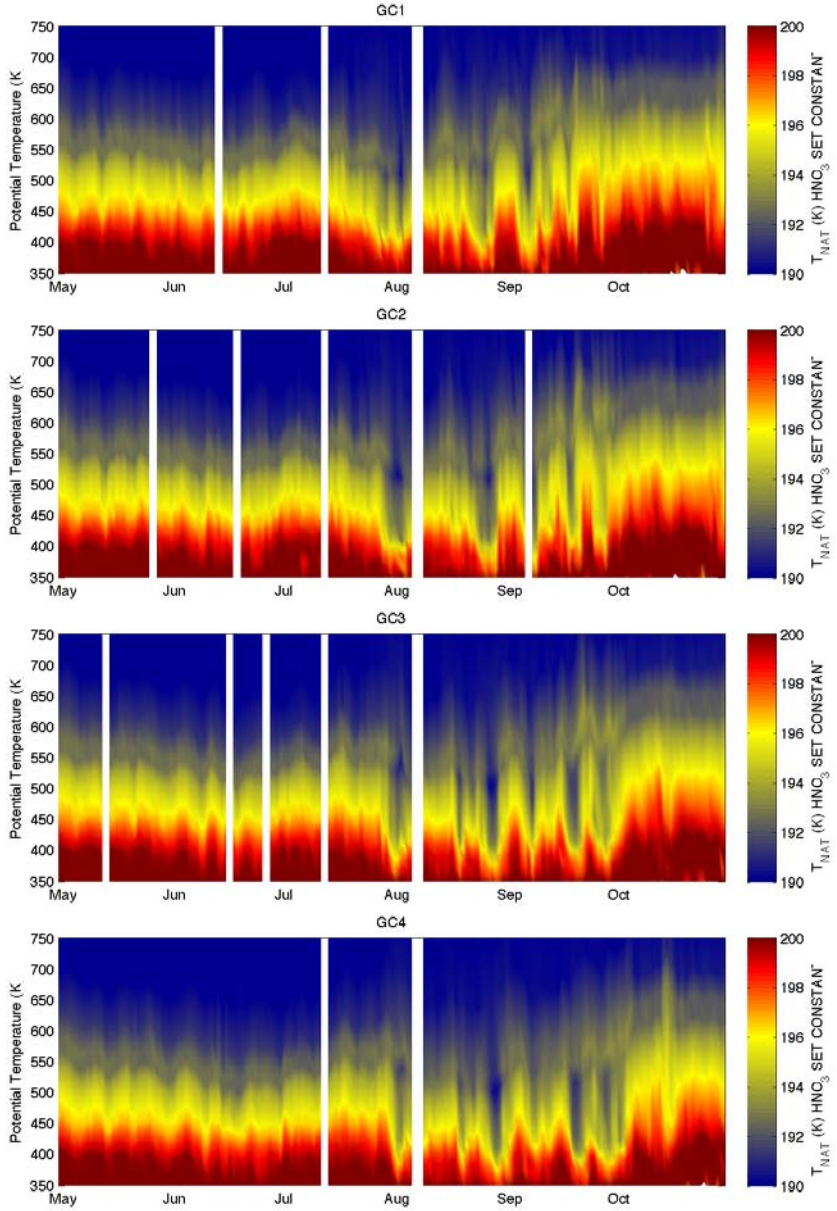

Figure 8.18. Mean T_{NAT} as function of time and potential temperature in 2007 derived from Aura MLS H_2O zonally averaged over Antarctic Grid Cells (GC) 1, 2, 3 & 4 (from Top to Bottom) and HNO_3 set constant at 10 ppbv.

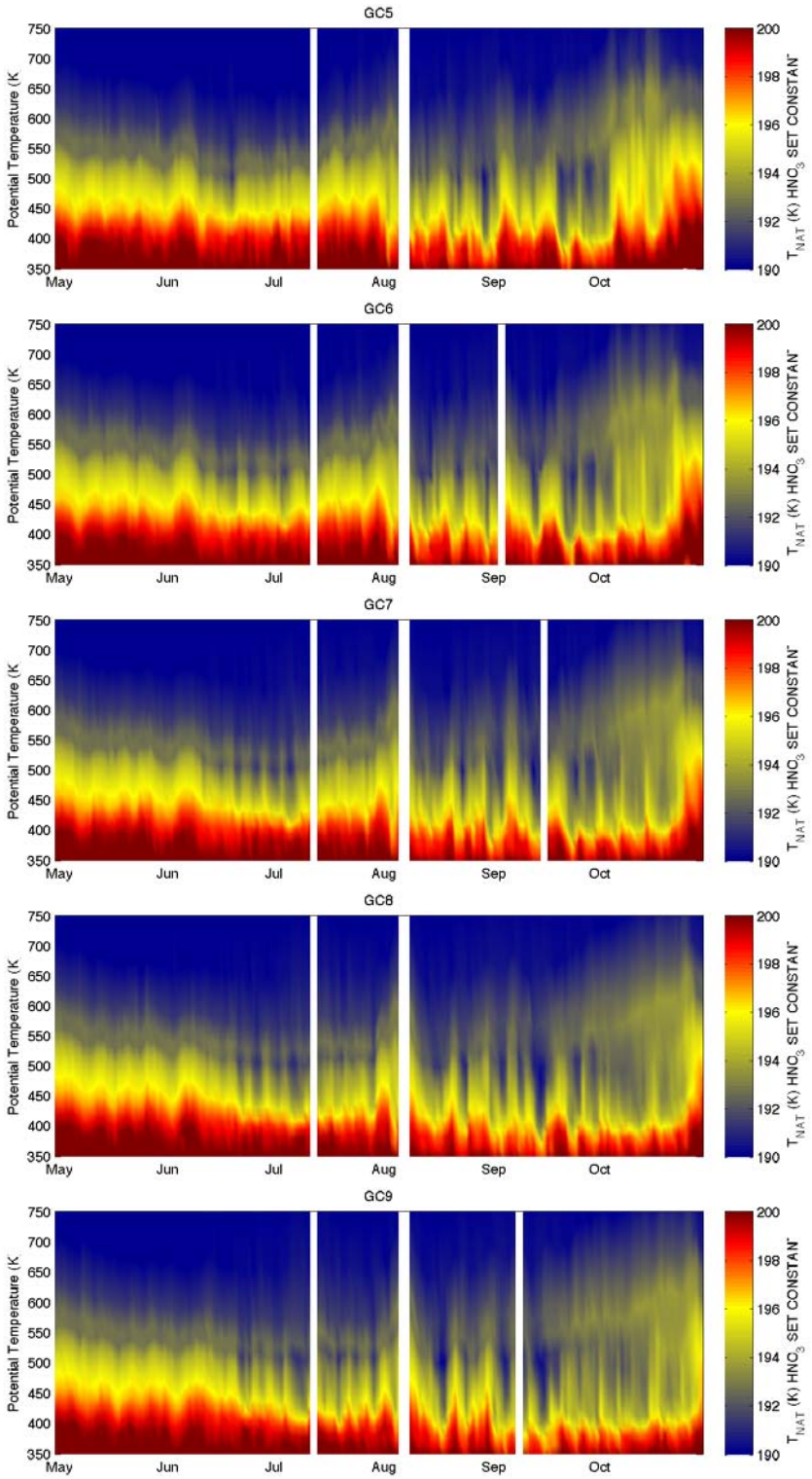

Figure 8.19. Like Figure 8.18, but for Antarctic Grid Cells 5 to 9.

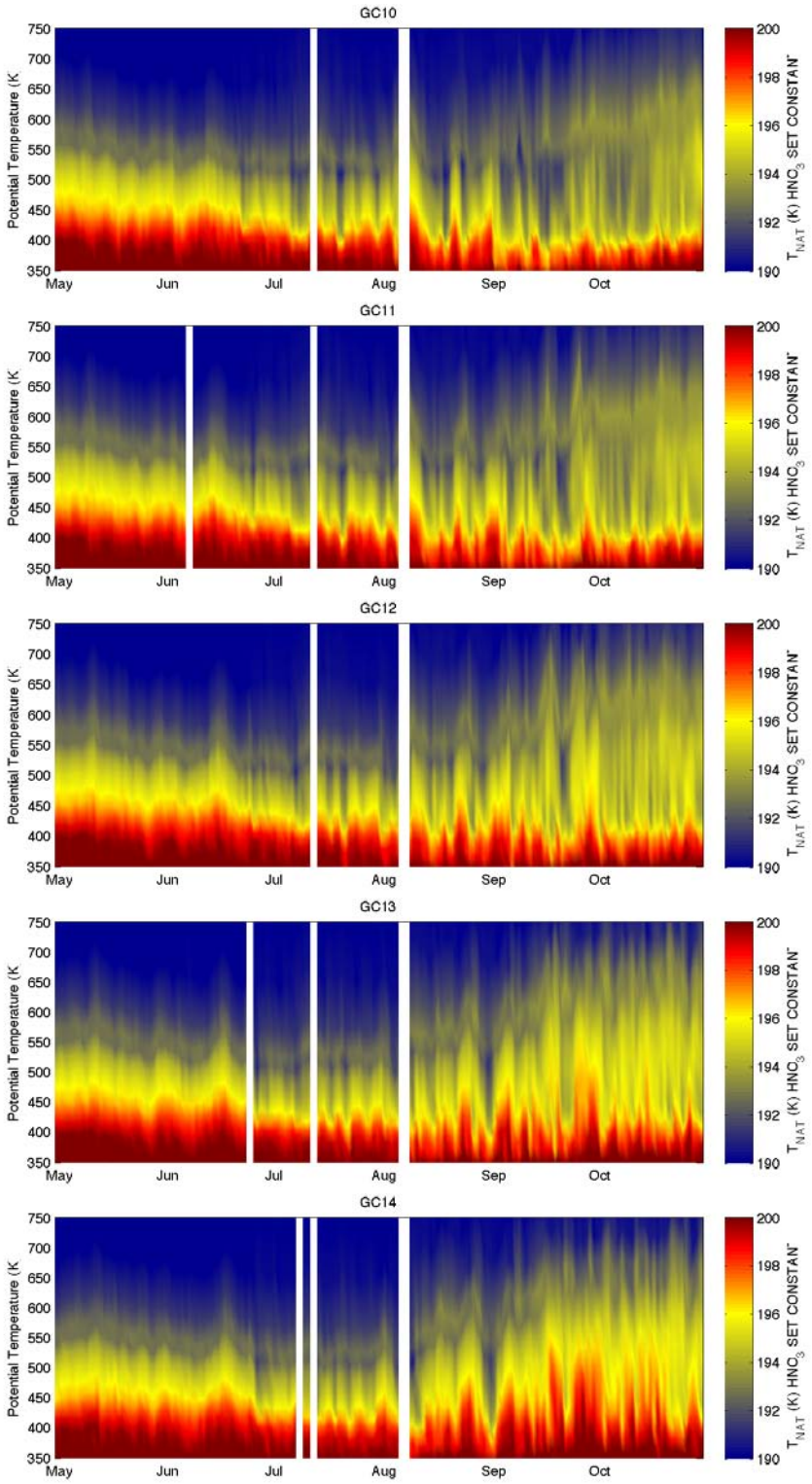

Figure 8.20. Like Figure 8.18, but for Antarctic Grid Cells 10 to 14.

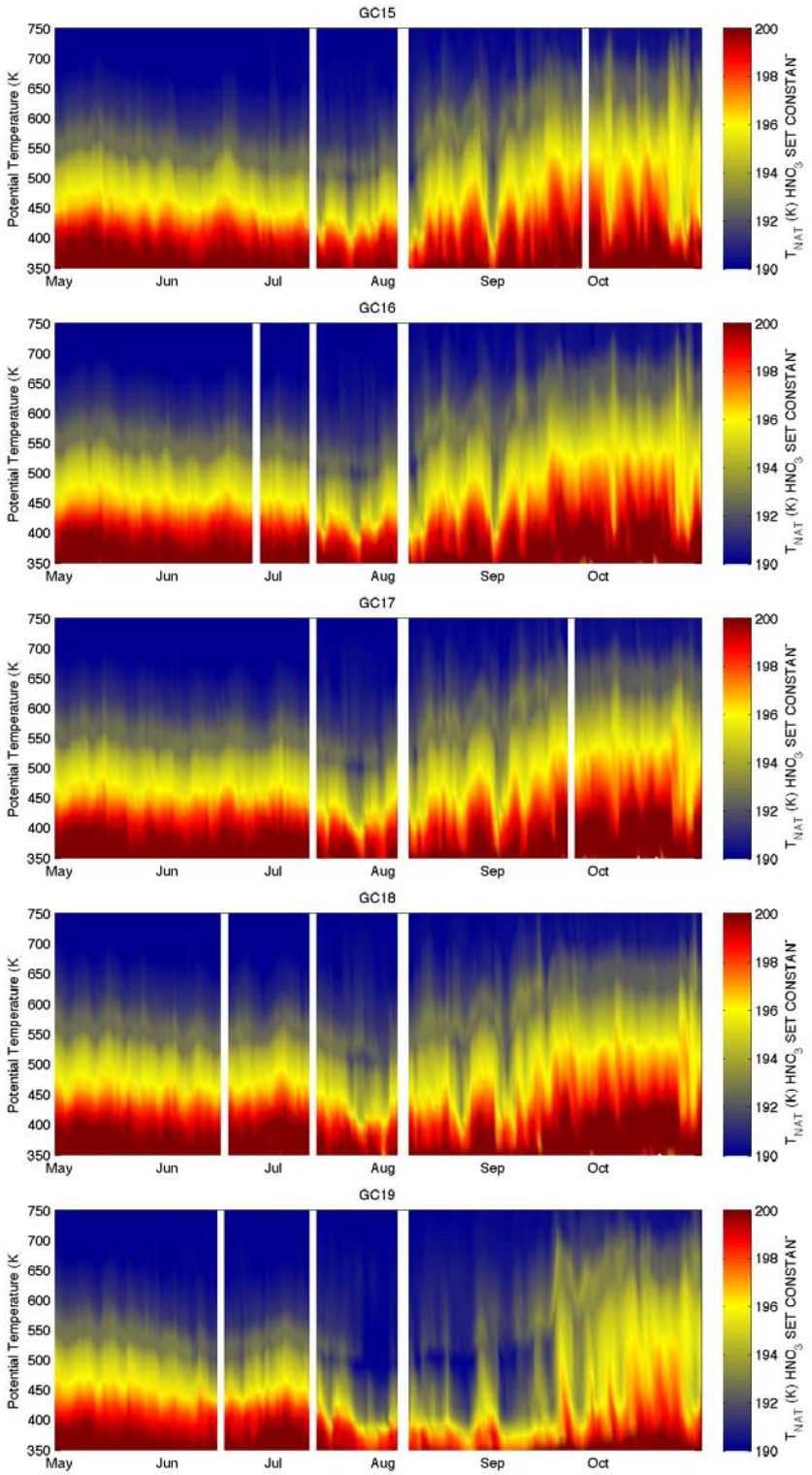

Figure 8.21. Like Figure 8.18, but for Antarctic Grid Cells 15 to 19.

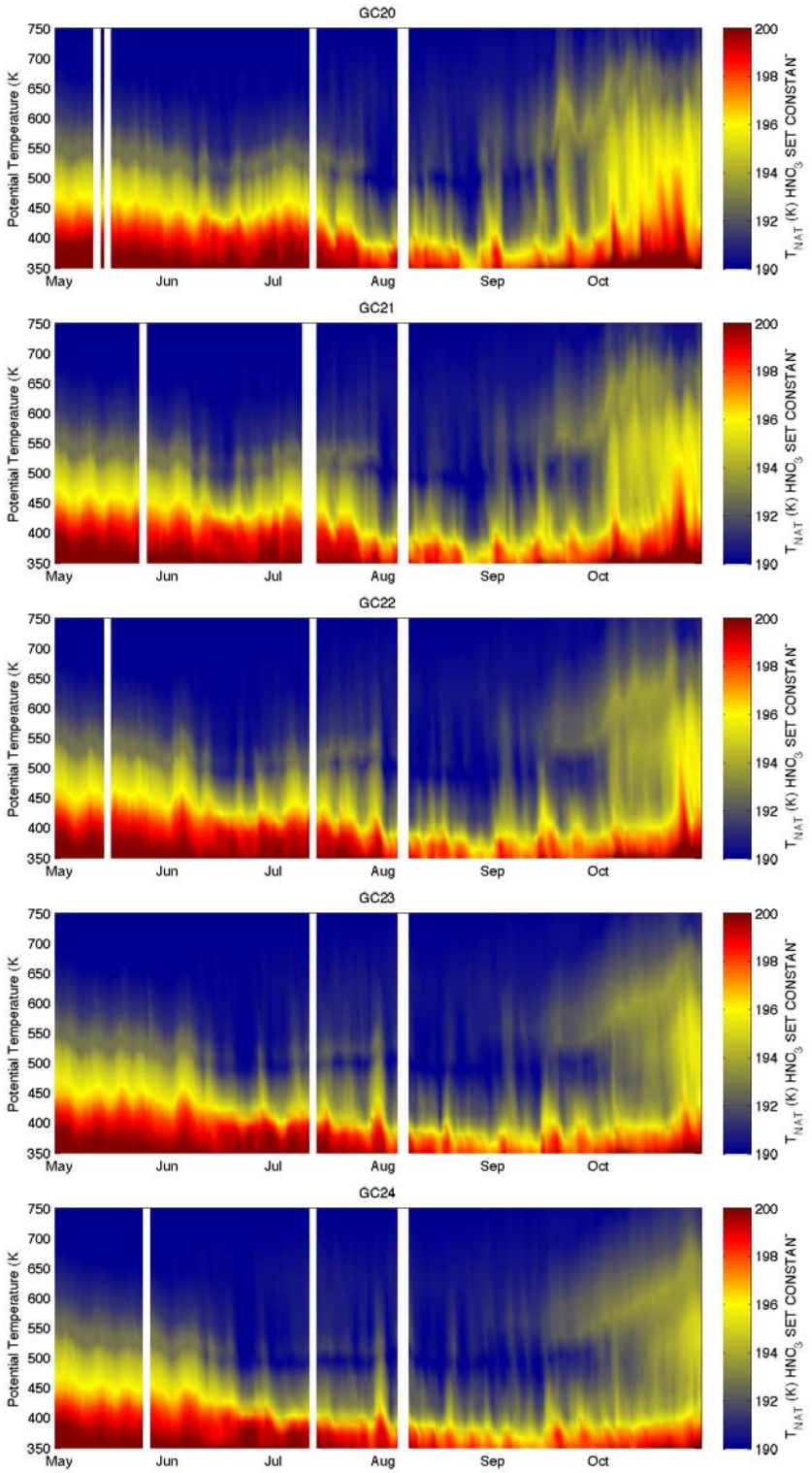

Figure 8.22. Like Figure 8.18, but for Antarctic Grid Cells 20 to 24.

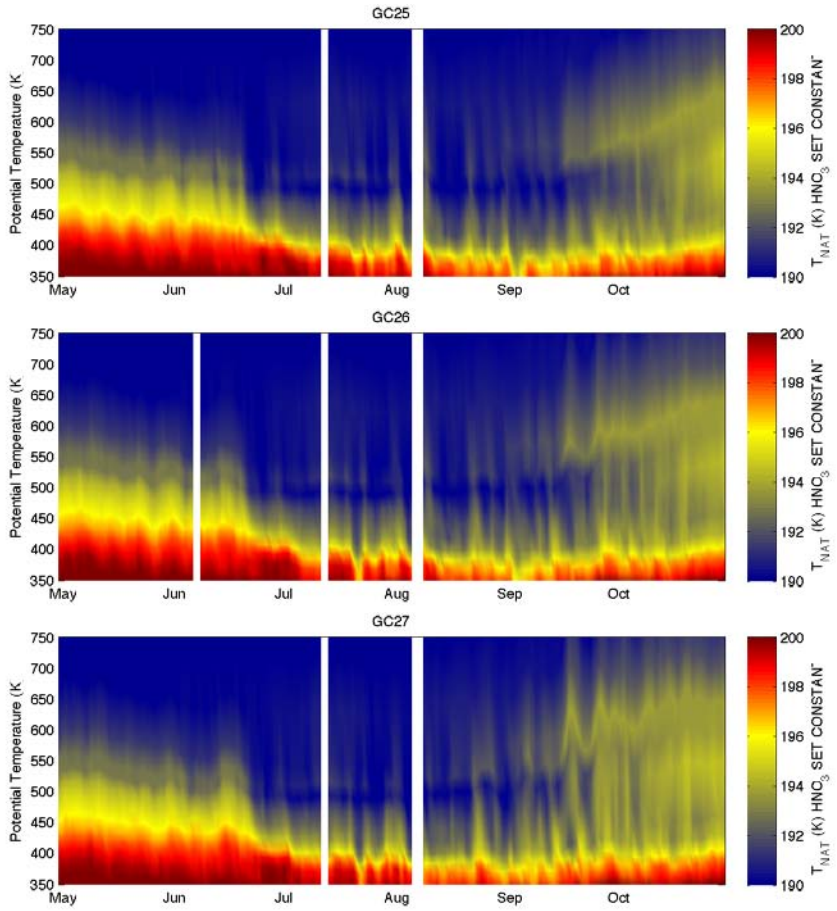

Figure 8.23. Like Figure 8.18, but for Antarctic Grid Cells 25, 26 & 27.

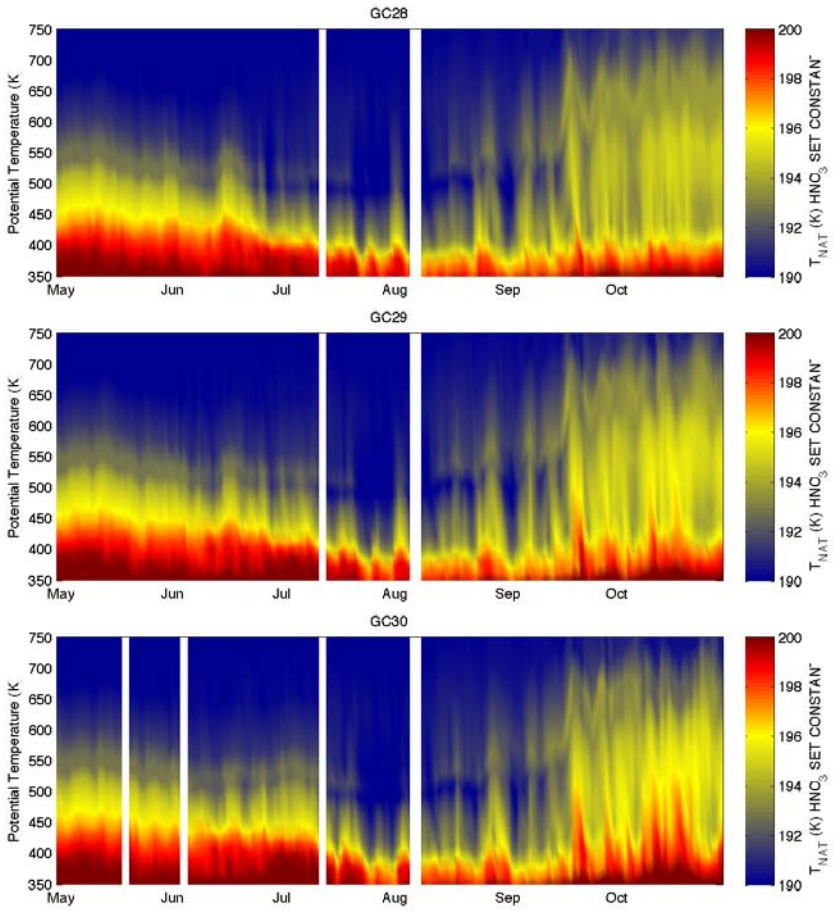

Figure 8.24. Like Figure 8.18, but for Antarctic Grid Cells 28, 29 & 30.

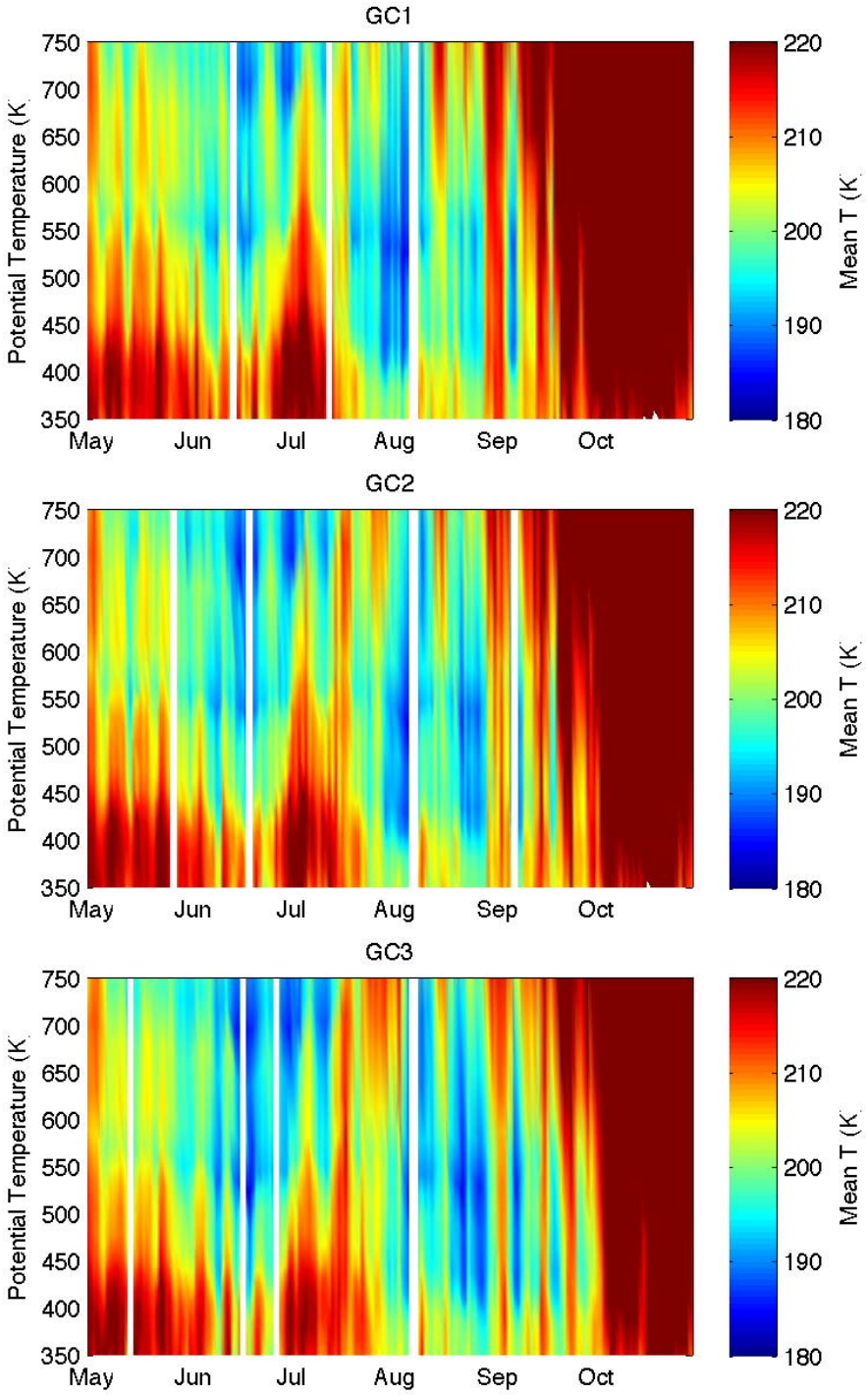

Figure 8.25. Mean MLS Temperature as function of time and potential temperature in 2007 zonally averaged over Antarctic Grid Cells (GC) 1, 2 & 3 (from Top to Bottom).

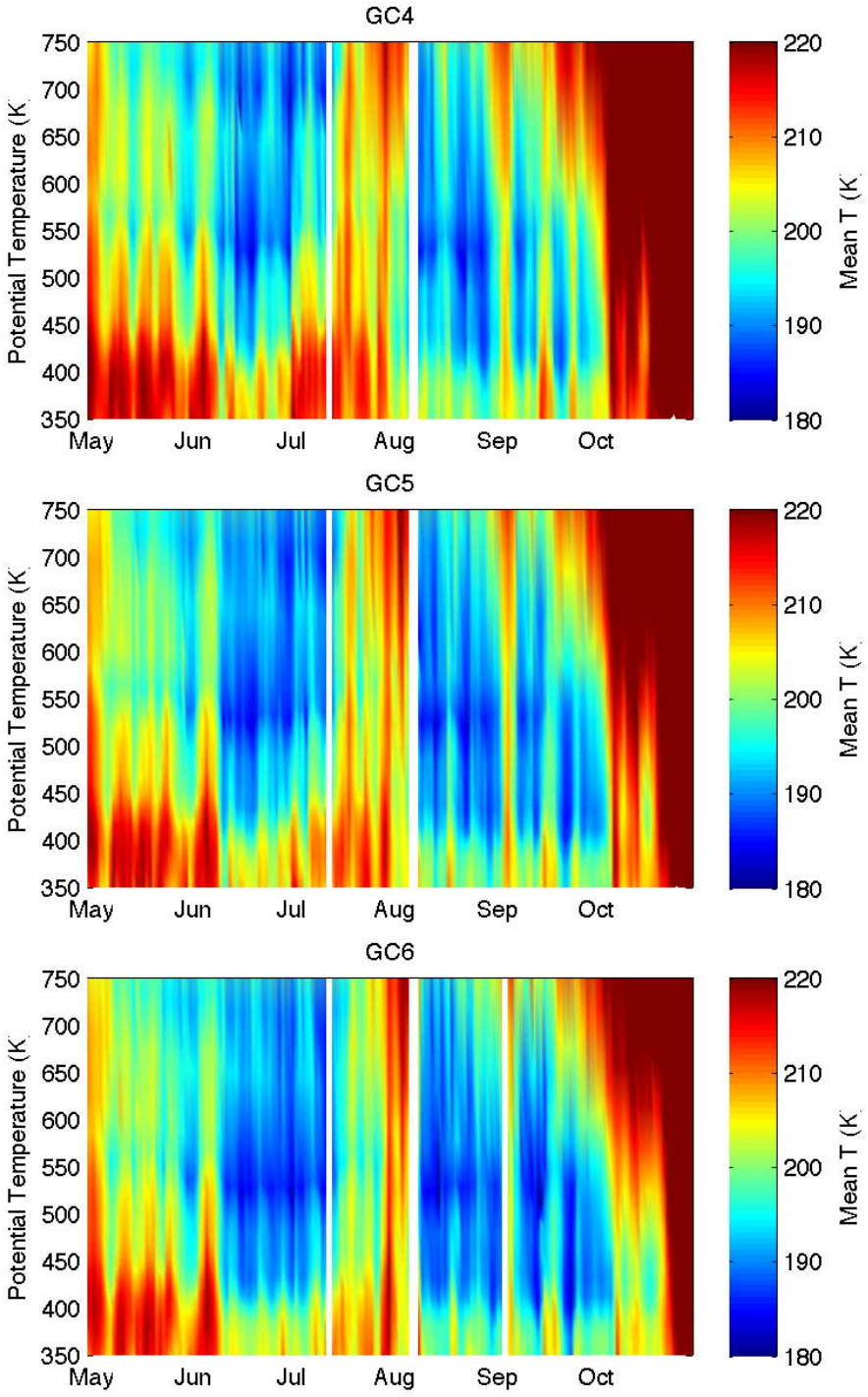

Figure 8.26. Like Figure 8.25, but for Antarctic Grid Cells 4, 5 & 6.

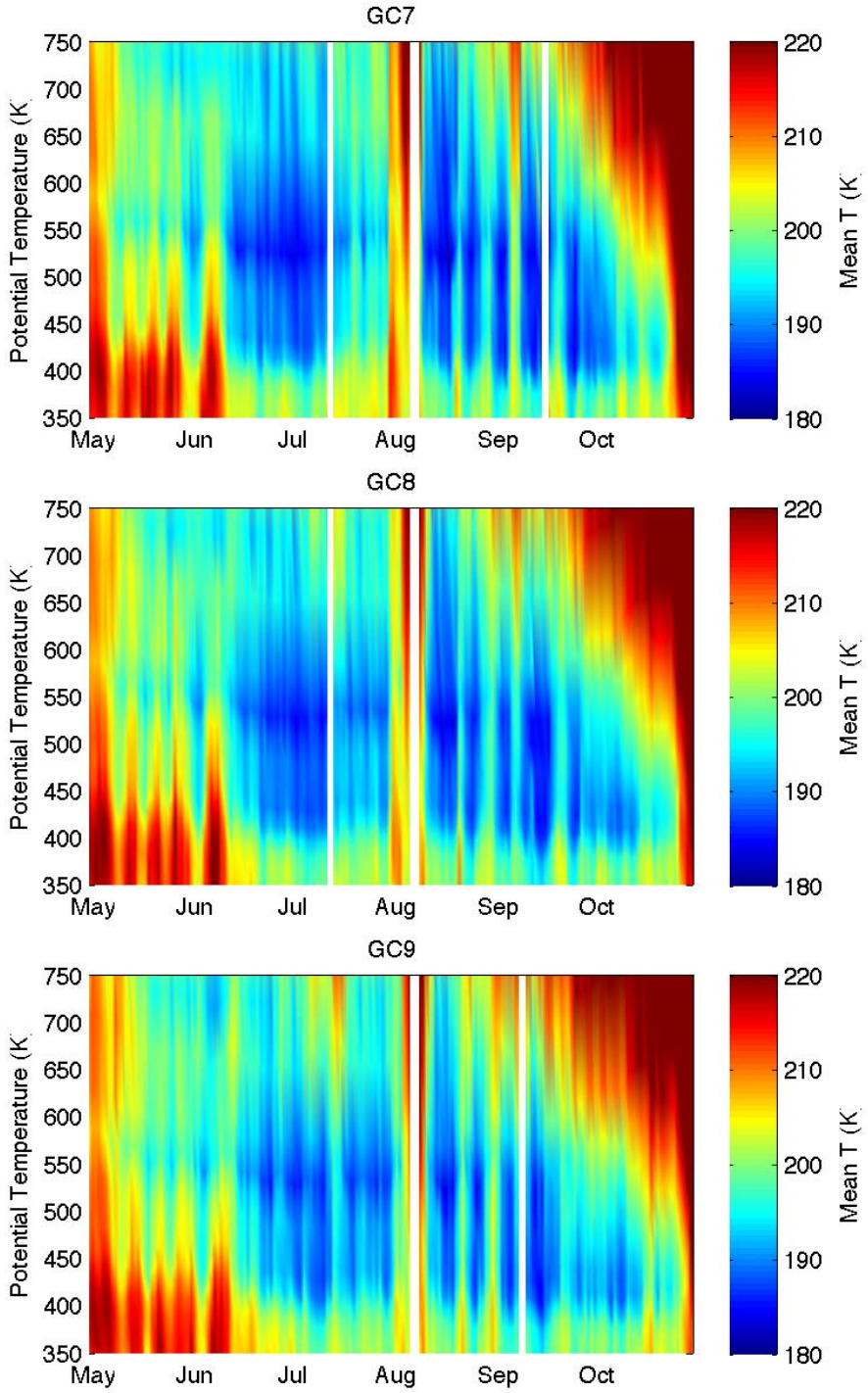

Figure 8.27. Like Figure 8.25, but for Antarctic Grid Cells 7, 8 & 9.

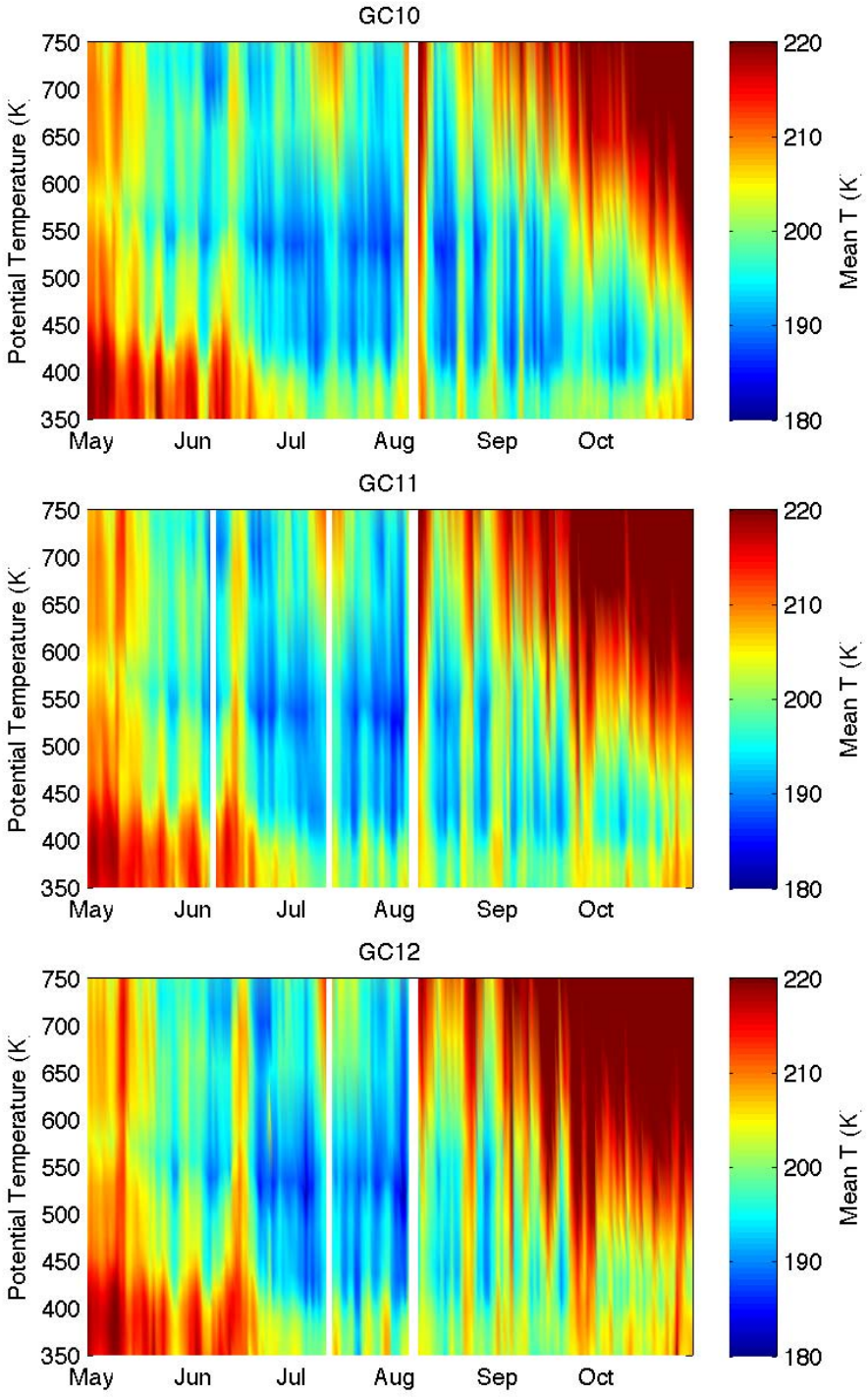

Figure 8.28. Like Figure 8.25, but for Antarctic Grid Cells 10, 11 & 12.

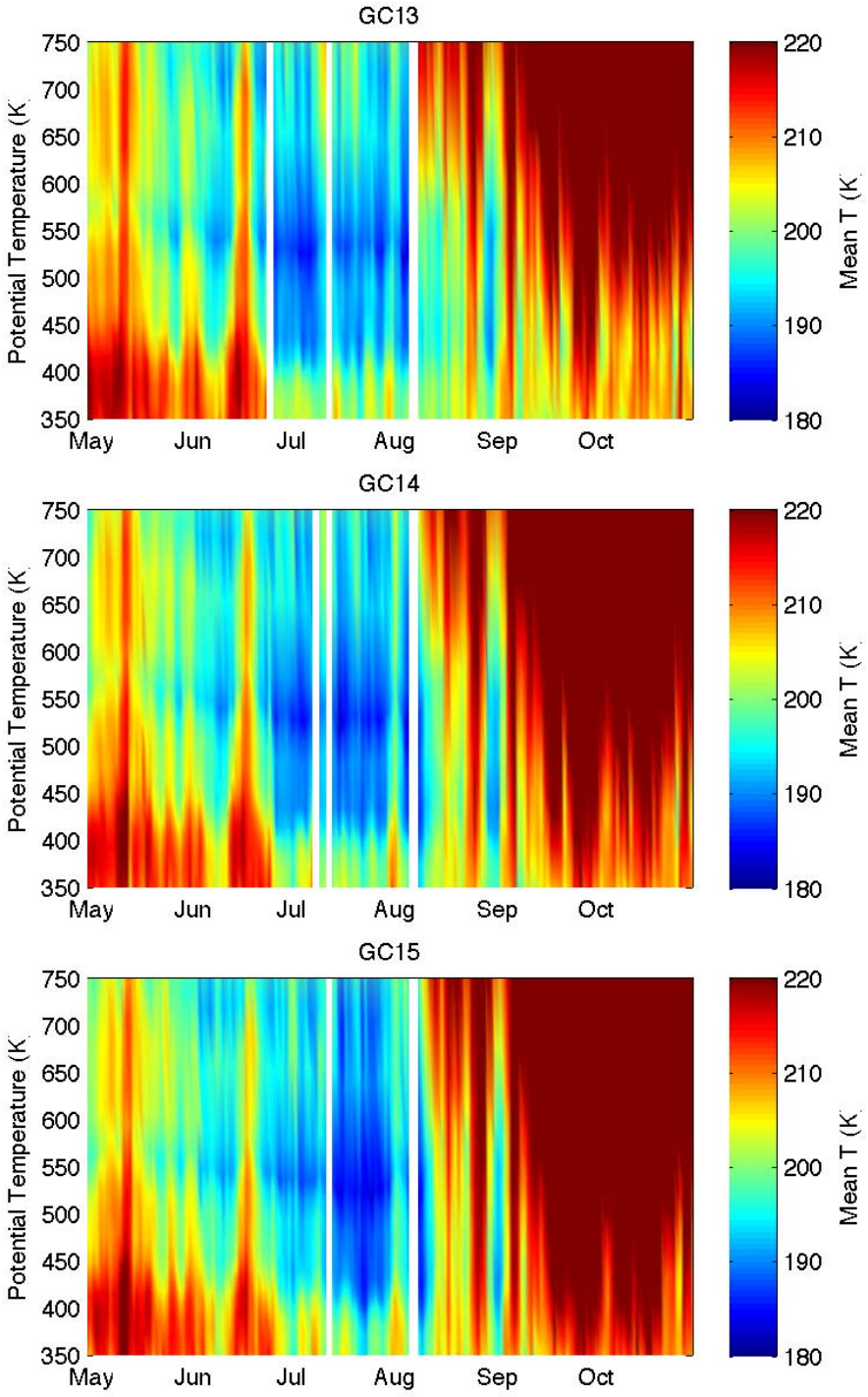

Figure 8.29. Like Figure 8.25, but for Antarctic Grid Cells 13, 14 & 15.

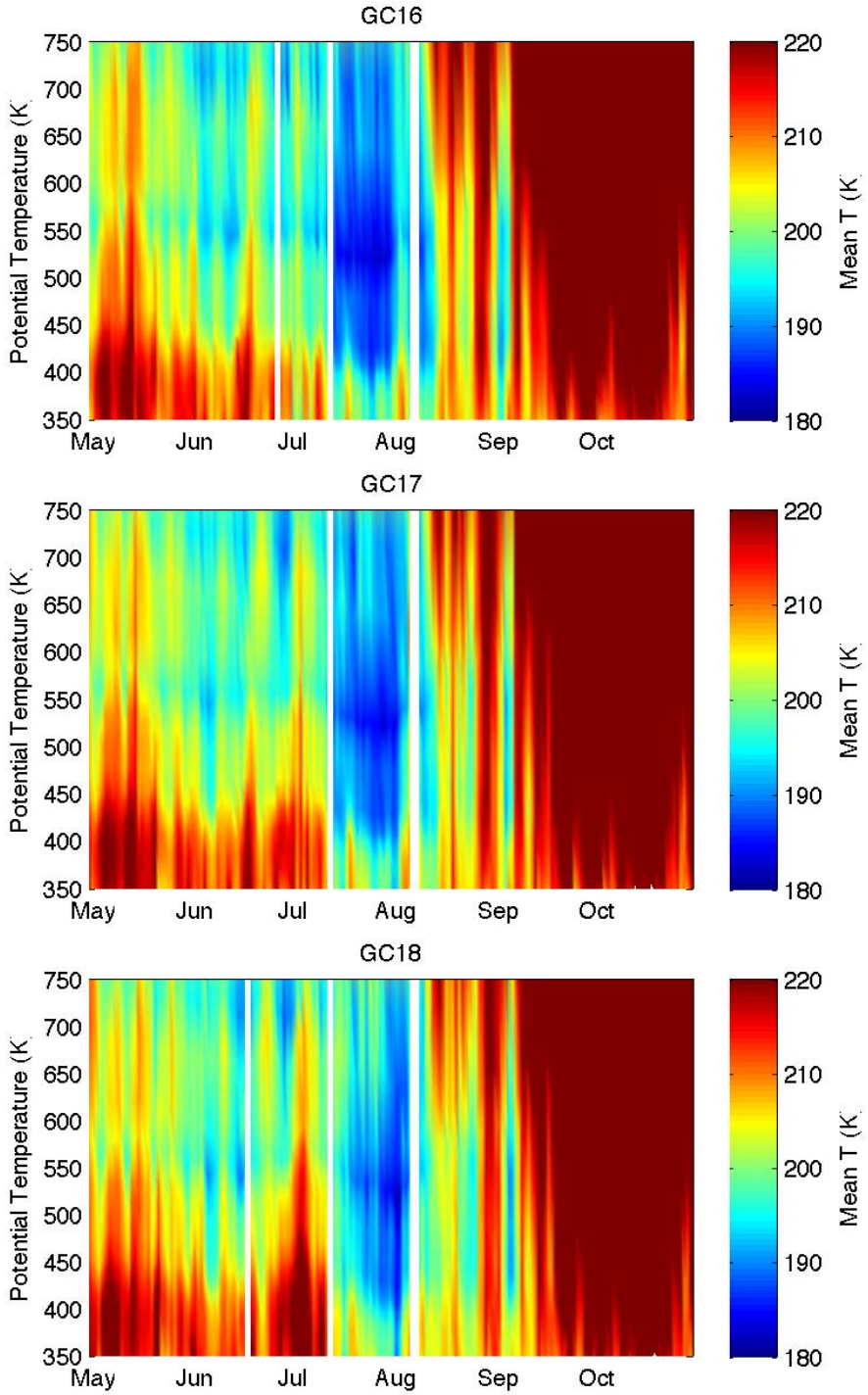

Figure 8.30. Like Figure 8.25, but for Antarctic Grid Cells 16, 17 & 18.

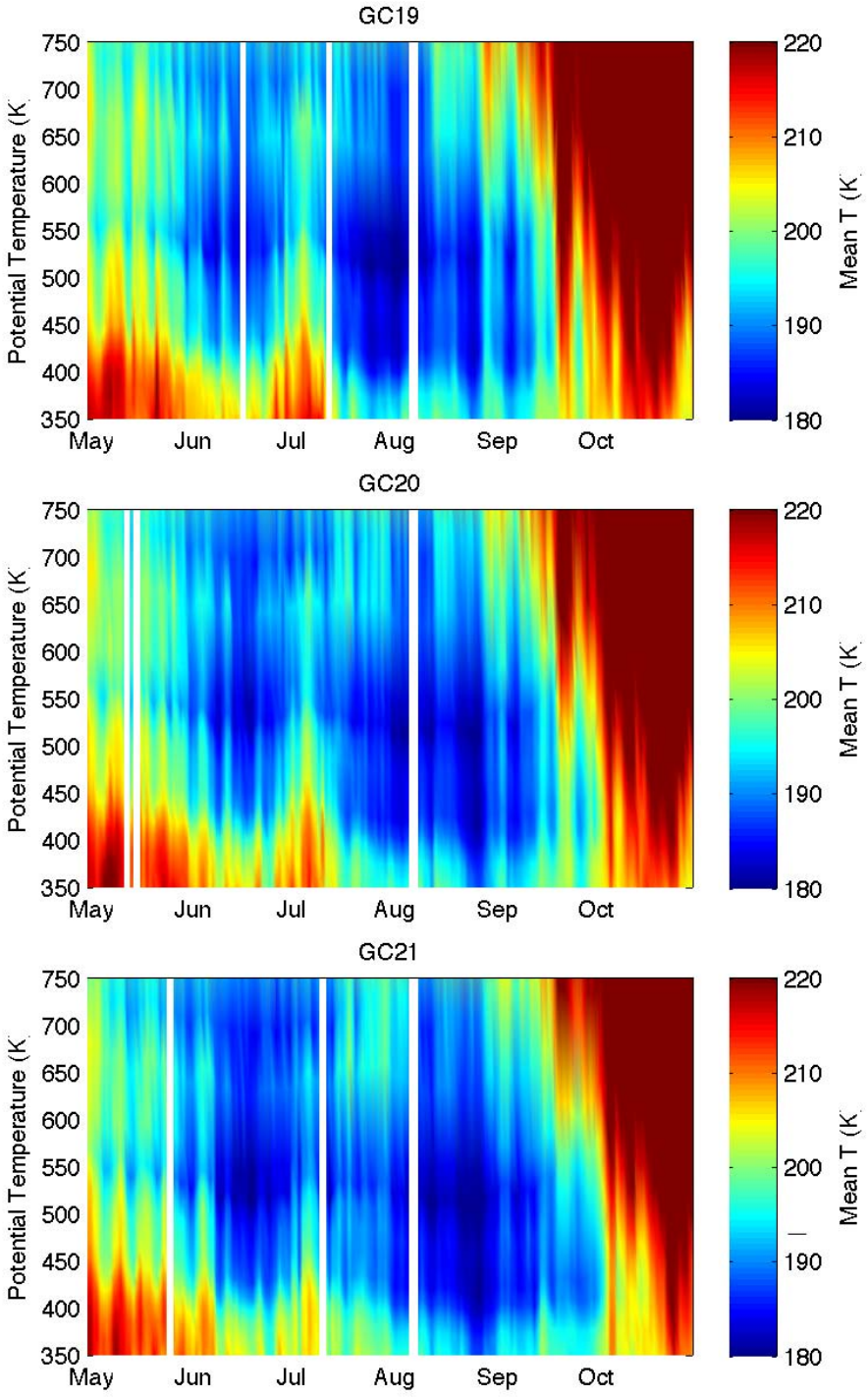

Figure 8.31. Like Figure 8.25, but for Antarctic Grid Cells 19, 20 & 21.

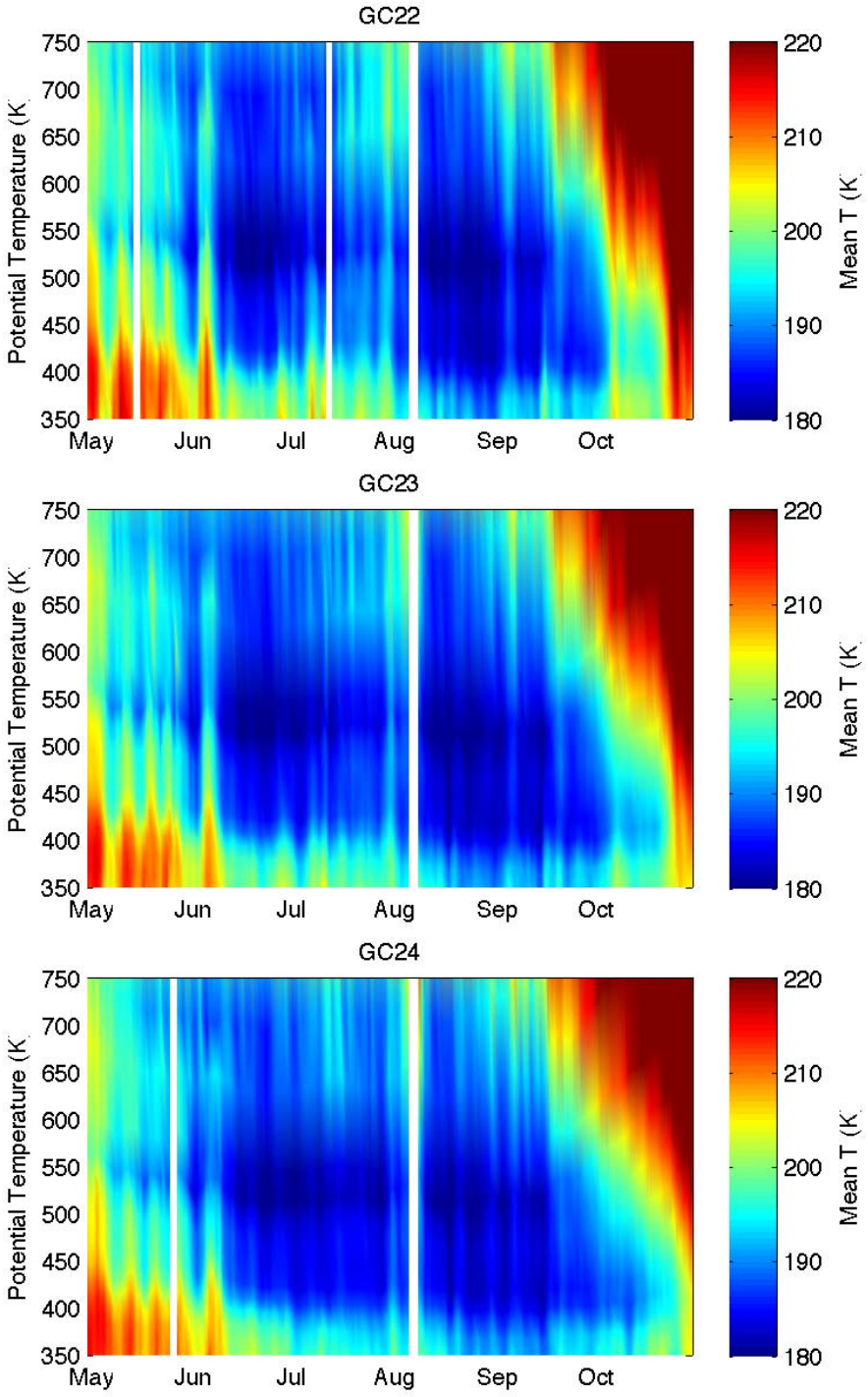

Figure 8.32. Like Figure 8.25, but for Antarctic Grid Cells 22, 23 & 24.

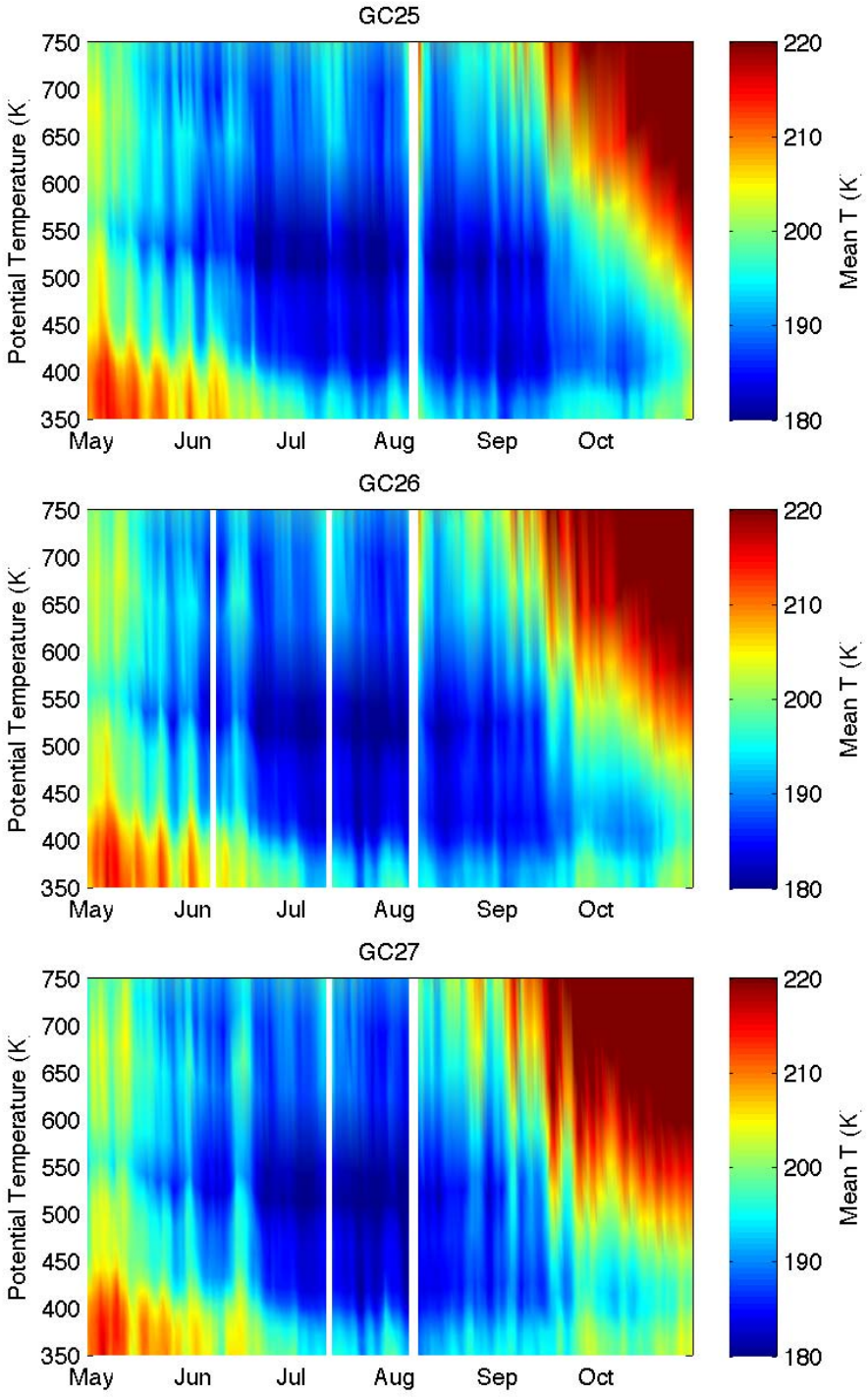

Figure 8.33. Like Figure 8.25, but for Antarctic Grid Cells 25, 26 & 27.

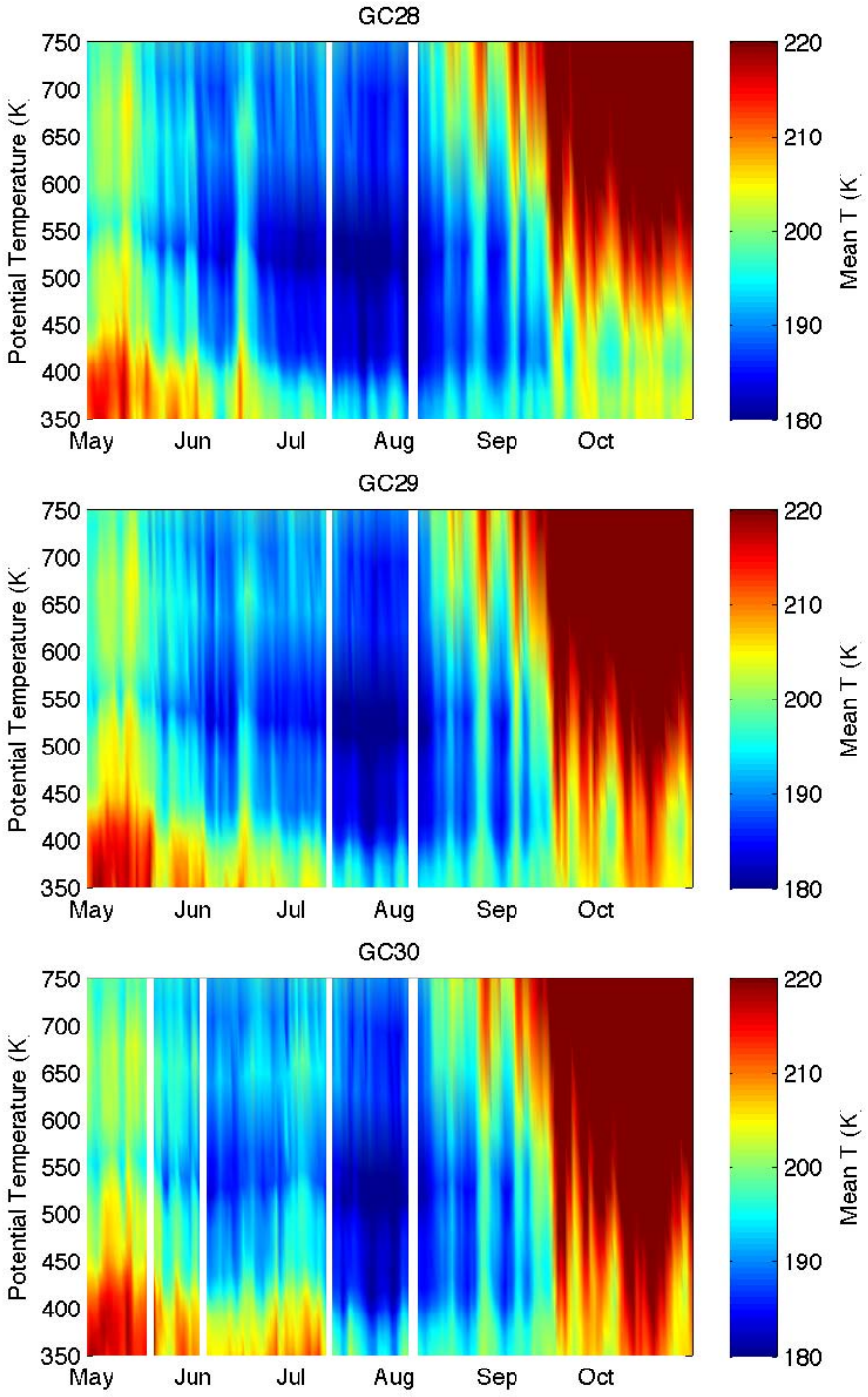

Figure 8.34. Like Figure 8.25, but for Antarctic Grid Cells 28, 29 & 30.

Chapter 9

DISCUSSION, SUMMARY AND CONCLUSIONS, FUTURE WORK.

9.1 Discussion

Santee et al. [2008b], using data from 2004 to 2005, recently reported HCl/Cl_y ratios of 70-80% of total inorganic chlorine before the onset of chlorine activation (nominal values) in the Antarctic stratosphere. The work employed three chlorine species in the stratosphere that were derived from two different datasets. The difference between the results of Santee et al. [2008b] and the work presented here, over the same timescale, rests in the fact that that for this work only two chlorine species were used to identify chlorine activation and deactivation, when assuming that HCl is the most important chlorine reservoir in the Antarctic stratosphere (e.g. *Jaeglé et al*., [1997]; *Michelsen et al*., [1999]; *Hayashida and Sugita*, [2007]; *Santee et al*., [2008b]). The identification of changes in HCl from the nominal period to the depletion phase may, therefore, identify regions for which inorganic chlorine has been activated in Antarctica. The motivation behind Figure 6.1 was to show the structure of HCl-ClO as an additional proxy for deriving changes in HCl species.

In addition to the factors mentioned above, the effect of increasing cloud evaporation rates due to ice NO_3^- coating [*Goodman et al*., 1997] and as function of altitude may play a role in chlorine activation. If PSCs remain in the stratosphere for a

longer period, and, thus, provide more surfaces on which the reaction shown in Equation 1.1.1 can take place the result is possible. Additionally, the solvation/dissolution of HCl in the quasi-liquid over-layer of solid PSCs [*Molina et al.*, 1993; *Bogdan et al*., 2003] is another possible implication for the microphysics of PSC (dynamically induced PSCs) and chlorine activation. However, the contribution of these factors over the Antarctic stratosphere is still an area for future work. Currently there is a lack of quantification of their contribution to chlorine activation observed above this region and the EOS MLS is unable to observe NO_3^- coated particles.

As noted in previous chapters, the pressure range of 100 hPa – 21.5 hPa (corresponding to an altitude range of approximately 17 km – 29 km) over which the Aura MLS measured significant HCl losses (not shown) during the winter corresponds to the altitude range reported by *Nedoluha et al*. [2003] and *Pitts et al*. [2009] for PSC. That the region of air depleted in HCl in the early season is much larger than the area of PSC identified using temperature data for different PSC formation threshold scenarios is clear. The work presented here represents the first time that the PSC area vs. the HCl area discrepancy in 2006 has been noted.

Additionally, the results provided for the ramp-up to HCl depletion shown in Panel 6a are consistent with the short timescale for the reaction shown in Equation 1.1.1. The result was experimentally measured by *Molina et al*. [1987] and calculated using the coupled microphysical/chemical model reported by *Drdla and Schoeberl* [2002]. The results (Figure 6.2) of inorganic chlorine partitioning changes in the lower and middle stratosphere show a correlation with temperature, particularly during the HCl uptake phase in agreement with *Zhang et al*. [1994]. The results of *Zhang et al.* [1994] were derived from experimental measurements of HCl uptake on SAT surfaces. Calculations

(not shown) for PSC areal coverage, when choosing a T_{NAT} threshold of [195 K ± 3 K], show the sensitivity of PSC areas.

A brief analysis of zonal means for Antarctic ozone (O_3) mixing ratios measured by the Aura MLS in the region [60ºS – 80ºS] during 2006 (not shown) revealed that ozone losses are larger at higher latitudes for different altitudes, consistent with the fact that HCl depletion lasts longer at higher latitudes (HCl recovery is slower) and with the role that O_3 plays in the rate of HCl production [*Prather and Jaffe*, 1990; *Mickley et al.*, 1997; *Michelsen et al.*, 1999; *Wilmouth et al.*, 2006]. At lower polar latitudes HCl recovery is faster and O_3 losses are smaller, compared to those closer to the pole where O_3 losses are larger. Thus, the timing of the large increase in HCl concentration (HCl recovery phase starts) is a good indicator of the efficiency of ozone destruction during the season. *Douglass et al*. [1995] state that HCl increases more rapidly in Antarctica than in the Arctic, consistent with the total ozone destroyed above each polar region each season.

Additionally, the different patterns of HCl depletion shown in Figure 6.2, as a function of latitude, are consistent with *Jaeglé et al*. [1997], whose work suggested that different amounts of ozone loss may have had an impact on the regime of chlorine recovery, as also proposed by previous studies [*Douglass et al.*, 1995; *Mickley et al.*, 1997; *Douglass and Kawa*, 1999; and *Grooß et al.*, 1997, 2005b]. Different patterns of HCl depletion as a function of altitude, shown in Panel 6a, could also be explained in a similar manner as those for Figure 6.2 for different polar latitudes in relation to ozone depletion. Nevertheless, other reasons the 60-65ºS data indicate faster HCl recovery or less depletion may be due to the irregular geometry of the vortex, which may less perturb the results if PV or equivalent latitudes are used to sort the data and mixing across the edge of the vortex.

Results for the inferred HCl, using Equation 6.5.1 and Aura MLS nitrous oxide (not shown), agreed well with HCl values measured by Aura MLS in Antarctica (not shown) before the onset of chlorine activation during 2006. For comparison, the mixing ratios of inferred HCl were examined using the expression of *Bonne et al*. [2000], which was derived from chlorine data in the Arctic. The inferred HCl values obtained using this expression, carried to Antarctic stratospheric conditions, underestimated HCl concentrations at high levels when compared to HCl values measured using Aura MLS values averaged over the region [60ºS – 80ºS] during 2006 (not shown). The findings may suggest that the dynamics affecting chlorine activation are peculiar to each region and time. Therefore, they should be considered for the bulk of chlorine activation above each polar region.

The H_2O–temperature relationship shown in Figure 6.4 suggests that the dehydration process observed during the season using Aura MLS data is consistent with PSC formation, given that the region and the timing of both events seem to match relatively well.

The relative lack of correspondence of T_{ACL} and HCl-depleted areas at altitudes above 20 km (not shown) reinforces the explanation provided here that the dynamics, due to small-scale temperature perturbations for stratospheric gravity waves, may also be impacting the rate and the extent of chlorine activation observed during the early season. The results may also reveal that the role of sulfate aerosols in chlorine activation alone may be more important at lower altitudes than previously thought.

Motivated by results presented by *Carslaw et al*. [1998] and *Kühl et al*. [2004] in the Arctic, and the results presented in this work together with the results of *Drdla and Müller* [2010], a robust quantification of the dynamic wave activity above Antarctica and its counterpart in the Arctic that contributes to chlorine activation as recently

presented by *Alexander et al*. [2011] for Antarctic PSC in 2007, leading to dynamically induced ozone losses, may offer a greater understanding of the role of dynamically induced PSC in chlorine activation, and, therefore, in ozone depletion.

9.2 SUMMARY AND CONCLUSIONS

In this work, the seasonal evolution of stratospheric chlorine partitioning over Antarctica during the winter 2006 season, as derived from Aura MLS satellite observations, was analyzed. Two different temperature data sets and five atmospheric chemical molecules for quantifying the role of PSC in chlorine activation were then utilized. Losses of the main chlorine reservoirs above Antarctica were tracked and quantified using a HCl depression identification algorithm developed for three different scenarios during the PSC season. PSC area was derived by thresholding the satellite and reanalysis standard temperature for three NAT formation threshold schemes.

The results, as presented in Table 6.1, did not reveal a consistent relationship between PSC and HCl depleted areas for different PSC formation temperature thresholds at four different altitudes. The result was particularly clear at lower levels, where correlation coefficients calculated over a full PSC season from 2005 to 2009 were found to be the lowest in the Antarctic polar stratosphere. The result is comparable to the work of *Harris et al.* [2010] who used a different methodology for the Arctic, but found that the largest discrepancy for ozone loss and PSC areas (deduced from NAT existence) occurred at lower stratospheric altitudes.

The results also indicated that HCl depletion areas were generally larger than PSC areas derived from different T_{NAT} thresholds, especially during the HCl uptake phase in the early Antarctic winter season at 20 km and 23 km. The lack of correspondence may either be due to air mass processing by PSC or to small-scale temperature perturbations

that standard satellite products do not observe. The results indicate that liquid aerosols are relatively more effective in heterogeneous processing at lower polar altitudes, while frozen aerosols (NAT) are potentially more effective at higher altitudes, in agreement with *Portmann et al.* [1996] and the previous suggestions of *Hofmann and Oltmans* [1992].

While limitations due to available data for the chlorine activation analysis presented in this work must be kept in mind, it does appear that the first approach that used HCl extensively as a proxy for chlorine activation surrounding the Antarctic continent yielded diagnostic results which suggest that using T_{NAT} as a threshold for chlorine activation in the lower stratosphere may not be sufficient. The results may have implications for ozone depletion and highlight the importance of considering this as a source of likely uncertainty in current model simulations of ozone loss that should, at least, be calculated and stated. *Morgenstern et al.* [2011] suggested that for almost every single process relevant to stratospheric climate chemistry modelling, there are a variety of different approaches taken in CCMs. Therefore, this diversity complicates the interpretation of any differences found between individual models. In this regard, the CCM community should assess a consensus threshold for chlorine activation in order to avoid discrepancies in models due to the utilized Cl activation threshold.

The results presented also help sharpen our understanding of the microphysics and the availability of PSC/aerosols in the early season, as well as their role in chlorine activation as catalysts over this period. Descent in the vortex and mixing across the vortex edge could strongly perturb the results of this study. Unless these processes and their outcomes are quantified, little can be said conclusively regarding the co-locations of PSCs and chlorine activation.

9.3 FUTURE WORK

Future work will aim to extend the analysis presented here for HCl depletion to winter seasons in the Arctic, as well as Antarctica, and will incorporate a dynamic analysis of the quantification of HCl losses inside the Antarctic vortex as a function of location and time. Ultimately, this analysis should provide a mechanism for characterizing chlorine activation as a function not only of PSC (namely T_{NAT}) and sulfate aerosol loading (namely T_{ACL}), but also of dynamics (e.g. *Hertzog et al.*, [2011]). Future work will also seek to collaborate with a photochemical modeller, since it is outside of the scope of this study.

The research undertaken in this thesis has raised several issues regarding both the derivation of the HCl depletion algorithm and the application of the results to current theory. Further study of the results, particularly in combination with meteorological datasets and photochemical models, should lead to significant new information on the formation and existence of PSC and its exact relationship with dynamical effects such as gravity waves in chlorine activation. It also will give us further information on the usage of one, two, or three different satellite-based datasets's versions and whether to use the three of them to solve one problem, or only one, within the timeframe defined for a research project of the present nature.

9.3.1. Chlorine Activation Threshold: A Robust parameterization

The link between chlorofluorocarbons (CFCs) and ozone depletion [*Molina and Rowland*, 1974] via polar heterogeneous ozone-chemistry [*Solomon* et al, *et al.*, 1986; *Solomon* 1999] is widely known. However, the core role of Polar Stratospheric Clouds (PSCs) in chlorine activation, and the conversion of inert chlorine reservoirs (e.g. HCl and $ClONO_2$) into highly photochemical reactive chlorine forms (e.g. Cl_2, Cl^-, HOCl,

$ClNO_2$) still remains, in some respects, poorly quantified [e.g. *Portmann et al, et al.*, 1996; *Lowe and MacKenzie*, 2008]. According to previous studies, the need for an appropriate mapping tool and/or an efficient parameterization that comprehensively associates aerosol types from the set of PSC types currently known to be associated with chlorine activation in global-scale model calculations is missing in the literature.

9.3.2. Photochemical model.

To seek collaboration with a photochemical modeller and/or comparison of the relevant data presented in this thesis with a photochemical model, possibly one that includes transport, especially descent within the vortex in the future.

9.3.3. Small-scale Temperature fluctuations, PSC and chlorine activation.

Chemical response to the application of the work by *Wright* [2010b] in detection of stratospheric gravity waves for analysis of the response of the chemical perturbations work approach described in this dissertation, to temperature fluctuations in both the polar stratospheres via this work and *Murphy and Ravishankara's* [1994]. On the other hand, none of the existing parameterizations (to my knowledge) tries to directly simulate temperature perturbations that are of interest for PSC studies. This would probably be very interesting but would require a devoted study on its own. One approach that could be used on this topic, though, is to perform mesoscale numerical simulations of such wave-induced PSCs (e.g., [*Noel, V. et al.*, 2009]) and try to obtain some general knowledge from these [*Hertzog*, 2011].

9.3.4. Methane and chlorine nitrate data.

Acquisition of methane and chlorine nitrate data relevant to this study in order to

evaluate HCl production more comprehensively above Antarctica (and the Arctic) derived from satellite measurements or others may be relevant.

9.3.5. AH's Infrared Fourier Transform Spectrometer (FTIR) equipment implementation.

The total column abundance measurements of HCl from the ground-based FTIR system operating at Arrival Heights (AH): the HCl data only is measured when there are clear sky conditions. Usually the data are averaged from 2–3 measurements per week. Total column data only is submitted to the NDACC Database. The retrieval of profile data is still under consideration, since there are too many caveats and errors for general use at the current time [*Smale*, 2011].

Appendix A

EOS MLS v2.2 temperature: Quality Control Analysis

EOS MLS v2.2 temperature
Antarctic vortex region (-60º --> -82.5º)

F1: 4 flags + T_error >=0 *'double qual-ctrl'*
F2: 4 flags + T_error >=0 + ±3 std *'double + statistical ctrl'*
F3: 4 flags *'simple qual-ctrl'*
F4: 0 flags *'no qual-ctrl'*

2004(nonzeros), average of temperature points per month:
same values for each pressure level

Month	F1	F2	F3	F4
Aug	523.3500	523.3500	523.3500	**561.9000**
Sep	533.0800	533.0800	533.0800	**568**
Oct	555.8571	555.8571	559.1071	**570.9286**
Nov	560.7000	560.7000	561.0667	**565.1667**
Dec	562.8696	562.8696	562.8696	**563**
			mean: 565.8	

2005

Month	F1	F2	F3	F4
Jan	567.0323	567.0323	567.0323	**569**
Feb	560.1613	560.1613	560.1613	**561.7097**
Mar	565.8387	565.8387	566.1613	**569.9677**
Apr	430.3448	430.3448	430.3448	**568.5517**
May	210	210	210	**564.6333**
Jun	350.1333	350.1333	357.5667	**644.9667**
Jul	472.9333	472.9333	473.2667	**568.3667**
Aug	548	548	548.3448	**567.1724**
Sep	529.5161	529.5161	531.0323	**568.3548**
Oct	559.4828	559.4828	559.4828	**565.3448**
Nov	564.8462	564.8462	564.8462	**567.3462**
Dec	566.0357	566.0357	566.0357	**567.0714**
			mean: 573.5	

2006

Month	F1	F2	F3	F4
Jan	564.8710	564.8710	565.1935	**566.5161**
Feb	551.8667	551.8667	552	**568.6667**
Mar	562.0800	562.0800	563	**566.8800**
Apr	500.7037	500.7037	500.7037	**567.3333**
May	364.5161	364.5161	365.5806	**554.7097**
Jun	322.4000	322.4000	322.4000	**565.7000**
Jul	517.4667	517.4667	517.5333	**561.9333**
Aug	558.4444	558.4444	559.7222	**568.7778**
Sep	491.7600	491.7600	494.0400	**566.3200**

Oct	554.1333	554.1333	554.2000	**567.7333**
Nov	561.8621	561.8621	561.8621	**565.7586**
Dec	568.3548	568.3548	568.3548	**569.1613**
			mean: 565.8	

2007

Month	F1	F2	F3	F4
Jan	564.0645	564.0645	564.0645	**566.4194**
Feb	567.6333	567.6333	567.6333	**569.1667**
Mar	566.6333	566.6333	566.6333	**567.9333**
Apr	482.5357	482.5357	482.5357	**569.3571**
May	260.1613	260.1613	260.1613	**565.2258**
Jun	396.4194	396.4194	396.7419	**566.1290**
Jul	495.4839	495.4839	495.4839	**549.3226**
Aug	549.5862	549.5862	549.5862	**567.1379**
Sep	510.4839	510.4839	511.2258	**568.7742**
Oct	562.7742	562.7742	562.7742	**569.7419**
Nov	558.9583	558.9583	558.9583	**560.5417**
Dec	562.1379	562.1379	562.2759	**563.3448**
			mean: 565.26	

2008

Month	F1	F2	F3	F4
Jan	565.8065	565.8065	566.1290	**569.7097**
Feb	566.6129	566.6129	566.7097	**569.7742**
Mar	547.2258	547.2258	547.4839	**548.7419**
Apr	482.5161	482.5161	482.5161	**568.8387**
May	292.0645	292.0645	292.6452	**560.2258**
Jun	335.8387	335.8387	335.8387	**564.5161**
Jul	538.5806	538.5806	539.2258	**568.9355**
Aug	554.0645	554.0645	554.5161	**567.6774**
Sep	496.2857	496.2857	496.2857	**568**
			mean: 565.2	

Appendix B

EOS MLS measurement locations and objectives

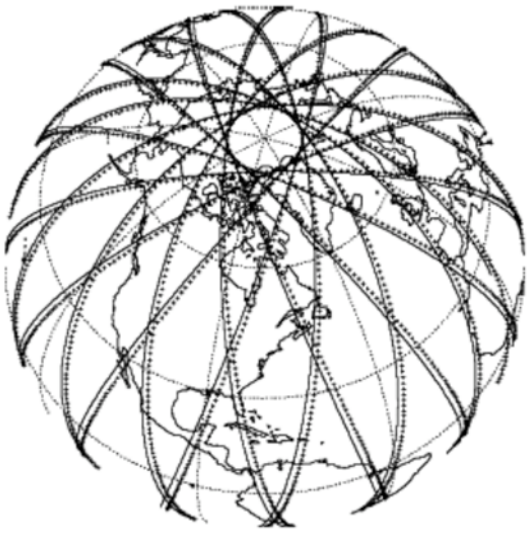

Figure B1. EOS MLS measurements locations (crosses) for a 24-h period. The suborbital track (continuous line) is slightly displaced because of Earth's rotation during the time the satellite moves forward to the MLS tangent point latitude. From *Waters et al.* [2006].

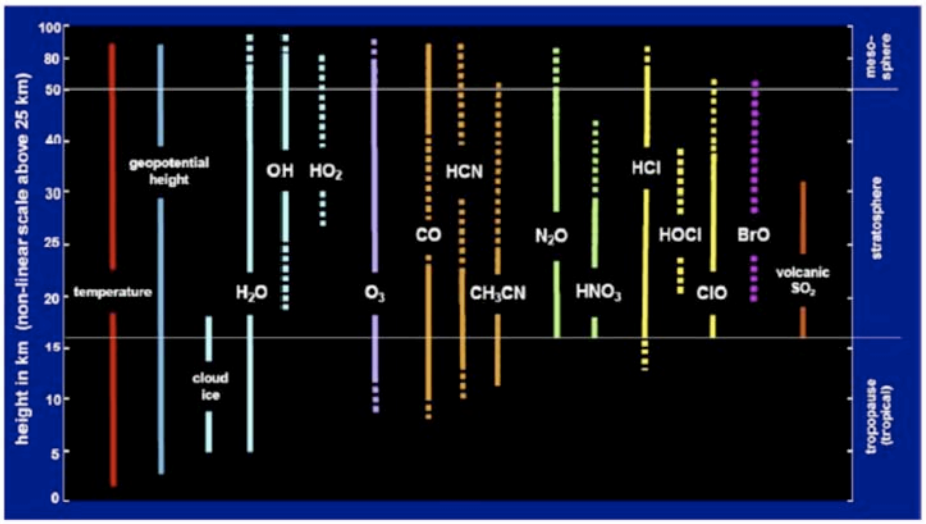

Figure B2. EOS MLS scientific measurement objectives. Solid lines indicate generally useful precision for individual profiles. Dotted lines indicate that zonal (or other) averages are generally needed to obtain useful precision. The height ranges shown here indicate what is ultimately expected to be achieved, and not necessarily achieved with initial data processing. Different colors indicate different chemical families. From *Waters et al.* [2006].

Appendix C

T_{NAT}, T_{ice} and T_{STS} computation derived from Aura MLS v.2.2--2005--

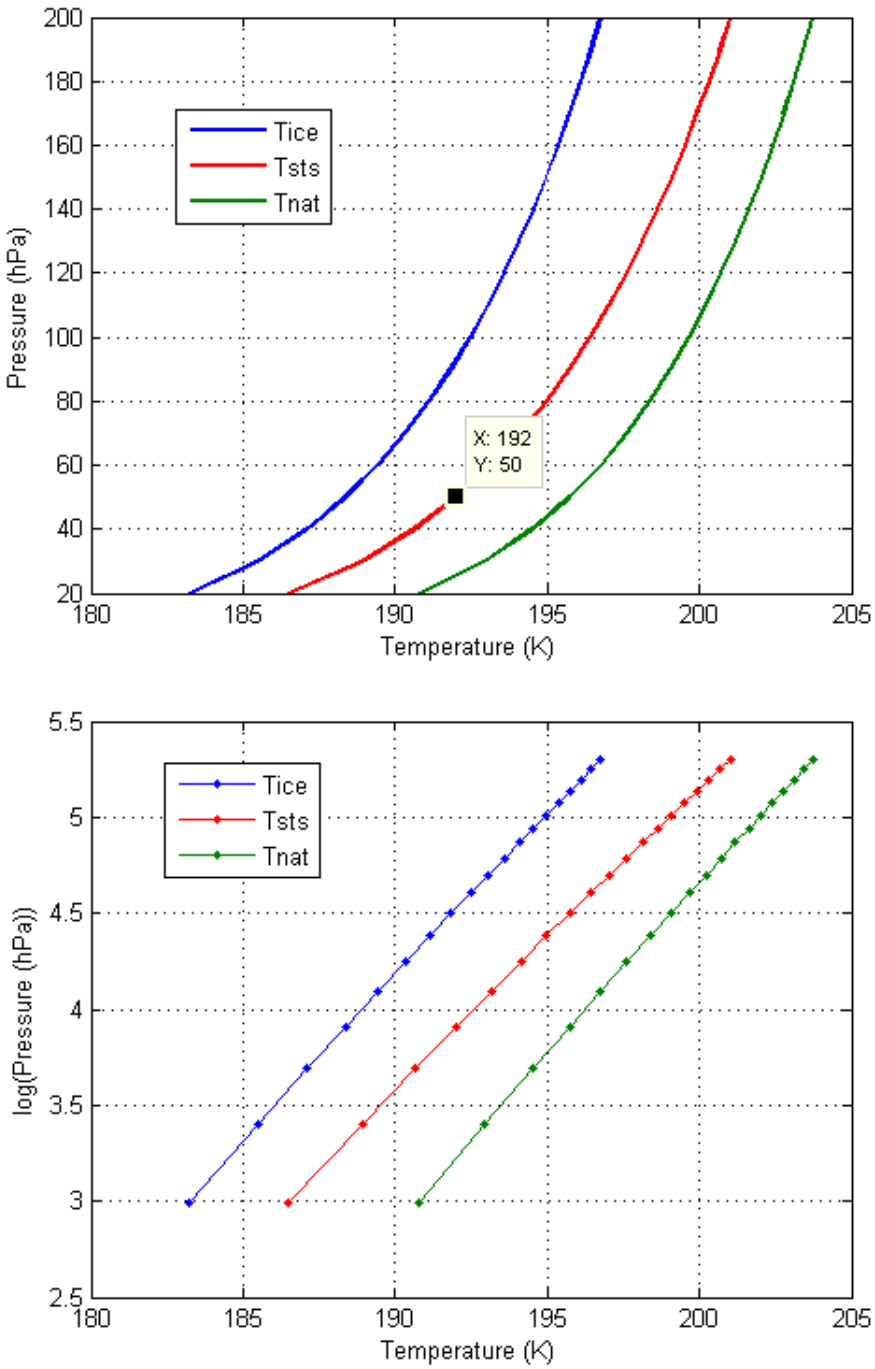

Figure C1. Computation of T_{ice} (blue), T_{NAT} (green) and T_{STS} (red) derived from Aura MLS observations of water vapor and nitric acid in 2005.

Appendix D

UT, LST and SZA programming routines

From EOS MLS v2.2 we can obtain information of time of two kinds: UT & LST (Local Solar Time). An extra field was added to the read_EOS_MLS_version2_data_plus.m function in order to get the LST directly from the v2.2 dataset. Thus, here are illustrated the three lines of code about this for each relevant EOS MLS retrieval:

```
EOS_MLS_data.time =
        hdf5read(FILENAME,'/HDFEOS/SWATHS/Temperature/GeolocationFields/Time');
EOS_MLS_data.lst    =
        hdf5read(FILENAME,'/HDFEOS/SWATHS/Temperature/GeolocationFields/LocalSolarTime');
EOS_MLS_data.sza    =
        hdf5read(FILENAME,'/HDFEOS/SWATHS/Temperature/GeolocationFields/SolarZenithAngle');
```

Results from doing a refinement to an original function conceived to calculate the parameter solar zenith angle (SZA) successfully from Aura MLS database receiving day, hour, and latitude as input parameters are shown in Figure D1. It can be noted that this old function was stored in the data_store node of the University of Canterbury's Department of Physics and Astronomy's Atmospheric Group before the author arrived, and it was improved/corrected by the author in order to calculate SZA. Ultimately, it was decided to utilize this parameter directly from Aura MLS dataset, with no programming function, just for simplicity.

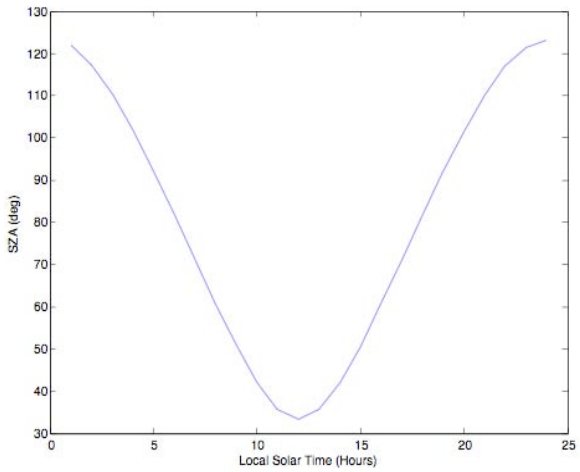

Figure D1. SZA calculations derived from modified solarzenithangle_function.m, at Latitude = 45º and day 111 for different hours of the day.

References I

Abbatt, J. P. D. and Molina, M. J. (1992), Heterogeneous interactions of $ClONO_2$ and HCl on nitric acid trihydrate at 202 K, *J. Phys. Chem*., 96(19), 7674-7679.

Alexander, S. P., Klekociuk, A. R., Pitts, M. C., McDonald, A. J., and Arevalo-Torres, A. (2011), The effect of orographic gravity waves on Antarctic Polar Stratospheric Cloud (PSC) occurrence and composition, *J. Geophys. Res*., *116*, D06109, doi:10.1029/2010JD015184.

Alexander, S. P., (2011), Personal Communication.

Austin, J., Shindell, D., Beagley, S. R., Bruhl, C., Dameris, M., Manzini, E., Nagashima, T., Newman, P., Pawson, S., Pitari, G., Rozanov, E., Schnadt, C., and Shepherd, T. G. (2003), Uncertainties and assessments of chemistry-climate models of the stratosphere, *Atmos. Chem. Phys*., 3, 1-27.

Barber, C. B., Dobkin, D. P. and Huhdanpaa, H. (1996), The Quickhull algorithm for convex hulls, *ACM Trans. Math. Softw*. 22, 469–483.

Barnett, J. J., C. L. Hepplewhite, S. Osprey, J. C. Gille, and R. Khosravi, 2008: Cross-validation of HIRDLS and COSMIC radio-occultation retrievals, particularly in relation to fine vertical structure. Proceedings of the SPIE, 7082, 16 – 16–7, doi:10.1117/12.800702.

Berthet, S. (2011), Personal communication.

Bevilacqua, R. M., Fromm, M. D., Alfred, J. M., Hornstein, J. S., Nedoluha, G. E., Hoppel, K. W., Lumpe, J. D., Randall, C. E., Shettle, E. P., Browell, E. V., Butler, C., Dornbrack, A., and Strawa, A. W. (2002), Observations and analysis of polar stratospheric clouds detected by POAM III during the 1999/2000 Northern Hemisphere winter, *J. Geophys. Res*., 107(D20), doi: 10.1029/2001JD000477.

Bogdan, A., Kulmala, M., MacKenzie, A. R., and Laaksonen, A. (2003), Study of finely divided aqueous systems as an aid to understanding the surface chemistry of polar stratospheric clouds: Case of HCl/H_2O and $HNO_3/HCl/H_2O$ systems, *J. Geophys. Res*., 108(D10), doi: 10.1029/2002JD002606.

Bonne, G. P., Stimpfle, R. M., Cohen, R. C., Voss, P. B., Perkins, K. K., Anderson, J. G., Salawitch, R. J., Elkins, J. W., Dutton, G. S., Jucks, K. W., and Toon, G. C. (2000), An examination of the inorganic chlorine budget in the lower stratosphere, *J. Geophys. Res*., 105(D2), 1957-1971.

Brasseur, G. P. and Solomon, S. (2005), Aeronomy of the Middle Atmosphere. Chemistry and Physics of the Stratosphere and Mesosphere, Third revised and enlarged edition, *Springer*, The Netherlands.

Browell, E. V., Butler, C. F., Ismail, S., Robinette, P. A., Carter, A. F., Higdon, N. S., Toon, O. B., Schoeberl, M. R., and Tuck, A. F. (1990), Airborne lidar

observations in the wintertime Arctic stratosphere - polar stratospheric clouds, *Geophys. Res. Lett*., 17(4), 385-388.

Campbell, J. R., and K. Sassen (2008), Polar stratospheric clouds at the South Pole from 5 years of continuous lidar data: Macrophysical, optical, and thermodynamic properties, *J. Geophys. Res.*, *113*, D20204, doi:10.1029/2007JD009680.

Cariolle, D., Muller, S., Cayla, F., and McCormick, M. P. (1989), Mountain waves, polar stratospheric clouds, and the ozone depletion over Antarctica, *J. Geophys. Res*., 94(D9), 11233-11240.

Carslaw, K. S., Wirth, M., Tsias, A., Luo, B. P., Dörnbrack, A., Leutbecher, M., Volkert, H., Renger, W., Bacmeister, J. T., Reimer, E., and Peter, T. (1998), Increased stratospheric ozone depletion due to mountain-induced atmospheric waves, *Nature*, 391(6668), 675-678.

Chubachi, S., 1984, Preliminary result of ozone observations at Syowa station from February 1982 to January 1983. *Memoirs of National Institute of Polar Research Special Issue*, 34, pp. 13–19.

Cox, R. A., MacKenzie, A. R., Müller, R. H., Peter, T., and Crutzen, P. J. (1994), Activation of stratospheric chlorine by reactions in liquid sulfuric acid, *Geophys. Res. Lett*., 21(13), 1439-1442.

Crutzen, P. J., Müller, R., Brühl, C., and Peter, T. (1992), On the potential importance of the gas phase reaction CH3O2 + ClO → ClOO + CH3O and the heterogeneous reaction HOCl + HCl → H2O + Cl2 in “ozone hole” chemistry, *Geophys. Res. Lett.*, *19*(11), 1113–1116, doi:10.1029/92GL01172.

Drdla, K. and Müller, R. (2010), Temperature thresholds for polar stratospheric ozone loss, *Atmos. Chem. Phys. Discuss*, 10, 28687-28720, doi:10.5194/acpd-10-28687-2010.

Drdla, K. and Schoeberl, M. R. (2002), Microphysical modeling of the 1999-2000 Arctic winter 2. Chlorine activation and ozone depletion, *J. Geophys. Res*., 108(D5), 8319, doi: 10.1029/2001JD001159.

Douglass, A. R., Schoeberl, M. R., Stolarski, R. S., Waters, J. W., Russell, J. M., Roche, A. E., and Massie, S. T. (1995), Interhemispheric differences in springtime production of HCl and ClONO2 in the polar vortices, *J. Geophys. Res*., 100(D7), 13967-13978.

Douglass, A. and Kawa, S. (1999), Contrast between 1992 and 1997 high-latitude spring Halogen Occultation Experiment observations of lower stratospheric HCl, *J. Geophys. Res*., 104(D15), 18739-18754.

Fahey, D. W., Kelly, K. K., Ferry, G. V., Poole, L. R., Wilson, J. C., Murphy, D. M., Loewenstein, M., and Chan, K. R. (1989), In situ measurements of total reactive nitrogen, total water, and aerosol in a polar stratospheric cloud in the Antarctic, *J. Geophys. Res*., 94(D9), 11299-11315.

Farman, J.C., Gardiner, B.G. and Shanklin, J.D., 1985, Large losses of total ozone in Antarctica reveal seasonal ClO_x/NO_x interaction. *Nature*, 315, pp. 207–210.

Froidevaux, L., et al. (2006), Early validation analyses of atmospheric profiles from EOS MLS on the Aura satellite, *IEEE Trans. Geosci. Remote Sens.*, 44, 1106–1121.

Froidevaux, et al. (2008), Validation of Aura Microwave Limb Sounder HCl measurements, *J. Geophys. Res*., 113(D15), D15S25, doi: 10.1029/2007JD009025.

Goodman, J., Verma, S., Pueschel, R. F., Hamill, P., Ferry, G. V., and Webster, D. (1997), New evidence of size and composition of polar stratospheric cloud particles, *Geophys. Res. Lett*., 24(5), 615-618.

Grooß, J., Pierce, R., Crutzen, P., Grose, W., and Russell, J. (1997), Re-formation of chlorine reservoirs in southern hemisphere polar spring, *J. Geophys. Res*., 102(11D), 13141-13152.

Grooß, J. U., Günther, G., Müller, R., Konopka, P., Bausch, S., Schlager, H., Voigt, C., Volk, C. M., and Toon, G. C. (2005a), Simulation of denitrification and ozone loss for the Arctic winter 2002/2003, *Atmos. Chem. Phys*., 5, 1437-1448.

Grooß, J. and Russell, J. (2005b), Technical note: A stratospheric climatology for O(3), H(2)O, CH(4), NO(x), HCl and HF derived from HALOE measurements, *Atmos. Chem. Phys*., 5, 2797-2807.

Hanson, D. and Mauersberger, K. (1988), Laboratory studies of the nitric-acid trihydrate – implications for the south polar stratosphere, *Geophys. Res. Lett*., 15(8), 855-858.

Harris, N.R.P., Lehmann, R., Rex, M., and von der Gathen, P. (2010), A closer look at Arctic ozone loss and polar stratospheric clouds, *Atmos. Chem. Phys*., 10(17), 8499-8510.

Hayashida, S. and Sugita, T. (2007), Hemispheric Contrast of Inorganic Chlorine Partitioning in the Polar Lower Stratosphere during Ozone Recovery Period Observed from Space, *SOLA*, 3, 117-120.

Hertzog, A., Vincent, R., Boccara, G., Vial, F. (2011), Balloon-Borne Observations of Gravity-Wave Momentum Fluxes over Antarctica and Surrounding Areas, paper presented at Chapman Conference on Atmospheric Gravity Waves and Their Effects on General Circulation and Climate, AGU, Hawaii, United States.

Hertzog, A., Vincent, R., (2011), Personal Communication.

Hofmann, D. J., and Oltmans, S. J. (1992), The effect of stratospheric water vapor on the heterogeneous reaction rate of $ClONO_2$ and H_2O for sulfuric acid aerosol, *Geophys. Res. Lett.*, *19*(22), 2211–2214, doi:10.1029/92GL02493.

Höpfner, M., Larsen, N., Spang, R., Luo, B. P., Ma, J., Svendsen, S. H., Eckermann, S. D., Knudsen, B., Massoli, P., Cairo, F., Stiller, G., Von Clarmann, T., and Fischer, H. (2006), MIPAS detects Antarctic stratospheric belt of NAT PSCs caused by mountain waves, *Atmos. Chem. Phys*., 6, 1221-1230.

Jaeglé, L., Y. L. Yung, G. C. Toon, B. Sen, and J. Blavier (1996), Balloon observations of organic and inorganic chlorine in the stratosphere: The role of HClO4 production on sulfate aerosols, *Geophys. Res. Lett.*, *23*(14), 1749–1752, doi:10.1029/96GL01543.

Jaeglé, L., Webster, C. R., May, R. D., Scott, D. C., Stimpfle, R. M., Kohn, D. W., Wennberg, P. O., Hanisco, T. F., Cohen, R. C., Proffitt, M. H., Kelly, K. K., Elkins, J., Baumgardner, D., Dye, J. E., Wilson, J. C., Pueschel, R. F., Chan, K. R., Salawitch, R. J., Tuck, A. F., Hovde, S. J., and Yung, Y. L. (1997), Evolution and stoichiometry of heterogeneous processing in the Antarctic stratosphere, *J. Geophys. Res*., 102(11D), 13235-13253.

Kalnay, E., et al. (1996), The NCEP/NCAR 40-year reanalysis project, *Bull. Amer. Meteor. Soc*., 77(3), 437-471.

Kent, G. S., Poole, L. R., and McCormick, M. P. (1986), Characteristics of Arctic polar stratospheric clouds as measured by airborne lidar, *J. Atmos. Sci*., 43(20), 2149-2161.

Kühl, S., Dornbrack, A., Wilms-Grabe, W., Sinnhuber, B. M., Platt, U., and Wagner, T. (2004), Observational evidence of rapid chlorine activation by mountain waves above northern Scandinavia, *J. Geophys. Res*., 109(D22),

Lambert, A., et al., (2007), Validation of the Aura Microwave Limb Sounder middle atmosphere water vapor and nitrous oxide measurements, *J. Geophys. Res.*, 112(D24), D24S36, doi: 10.1029/2007JD008724.

Leu, M. T. and Keyser, L. F. (2009), Vapor-deposited water and nitric acid ices: Physical and chemical properties, *Int. Rev. Phys. Chem.*, 28(1), 53-109.

Livesey, N.J., et al. (2007), Results for 'standard' MLS data products, in *Version 2.2 Level 2 data quality and description document*, *Tech. Rep. D-33509*, pp. 17-105, Jet Propul. Lab., Pasadena, Calif.

Livesey, N.J., et al. (2011), Results for 'standard' MLS data products, in *Version 3.3 Level 2 data quality and description document*, *Tech. Rep. D-33509*, pp. 20-151, Jet Propul. Lab., Pasadena, Calif.

Lowe, D. and MacKenzie, A. R. (2008), Polar stratospheric cloud microphysics and chemistry, *J. Atmos. Sol. Terr. Phys*., 70(1), 13-40.

Manney, G. L., et al. (2007), Solar occultation satellite data and derived meteorological products: Sampling issues and comparisons with Aura Microwave Limb Sounder, J. Geophys. Res., 112, D24S50, doi:10.1029/2007JD008709.

Manney, G. L. (2011), Personal communication.

Marti, J., and K. Mauersberger (1993), A survey and new measurements of ice vapor pressure at temperatures between 170 and 250K, *Geophys. Res. Lett.*, *20*(5), 363–366, doi:10.1029/93GL00105.

McCormick, M. P., Steele, H. M., Hamill, P., Chu, W. P., and Swissler, T. J. (1982), Polar stratospheric cloud sightings by SAM-II, *J. Atmos. Sci*., 39(6), 1387-1397.

McDonald, A. J., George, S. E., and Woollands, R. M. (2009), Can gravity waves significantly impact PSC occurrence in the Antarctic?, *Atmos. Chem. Phys*., 9(22), 8825-8840.

Michelsen, H. A., Webster, C. R., Manney, G. L., Scott, D. C., Margitan, J. J., May, R. D., Irion, F. W., Gunson, M. R., Russell, J. M., and Spivakovsky, C. M. (1999), Maintenance of high HCl/Cl-y and NOx/NOy in the Antarctic vortex: A chemical signature of confinement during spring, *J. Geophys. Res*., 104(D21), 26419-26436.

Mickley, L., Abbatt, J., Frederick, J., and Russell, J. (1997), Evolution of chlorine and nitrogen species in the lower stratosphere during Antarctic spring: Use of tracers to determine chemical change, *J. Geophys. Res*., 102(D17), 21479-21491.

Mogensen et al. (2011), Modelling atmospheric OH-reactivity in a boreal forest ecosystem, *Atmos. Chem. Phys*., 11(18), 9709-9719.

Molina, M. J. and Rowland, F. S. (1974), Stratospheric sink for chlorofluoromethanes – chlorine atomic-catalysed destruction of ozone, *Nature*, 249(5460), 810-812.

Molina, L. T. and Molina, M. J. (1987), Production of Cl_2O_2 from the self-reaction of the ClO radical, *J. Phys. Chem*., 91(2), 433-436.

Molina, M. J., Tso, T. L., Molina, L. T., and Wang, F. C. Y. (1987), Antarctic stratospheric chemistry of chlorine nitrate, hydrogen chloride, and ice: release of active chlorine, *Science*, 238(4831), 1253-1257.

Molina, M. J., Zhang, R., Wooldridge, P. J., McMahon, J. R., Kim, J. E., Chang, H. Y., and Beyer, K. D. (1993), Physical-chemistry of the $H_2SO_4/HNO_3/H_2O$ system: Implications for polar stratospheric clouds, *Science*, 261(5127), 1418-1423.

Morgenstern, O., P. Braesicke, F. M. O'Connor, A. C. Bushell, C. E. Johnson, S. M. Osprey, and J. A. Pyle (2009), Evaluation of the new UKCA climate-composition model—Part 1: The stratosphere, *Geosci. Model Dev*., 2, 43–57, doi:10.5194/gmd-2-43-2009.

Morgenstern, O., et al. (2010), Review of the formulation of present- generation stratospheric chemistry-climate models and associated external forcings, *J. Geophys. Res*., 115, D00M02, doi:10.1029/ 2009JD013728.

Morgenstern, O. (2011). Personal communication.

Murphy, D. M. and Koop, T. (2005), Review of the vapour pressures of ice and supercooled water for atmospheric applications, *Q. J. R. Meteorol. Soc*., 131(608), 1539-1565.

Murphy, D. M., and A. R. Ravishankara (1994), Temperature averages and rates of stratospheric reactions, *Geophys. Res. Lett.*, *21*(23), 2471–2474, doi:10.1029/94GL02287.

Nedoluha, G. E., Bevilacqua, R. M., Fromm, M. D., Hoppel, K. W., and Allen, D. R. (2003), POAM measurements of PSCs and water vapor in the 2002 Antarctic vortex, *Geophys. Res. Lett*., 30(15), 1796, doi: 10.1029/2003GL017577.

Noel, V., A. Hertzog, and H. Chepfer (2009), CALIPSO observations of wave-induced PSCs with near-unity optical depth over Antarctica in 2006–2007, *J. Geophys. Res.*, 114, D05202, doi:10.1029/2008JD010604.

Parrondo, M.C., Yela, M., Gil, M., von der Gathen, P., Ochoa, H., 2007, Mid-winter lower stratosphere temperaturas in the Antarctic vortex: comparison between observations and ECMWF and NCEP operacional models. *Atmos. Chem. Phys.*, 7, 435-441.

Pitts, M. C., Thomason, L. W., Poole, L. R., and Winker, D. M. (2007), Characterization of Polar Stratospheric Clouds with spaceborne lidar: CALIPSO and the 2006 Antarctic season, *Atmos. Chem. Phys*., 7(19), 5207-5228.

Pitts, M. C., Poole, L. R., and Thomason, L. W. (2009), CALIPSO polar stratospheric cloud observations: second-generation detection algorithm and composition discrimination, *Atmos. Chem. Phys*., 9(19), 7577-7589.

Poole, L. R. and McCormick, M. P. (1988), Polar stratospheric clouds and the Antarctic ozone hole, *J. Geophys. Res*., 93(D7), 8423-8430.

Portmann, R. W., S. Solomon, R. R. Garcia, L. W. Thomason, L. R. Poole, and M. P. McCormick (1996), Role of aerosol variations in anthropogenic ozone depletion in the polar regions, *J. Geophys. Res.*, *101*(D17), 22,991–23,006, doi:10.1029/96JD02608.

Prather, M., and A. H. Jaffe (1990), Global Impact of the Antarctic Ozone Hole: Chemical Propagation, *J. Geophys. Res.*, *95*(D4), 3473–3492, doi:10.1029/JD095iD04p03473.

Read, W. G., et al. (2007), Aura Microwave Limb Sounder upper tropospheric and lower stratospheric H2O and relative humidity with respect to ice validation, *J. Geophys. Res*., 112(D24), D24S35, doi: 10.1029/2007JD008752.

Sander, S. P., R. R. Friedl, and Y. L. Yung (1989), Rate of formation of the ClO dimer in the polar stratosphere: Implications for ozone loss, *Science*, 245, 1095–1098.

Santee, M. L., Froidevaux, L., Manney, G. L., Read, W. G., Waters, J. W., Chipperfield, M. P., Roche, A. E., Kumer, J. B., Mergenthaler, J. L., and Russell, J. M. (1996), Chlorine deactivation in the lower stratospheric polar regions during late winter: Results from UARS, *J. Geophys. Res*., 101(D13), 18835-18859.

Santee, M. L., Manney, G. L., Livesey, N. J., Froidevaux, L., MacKenzie, I. A., Pumphrey, H. C., Read, W. G., Schwartz, M. J., Waters, J. W., and Harwood, R. S. (2005), Polar processing and development of the 2004 Antarctic ozone hole: First results from MLS on Aura, *Geophys. Res. Lett*., 32(12), L12817, doi: 10.1029/2005GL022582.

Santee, M. L., et al., (2007), Validation of the Aura Microwave Limb Sounder HNO_3 measurements, *J. Geophys. Res*., 112(D24), D24S40, doi: 10.1029/2007JD008721.

Santee, M. L., et al., (2008a), Validation of the Aura Microwave Limb Sounder ClO measurements, *J. Geophys. Res*., 113(D15), D15S22, doi: 10.1029/2007JD008762.

Santee, M. L., MacKenzie, I. A., Manney, G. L., Chipperfield, M. P., Bernath, P. F., Walker, K. A., Boone, C. D., Froidevaux, L., Livesey, N. J., and Waters, J. W. (2008b), A study of stratospheric chlorine partitioning based on new satellite

measurements and modeling, *J. Geophys. Res*., 113(D12), D12307, doi: 10.1029/2007JD009057.

Santee, M. L., Sander, S. P., Livesey, N. J., and Froidevaux, L. (2010), Constraining the chlorine monoxide (ClO)/chlorine peroxide (ClOOCl) equilibrium constant from Aura Microwave Limb Sounder measurements of nighttime ClO, *Proc. Nat. Acad. Sci.*, 107(15), 6588-6593.

Santee, M. L. (2010), Personal communication.

Seinfeld J. H. and Pandis S. N., (1998), Atmospheric chemistry and physics. From air pollution to climate change, *John Wiley, Sons, Inc*., New York, 1326 pp.

Schwartz, M. J., et al. (2008), Validation of the aura microwave limb sounder temperature and geopotential height measurements, *J. Geophys. Res*., 113(D15), D15S11, doi: 10.1029/2007JD008783.

Shindell, D. T., Rind, D., and Lonergan, P. (1998), Increased polar stratospheric ozone losses and delayed eventual recovery owing to increasing greenhouse-gas concentrations, *Nature*, 392(6676), 589-592.

Smale, Dan, (2011). Personal communication.

Solomon, S., Garcia, R. R., Rowland, F. S. and Wuebbles, D. J. (1986), On the depletion of Antarctic ozone, *Nature*, 321(6072), 755-758.

Solomon, S. (1999), Stratospheric ozone depletion: A review of concepts and history, *Rev. Geophys*., 37(3), 275-316.

Solomon, Susan, (2011), Personal Communication.

SPARC CCMVal (2010), Report on the Evaluation of Chemistry-Climate Models, V. Eyring, T. G. Shepherd, D. W. Waugh (Eds.), SPARC Report No. 5, WCRP-X, WMO/TD-No. X, 2010.

Tabazadeh, A., Turco, R. P., Drdla, K., Jacobson, M. Z., and Toon, O. B. (1994), A study of Type-I polar stratospheric cloud formation, *Geophys. Res. Lett.*, 21(15), 1619-1622.

The World Factbook 2010. Washington, DC: Central Intelligence Agency, 2010.

Tilmes, S., D. E. Kinnison, R. R. Garcia, R. Müller, F. Sassi, D. R. Marsh, and B. A. Boville (2007), Evaluation of heterogeneous processes in the polar lower stratosphere in the Whole Atmosphere Community Climate Model, J. Geophys. Res., 112, D24301, doi:10.1029/2006JD008334.

Tolbert, M. A., Rossi, M. J., Malhotra, R., and Golden, D. M. (1987), Reaction of chlorine nitrate with hydrogen chloride and water at Antarctic stratospheric temperatures, *Science*, 238(4831), 1258-1260.

Tolbert, M. A. and Toon, O. B. (2001), Atmospheric science - Solving the PSC mystery, *Science*, 292(5514), 61-63.

Toohey, D.W., Availone, L.M., Lait, L.R., Newman, P.A., Schoeberl, M.R., Fahey, D.W., Woodbridge, E.L., Anderson, J.G. (1993), The seasonal evolution of reactive chlorine in the northern hemisphere stratosphere. *Science* 261, 1134–1136.

Toon, O. B., Browell, E. V., Kinne, S., and Jordan, J. (1990), An analysis of lidar observations of polar stratospheric clouds, *Geophys. Res. Lett.*, 17(4), 393-396.

Turco, R. P., Toon, O. B., and Hamill, P. (1989), Heterogeneous physicochemistry of the polar ozone hole, *J. Geophys. Res*., 94(D14), 16493-16510.

Urban, J., Pommier, M., Murtagh, D. P., Santee, M. L., and Orsolini, Y. J. (2009), Nitric acid in the stratosphere based on Odin observations from 2001 to 2009-Part 1: A global climatology, *Atmos. Chem. Phys*., 9(18), 7031-7044

Voigt, C., Schlager, H., Roiger, A., Stenke, A., de Reus, M., Borrmann, S., Jensen, E., Schiller, C., Konopka, P., and Sitnikov, N. (2008), Detection of reactive nitrogen containing particles in the tropopause region - evidence for a tropical nitric acid trihydrate (NAT) belt, *Atmos. Chem. Phys*., 8(24), 7421-7430.

Waters, J. W., et al. (2006), The Earth observing system microwave limb sounder (EOS MLS) on the Aura satellite, *IEEE Trans. Geosci. Remote Sens*., 44(5), 1075-1092.

Webster, C. R., May, R. D., Toohey, D. W., Avallone, L. M., Anderson, J. G., Newman, P., LAIT, L., Schoeberl, M. R., Elkins, J. W., and Chan, K. R. (1993), Chlorine chemistry on polar stratospheric cloud particles in the Arctic winter, *Science*, 261(5125), 1130-1134.

Webster, C. R., May, R. D., Michelsen, H. A., Scott, D. C., Wilson, J. C., Jonsson, H. H., Brock, C. A., Dye, J. E., Baumgardner, D., Stimpfle, R. M., Koplow, J. P., Margitan, J. J., Proffitt, M. H., Jaegle, L., Herman, R. L., Hu, H., Flesch, G. J., and Loewenstein, M. (1998), Evolution of HCl concentrations in the lower stratosphere from 1991 to 1996 following the eruption of Mt. Pinatubo, *Geophys. Res. Lett*., 25(7), 995-998.

Webster, C. R., Michelsen, H. A., Gunson, M. R., Margitan, J. J., Russell, J. M., Toon, G. C., and Traub, W. A. (2000), Response of lower stratospheric HCl/Cl-y to

volcanic aerosol: Observations from aircraft, balloon, space shuttle, and satellite instruments, *J. Geophys. Res*., 105(D9), 11711-11719.

Weisstein, E. W. (2011), "Spherical Trigonometry." From MathWorld--A Wolfram Web Resource. http://mathworld.wolfram.com/SphericalTrigonometry.html

Weisstein, E. W. (2011), "Great Circle." From MathWorld--A Wolfram Web Resource. http://mathworld.wolfram.com/GreatCircle.html

Wilmouth, D. M., Stimpfle, R. M., Anderson, J. G., Elkins, J. W., Hurst, D. F., Salawitch, R. J., and Lait, L. R. (2006), Evolution of inorganic chlorine partitioning in the Arctic polar vortex, *J. Geophys. Res*., 111(D16), D16308, doi: 10.1029/2005JD006951.

Wohltmann, I. and Rex, M. (2008). Improvement of vertical and residual velocities in pressure or hybrid sigma-pressure coordinates in analysis data in the stratosphere, *Atmos. Chem. Phys*., 8(2), 265-272

World Meteorological Organization (2006), Scientific Assessment of Ozone Depletion: 2006, *Global Ozone Res. and Monit. Proj. Rep. 50, Executive Summary*, Geneva, Switzerland.

Wright, C. J., S. M. Osprey, J. J. Barnett, L. J. Gray, and J. C. Gille (2010a), High Resolution Dynamics Limb Sounder measurements of gravity wave activity in the 2006 Arctic stratosphere, *J. Geophys. Res*., 115, D02105, doi:10.1029/2009JD011858.

Wright, C., (2010b). Detection of stratospheric gravity waves using HIRDLS data, *DPhil*, University of Oxford.

Wright, C. J., Rivas, M. B., and Gille, J. C. (2011), Intercomparisons of HIRDLS, COSMIC and SABER for the detection of stratospheric gravity waves, Atmos. Meas. Tech., 4, 1581-1591, doi:10.5194/amt-4-1581-2011.

Zhang, R. Y., Jayne, J. T., and Molina, M. J. (1994), Heterogeneous interactions of $ClONO_2$ and HCl with sulfuric-acid tetrahydrate – implications for the stratosphere, *J. Phys. Chem*., 98(3), 867-874.

Zhou, L. (2011), Personal communication.

Zondlo, M. A.; Hudson, P. K.; Prenni, A. J. and Tolbert, M. A. (2000), Chemistry and Microphysics of Polar Stratospheric Clouds and Cirrus Clouds, *Annu. Rev. Phys. Chem*., 51, 473.

Zou, P., Derecskei-Kovacs, A., and North, S. W. (2003), Theoretical calculation of $ClONO_2$ and $BrONO_2$ bond dissociation energies, *J. Phys. Chem*. A, 107(6), 888-896.

References II

Bernath, David. (1987). Technical Memo 33. Standard UTM-to-GEO/GEO-to-UTM Coordinate Conversion Algorithms. US Army Jet Propulsion Laboratory.

Bugayevskiy, L.M., Snyder, J.P. Map projections: a reference manual. Taylor & Francis Ltd, 1995.

Defense Mapping Agency Technical Manual 8358.2 (DMA TM 8358.2), The Universal Grids: Universal Transverse Mercator (UTM) and Universal Polar Stereographic (UPS), Defense Mapping Agency (1989).

Kern, W. F. and Bland, J. R. Solid Mensuration with Proofs, 2nd ed. New York: Wiley, 1948.

Maling, D. H. Coordinate Systems and map projections. Pergamon Press, 1992. 357, 443.

McDonnell, P.W. Introduction to map projections.. Marcel Dekker, Inc, 1979.

Pearson, F. II. Map projections: theory and applications. CRC Press, 1990. 182.

POSC, Epicentre Version 2.2 Logical Data Model. Projections and Projected Coordinate Systems, 2008, Petrotechnical Open Software Corporation (POSC) Specifications.

Richardus, P., Adler, R.K. Map projections for geodesists, cartographers and geographers. North-Holland Publishing Company, 1972. 137.

Snyder, John P. (1987). Map Projections - A Working Manual. U.S. Geological Survey Professional Paper 1395. 57, 157.